

Exploring the Chemical Modifications in Periodic Mesoporous Silica Materials for Heterogeneous Catalytic Applications

by

Betsy K. J.

AcSIR Registration Number: 10CC18A26061

A thesis submitted to the
Academy of Scientific & Innovative Research
for the award of the degree of
DOCTOR OF PHILOSOPHY
in
SCIENCE

Under the supervision of
Dr. C. P. Vinod



CSIR- National Chemical Laboratory, Pune



Academy of Scientific and Innovative Research
AcSIR Headquarters, CSIR-HRDC campus
Sector 19, Kamla Nehru Nagar,
Ghaziabad, U.P. – 201 002, India

January 2022

Certificate

This is to certify that the work incorporated in this Ph.D. thesis entitled, "Exploring the Chemical Modifications in Periodic Mesoporous Silica Materials for Heterogeneous Catalytic Applications", submitted by Betsy K. J. to the Academy of Scientific and Innovative Research (AcSIR) in fulfillment of the requirements for the award of the Degree of Doctor of Philosophy in Science, embodies original research work carried-out by the student. We, further certify that this work has not been submitted to any other University or Institution in part or full for the award of any degree or diploma. Research material(s) obtained from other source(s) and used in this research work has/have been duly acknowledged in the thesis. Image(s), illustration(s), figure(s), table(s) etc., used in the thesis from other source(s), have also been duly cited and acknowledged.



Signature of the Student

Name : Betsy K. J.

Date : 05-01-2022

Place : Pune



Signature of the Supervisor

Name : Dr. C. P. Vinod

Date : 05-01-2022

Place : Pune

STATEMENTS OF ACADEMIC INTEGRITY

I Betsy K. J., a Ph.D. student of the Academy of Scientific and Innovative Research (AcSIR) with Registration No. 10CC18A26061 hereby undertake that, the thesis entitled “Exploring the Chemical Modifications in Periodic Mesoporous Silica Materials for Heterogeneous Catalytic Applications” has been prepared by me and that the document reports original work carried out by me and is free of any plagiarism in compliance with the UGC Regulations on “*Promotion of Academic Integrity and Prevention of Plagiarism in Higher Educational Institutions (2018)*” and the CSIR Guidelines for “*Ethics in Research and in Governance (2020)*”.



Signature of the Student

Date : 05/01/2022

Place : Pune

It is hereby certified that the work done by the student, under my/our supervision, is plagiarism-free in accordance with the UGC Regulations on “*Promotion of Academic Integrity and Prevention of Plagiarism in Higher Educational Institutions (2018)*” and the CSIR Guidelines for “*Ethics in Research and in Governance (2020)*”.



Signature of the Supervisor

Name : Dr. C. P. Vinod

Date : 05/01/2022

Place : Pune

Acknowledgements

This thesis work would never have been accomplished without the encouragement, love, and support of some incredible people who made this Ph.D. journey a lifetime experience. All the precious moments I have spent here in CSIR-NCL, especially in my CAT & MOSS family, will always be cherished. I want to acknowledge all my teachers, family members, friends, and well-wishers who always motivated me to complete this long journey confidently.

First and foremost, I would like to express my deepest gratitude and respect to my research supervisor Dr. C. P. Vinod, who gave me an opportunity to be a part of this wonderful CAT & MOSS group. I am deeply indebted to him for his constant encouragement, guidance, patience, and support throughout my research tenure in NCL. The extensive lab facilities and creative freedom from his side were instrumental to the success of this journey. He always acted like a friend, a philosopher, and a true mentor whose thoughtful advice always motivated me to keep going during my most difficult times in research life. Thank you, sir, for believing in me and guiding me at every step of my Ph.D. work.

I would like to thank Dr. Ashish Lele, Director NCL, Prof. Ashwini Kumar Nangia (former director), Dr. Shubhangi Umbarkar, Head of Catalysis Division, Dr. C. S. Gopinath (former HOD) for providing me the opportunity to complete my Ph.D. work in this prestigious laboratory. I thank CSIR for the research fellowship. I extend my sincere thanks to Dr. T. Raja and Dr. E. Balaraman for their support. My sincere gratitude goes to my DAC members Dr. Ashok Giri, Dr. Ajithkumar, and Dr. Moneesha Fernandes, for their timely evaluation and suggestions throughout my Ph.D. program.

I acknowledge Dr. Dibyendu Bhattacharya and Chandrani Nayak from BARC, Mumbai, and RRCAT, Indore, for helping me to perform XAS experiments on Synchrotron Beamline. It was a wonderful experience visiting RRCAT and learning the functionality of Synchrotron radiations.

I take this occasion to thank all my seniors in NCL Dr. Sreedhala, Dr. Vysakh, Dr. Sunil Sekhar, Dr. Anish Lazar, for their support and helping me during the initial years of my research work. I thank Dr. Subha, Dr. Yogita, Dr. Rikta, Dr. Sharad, Dr. Preeti, Govind, Sumanta, Mahesh, Anuradha, Sisira, Bhargavi, Sanket, Pawan, Joytsna, Manali, Danu, and Pooja for creating a family atmosphere and making my Ph.D. tenure easy and joyous. I always appreciate their care and concern towards me. Thank you guys for your love and support. I personally thank all my

juniors Athira Krishnan, SreeDurga, Anjuna, and Anju who helped me to put up my thesis in current format. I wish you all the best for your bright future. I also thank all the M.Tech and M.Sc. trainees Cygnet, Neethu, Irine, Shebin, Nitheesh, Irfana, and Haripriya. I would like to thank my friends in NCL Dr. Aswathy, Dr. Ashok. Dr. Anju, Dr. Sudheesh, Periyasami, Prabu M., Prabu K., Arunima, Mira, Shabeeb, Vipin, Zinoy, Vidyanand, Kiran, and the A-14 team, for their help during the period. I thank all the technical staff in NCL Ms. Violet Samuel, Mr. R. K. Jha, Mr. Gholap for helping me to do various characterization. Thanks to all my non-NCL friends Anu, Praveen, Vipin and Anil, for always being there as support.

Finally, the most integral part of my life, my parents and my family, whose immense love and faith made it possible to complete my thesis successfully. I do not have words to express my gratitude to Appachan and Amma, who always gave me the freedom, strength, and confidence to achieve my goals. Sincere thanks to my elder brother Benny for taking care of me and making me feel protected. My sister-in-law, Ciya, for being there with me always. I thank Bonsy, my younger sister, and my best friend, who always stood by me. Lots of love to my niece, Ameya kutty, for making this journey cheerful. My Steadfast husband, Anish, for his enduring love, caring, and constant support throughout helped me to reach this goal of completing this task. I also thank my in-laws for being as supportive which added to the successful completion of my thesis.

Above all, praises and thanks to Almighty God for his showers of blessing and granting me the capability to proceed successfully.

Betsy K. J.

.....Dedicated to My Parents.....

Table of Contents

Chapter 1: General Introduction.....	1
1.1 Catalysis	2
1.2 Homogeneous Catalysis.....	3
1.3 Heterogeneous Catalysis	3
1.4 Nanocatalysis.....	3
1.5 Metal Nanoparticles in Catalysis.....	5
1.6 Porous Support Materials.....	6
1.7 Hybrid Mesoporous Silica Materials.....	7
1.8 Characterization of Nanocatalysts.....	10
1.8.1 Diffuse Reflectance UV-Visible Spectroscopy.....	10
1.8.2 X-Ray Diffraction Analysis.....	11
1.8.3 N ₂ Porosimetry Analysis.....	11
1.8.4 Thermal Analysis.....	12
1.8.5 Inductively Coupled Plasma Atomic Emission Spectroscopy	13
1.8.6 CHNS Elemental Analysis.....	13
1.8.7 Fourier Transform Infrared Spectroscopy.....	13
1.8.8 Raman Spectroscopy.....	14
1.8.9 Nuclear Magnetic Resonance (NMR) Spectroscopy.....	14
1.8.10 X-ray Photoelectron Spectroscopy.....	15
1.8.11 X-ray Absorption Spectroscopy.....	16
1.8.12 Transmission Electron Microscopy (TEM).....	17
1.8.13 Scanning Electron Microscopy (SEM).....	18
1.9 Catalytic Reaction over Nanostructured Catalysts	18
1.9.1 Cyclohexane Oxidation.....	18
1.9.2 Phenol Hydrogenation.....	19
1.9.3 Olefin Epoxidation	20
1.9.4 CO ₂ Hydrogenation	20
1.9.5 Reductive Amination Reaction	22

1.10 Scope and Objective of the Thesis.....	23
---	----

1.11 References.....	25
----------------------	----

Chapter 2: Metal-oxide (Cr and Ru) Supported Periodic Mesoporous Silica for Heterogeneous Catalysis

Part 2A. Cyclohexane Oxidation Reaction over Cr-oxide Supported MCM-41 Catalyst

2A.1 Introduction.....	32
------------------------	----

2A.2 Experimental.....	33
------------------------	----

2A.2.1 Synthesis of MCM-41 Nanospheres	33
--	----

2A.2.2 Synthesis of CrO _x -MCM-41.....	33
---	----

2A.2.3 Catalysts Characterization.....	34
--	----

2A.2.4 Catalytic Activity Test.....	35
-------------------------------------	----

2A.3 Result and Discussion.....	36
---------------------------------	----

2A.3.1 X-ray Diffraction.....	36
-------------------------------	----

2A.3.2 N ₂ Porosimetry.....	37
--	----

2A.3.3 Electron Microscopy.....	38
---------------------------------	----

2A.3.4 Solid-State NMR Spectroscopy.....	39
--	----

2A.3.5 DRUV-Visible Spectroscopy Analysis.....	40
--	----

2A.3.6 IR Spectroscopy.....	41
-----------------------------	----

2A.3.7 Raman Spectroscopy	42
---------------------------------	----

2A.3.8 X-ray Absorption Spectroscopy (XAS).....	43
---	----

2A.3.9 X-ray Photoelectron Spectroscopy.....	46
--	----

2A.3.10 Cyclohexane Oxidation Activity.....	47
---	----

Part 2B. Phenol Hydrogenation Reaction over Ru-oxide Supported MCM-41 Catalyst

2B.1 Introduction.....	52
------------------------	----

2B.2 Experimental.....	54
------------------------	----

2B.2.1 One-pot Synthesis of RuO ₂ Nanoparticles Supported on MCM-41.....	54
---	----

2B.2.2 Catalytic Aqueous Phase Hydrogenation of Phenols.....	55
--	----

2B.3 Result and Discussion.....	55
---------------------------------	----

2B.3.1 X-ray Diffraction	55
--------------------------------	----

2B.3.2 N ₂ Adsorption and ICP-AES Analysis.....	56
--	----

2B.3.3 Electron Microscopy.....	57
2B.3.4 Solid-state NMR Spectroscopy.....	58
2B.3.5 H ₂ -TPR Analysis.....	59
2B.3.6 X-ray Photoelectron Spectroscopy.....	60
2B.4 Catalytic Activity.....	60
2.1 Conclusion.....	68
2.2 References.....	70

Chapter 3: Confinement of Single Au Nanoparticles inside Titanium Doped Hollow Structured Mesoporous Organosilica for Alkene Oxidation

3.1 Introduction.....	75
3.2 Experimental Section.....	77
3.2.1 Synthesis of Gold Colloid.....	77
3.2.2 Encapsulation of Single Gold Nanoparticles inside the Ti- Incorporated Hollow Structured Spherical Periodic Mesoporous Organosilica Nanohybrid.....	77
3.2.3 Analytic Equipment	78
3.2.4 Catalytic Screening for Liquid Phase Olefin Oxidation.....	79
3.3 Result and Discussions.....	79
3.3.1 UV-Visible Spectroscopy.....	79
3.3.2 X-ray Diffraction	81
3.3.3 N ₂ Porosimetry	82
3.3.4 Solid-state NMR Spectroscopy	83
3.3.5 X-ray Photoelectron Spectroscopy.....	84
3.3.6 Scanning Electron Microscopy (SEM).....	85
3.3.7 Transmission Electron Microscopy (TEM).....	86
3.3.8 Catalytic Activity for Olefin Epoxidation.....	90
3.4 Conclusions.....	94
3.5 References.....	95

Chapter 4: Hydrogenation Catalysis by Fine Pd-nanoparticles on N-incorporated Periodic Mesoporous Organosilica (NPMO)

4.1 Introduction.....	98
------------------------------	-----------

4.2	Experimental Section	99
4.2.1	Synthesis of N-incorporated Organo-silane Precursor.....	99
4.2.2	Synthesis of N-incorporated Mesoporous Hybrid Organosilica Nanospheres.....	100
4.2.3	Pd Nanoparticles Supported NPMO Nanosphere Catalyst (Pd@NPMO)	100
4.2.4	Catalysts Characterization.....	100
4.2.5	Catalytic Studies on the Hydrogenation of Phenol.....	101
4.2.6	Aqueous Phase Catalytic Hydrogenation of CO ₂	101
4.3	Result and Discussions	102
4.3.1	N ₂ Adsorption and Micro-elemental Analysis.....	104
4.3.2	Thermogravimetric Analysis	105
4.3.3	X-ray Diffraction	105
4.3.4	FTIR-Spectroscopy	106
4.3.5	Solid-state NMR Spectroscopy.....	108
4.3.6	Electron Microscopy	110
4.3.7	ICP-AES.....	114
4.3.8	X-ray Photoelectron Spectroscopy.....	114
4.3.9	Catalytic Activity	116
PART 4A. Pd-NPMO Catalyzed Low-temperature and Atmospheric Pressure Phenol Hydrogenation Reaction		
4A.1	Catalytic Hydrogenation of Phenol	118
PART 4B. Aqueous-phase Hydrogenation of CO₂ to Formate on Pd-NPMO Catalyst		
4B.1	Aqueous-phase Hydrogenation of CO₂	125
4.4	Conclusion	133
4.5	References	135
Chapter 5: Pd-supported Bridged Organo-aluminosilicate Hybrid Catalyst for Reductive-amination of Furfural		
5.1	Introduction	140
5.2	Experimental Section	142
5.2.1	One-pot Synthesis of Organo-aluminosilicate (N-Al-silicates).....	142
5.2.2	Supported Pd Nanoparticles over N-Al-silicate Catalyst (Pd-N-Al-silicate).....	142

5.2.3 Catalysts Characterization.....	143
5.2.4 Catalytic Screening for the Liquid Phase Direct Reductive Amination of Furfural.....	144
5.3 Result and Discussions.....	144
5.3.1 X-ray Diffraction.....	144
5.3.2 N ₂ Porosimetry and Micro-elemental Analysis.....	145
5.3.3 Thermogravimetric Analysis	146
5.3.4 Infra-red Spectroscopy	147
5.3.5 Solid-state NMR Spectroscopy.....	148
5.3.6 Electron Microscopy	151
5.3.7 Acidity Measurements.....	152
5.3.8 X-ray Photoelectron Spectroscopy.....	154
5.3.9 Catalytic Reductive Amination of Furfural	155
5.4 Conclusion.....	161
5.5 References.....	162
Chapter 6: Summary and Conclusions.....	164
Abstract of Thesis.....	169
List of Publications.....	170
List of Conferences and Seminars.....	171
Copy of Publications	
About the Author	

List of Abbreviations

UV-Vis	Ultraviolet-Visible
DRUV	Diffuse Reflectance Ultraviolet
XRD	X-ray Diffraction
SEM	Scanning Electron Microscopy
TEM	Transmission Electron Microscopy
STEM	Scanning Transmission Electron Microscopy
HAADF	High Angle Annular Dark Field
EDAX	Energy Dispersive X-ray Analysis
BET	Brunauer-Emmett-Teller
BJH	Barrett-Joyner-Halenda
ICP-AES	Inductively Coupled Plasma Atomic Emission Spectroscopy
NMR	Nuclear Magnetic Resonance
CPMAS	Cross Polarization Magic Angle Spinning
XPS	X-ray Photoelectron Spectroscopy
XAS	X-ray Absorption Spectroscopy
XANES	X-ray Absorption Near Edge Spectroscopy
EXAFS	Extended X-ray Absorption Fine Spectroscopy
TPD	Temperature Programmed Desorption
TGA	Thermogravimetric Analysis
IR	Infra Red
GC	Gas Chromatography

HPLC	High-Performance Liquid Chromatography
TCD	Thermal Conductivity Detector
FID	Flame Ionization Detector
DP	Deposition Precipitation
MCM	Mobil Crystalline Materials
PMO	Periodic Mesoporous Organosilica
SBA	Santa Barbara Amorphous
APTMS	Amino Propyl Trimethoxy Silane
TEOS	Tetraethyl Ortho Silicate
BTEE	1,2-Bis(triethoxysilyl)ethane
BP	4,4'-bis(triethoxysilyl)1,1'-biphenyl
NPs	Nanoparticles
CTAB	Cetyl Trimethyl Ammonium Bromide
SPR	Surface Plasmon Resonance
FWHM	Full Width at Half Maxima
FCC	Face Centred Cubic
RT	Room Temperature
TON	Turnover Number
TOF	Turnover Frequency

List of Figures

Figure No.	Figure Caption	Page No.
1.1	Energy profile diagram for the catalyzed and uncatalyzed reaction.	2
1.2	Schematic showing the dependence of particle size on band gap.	4
1.3	Schematic showing the classification of porous materials.	6
1.4	Synthetic approaches to different mesoporous silica materials.	8
1.5	Various PMO precursors designed for advanced applications.	9
1.6	Schematic representation of plasmon oscillation (SPR) in metal NPs.	10
1.7	Schematic illustration of XPS spectroscopy (photoelectric effect).	16
1.8	Schematic illustrations of XAS spectroscopy data.	17
1.9	Reaction pathways involved in the phenol hydrogenation reaction.	19
1.10	Catalytic CO ₂ hydrogenation to various chemicals and fuels.	21
1.11	Various applications of reductive amination reaction.	22
2A.1	XRD plots of CrO _x -MCM-41 catalysts (a) small-angle XRD and (b) wide-angle XRD.	36
2A.2	(A) N ₂ adsorption-desorption isotherm (a) MCM-41, (b) 0.5CrO _x -MCM-41, (c) 5CrO _x -MCM-41, and 10CrO _x -MCM-41 and (B) pore size distribution of CrO _x -MCM-41 catalysts.	37
2A.3	TEM images of (a) pure MCM-41 and (b) 5CrO _x -MCM-41.	38

Figure No.	Figure Caption	Page No.
2A.4	SEM image for 5CrO _x -MCM-41.	39
2A.5	²⁹ Si CPMAS NMR spectra (a) pure MCM-41 and (b) 5CrO _x -MCM-41.	40
2A.6	UV- Visible spectra of (a) pure MCM-41, (b) 0.5CrO _x -MCM-41, (c) 1CrO _x -MCM-41, (d) 2.5CrO _x -MCM-41, (e) 4CrO _x -MCM-41, (f) 5CrO _x -MCM-41, (g) 7CrO _x -MCM-41, and (h) 10CrO _x -MCM-41.	41
2A.7	FT-IR spectra of (a) 0.5CrO _x -MCM-41, (b) 1CrO _x -MCM-41, (c) 2.5CrO _x -MCM-41, (d) 4CrO _x -MCM-41, (e) 5CrO _x -MCM-41, (f) 7CrO _x -MCM-41 and (g) 10CrO _x -MCM-41.	42
2A.8	Raman spectra of (a) 0.5CrO _x -MCM-41, (b) 1CrO _x -MCM-41, (c) 2.5CrO _x -MCM-41, (d) 4CrO _x -MCM-41, (e) 5CrO _x -MCM-41, (f) 7CrO _x -MCM-41 and (g) 10CrO _x -MCM-41.	43
2A.9	(a) XANES and (b) EXAFS spectra of nCrO _x -MCM-41 catalysts.	44
2A.10	Experimental EXAFS ($\mu(E)$ versus E) spectra of nCrO _x -MCM-41 catalysts.	45
2A.11	Cr 2p XPS plot for (a) 2.5CrO _x -MCM-41, (b) 4CrO _x -MCM-41, (c) 5CrO _x -MCM-41 and (d) 10CrO _x -MCM-41.	46
2A.12	Plot showing the relative effectiveness of Cr ³⁺ /Cr ⁶⁺ in catalyzing the oxidation of cyclohexane over different wt % nCrO _x -MCM-41 catalysts.	49
2A.13	Diffuse reflectance UV-Vis spectra of fresh and spent 5CrO _x -MCM-41 catalyst.	51

Figure No.	Figure Caption	Page No.
2B.1	Powder XRD patterns of RuO ₂ -MCM-41 catalysts in two different 2θ regions. A) Small angle-XRD and B) Wide angle-XRD.	56
2B.2	N ₂ adsorption-desorption isotherms and pore size distributions.	57
2B.3	TEM images and corresponding particle size distributions of RuO ₂ -MCM-41 catalyst.	58
2B.4	²⁹ Si CPMAS NMR spectra of (a) 2.5RuO ₂ -MCM-41, (b) 4RuO ₂ -MCM-41, (c) 5RuO ₂ -MCM-41 and 10RuO ₂ -MCM-41.	59
2B.5	TPR profiles for various metal loading on MCM-41 catalysts.	59
2B.6	Ru XPS spectra of 5RuO ₂ -MCM-41 catalyst. (a) Ru 3d and (b) Ru 3p.	60
2B.7	Influence of reaction temperature on phenol conversion over 5RuO ₂ -MCM-41 catalyst.	62
2B.8	Effect of reaction time on phenol conversion over 5RuO ₂ -MCM-41 catalyst.	63
2B.9	Effect of the bi-solvent system on phenol conversion over 5RuO ₂ -MCM-41 catalyst.	64
2B.10	Reusability of 5RuO ₂ -MCM-41 catalyst in aqueous phase phenol hydrogenation reaction.	67
2B.11	Spent catalyst analysis of 5RuO ₂ -MCM-41 catalyst (a) XRD and (b) TEM.	68
3.1	UV-Vis spectra of Ti-HPMOs and Au@Ti-HPMO catalysts.	80

Figure No.	Figure Caption	Page No.
3.2	XRD pattern for Ti-HPMOs and Au@Ti-HPMO catalysts.	81
3.3	(a) N ₂ adsorption-desorption isotherms and (b) pore size distribution of Ti-HPMO _e catalysts.	82
3.4	Solid-state NMR spectra of Ti-HPMO _e (a) ¹³ C and (b) ²⁹ Si.	83
3.5	Solid-state NMR spectrum for Ti-HPMO _{bp} (a) ¹³ C and (b) ²⁹ Si.	84
3.6	(a) Ti 2p XPS spectra of Ti-HPMO _e -(Si/Ti) catalysts and (b) percentage fraction of different Ti species on the surface of hollow hybrid titanosilicate catalysts.	85
3.7	SEM images of Ti-HPMO _e -100 and Ti-HPMO _e -25.	86
3.8	TEM images of (a) Ti-PMO _e -100 (scale 50 nm) and (b) Ti-PMO _e -25 (scale 20 nm).	86
3.9	TEM images of Au@Ti-PMO _e -100 (a) scale 50 nm and (b) 20 nm.	87
3.10	(a) HAADF-STEM image of Au@Ti-HPMO _e -100 (scale 50 nm), (b-f) STEM-EDX elemental mapping of (b) Si K, (c) O K, (d) Ti K, (e) Au M edges, and (f) overlay image, line scan profile of Au@Ti-HPMO _e -100 (g) line scan region and (h) line scan profile image.	88
3.11	TEM images for Au@Ti-HPMO _{bp} -100, scale (a) 100 nm and (b) 50 nm.	89
3.12	(a) HAADF-STEM image of Au@Ti-HPMO _{bp} -100 (scale 25 nm), (b-g) STEM-EDX elemental mapping of (b) Si K, (c) C K, (d) Ti K, (e) O K, (f) Au M edges and (g) overlay image, (h) line scan profile of Au@Ti-HPMO _{bp} -100 (inset: line scan region).	89

Figure No.	Figure Caption	Page No.
3.13	Catalytic oxidation of cyclooctene over Ti-HPMO _{e-x} (x= Si/Ti) catalysts.	91
3.14	Au@Ti-HPMO _e spent catalyst analysis (a) TEM image and (b) Ti 2p XPS plot.	94
4.1	N ₂ adsorption-desorption isotherms of Pd supported silica catalysts.	104
4.2	TGA study on various NPMO catalysts under O ₂ atmosphere.	105
4.3	PXRD plots of Pd@NPMO catalysts (a) small-angle XRD of Pd@NPMO(1:5) and (b) wide-angle PXRD of Pd loaded NPMO catalysts.	106
4.4	FTIR spectra of hybrid NPMO silica.	107
4.5	FTIR spectra of all Pd@NPMO hybrid catalysts.	108
4.6	Solid-state NMR spectra of all Pd@NPMO catalysts (a) ¹³ C, (b) ²⁹ Si, and (c) ¹⁵ N.	109
4.7	Characterizations of the Pd@NPMO(x:y) catalysts.	111
4.8	Transmission electron microscopy images of (a) SBA-15 (scale 50 nm) and (b-d) 5Pd@SBA-15 catalyst (scale 100, 50 and 50 nm, respectively).	112
4.9	Transmission electron microscopy images of Pd@SBA-15(DP) catalyst show small, well-disposed Pd nanoparticles inside the SBA-15 channels.	113
4.10	SEM images for Pd catalysts.	114

Figure No.	Figure Caption	Page No.
4.11	(a) Comparative XPS plots of (a) Pd@NPMO(x:y) and (b) comparison of % Pd species in Pd@NPMO(x:y) catalysts as calculated from XPS.	115
4.12	N1s spectrum of Pd@NPMO(1:5) catalyst.	116
4A.1	Optimization of reaction parameters for the reduction of phenol. (a) the reaction temperature and (b) reaction time.	120
4A.2	(a) catalytic activity plot showing the recycling study on the Pd@NPMO(1:5) catalyst (b) TEM of spent Pd@NPMO(1:5) catalyst after three cycles of the catalytic run, (c) histogram showing the Pd particle-size distribution over the spent Pd@NPMO(1:5) catalyst.	122
4A.3	Pd 3d XPS spectrum for spent Pd@NPMO(1:5) catalyst.	122
4B.1	Transmission electron microscopy images of spent 5Pd@NPMO catalyst after reaction at 150 °C for 20 h in 0.5 M aqueous KOH solution.	126
4B.2	Effect of KOH conc. in CO ₂ hydrogenation on Pd catalysts.	127
4B.3	(a) Screening of CO ₂ reduction to formate on various Pd catalysts to highlight the effect of N-incorporation in the hybrid PMO. (b) Time courses of CO ₂ hydrogenation to formate catalyzed by 5Pd@NPMO.	128
4B.4	(a) Heterogeneity study of Pd@NPMO catalyst by hot-filtration test (catalyst removed after 12 h reaction and further reaction carried in the absence of catalyst). (b) Recycling experiment to study reusability.	129
4B.5	Transmission electron microscopy images of spent 5Pd@NPMO catalyst after 2 cycles.	130

Figure No.	Figure Caption	Page No.
4B.6	Structural characterization of 5Pd@NPMO spent catalyst (after 2 cycles). (a) HAADF-STEM image (scale 100 nm) and (b-f) STEM-EDX elemental mapping of the (b) Si K, (c) N K, (e) Pd L, (f) O K edges and (d) overlay image.	130
4B.7	Transmission electron microscopy images of spent 3Pd@SBA-15 (DP) catalyst after 2 cycles.	131
4B.8	Comparison of XPS plot of fresh and spent Pd@NPMO catalyst.	132
4B.9	N1s XPS spectrum for spent Pd@NPMO catalyst.	132
5.1	XRD pattern of the supported Pd catalysts.	145
5.2	N ₂ adsorption-desorption isotherms of N-Al-silicate catalysts	146
5.3	The thermogravimetric analysis (TGA) of the Pd-N-Al-silicate sample after the solvent extraction.	147
5.4	FT-IR spectra of Pd-Al-silicate catalysts.	148
5.5	Solid-state ¹³ C NMR spectrum of Pd-N-Al-silicate catalyst.	148
5.6	Solid-state ²⁹ Si NMR spectra of Pd-N-Al-silicate and Pd-Al-silicate catalysts.	149
5.7	Solid-state ¹⁵ N NMR spectrum of Pd-N-Al-silicate catalyst.	150
5.8	Solid-state ²⁷ Al NMR spectrum of Pd-N-Al-silicate catalyst.	150
5.9	TEM images of Pd-N-Al-silicate catalyst.	151

Figure No.	Figure Caption	Page No.
5.10	TEM images of Pd-Al-silicate catalyst.	151
5.11	SEM images of (a) Pd-N-Al-silicate and (b) Pd-Al-silicate catalyst.	152
5.12	FTIR analysis of Pd-N-Al-silicates and Pd-Al-silicates using pyridine as a probe molecule.	153
5.13	NH ₃ TPD profile for Pd-N-Al-silicate and Pd-Al-silicate catalysts.	153
5.14	XPS plots of Pd-N-Al-silicate catalyst (a) Pd 3d and (b) N 1s.	154
5.15	Pd 3d XPS plots of Pd-Al-silicate catalyst.	155
5.16	Supported Pd catalyst screening for RA of furfural.	156
5.17	Effect of reaction temperature on RA reaction over Pd-N-Al-silicate catalyst.	157
5.18	Effect of reaction time on RA reaction over Pd-N-Al-silicate catalyst.	157
5.19	Effect of Pd loading on RA reaction over Pd-N-Al-silicate catalyst.	158
5.20	Reusability test of Pd-N-Al-silicate catalyst for RA of furfural.	159
5.21	Heterogeneity study of Pd-N-Al-silicate catalyst by hot-filtration test.	160
5.22	Spent Pd-N-Al-silicate catalyst analysis using (a) Pd 3d XPS and (b) TEM.	160

List of Schemes

Scheme No.	Scheme Caption	Page No.
2B.1	One-pot synthesis of RuO ₂ -MCM-41 catalyst using ethylenediamine.	54
3.1	Synthesis of gold encapsulated mesoporous Ti-incorporated hollow structured spherical periodic mesoporous organosilica nanohybrid (Au@Ti-HPMO).	78
4.1	Synthesis of N-containing tris-organic silane precursor by reaction of 1,3,5-triformylphloroglucinol (TFPG) with (3-aminopropyl)trimethoxysilane.	103
4.2	Synthesis of Pd@NPMO hybrid silica catalyst.	103
4A.1	Reaction pathway for atmospheric pressure selective hydrogenation of phenol to cyclohexanone in water.	117
4A.2	Proposed reaction mechanism explaining the role of bridged N-containing organic moiety in Pd@NPMO catalyst for low-temperature selective hydrogenation of phenol to cyclohexanone.	123
5.1	Furfural derivatives and their applications.	141
5.2	Synthesis of Pd-N-Al-silicate hybrid catalyst.	143
5.3	Catalytic reductive amination of furfural over Pd catalyst.	144
5.4	Reaction pathways for the reductive amination of furfural with n-BuNH ₂ in the presence of H ₂ over supported Pd catalyst.	155

List of Tables

Table No.	Table Caption	Page No.
2A.1	The textural properties of MCM-41 and nCrO _x -MCM-41 catalysts.	37
2A.2	Result of linear combination fitting of the Cr K edge XANES spectra.	44
2A.3	Cr K edge EXAFS fitting results.	45
2A.4	Catalytic oxidation of cyclohexane to cyclohexanone.	47
2A.5	Recycling study of 5CrO _x -MCM-41 catalyst in the cyclohexane oxidation reaction.	50
2B.1	The textural properties of nRuO ₂ -MCM-41 catalysts.	56
2B.2	Aqueous-phase phenol hydrogenation with nRuO ₂ -MCM-41 catalysts.	61
2B.3	Effect of solvent in aqueous-phase phenol hydrogenation reaction.	64
2B.4	Substrate scope study on 5RuO ₂ -MCM-41 catalyst.	66
3.1	Textural properties of different Ti-HPMO catalysts.	83
3.2	Liquid-phase catalytic oxidation of styrene.	92
4.1	Textural properties of different NPMO(x:y) hybrid silica supports.	104
4A.1	Hydrogenation of phenol on Pd supported silica catalysts in water.	119
4A.2	Hydrogenation of phenol derivatives on Pd@NPMO(1:5) catalyst in water.	121

Table No.	Table Caption	Page No.
4B.1	CO ₂ hydrogenation catalyzed by Pd@NPMO.	125
5.1	Textural properties of different modified silica supports.	146

CHAPTER-1

General Introduction

1.1 Catalysis

Catalysis and catalytic process have a considerable impact on almost everything in the day-to-day life of humankind.¹ As rightly said by Wilhelm Ostwald, “there is probably no chemical reaction which cannot be influenced catalytically.”² The term ‘catalysis’ describes the process in which the rate and the outcome of a chemical reaction are influenced by the substance called catalyst which is not consumed during the process. Swedish chemist Berzelius first coined the term in 1836 to describe a new force operating to carry out a chemical reaction, and the term was derived from Greek which means ‘to loosen.’ Later in 1925, Sabatier and Taylor revealed the significance of specific sites on the catalyst surface, which behave as catalysts in reactions.² A catalyst offers an alternative reaction pathway compared to non-catalyzed reactions by lower activation energy resulting in a faster reaction rate.

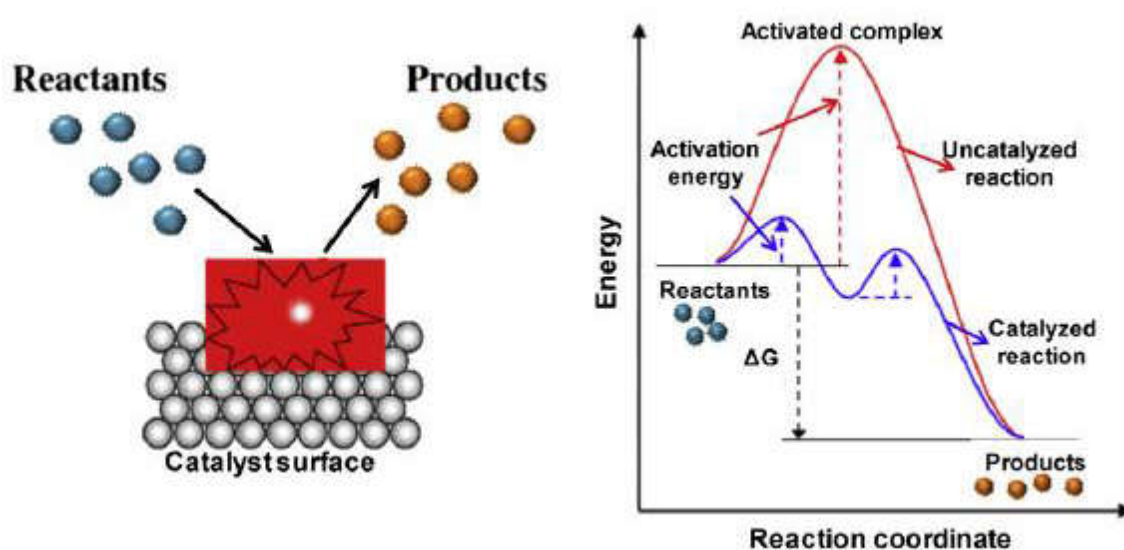


Figure 1.1: Energy profile diagram for the catalyzed and uncatalyzed reaction.³

The role of catalyst in a chemical reaction is depicted in the energy profile diagram shown in Figure 1.1. Compared to an uncatalyzed reaction, the catalyzed reaction chooses for a lower energy pathway by minimizing the activation energy of the transition state, whereas, irrespective of the reaction route, the overall energy of the reaction maintains the same. Hence, by choosing a reaction-specific catalyst, the catalytic conversion and selectivity can be efficiently accelerated and tuned in a chemical process. Generally, the catalytic reactions are categorized into homogeneous, heterogeneous, and biocatalysis (considered a separate branch).

1.2 Homogeneous Catalysis

In homogeneous catalysis, the catalysts and reactants exist in the same phase, which possesses special features like easy accessibility of active catalytic sites and high selectivity towards the desired product.⁴ But there exist some significant issues in the process like the difficulty in catalyst separation, regeneration, corrosion, and the large amount of solid wastes, which bothers in their industrial applications. Most industrial processes are highly dependent on homogeneous catalysis, including reactions like polymerization,^{5, 6} and hydroformylation.⁷ Majorly, the branch homogeneous catalysis is dominated by the coordination and the organometallic complexes.

1.3 Heterogeneous Catalysis

In heterogeneous catalysis, the catalysts and reactants exist in different phases, exhibiting unique characteristics like easy separation, minimum waste production, better thermal and mechanical stability, highly recyclable, and easy handling compared to their homogeneous counterparts.⁸ Among the well-known examples for the heterogeneous catalytic process includes the finely divided iron in ammonia synthesis through the Haber process and the synthesis of sulfuric acid using the vanadium oxide in the contact process.⁹ The ability of the solid catalyst surface to break and make chemical molecules in different phases is the basis of this phenomenon. The heterogeneous catalysts are primarily supported systems where the main constituent is immobilized or stabilized on a second material called supports. Since the catalyst surface plays a critical role in the process, the highly porous materials with a high surface area are much more attracted than the nonporous materials in the industrial catalysis, enhancing the optimum dispersion of the active centers.¹⁰ This catalytic process involves the fundamental steps where the reactants diffuse and adsorb on the solid catalyst surface, followed by their chemical interactions with the surface to undergo the chemical reaction to form desired products and finally the product desorption from the catalyst and regeneration for the next cycle. The nature of the support materials influences the catalysis by altering the rate of chemical reaction by varying interactions of the reactants with the supported catalysts. Hence, in short, the significant components in heterogeneous catalysis are the active sites (usually metals) and supports.

1.4 Nanocatalysis

Nanocatalysis is one of the emerging sub-fields in nanoscience which utilizes the nanomaterials as catalysts capable of integrating the benefits of both homogeneous and heterogeneous

catalysis.¹¹ The nano-sized particles can mimic the homogeneous catalysts due to their increased exposed active centers, enhancing the interaction between the reactant molecules during catalysis. The insolubility of nanocatalysts in the reaction medium offers the effortless isolation of products and makes the process heterogeneous in nature. The nanocatalysts performance, such as activity and selectivity, can be tuned by altering the physical and chemical properties like composition, size, shape, and morphology. The scientific challenge associated with the synthesis of nanocatalysts with controlled physical and chemical properties has been overcome by the advancement in nanotechnology.¹² Nanocatalysts render selective and rapid chemical transformations with durability and recoverability due to homo- and hetero- catalysis advantages.

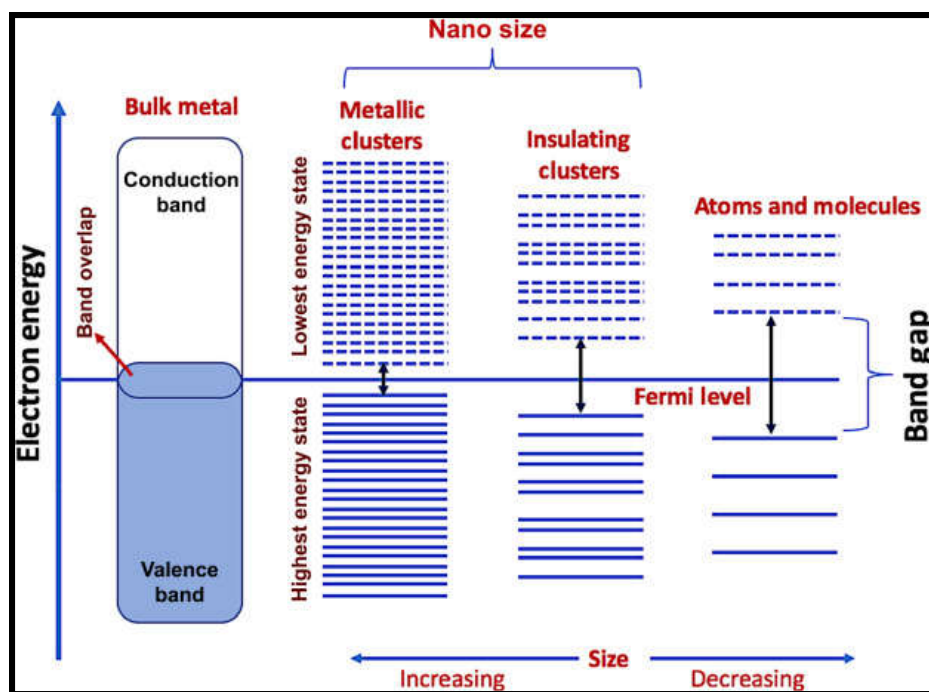


Figure 1.2: Schematic showing the dependence of particle size on band gap.¹³

Generally, the metal nanoparticles (NPs) are used as catalysts for most chemical reactions, where the nanocatalysts behave as ‘semi-heterogeneous’ catalysts owing to their unique properties. The special characteristics of metal NPs originate majorly from the reduction in the particle size to the nano-regime. The quantization effects come visible in the nano regime due to the emergence of discrete electronic states and many under coordination sites that act as the site for catalysis (Figure 1.2). The evolution of discrete energy levels in the small-sized NPs improves diverse

physical and chemical properties compared to its bulk counterparts. The modified geometric and electronic effects in these NPs display unprecedented catalytic performance in terms of conversion and selectivity as compared to the bulk material.

1.5 Metal Nanoparticles in Catalysis

The major components in a nanocatalyst are the metal nanoparticles and support to catalyze diverse chemical reactions. Both noble (Au, Pt, Pd, Ru, etc.) and non-noble (Co, Fe, Cu, Ni, etc.) transition metal NPs constitute nanocatalysts' major section, catalyzing enormous industrially critical chemical transformations due to its unique property to showcase multiple oxidation states.¹⁴⁻¹⁷ The tunable catalyst properties like activity and selectivity can be achieved by altering the oxidation state of metal NPs, size, shape, composition, and support materials.¹⁸⁻²¹ Along with the metal NPs, bringing down the bulk support to the nano regime can impart major enhancement in the catalysis.^{22, 23} By decreasing the particle size of catalytically active component results in an increase in the S/V ratio (surface to volume) leading to large fraction of under coordinated sites that act as catalytic hot spots. This also help to reduce the high consumption of high-cost of catalytically active components.^{24, 25} The exposed NP facet also alters the rate of reaction by offering different adsorption modes of reactants on the active metal sites.^{26, 27} The edge and corner atoms of NPs are considered more active compared to that on the terraces, and their count is inversely proportional to the metal NPs size. Hence, controlling the metal NPs size is critical to obtain significant catalytic activity. Among the various methodologies available for the synthesis of metal NPs, bottom-up and top-down approaches are fundamental. In bottom-up methodology, metal NPs are synthesized from their precursor using chemical way, whereas, in a top-down approach, the bulk material is torn into NPs in physical ways. Among these methods, the bottom-up approach is mainly implemented for the metal NPs synthesis with stabilizers and capping agents to control the size and shape of NPs. These metal NPs are relatively unstable under the thermal and other reaction conditions due to the high surface energy at smaller sizes, leading to a phenomenon called sintering (particle growth), which will decrease its catalytic activity. Sintering can be overcome by immobilizing or stabilizing the metal NPs on solid support materials, suitably porous supports like metal oxides, silica, carbonaceous materials, etc., can lead to a synergistic effect between the NPs and the

support, which is mentioned chiefly as SMSI (strong metal-support interaction) which finely tune the catalyst performance in terms of selectivity, conversion, and stability.

1.6 Porous Support Materials

Porous solids are favorable candidates as catalyst support in heterogeneous catalysis. Mainly they are classified into two depending on their pore size and building framework (Figure 1.3). According to the IUPAC, based on the pore size, porous materials can be classified as micro (<2 nm), meso (2-50 nm), and macro (>50 nm).²⁸ Again, depending on the building framework can be classified as purely inorganic, inorganic-organic hybrid, and purely organic materials.

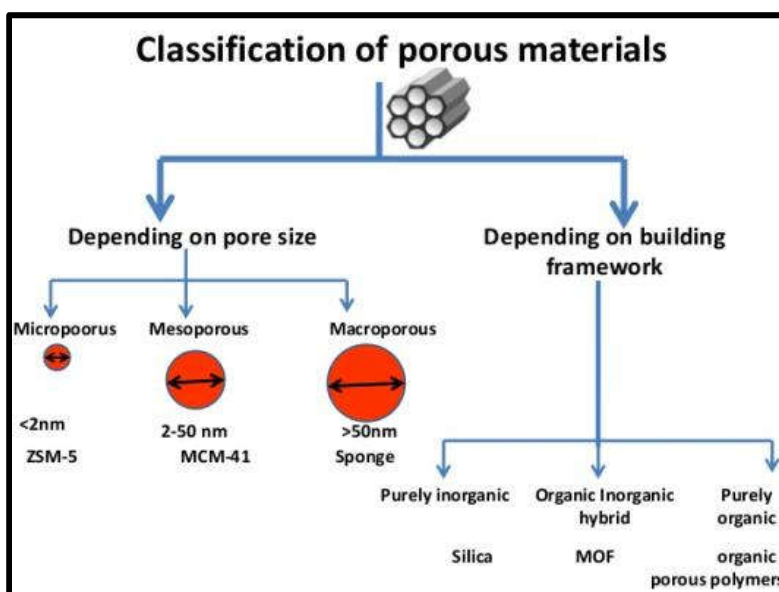


Figure 1.3: Schematic showing the classification of porous materials (slideshare.net).⁸

The major portion of the heterogeneous catalyst is the support material, where the active metal phase is well dispersed. The most extensively studied support materials are SiO₂, Al₂O₃, metal oxides like CeO₂, TiO₂, transition metal oxides, etc. Catalyst support materials can be divided into active and inactive supports based on their role in catalysis. Mostly the transition metal-based oxide supports are considered active supports due to their variable oxidation state as well as better SMSI with the metal NPs. The supports like silica, alumina, and carbon are inactive support due to their poor interaction with the metal NPs. SiO₂ and Al₂O₃ materials are widely utilized in heterogeneous catalysis due to their easy availability, less expensive, ease in bulk synthesis, and high thermal stability. The use of zeolites having micropores in shape-selective

catalysis has made evolution in porous materials and is well utilized for industrial catalysis. Their tiny pores brought disadvantages in the liquid phase reactions, which forced designing hierarchical material with large pore sizes in the nanoscale regime. The macroporous materials with low surface area and pores of wide size range were found not a suitable support candidate for the liquid phase reactions. These shortcomings led to the discovery of ordered mesoporous materials, where, surfactant-directed cooperative self-assembly method was extensively utilized for the mesoporous silica materials. Mesoporous solids displayed better diffusion of reactants and products in liquid-phase reactions. Among these, ordered mesoporous silica materials showed intrinsic textural properties like the high density of surface silanol groups, narrow pore size distribution, high surface area, high thermal stability, good adsorption capacity, etc.²⁹ The discovery of MCM-41,³⁰ SBA-15,³¹ and PMO,³²⁻³⁴ based periodic mesoporous ordered materials brings a breakthrough in materials chemistry and heterogeneous catalysis.

1.7 Hybrid Mesoporous Silica Materials

Hybrid mesoporous materials take advantage of the properties of both inorganic support as well as the organic component. The hybrid silica materials can be synthesized either by integrating heteroatoms into the silica framework by the isomorphic substitution (Ti, Al, W, etc.) or by the covalently binding of the organic functionality either into the framework or as the surface silanol functionalization.³⁵⁻³⁸ The polymeric silica framework provides structural order, thermal and mechanical stability, where the incorporated organic species permit versatile control of interfacial and bulk material properties like porosity, hydrophobicity, and electrical, optical, or magnetic properties. Organic functionalization of the internal surface of a silica host can be achieved either by covalently grafting various organic species onto the channel walls or by incorporating functionalities directly during the preparation (Figure 1.4). The first approach, the post-synthesis grafting (PSG) process, has been widely employed to anchor specific organic groups onto surface silanols of diverse silica supports. Control over the concentration and distribution of organic moieties in silica by the PSG method is limited by the number of surface silanol groups and their accessibility. The grafting rates mainly depend on the reactivity of precursors, diffusion limitations, and steric factors.

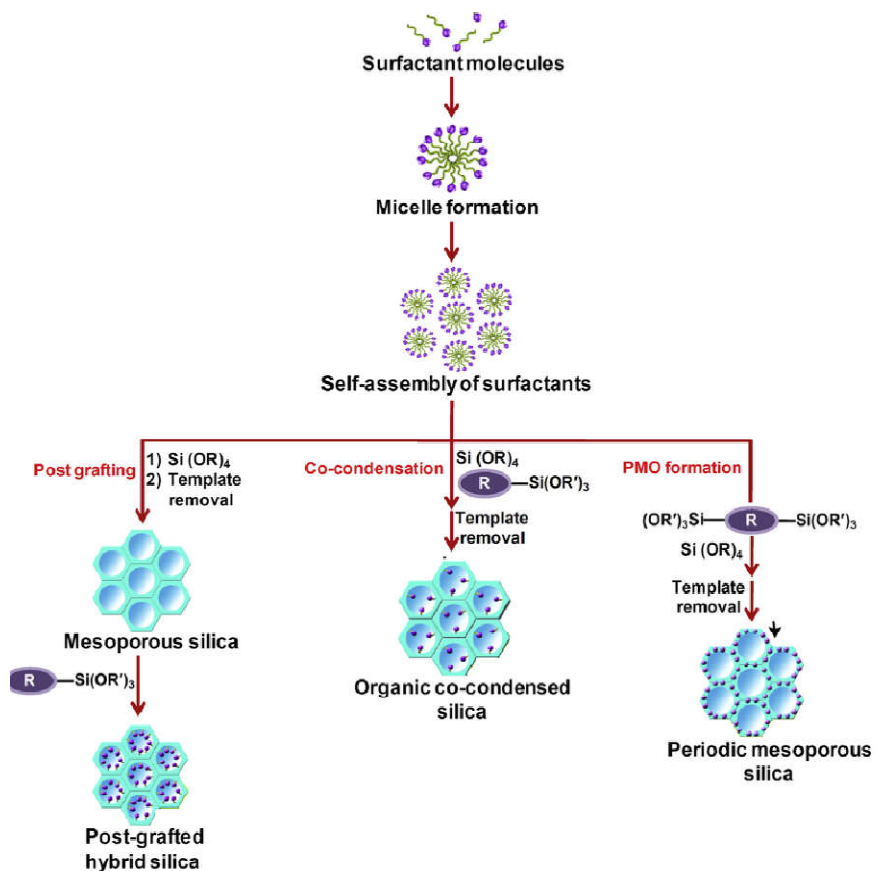


Figure 1.4: Synthetic approaches to different mesoporous silica materials.³⁹

Mostly SiO_2 contains isolated surface silanols and less number of strained siloxane bridges⁴⁰ and ideally obtains monografted surface species. Porous silica with random and broad pore-size distribution (1st generation silica solids)⁴¹ adopted for hybrid immobilized catalysts considerably influences the grafting process and its stabilization and catalyst performance.⁴² Hence porous silica materials with an array of periodically ordered pores become an ideal target for heterogeneous supports. Mobil group synthesized the first long-range ordered periodic mesoporous silica having a channel like pores, which was named as M41S silica materials.^{30, 43} Later on, a large class of new silica phases were synthesized by changing the templates and synthesis conditions, e.g., series of SBA-n,⁴⁴⁻⁴⁶ KIT-n,⁴⁷⁻⁴⁹ MSU-n,⁵⁰⁻⁵² FDU-n,⁵² etc. These materials do not contain organic moieties on silica framework but form decorated surface silyl functionality of the inorganic wall either by post-grafting method or by the co-condensation process. Various organic groups have been successfully incorporated into ordered mesoporous silica through either grafting the organo-trialkoxysilanes $\text{RSi}(\text{OR})_3$ or the direct co-assembly of

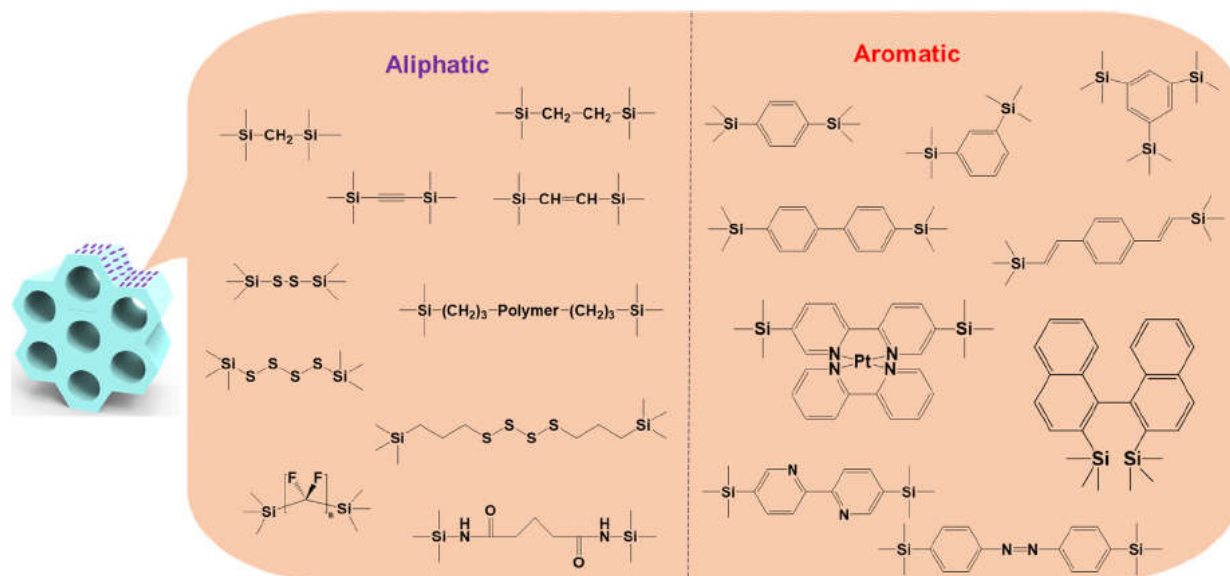


Figure 1.5: Various PMO precursors designed for advanced applications.⁵³

organo-bridged silanes, resulting in the terminally bonding organic groups on the pore surfaces or the PMO with organic groups as the integral part of the pore walls. In 1999, the research groups of Ozin (ethylene PMO), Inagaki (Ethylene bridged PMO ($-\text{CH}_2-\text{CH}_2-$)), and Stein (both ethylene- and ethenylene-bridged PMO) independently reported the Periodic Mesoporous Organosilica (PMO) for the first time.³²⁻³⁴ In 2002, Inagaki reported the crystal-like phenylene bridged PMO material⁵⁴ with molecular simulation, and later in 2010, the acronym “PMO” was first coined by Ozin et al.⁵⁵ After the discovery, a good number of PMO precursors have been reported by different groups.⁵⁶⁻⁶³ Nitrogen-containing organic bridges are another class of advanced PMO materials. It is very challenging to incorporate flexible functionalities into the framework. Besides the above-mentioned linear precursors, several groups have attempted to incorporate nitrogen-containing cyclic units into the framework.⁶⁴⁻⁷⁰ The parameters like surface rigidity, capable of preventing the deactivation through bimolecular reactions, both chemical (redox, acidic/ basic, etc.) and physical surface properties (hydrophilic/ hydrophobic, porosity, etc.) could be incorporated into the final material. Hence this approach is the collective properties from both the active metal sites/ ligand related with the support properties making this field unique compared to the classical homogeneous and heterogeneous catalysis. The synergistic cooperative effect of well-defined bifunctionality in the PMO materials will open the new possibility of enhanced potential applications, particularly in catalysis and adsorption. The high

hydrothermal stability of PMOs compared to the typical mesoporous silica takes the advantage in catalysis, where the presence of water is unavoidable.

1.8 Characterization of Nanocatalysts

Advanced characterization of nanocatalysts is requisite to make the catalyst design and engineering more rational. Nano-effects like changes in structure, size, and confinement substantially impact nanocatalysts physical, optical, and electronic properties. A structure-activity correlation can also be established using multiple spectroscopic and microscopic techniques. This section briefly discusses the characterization tools utilized for the nanocatalysts studied in this thesis.

1.8.1 Diffuse Reflectance UV-Visible Spectroscopy (DR UV-Vis)

UV-visible spectroscopy is a relatively facile and low-price technique often used for the investigation of nanoscale materials. The optical properties of NPs are sensitive to concentration, size, shape, oxidation state, agglomeration, and coordination environment, which fabricate this technique as an essential tool to evaluate such materials. It measures discrete wavelengths of light (UV/ Vis) transmitted or absorbed through a compound compared to a reference sample. The metal NPs have surface free electrons called plasmons, which start oscillating when absorbing light, and there comes a situation where the energy of these plasmons matches with

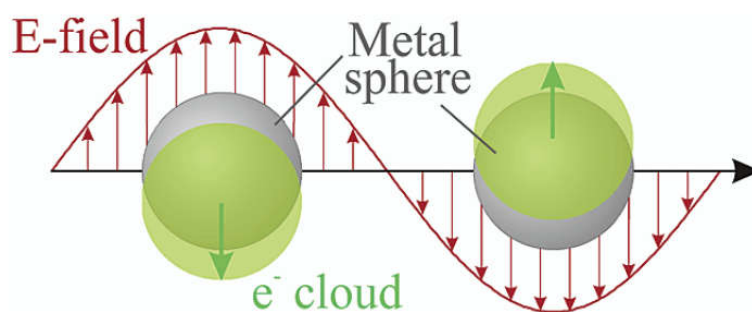


Figure 1.6: Schematic representation of plasmon oscillation (SPR) in metal NPs.⁷¹

that of the incident light, which results in a phenomenon called surface plasmon resonance (SPR). The metal nanostructures of Au, Ag, and Cu, exhibits SPR spectra in the UV-visible region.⁷¹ This SPR property can vary with the shape and size of metal NPs thus making them advantageous for optical applications. DR UV-Vis spectra analysis helps determine the ligand to

metal charge transitions (LMCT) or vice versa (MLCT) and d-d transitions of molecules.⁷² The UV-visible spectra in this thesis were acquired using Shimadzu 2700 spectrophotometer equipped with a dual-beam light source of tungsten and He for visible and UV light, respectively. DRUV analysis for powder samples was performed using BaSO₄ as the standard.

1.8.2 X-ray Diffraction Analysis (XRD)

XRD is most widely used for the characterization of crystalline and polycrystalline solids. Typically, XRD details lattice parameters, phase purity, crystalline structure, and grain structure. It is based on the interaction of the sample with incident rays that create constructive interference when conditions of Bragg's law are satisfied (Bragg's equation is given below).

$$n\lambda = 2d\sin\theta$$

where n is the order of diffraction (normally an integer), λ is the wavelength of X-rays used, d is the interplanar distance, and θ is the angle between X-rays and diffracting lattice plane. The X-ray peaks have significance in calculating the crystallite size through the Scherer equation, which relates the crystallite size to the full width at half maximum (FWHM) of the peak as:

$$\tau = \frac{k\lambda}{\beta\cos\theta}$$

where τ is mean crystallite size, λ is the wavelength of X-rays, k is the constant often taken as 0.9, β is the FWHM, and θ is the angle between beam and normal to reflecting plane. In the present thesis, X-ray analysis on the powder catalysts were measured on Rigaku D MAX with a Cu K α source of wavelength 1.54 Å with an operational voltage of 40 mV and 15 mA current.

1.8.3 N₂ Porosimetry Analysis

The N₂ adsorption-desorption analysis provides information regarding porous materials like surface area, porosity, and textural properties. This technique works on the Brunner, Emmet, and Teller theory (BET) for the solid surface's multilayer N₂ gas molecules (probe molecule). The BET equation is,

$$\frac{P}{V(P_0 - P)} = \frac{1}{V_m C} + \frac{C - 1}{V_m C} \frac{P}{P_0}$$

where P is the equilibrium and P_0 is the saturation pressure of the adsorbate at the analysis temperature, V is the volume of N₂ gas adsorbed at pressure P , and V_m is the volume of N₂

required monolayer adsorption, and C is the BET constant related to the energy of adsorption.⁷³ The BET method is extensively used for calculating the surface area of solid material by physical adsorption of the gas molecule by the following equation:

$$S = \frac{V_m N_\alpha}{m \times 22400}$$

where m is the weight of the sample, N is the Avogadro constant, and α is the cross-sectional area covered by the N_2 molecule, which is 0.162 nm^2 for N_2 . The Barrett-Joyner-Halenda (BJH) model is used to derive the pore size distribution of material from N_2 -physisorption.⁷⁴ The mesoporosity of silica materials can be calculated by assuming the pore shape as cylindrical with Kelvin equation given as,

$$r_k = \frac{-2\gamma V_m}{RT \ln \left(\frac{P}{P_0}\right)}$$

where r_k is Kelvin pore radius, V_m is the molar volume of N_2 , γ is the surface tension of N_2 , T is boiling temperature of N_2 , P/P_0 is relative pressure, and R is gas constant. The textural properties from N_2 porosimetry analysis for this thesis were determined using an Autosorb 1C Quantachrome USA. The program consists of adsorption and desorption branches that typically run at $-196 \text{ }^\circ\text{C}$ after the samples were degassed at $110 \text{ }^\circ\text{C}$ for 8 h. The BET method was used to calculate the total surface area at relative pressures of $P/P_0 = 0.65\text{--}0.45$, and the BJH method was applied to the desorption branch of the isotherm to determine the total pore volume and average pore diameter at a relative pressure of $P/P_0 = 0.99$.

1.8.4 Thermal Analysis

Thermogravimetric analysis (TGA) is the technique used to determine the thermal stability of materials by monitoring the change in weight of the sample at an elevated temperature at a constant heat rate under a controlled atmosphere. The differential thermal analysis (DTA) provides information regarding the exo- and endothermic reactions and their phase transformations. TGA gives the details regarding the composition and mass of organic functionalities and stabilizers present in the nanocatalysts. Thermal analysis of the samples in this thesis was conducted using a Pyris Diamond TGA analyzer with a heating rate of $10 \text{ }^\circ\text{C min}^{-1}$ under an air atmosphere.

1.8.5 Inductively Coupled Plasma-Atomic Emission Spectroscopy

The ICP-AES spectroscopy technique quantitatively calculates the elements and metals present in the sample. The sample is ionized into constituent atoms or ions using a plasma source that is excited to higher energy levels. These excited electrons relax back to their ground state by the emission of energy radiations, particularly for each element. Quantification and identification of the intensity of emitted radiation give the concentration of elements present in the sample. ICP-AES offers the detection of almost all cations and anions except alkali and light metals; detection level is down to parts per million and highly selective and quantitative determination of elements. In this thesis, determination by inductively coupled plasma-optical emission spectrometer (ICP-OES) measurements was done on a Thermo IRIS Intrepid II XSP. HF solution and aqua regia is used for the complete digestion of the sample for the analysis.

1.8.6 CHNS Elemental Analysis

This technique is used to predict the structure of organic compounds and establish the purity of the materials. This works based on the Dumas method, which requires the instantaneous and complete oxidation of the sample through flash combustion. It helps to determine the percentage of C, H, N, and S percentage in organic compounds. During the analysis, samples are exposed to combustion by an excess of O₂ to form oxides of C, H, and N, effectively collected through different traps. The mass of these oxide products after combustion is used to calculate the percentage and composition of the compound. This thesis work performed elemental analysis (C, H, and N) on a Carlo Erba (Model EA 1108) elemental analyzer.

1.8.7 Fourier Transform Infrared Spectroscopy

FTIR spectroscopy measures the absorption of electromagnetic radiation within the sample's mid-IR region (4000-400 cm⁻¹). The recorded spectra give the information regarding the position of bands specifying the nature and strength of bonds, presence of specific functional groups, thus providing the details of molecular structures and their interactions. An IR spectrum of a molecule is considered as its fingerprint for chemical identification. When a molecule is exposed to IR radiation, the molecule absorbs radiation selectively, and there should be a change in dipole moment so that molecule becomes IR active. IR spectroscopy depends on Hooke's law,

$$\lambda = \frac{1}{2\pi} \sqrt{\frac{k}{\mu}}$$

where λ is the wavelength of IR radiations, k is force constant, and μ is the reduced mass, where the vibrational frequency of molecules depends on the bond strength (force constant) and reduced mass of materials. The IR analysis in this thesis was carried out on Bruker Tensor 27 FTIR spectrophotometer, and Thermo Nicolet is 50 using KBr as the reference at room temperature.

1.8.8 Raman Spectroscopy

Raman spectroscopy is a complementary technique to infrared spectroscopy, where the scattering of light occurs by the rotations and vibrations of molecules depending on the change in polarisability. When a monochromatic light (typically a laser) has a suitable wavelength, it incident on the sample and interacts, leading to absorption, reflection, and scattering. The information of molecular structures is obtained from the scattering of light in Raman spectroscopy. The majority of the radiation was scattered elastically, called Rayleigh scatter, and a small portion is scattered inelastically, known as Raman scatter, composed of Stokes and anti-Stokes lines. From this Raman scatters where the useful information of the sample is obtained. For the present thesis study, Raman analysis was acquired in the visible region on LabRam spectrometer made HJY with a laser wavelength of 633 nm with a He-Ne laser.

1.8.9 Nuclear Magnetic Resonance (NMR) Spectroscopy

NMR spectroscopy is a technique used to identify the physical and chemical nature of the material by using the magnetic properties of nuclei under study. The atomic nuclei with an odd number of neutrons and protons having nuclear spin (I) greater than zero generates a nuclear magnetic moment (μ) in an applied magnetic field (B_0). The chemical shift in peaks is observed due to the generated secondary magnetic fields through the interaction of neighboring electrons with the nuclei. This secondary magnetic field opposes the applied external magnetic field results in the shielding of the nucleus.⁷⁵ Due to the dipolar and quadrupolar interactions with the nucleus, it finds difficult to interpret the solid-state NMR spectra of molecules (wider line width). However, these shortcomings can be overcome by using high-resolution NMR spectroscopy for solid materials and extended for the structural elucidation of nuclei like ^{13}C ,

^{15}N , ^{27}Al , ^{29}Si , etc. Magic-angle spinning (MAS) is used for solid-state NMR to achieve higher resolution with narrow line width. This was obtained by the fast rotation of the samples in an axis at a magic angle of $\theta = 54.74^\circ$ with respect to the static magnetic field. In order to obtain enhanced sensitivity (signal to noise ratio) for the nuclei of elements with less natural abundance, the cross-polarization (CP) technique is applied. This is achieved by transferring the magnetization power of the highly abundant ^1H spin system for the excitation process. The solid-state NMR spectra in this thesis for ^{13}C , ^{15}N , and ^{27}Al nuclei were recorded on Jeol ECX-400 MHz spectrometer (frequency of 100.6 MHz on solid 4 mm MAS probe). Magic-angle spinning (MAS) NMR spectra for ^{29}Si nuclei was recorded on BRUKER DSX300 spectrometer at 7.05 T (resonance frequencies 59.595 MHz, rotor speed 10000 Hz and 75.43 MHz, rotor speed 10000 Hz).

1.8.10 X-ray Photoelectron Spectroscopy (XPS)

XPS is one of the most powerful investigation techniques used in the field of heterogeneous catalysis. This surface-sensitive technique offers the measurement of elemental composition and their chemical state on the active catalyst surface. The working principle of XPS, also referred to as ESCA (Electron Spectroscopy for Chemical Analysis), is based on the photoelectric effect. The XPS spectra are obtained by the irradiation of X-rays having the energy $h\nu$ (Al $K\alpha$ or Mg $K\alpha$ as source) on the sample from where the photoelectrons with binding energy (B.E) are ejected with kinetic energy (K.E) which is measured. The mean free path of these ejected electrons is 10 nm which makes the technique purely surface sensitive. The B.E is calculated using the equation, $\text{K.E.} = h\nu - \text{B.E} - \Phi$, where Φ , ν , and h , are work function of the instrument, frequency of radiation, and Planck's constant, respectively. XPS measurements reveal the identification of element, composition, and oxidation state and coordination environment, etc. Binding energies are considered characteristic for a specific element and composition and are evaluated based on their peak area and sample cross-section for photoemission.

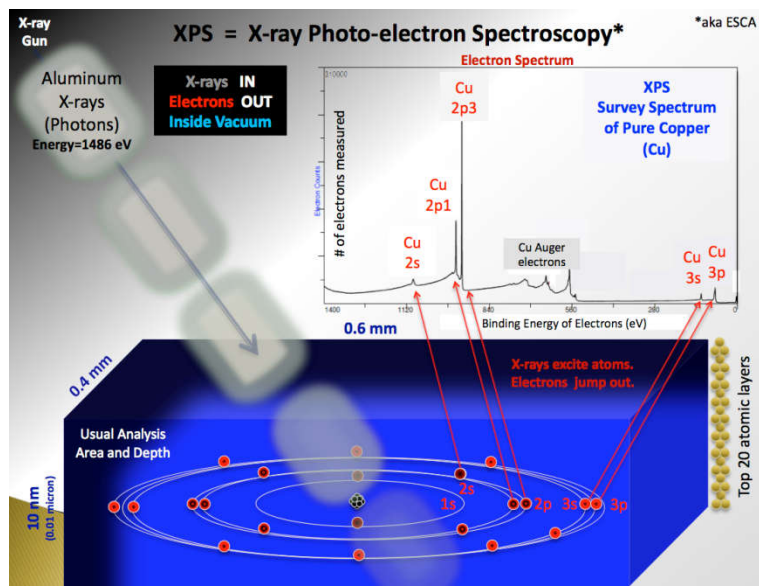


Figure 1.7: Schematic illustration of XPS spectroscopy (photoelectric effect). (Image Source Wikipedia)

The XPS measurements collected for this thesis were done on a Thermo Kalpha+ spectrometer using micro-focused and monochromated Al $K\alpha$ radiation (1486.6 eV) operating at a vacuum better than 10^{-9} millibar. The pass energy for the spectral acquisition was kept at 50 eV for individual core levels and 100 eV for the wide-area scan. The peak fitting was done using CasaXPS software with Shirley-type background.

1.8.11 X-Ray Absorption Spectroscopy (XAS)

XAS spectroscopic technique is extensively used to study the electronic and geometric structure of the material. The unique sensitivity of this technique to determine the local structure compared to XRD has been much exploited. The sample of analysis can be of solid, liquid, or gas phase. The experiment measurements are usually performed at the synchrotron radiation facilities, which provide intensified tunable X-rays. The X-rays with sufficient energy can excite a core level electron in an atom to a vacant bound state called an excitonic state, which is below the ionization threshold or to the continuum above the ionization potential. There exist three main regions in typical XAS data:

- 1) Absorption threshold: determined from the transition of excitation electron to the lowest unoccupied states.

- 2) X-ray Absorption Near Edge Spectroscopy (XANES): The pre-edge and near-edge regions in the XAS spectra provide the XANES spectrum. The ejection of core-level photoelectrons to a quasi-bound state is above the chemical potential with kinetic energy in the range of 10- 100 eV. These electronic transitions result in multiple scattering resonances of photoelectrons.
- 3) Extended X-ray Absorption Fine Structure (EXAFS): The photoelectrons having a dual nature (both particle and wave) ejected can be backscattered in the lattice by neighbouring atoms. These interactions can lead to an interference pattern beyond 100 eV high-energy regions of the spectrum.
- 4) X-ray Absorption Spectroscopy (XAS) analysis in this thesis chapter 2A was performed at Cr K-edge in fluorescence mode at the Scanning EXAFS Beamline (BL-9) at the INDUS-2 Synchrotron Source (2.5 GeV, 100 mA) at the Raja Ramanna Centre for Advanced Technology (RRCAT), Indore, India.

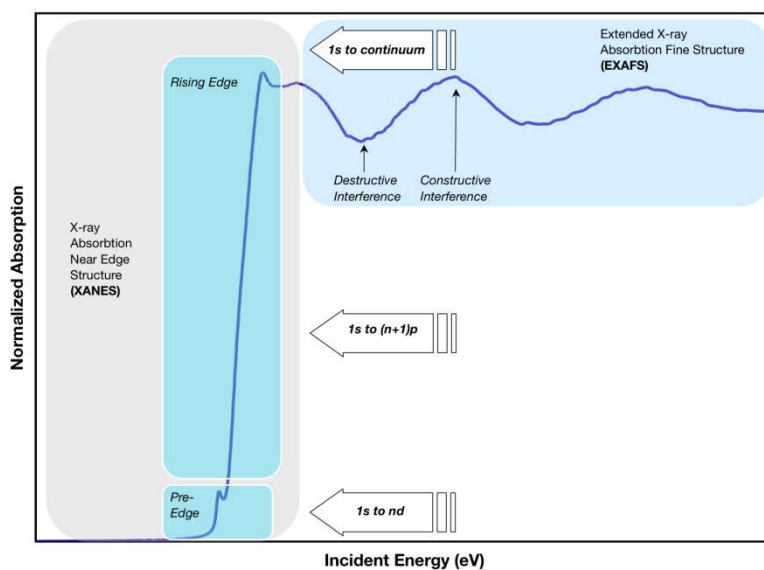


Figure 1.8: Schematic illustrations of XAS spectroscopy data. (Image Source Wikipedia)

1.8.12 Transmission Electron Microscopy (TEM)

TEM is an electron microscopic technique that provides the morphology and visualization at the atomic scale of the sample where the high-energy electron beam is transmitted through the specimen to generate a 2D image of the sample. The image is obtained from the interaction of the incident electrons with the specimen, where the electron beam is transmitted through the sample. These transmitted electrons are magnified and focused by the electron optics onto a

photographic plate, fluorescent screen, or charge-coupled device (CCD). The use of electron source over optical light source offers the advantage of high resolution in nanometer level due to the lower de-Broglie wavelength. The modified features of TEM include the scanning transmission electron microscopy (STEM) and high angle annular dark-field (HAADF) imaging modes which can provide information regarding the elemental composition and distribution of atoms in nanomaterials by coupling with the energy dispersive spectroscopy (EDS). The TEM analysis in this thesis was done on FEI Technai instruments (TF 30) by drop-casting the diluted samples on carbon-coated copper grids. The HRTEM and HAADF STEM analysis was done on JEOL JEM-F200 HRTEM.

1.8.13 Scanning Electron Microscopy (SEM)

SEM is a powerful electron microscopic technique used to investigate the sample's surface topography in 3D form. Performing the visual analysis of the specimen using a focused beam of electrons contributes to identifying the wear properties of the materials like morphology, composition, number, and size of the particles, etc. In SEM, the backscattered or secondary electrons from the sample are detected. The SEM micrographs in this thesis were obtained on an FEI model Quanta 200 3D in a dual-beam scanning microscope.

1.9 Catalytic Reactions over Nanostructured Catalysts

Heterogeneous nanocatalysis by the metal nanoparticles supported over porous solid materials for various organo-transformation reactions has massive significance in both industrial and academic points of view. The catalytic reactions carried out in the present thesis are discussed in the following section:

1.9.1 Cyclohexane Oxidation: Catalytic oxidation of hydrocarbons under mild reaction conditions has great importance by virtue of various valuable products from the feedstock. The selective transformation of cyclohexane to high-value products is a challenging issue because of the significance of the oxidized products, which acts as the intermediate for manufacturing the caprolactam and adipic acid.⁷⁶ KA oil (cyclohexanone and cyclohexanol) has a global consumption of $\sim 10^6$ tons per year.⁷⁷ The current commercial cyclohexane oxidation process is limited to a very low conversion of $\sim 4\%$ in order to assure a reasonable selectivity.⁷⁸

Cyclohexane oxidation requires high activation energy for C-H bond cleavage, which dictates harsh reaction conditions such as a high temperature (413-433 K) and pressure (1-2 MPa).⁷⁹ Moreover, these processes suffer from significant shortcomings such as a low yield, low selectivity, and high waste production.^{80, 81} The great demand for these oxidation products and the high energy consumption of the existing process necessitate a more effective, stable, feasible, and sustainable catalytic process. Many supported metal catalysts (V, Co, Cr, Au, and Fe) have been tested for the selective conversion of cyclohexane to KA oil in the past, among which the transition metal Cr-based catalysts displayed better activity.⁸²⁻⁸⁸ The major drawback associated with Cr supported silica-based catalyst is the leaching of Cr active species to the reaction medium which can be overcome by modifying the Cr-silica catalysts.⁸⁹ In the present thesis CrO_x-MCM-41 catalysts have been utilized for the selective cyclohexane oxidation to cyclohexanone and the structure activity correlation has been established.

1.9.2 Phenol Hydrogenation: Phenols are chemical compounds with hydroxyl groups directly bonded to the aromatic hydrocarbon ring. The selective hydrogenation of phenols to cyclohexanone and cyclohexanol is considered a challenging task. The tremendous commercial significance of cyclohexanone and cyclohexanol in producing nylon 6 and nylon 66 makes the phenol hydrogenation process attractive.⁹⁰ The first industrial-scale production of cyclohexanone and cyclohexanol is achieved by the hydrogenation of phenol. The current industrial production of KA oil is classified into three reaction routes: the Asahi process,⁹¹ cyclohexane oxidation,⁹² and phenol hydrogenation.⁹³ The catalytic hydrogenation of phenol is established by the interaction between the chemisorbed phenol and the activated H₂. Depending on the adsorption mode of phenol on the catalyst surface tunes the product selectivity. Hence depending on the choice of metal and support, the hydrogenation activity varies and alters the selective product.

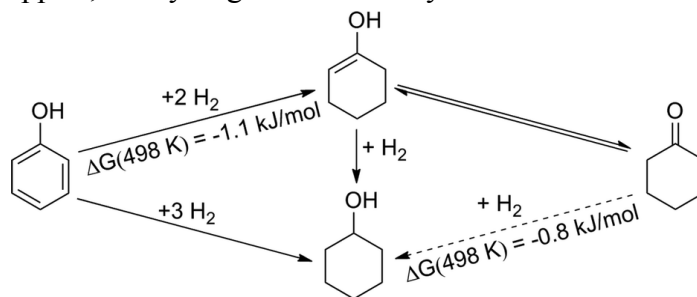


Figure 1.9: Reaction pathways involved in the phenol hydrogenation reaction.⁹⁴

In this thesis work, Ru supported MCM-41 and Pd-NPMO new hybrid catalyst have been studied for the selective phenol hydrogenation reaction under mild conditions and explored the scientific reasoning for the enhanced catalysis.

1.9.3 Olefin Epoxidation: Epoxidation is a chemical reaction that converts the C=C bond into epoxides (oxiranes). Oxidation of alkenes to the corresponding epoxide using a variety of oxidizing reagents like air/ O₂, hydrogen peroxide, organic peracid, and hypochlorous acid are reported.⁹⁵ Among which the reactions using the green oxidant are always industrially attractive and much accepted. Even though organic oxidants are less eco-friendly, they can efficiently convert olefins to corresponding epoxides offering mild reaction conditions. The best alternative to organic oxidants is H₂O₂, where the only by-product that can form is water and also offers atom efficiency due to more active oxygen content. The associated significant drawback of using H₂O₂ is its easy decomposition under the reaction conditions, resulting in undesired oxidation products. Thus, designing active centers capable of preventing the decomposition of H₂O₂ over the catalyst surface is highly desirable. Both the homo and hetero tagged catalysts using the transition metals like Ti, W, Nb, Fe, and Mn performs very efficiently in epoxidation reaction.⁹⁶⁻⁹⁹ The transition metals like Ti, W, Nb in the silica framework are reported to work efficiently for the reaction.¹⁰⁰⁻¹⁰² The existence of these metals as single sites in silica lattice or as amorphous metal oxides can effectively catalyze the epoxidation reaction with excellent activity and selectivity. From previous literatures, the isolated single sites incorporated in the silica matrix are known to be active for the better yield of epoxides.^{103, 104} Development of titanosilicate (TS) materials maintaining the isolated Ti centers in silica matrix has overcome these difficulties in reactions.¹⁰⁵ For the gas phase and liquid phase epoxidation of a variety of alkenes, TS materials has been a choice of a suitable catalyst to yield maximum epoxide in the presence of H₂O₂ as well as organic peroxides like TBHP.^{106, 107} In this thesis work hybrid hollow structured Ti-containing PMOs (Ti-HPMO) and Au encapsulated nanoarchitectures (Au@Ti-HPMO) have been synthesized and their activity has been explored for olefin epoxidation.

1.9.4 CO₂ Hydrogenation: CO₂ is the major component of greenhouse gas that possesses both advantages and disadvantages. Even though CO₂ provides a warm environment for the living on earth, a considerable increase in its concentration in the atmosphere leads to an irreversible

change in the world's climate.¹⁰⁸ By October 2021, the CO₂ concentration on the planet is 413.88 ppm (according to the Mauna Loa, Hawaii) which is much higher than in the past. Undoubtedly, the strategies to alleviate CO₂ have become an urgent demand which can probably offer the solutions to the global “3E” issues (Energy-Environment-Economy challenges).¹⁰⁹ As a significant part of carbon capture, utilization, and storage (CCUS), CO₂ utilization has attracted worldwide attention due to the advances in the energy-efficient catalytic transformation of CO₂, which can potentially reduce the emission and slow down the dependence on non-renewable fossil resources.¹¹⁰ Since CO₂ is a thermodynamically, kinetically, and chemically stable molecule, efficient catalyst systems play a crucial role to overcome this kinetic barrier for its conversion to useful oxygenate products like alcohols, formic acid/formate, DME, and hydrocarbons.¹¹¹

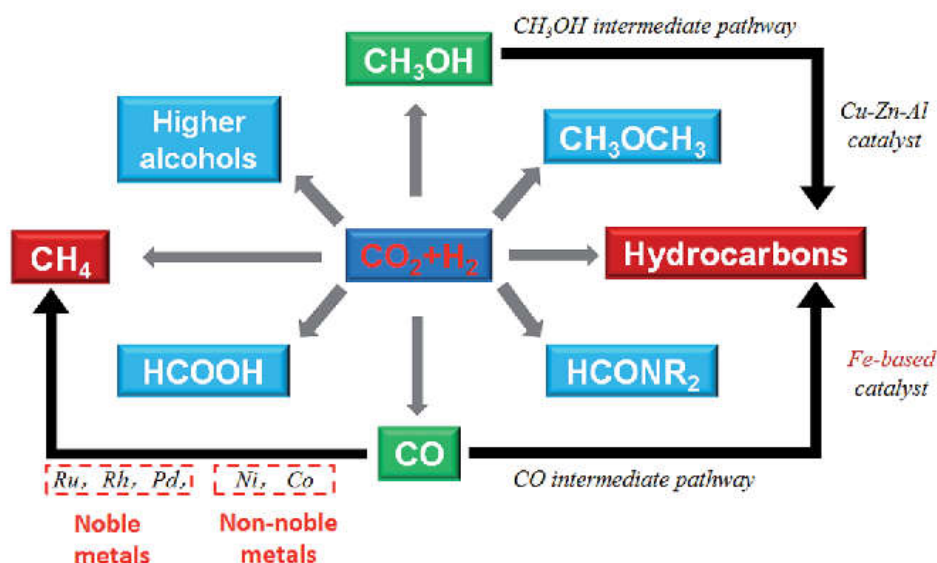


Figure 1.10: Catalytic CO₂ hydrogenation to various chemicals and fuels.¹¹²

Catalytic conversion of CO₂ to formate/formic acid is a promising approach to recognize a renewable energy supply as it serves as a liquid organic hydrogen carrier and endows a significant volumetric hydrogen capacity (53 g/L).¹¹³ The critical factors associated with the catalytic activity include the metal dispersion, basic functionalities, electron density, and the synergistic catalysis of metal and basic sites. The monometallic and bimetallic formulations of noble metals like Pd, Au, Ru, and Ag have been utilized for the reaction. The particle sizes of these nanocatalysts mainly lie in the range from sub-nanometers to nanoparticles. Generally, the

active metal centers are dispersed on the porous supports having basic properties and can be directly applied for the liquid-phase CO₂ reduction catalysts.¹¹³ In the present work the influence of Pd-based hybrid N-containing PMO catalysts have tested for the selective aqueous-phase CO₂ hydrogenation to formate.

1.9.5 Reductive Amination Reaction (RA): Reductive amination reactions are widely applied to produce N-containing compounds for pharmaceuticals, biomolecules, and agrochemicals.^{114, 115} specifically, the catalytic reductive amination reaction in the presence of molecular H₂ is highly



Figure 1.11: Various applications of reductive amination reaction.¹¹⁶

valued and essential for the sustainable production of various amines and their functionalization.¹¹⁷ In the presence of suitable catalysts facilitates the reaction between the carbonyl compounds (aldehydes/ketones) and amines, NH₃, or even nitro compounds which in the presence of H₂ enables the preparation of primary, secondary and tertiary amines.¹¹⁸⁻¹²⁰ In general, the direct RA reaction is challenging because it often suffers from non-selective reactions like reducing carbonyl groups to corresponding alcohols. Suitable catalyst development is of high priority to perform these reactions with high selectivity and activity under mild reaction conditions. Various heterogeneous catalysts have been extensively studied for the direct reductive amination to access a variety of amines. In this thesis, new Pd based heterogeneous hybrid N-Al-silicate catalyst for the direct reductive amination of furfural using n-butylamine as the N source is demonstrated under low temperature and atmospheric H₂ pressure.

1.10 Scope and Objective of the Thesis

The heterogeneous catalyst is one of the most crucial transformation technologies in the chemical industry and its great potential stimulates the increasing attention in developing new heterogeneous catalysts. Supported metal nanoparticle catalysts have been well explored for a large number of chemical reactions. Silica and silica-based supports are extensively studied because their unique properties, such as thermal stability, high surface area, tunable porosity, easy modification with other transition metals, etc., make it the most common and convenient support. However, synthesizing metal NPs of small size carrying many under coordination sites on silica support has always been challenging due to poor metal support interactions. This results in sintering (uncontrolled particle size growth) under high temperatures and reaction conditions, reflecting a deleterious effect on the catalytic activity. In order to create active sites for catalysis in the mesoporous silica, organic moieties with functional groups can be anchored onto their surface or framework. Subsequently, they can be functionalized by incorporating heteroatoms either in the pore wall or on the pore surface. Such homogeneously distributed organic moieties in silica framework and altering the structure, composition, and relative contents of the organic groups can increase its utility in catalysis. Though considerable progress has been made in periodic mesoporous organosilica (PMOs), it is still challenging to synthesize PMOs with desired morphology and structure. This is because the organic bridging groups tend to interfere with the assembly process during the hydrolysis of silane species around the surfactant micelles.

The primary objectives of this thesis are as follows:

- ❖ To investigate the chemical modifications in periodic mesoporous silica materials by changing framework chemistry or surface for oxidation (cyclohexane, alkenes) and hydrogenation (CO₂, phenol, furfural) reactions of industrially important molecules.
- ❖ To explore more flexible and controllable synthesis strategies to stabilize sinter-resistant metal nanoparticles over mesoporous silica support for enhanced catalysis.
- ❖ Synthesize hollow structured architectures of periodic mesoporous organosilica with size-controlled metal nanoparticles in order to overcome the active nanoparticle growth and associated diffusion limitations in liquid-phase reactions.
- ❖ Focus on correlating the structural merits of the fabricated silica-supported catalyst with the associated heterogeneous catalytic activity.

The sinter resistant, small-sized metal nanoparticles on silica support for catalysis have been designed using different strategies, including the chemical modifications by changing the silica framework chemistry with the desired functionality (framework metal sites (Ti and Al) and N-bridged organic hybrid centers), changing the morphological architectures (yolk-shell and core-shell), and supporting active metal oxide centers over silica (Cr and Ru oxides). Thus, this thesis work attempts to demonstrate a comprehensive strategy in mesoporous silica systems to stabilize well-dispersed active metal species for sustainable heterogeneous catalysis.

1.11 References

1. R. A. van Santen and J. W. Niemantsverdriet, in *Chemical Kinetics and Catalysis*, Springer US, Boston, MA, 1995, DOI: 10.1007/978-1-4757-9643-8_2, pp. 21-72.
2. B. Lindström and L. J. Pettersson, *CATTECH*, 2003, **7**, 130-138.
3. N. Pal and A. Bhaumik, in *Sustainable Catalytic Processes*, eds. B. Saha, M. Fan and J. Wang, Elsevier, Amsterdam, 2015, DOI: <https://doi.org/10.1016/B978-0-444-59567-6.00002-9>, pp. 23-60.
4. K. Wilson and J. H. Clark, *Pure and Applied Chemistry*, 2000, **72**, 1313-1319.
5. H. Sinn and W. Kaminsky, in *Advances in Organometallic Chemistry*, eds. F. G. A. Stone and R. West, Academic Press, 1980, vol. 18, pp. 99-149.
6. G. W. Coates, P. D. Hustad and S. Reinartz, *Angewandte Chemie International Edition*, 2002, **41**, 2236-2257.
7. I. Ojima, C.-Y. Tsai, M. Tzamarioudaki and D. Bonafoux, in *Organic Reactions*, DOI: <https://doi.org/10.1002/0471264180.or056.01>, pp. 1-354.
8. N. Pal and A. Bhaumik, *RSC Adv.*, 2015, **5**, 24363-24391.
9. X. S. Zhao, X. Y. Bao, W. Guo and F. Y. Lee, *Materials Today*, 2006, **9**, 32-39.
10. M. H. Valkenberg and W. F. Hölderich, *Catalysis Reviews*, 2002, **44**, 321-374.
11. V. Polshettiwar and R. S. Varma, *Green.Chem.*, 2010, **12**, 743-754.
12. G. A. Somorjai, H. Frei and J. Y. Park, *J. Am. Chem. Soc.*, 2009, **131**, 16589-16605.
13. A. B. Asha and R. Narain, in *Polymer Science and Nanotechnology*, ed. R. Narain, Elsevier, 2020, DOI: <https://doi.org/10.1016/B978-0-12-816806-6.00015-7>, pp. 343-359.
14. A. Dhakshinamoorthy and H. Garcia, *Chemical Society Reviews*, 2012, **41**, 5262-5284.
15. R. M. Crooks, M. Zhao, L. Sun, V. Chechik and L. K. Yeung, *Accounts of Chemical Research*, 2001, **34**, 181-190.
16. Y. Wang, S. De and N. Yan, *Chem.Commun.*, 2016, **52**, 6210-6224.
17. H. Kotani, R. Hanazaki, K. Ohkubo, Y. Yamada and S. Fukuzumi, *Chemistry – A European Journal*, 2011, **17**, 2777-2785.
18. M. Ahmadi, H. Mistry and B. Roldan Cuenya, *The Journal of Physical Chemistry Letters*, 2016, **7**, 3519-3533.
19. S. Mostafa, F. Behafarid, J. R. Croy, L. K. Ono, L. Li, J. C. Yang, A. I. Frenkel and B. R. Cuenya, *J. Am. Chem. Soc.*, 2010, **132**, 15714-15719.
20. A. G. M. da Silva, T. S. Rodrigues, T. J. A. Slater, E. A. Lewis, R. S. Alves, H. V. Fajardo, R. Balzer, A. H. M. da Silva, I. C. de Freitas, D. C. Oliveira, J. M. Assaf, L. F. D. Probst, S. J. Haigh and P. H. C. Camargo, *ACS Applied Materials & Interfaces*, 2015, **7**, 25624-25632.

21. H. Mistry, R. Reske, Z. Zeng, Z.-J. Zhao, J. Greeley, P. Strasser and B. R. Cuenya, *J. Am. Chem. Soc.*, 2014, **136**, 16473-16476.
22. T. Sirikajorn, O. Mekasuwandumrong, P. Praserttham, J. G. Goodwin and J. Panpranot, *Catal.lett.*, 2008, **126**, 313.
23. A. Trovarelli and J. Llorca, *ACS Catal.*, 2017, **7**, 4716-4735.
24. M. Zahmakiran and S. Özkar, *Nanoscale*, 2011, **3**, 3462-3481.
25. J. M. Campelo, D. Luna, R. Luque, J. M. Marinas and A. A. Romero, *ChemSusChem*, 2009, **2**, 18-45.
26. Q. Zhang and H. Wang, *ACS Catal.*, 2014, **4**, 4027-4033.
27. C.-H. Kuo, I. M. Mosa, S. Thanneeru, V. Sharma, L. Zhang, S. Biswas, M. Aindow, S. Pamir Alpay, J. F. Rusling, S. L. Suib and J. He, *Chem. Commun.*, 2015, **51**, 5951-5954.
28. K. S. W. Sing, *Pure and Applied Chemistry*, 1985, **57**, 603-619.
29. A. Taguchi and F. Schüth, *Microporous Mesoporous Mater.*, 2005, **77**, 1-45.
30. C. T. Kresge, M. E. Leonowicz, W. J. Roth, J. C. Vartuli and J. S. Beck, *Nature*, 1992, **359**, 710-712.
31. D. Zhao, Q. Huo, J. Feng, B. F. Chmelka and G. D. Stucky, *J. Am. Chem. Soc.*, 1998, **120**, 6024-6036.
32. T. Asefa, M. J. MacLachlan, N. Coombs and G. A. Ozin, *Nature*, 1999, **402**, 867-871.
33. S. Inagaki, S. Guan, Y. Fukushima, T. Ohsuna and O. Terasaki, *J. Am. Chem. Soc.*, 1999, **121**, 9611-9614.
34. B. J. Melde, B. T. Holland, C. F. Blanford and A. Stein, *Chem. Mater.*, 1999, **11**, 3302-3308.
35. Y. Wang, N. Homs and P. Ramírez de la Piscina, *Journal of Materials Research and Technology*, 2021, **14**, 2115-2123.
36. C.-C. Yang, J. Vernimmen, V. Meynen, P. Cool and G. Mul, *J. Catal.*, 2011, **284**, 1-8.
37. Y. Chen, Y. Huang, J. Xiu, X. Han and X. Bao, *Appl. Catal. A-Gen*, 2004, **273**, 185-191.
38. R. Srivastava, D. Srinivas and P. Ratnasamy, *Microporous Mesoporous Mater.*, 2006, **90**, 314-326.
39. F. Hoffmann, M. Cornelius, J. Morell and M. Fröba, *Angewandte Chemie International Edition*, 2006, **45**, 3216-3251.
40. P. Serna and B. C. Gates, *Accounts of Chemical Research*, 2014, **47**, 2612-2620.
41. Z.-l. Lu, E. Lindner and H. A. Mayer, *Chemical Reviews*, 2002, **102**, 3543-3578.
42. A. Choplin and F. Quignard, *Coordination Chemistry Reviews*, 1998, **178-180**, 1679-1702.
43. J. S. Beck, J. C. Vartuli, W. J. Roth, M. E. Leonowicz, C. T. Kresge, K. D. Schmitt, C. T. W. Chu, D. H. Olson, E. W. Sheppard, S. B. McCullen, J. B. Higgins and J. L. Schlenker, *J. Am. Chem. Soc.*, 1992, **114**, 10834-10843.

44. Q. Huo, D. I. Margolese, U. Ciesla, P. Feng, T. E. Gier, P. Sieger, R. Leon, P. M. Petroff, F. Schüth and G. D. Stucky, *Nature*, 1994, **368**, 317-321.
45. Q. Huo, R. Leon, P. M. Petroff and G. D. Stucky, *Science*, 1995, **268**, 1324.
46. D. Zhao, J. Feng, Q. Huo, N. Melosh, G. H. Fredrickson, B. F. Chmelka and G. D. Stucky, *Science*, 1998, **279**, 548.
47. R. Ryoo, J. M. Kim, C. H. Ko and C. H. Shin, *The Journal of Physical Chemistry*, 1996, **100**, 17718-17721.
48. F. Kleitz, S. Hei Choi and R. Ryoo, *Chemical Communications*, 2003, DOI: 10.1039/B306504A, 2136-2137.
49. F. Kleitz, D. Liu, G. M. Anilkumar, I.-S. Park, L. A. Solovyov, A. N. Shmakov and R. Ryoo, *The Journal of Physical Chemistry B*, 2003, **107**, 14296-14300.
50. P. T. Tanev, M. Chibwe and T. J. Pinnavaia, *Nature*, 1994, **368**, 321-323.
51. S. A. Bagshaw, E. Prouzet and T. J. Pinnavaia, *Science*, 1995, **269**, 1242.
52. C. Yu, Y. Yu, L. Miao and D. Zhao, *Microporous and Mesoporous Materials*, 2001, **44-45**, 65-72.
53. R. K. Kankala, S.-B. Wang and A.-Z. Chen, *iScience*, 2020, **23**, 101687.
54. S. Inagaki, S. Guan, T. Ohsuna and O. Terasaki, *Nature*, 2002, **416**, 304-307.
55. W. Wang, J. E. Lofgreen and G. A. Ozin, *Small*, 2010, **6**, 2634-2642.
56. W. J. Hunks and G. A. Ozin, *Journal of Materials Chemistry*, 2005, **15**, 3716-3724.
57. M. Jaroniec, *Nature*, 2006, **442**, 638-640.
58. K. M. P. and I. Shinji, *Bulletin of the Chemical Society of Japan*, 2006, **79**, 1463-1475.
59. A. Sayari, S. Hamoudi, Y. Yang, I. L. Moudrakovski and J. R. Ripmeester, *Chemistry of Materials*, 2000, **12**, 3857-3863.
60. B. Lee, H.-J. Im, H. Luo, E. W. Hagaman and S. Dai, *Langmuir*, 2005, **21**, 5372-5376.
61. M. C. Burleigh, S. Jayasundera, C. W. Thomas, M. S. Spector, M. A. Markowitz and B. P. Gaber, *Colloid and Polymer Science*, 2004, **282**, 728-733.
62. M. C. Burleigh, S. Jayasundera, M. S. Spector, C. W. Thomas, M. A. Markowitz and B. P. Gaber, *Chemistry of Materials*, 2004, **16**, 3-5.
63. X. Bao, X. S. Zhao, X. Li and J. Li, *Applied Surface Science*, 2004, **237**, 380-386.
64. M. Cornelius, F. Hoffmann, B. Ufer, P. Behrens and M. Fröba, *Journal of Materials Chemistry*, 2008, **18**, 2587-2592.
65. M. Alvaro, M. Benitez, D. Das, H. Garcia and E. Peris, *Chemistry of Materials*, 2005, **17**, 4958-4964.
66. D. Chandra, T. Yokoi, T. Tatsumi and A. Bhaumik, *Chemistry of Materials*, 2007, **19**, 5347-5354.
67. Y.-K. Seo, S.-B. Park and D. Ho Park, *Journal of Solid State Chemistry*, 2006, **179**, 1285-1288.

68. M. Benitez, D. Das, R. Ferreira, U. Pischel and H. García, *Chemistry of Materials*, 2006, **18**, 5597-5603.
69. C. D. Nunes, P. D. Vaz, P. Brandão, J. Rocha, P. Ferreira, N. Bion and M. J. Calhorda, *Microporous and Mesoporous Materials*, 2006, **95**, 104-111.
70. E.-B. Cho, O. H. Han, S. Kim, D. Kim and M. Jaroniec, *Chemical Communications*, 2010, **46**, 4568-4570.
71. K. L. Kelly, E. Coronado, L. L. Zhao and G. C. Schatz, *The Journal of Physical Chemistry B*, 2003, **107**, 668-677.
72. X. Gao, M. A. Bañares and I. E. Wachs, *Journal of Catalysis*, 1999, **188**, 325-331.
73. S. Brunauer, P. H. Emmett and E. Teller, *Journal of the American Chemical Society*, 1938, **60**, 309-319.
74. E. P. Barrett, L. G. Joyner and P. P. Halenda, *Journal of the American Chemical Society*, 1951, **73**, 373-380.
75. J. R. Lyerla, in *Methods in Experimental Physics*, ed. R. A. Fava, Academic Press, 1980, vol. 16, pp. 241-369.
76. S. Van de Vyver and Y. Román-Leshkov, *Catal.Sci.Technol*, 2013, **3**, 1465-1479.
77. M. T. Musser, in *Ullmann's Encyclopedia of Industrial Chemistry*, Wiley-VCH Verlag GmbH & Co. KGaA, 2000, DOI: 10.1002/14356007.a08_217.
78. E. T. D. I. V. Berezin, N. M. Emanuel, *Elsevier, Oxford—London—Edinburgh—New York—Ontario*, 1966, **304**.
79. R. A. Sheldon and J. K. Kochi, in *Adv.Catal.A*, eds. H. P. D.D. Eley and B. W. Paul, Academic Press, 1976, vol. Volume 25, pp. 272-413.
80. H. Hattori, Y. Ide, S. Ogo, K. Inumaru, M. Sadakane and T. Sano, *ACS Catal.*, 2012, **2**, 1910-1915.
81. C. Wang, L. Chen and Z. Qi, *Catal.Sci.Technol*, 2013, **3**, 1123-1128.
82. K. Wu, B. Li, C. Han and J. Liu, *Appl. Catal. A-Gen*, 2014, **479**, 70-75.
83. H. X. Yuan, Q. H. Xia, H. J. Zhan, X. H. Lu and K. X. Su, *Appl. Catal. A-Gen*, 2006, **304**, 178-184.
84. A. Sakthivel and P. Selvam, *J. Catal.*, 2002, **211**, 134-143.
85. S. A. C. Carabineiro, L. M. D. R. S. Martins, M. Avalos-Borja, J. G. Buijnsters, A. J. L. Pombeiro and J. L. Figueiredo, *Appl. Catal. A-Gen*, 2013, **467**, 279-290.
86. M. Dias Ribeiro de Sousa Martins Luísa, C. Carabineiro Sónia Alexandra, J. Wang, M. Rocha Bruno Gonçalo, J. Maldonado-Hódar Francisco and J. Latourrette de Oliveira Pombeiro Armando, *ChemCatChem*, 2016, **9**, 1211-1221.
87. D. Tsukamoto, A. Shiro, Y. Shiraishi and T. Hirai, *J. Phys. Chem. C*, 2011, **115**, 19782-19788.
88. S. Shylesh, C. Srilakshmi, A. P. Singh and B. G. Anderson, *Microporous Mesoporous Mater.*, 2007, **99**, 334-344.

89. N. Ulagappan and C. N. R. Rao, *Chem. Commun.*, 1996, DOI: 10.1039/CC9960001047, 1047-1048.
90. G. Dahlhoff, J. P. M. Niederer and W. F. Hoelderich, *Catalysis Reviews*, 2001, **43**, 381-441.
91. K. Wilson, *Applied Organometallic Chemistry*, 2007, **21**, 1002-1002.
92. Y. Wang, J. Zhang, X. Wang, M. Antonietti and H. Li, *Angewandte Chemie International Edition*, 2010, **49**, 3356-3359.
93. M. T. Musser, in *Ullmann's Encyclopedia of Industrial Chemistry*, DOI: https://doi.org/10.1002/14356007.a08_217.pub2.
94. J. Zhong, J. Chen and L. Chen, *Catal.Sci.Technol.*, 2014, **4**, 3555-3569.
95. S. K. Woo, in *Reference Module in Chemistry, Molecular Sciences and Chemical Engineering*, Elsevier, 2020, DOI: <https://doi.org/10.1016/B978-0-12-409547-2.14812-7>.
96. C. Hammond, J. Straus, M. Righettoni, S. E. Pratsinis and I. Hermans, *ACS Catalysis*, 2013, **3**, 321-327.
97. R. A. Moretti, J. Du Bois and T. D. P. Stack, *Organic Letters*, 2016, **18**, 2528-2531.
98. K. Hasan, N. Brown and C. M. Kozak, *Green Chemistry*, 2011, **13**, 1230-1237.
99. Y. Sawada, K. Matsumoto and T. Katsuki, *Angewandte Chemie International Edition*, 2007, **46**, 4559-4561.
100. D. T. Bregante, N. E. Thornburg, J. M. Notestein and D. W. Flaherty, *ACS Catalysis*, 2018, **8**, 2995-3010.
101. I. D. Ivanchikova, I. Y. Skobelev, N. V. Maksimchuk, E. A. Paukshtis, M. V. Shashkov and O. A. Kholdeeva, *Journal of Catalysis*, 2017, **356**, 85-99.
102. D. H. Koo, M. Kim and S. Chang, *Organic Letters*, 2005, **7**, 5015-5018.
103. J. Jarupatrakorn and T. D. Tilley, *Journal of the American Chemical Society*, 2002, **124**, 8380-8388.
104. T. Kamegawa, N. Suzuki, M. Che and H. Yamashita, *Langmuir*, 2011, **27**, 2873-2879.
105. G. P. M. Taramasso, B. Notari, *U.S. Patent 4*, 1983, **(410 501)**.
106. X. Lu, W.-J. Zhou, H. Wu, A. Liebens and P. Wu, *Applied Catalysis A: General*, 2016, **515**, 51-59.
107. T. Kamegawa, D. Yamahana, H. Seto and H. Yamashita, *Journal of Materials Chemistry A*, 2013, **1**, 891-897.
108. X. Jiang, X. Nie, X. Guo, C. Song and J. G. Chen, *Chem.Rev.*, 2020, **120**, 7984-8034.
109. J. P. Holdren, *Science*, 2008, **319**, 424-434.
110. B. M. Tackett, E. Gomez and J. G. Chen, *Nature Catalysis*, 2019, **2**, 381-386.
111. W. Wang, S. Wang, X. Ma and J. Gong, *Chemical Society Reviews*, 2011, **40**, 3703-3727.
112. W. Li, H. Wang, X. Jiang, J. Zhu, Z. Liu, X. Guo and C. Song, *RSC Adv.*, 2018, **8**, 7651-7669.

113. R. Sun, Y. Liao, S.-T. Bai, M. Zheng, C. Zhou, T. Zhang and B. F. Sels, *Energy & Environmental Science*, 2021, **14**, 1247-1285.
114. H. Kim and S. Chang, *Accounts of Chemical Research*, 2017, **50**, 482-486.
115. T. Schwob and R. Kempe, *Angewandte Chemie International Edition*, 2016, **55**, 15175-15179.
116. K. Murugesan, T. Senthamarai, V. G. Chandrashekar, K. Natte, P. C. J. Kamer, M. Beller and R. V. Jagadeesh, *Chemical Society Reviews*, 2020, **49**, 6273-6328.
117. S. Gomez, J. A. Peters and T. Maschmeyer, *Advanced Synthesis & Catalysis*, 2002, **344**, 1037-1057.
118. J. He, L. Chen, S. Liu, K. Song, S. Yang and A. Riisager, *Green Chemistry*, 2020, **22**, 6714-6747.
119. S. Jiang, C. Ma, E. Muller, M. Pera-Titus, F. Jérôme and K. De Oliveira Vigier, *ACS Catalysis*, 2019, **9**, 8893-8902.
120. C. Dong, H. Wang, H. Du, J. Peng, Y. Cai, S. Guo, J. Zhang, C. Samart and M. Ding, *Molecular Catalysis*, 2020, **482**, 110755.

CHAPTER-2

Metal-oxide (Cr and Ru) Supported Periodic Mesoporous Silica for Heterogeneous Catalysis

Part 2A. Cyclohexane Oxidation Reaction over Cr-oxide Supported MCM-41 Catalyst.

Part 2B. Phenol Hydrogenation Reaction over Ru-oxide Supported MCM-41 Catalyst.

This chapter has been adapted from:

- 1) **K. J. Betsy**, Chandrani Nayak, Anish Lazar, Athira Krishnan, D. Bhattacharyya, S. N. Jha and C. P. Vinod, Selective oxidation of cyclohexane to cyclohexanone using chromium oxide supported mesoporous MCM-41 nanospheres: Probing the nature of catalytically active chromium sites, *ChemCatChem*, **2018**, 10, 3291.
- 2) **K.J Betsy**, Anish Lazar, and C. P. Vinod, Highly selective aqueous phase hydrogenation of phenols over nanostructured RuO₂ on MCM-41 catalysts, *Nano-structures and Nano-Objects*, **2018**, 13, 36-43.

This chapter comprises the selective oxidation and hydrogenation reactions over metal-oxide supported mesoporous silica and are discussed in two parts: 2A and 2B.

Part 2A. Cyclohexane oxidation reaction over Cr-oxide supported MCM-41 catalyst.

2A.1 Introduction

Cyclohexanone and cyclohexanol (KA oil) are essential chemical feedstock in a variety of industrially essential commodities.¹ KA oil forms precursor to nylon-6 and nylon-6,6 polymers and demands a global consumption of $\sim 10^6$ tons per year. Cyclohexane oxidation reaction requires high activation energy for C-H bond cleavage, which dictates harsh reaction conditions like high temperature (413-433 K) and pressure (1-2 MPa).² Over the past decades, various transition metal-based heterogeneous catalyst systems, like V-MCM-41,³ Co/ZSM-5,⁴ (Cr)MCM-41,⁵ Au⁶⁻⁹ and Fe^{10, 11} heterogenized catalysts, Cr-Ti-Si ternary mixed oxides,¹² Cr-PMO,¹³ have been reported to be active for the cyclohexane oxidation reaction. Among them, chromium incorporated silica is most promising due to its better activity and stability.¹⁴ The enhanced activity exhibited by chromium oxide catalysts was attributed to the presence of variable oxidation states of Cr, coordination environments, and its degree of polymerization.¹⁵ Determining the active sites is one of the prime areas in heterogeneous catalysis, and active site determination in chromium oxide for oxidation reactions has also been attempted.^{16, 17} The nature of Cr active species depends on its location like framework or extra framework positions where Cr (VI) species has been found to be the active site in Cr incorporated silica framework.⁵ In contrast, the presence of coordinatively unsaturated Cr(III) or Cr(VI) species in chromium oxide as active sites in cyclohexane oxidation reactions has also been reported.^{18, 19} The dispersion of Cr species on the support and the Cr loading has also been recognized to be an important factor which influences the catalytic activity.²⁰ The nature of the active species in the Cr-oxide catalyst for different organo-transformation reactions has been the subject of interest for past few years.^{13, 19, 21, 22}

The major cause for the deactivation in chromium based catalysis is the leaching of active Cr ions, and a need for stable catalysts has led to the design of new heterogenized Cr catalysts.^{18, 23-25} There exists an intimate relationship between the compositional, structural, and physicochemical properties of the oxide support and the surface nature of chromium. The oxide

support acts as a ligand that controls the redox properties of the supported Cr ions. Hence the selection of support that can stabilize the active chromium sites is a tedious job. Among the several oxide supports, mesoporous M41S molecular sieves (MCM-41 and MCM-48) are promising candidates which exhibit better textural properties and act as an ideal scaffold for metal oxides incorporation on mesoporous channels. These properties prevent the agglomeration of Cr-oxide particles and also favour the diffusion of reacting molecules.²⁶

This contribution from chapter 2A aims to examine the nature of active Cr species on the silica-supported catalyst for the cyclohexane oxidation reaction. A series of samples with uniformly dispersed chromium oxide supported on mesoporous MCM-41 silica nanospheres by facile wet impregnation method were synthesized. The nature of Cr active species for cyclohexane oxidation reaction has been determined by correlating catalytic activity with characterization results. Under mild reaction conditions, the optimum catalyst gave 72 % conversion and 99 % selectivity towards cyclohexanone.

2A.2 Experimental

2A.2.1 Synthesis of MCM-41 nanospheres

The synthesis of spherical MCM-41 nanospheres was carried out using the modified sol-gel procedure reported in the literature.²⁷ In a typical synthesis, 3.5 mL of 2M NaOH solution was mixed with 480 mL of Millipore water. Then 1g of CTAB was added to the solution, and the mixture was heated at 70 °C with stirring. After the solution became homogeneous, 5 mL of TEOS was added in drops, forming a white slurry. The stirring was continued at 70 °C for 2 h. The resulting white residue was filtered and washed thoroughly with water and ethanol to remove excess NaOH and CTAB. The obtained powder was dried at 100 °C for 12 h and calcined in air at 500 °C for 4 h (at a ramp rate of 2 °C/min).

2A.2.2. Synthesis of CrO_x-MCM-41

The CrO_x-MCM-41 heterogeneous catalysts of different chromium loadings were synthesized using a wet impregnation method by utilizing a reported procedure elsewhere²⁸ with slight modifications. In brief, desired amount of active Cr(NO₃)₃·9H₂O metal precursor dissolved in a minimum amount of water to which 1g of MCM-41 was charged slowly with continuous stirring. The slurry was allowed to stir for 8 h, after which the resulting material was dried at 100 °C for

12 h and calcined at 600 °C for 8 h (at a ramp rate of 2 °C/min). The Cr loading on MCM-41 was controlled to 0.5, 1, 2.5, 4, 5, 7, and 10 wt % by varying the amount of metal precursor.

2A.2.3 Catalysts Characterization

Powder XRD analyses of all catalysts were measured using a PANalytical X'pert Pro dual-goniometer diffractometer with Ni-filtered Cu K α radiation (1.5418 Å) at 40 kV and 30 mA. A Shimadzu UV/Vis spectrophotometer with a dual-beam was used to measure UV/Vis spectra. N₂ adsorption-desorption isotherms and pore size distributions of the samples were collected using an Autosorb 1C Quantachrome, USA. The program consisted of both adsorption and desorption branches and was performed typically at 77 K after the samples were degassed at 150 °C for 4 h. Calculation of the specific surface area was done by the Brunauer-Emmett-Teller (BET) method at P/P₀=0.06–0.3. The Barrett-Joyner-Halenda (BJH) model was applied to the desorption branch of the isotherm to determine the total pore volume and average pore diameter. The BJH approach obtained pore size distribution curves. The solid samples' FTIR spectroscopy was performed using a Bruker Tensor 27 FTIR spectrophotometer with a DTGS detector at RT using KBr as an internal standard. TEM images were recorded by using an FEI Tecnai TF-20 electron microscope operated at 200 kV. SEM images were obtained by using a dual-beam scanning electron microscope (FEI company, model Quanta 200 3D) operated at 30 kV. ²⁹Si MAS NMR spectra were recorded by using a BRUKER DSX300 spectrometer at 7.05T (resonance frequencies 59.595 MHz, rotor speed 10000 Hz; and 75.43 MHz, rotor speed 10000 Hz). XPS was performed under ultra-high vacuum conditions using a near-ambient-pressure X-ray photoelectron spectrometer (NAP-XPS) from Prevac, Poland. All the spectra were charge corrected with respect to C1s at BE=284.6 eV. The peak-fitting of the Cr2p spectra was performed using Casa XPS software with a Shirley-type background. A Horiba Jobin Yvon Lab Raman HR 800 micro Raman spectrometer (HJY, Kyoto, Japan) with a laser wavelength of 514 nm was used to collect Raman spectra. XAS measurements of the catalysts were performed at the Cr Kedge in fluorescence mode at the Scanning EXAFS Beamline (BL-9) at the INDUS-2 Synchrotron Source (2.5 GeV, 100 mA) at the Raja Ramanna Centre for Advanced Technology (RRCAT), Indore, India.^{29, 30} A double crystal monochromator (DCM) was used as the beamline, which works in the photon energy range of 4-25 KeV with a resolution of 10⁴ at 10 KeV. A horizontal pre-mirror of 1.5 m with a meridional cylindrical curvature collimate the beam, and a higher harmonic rejection was used before the DCM. A sagittal cylinder with a radius of curvature of

1.28-12.91m was used as the second crystal. This provides the horizontal focusing of the beam, whereas a Rh/Pt-coated bendable post mirror that faced down was used for the vertical focusing of the beam. For fluorescence-mode measurements, the sample was placed at 45° to the incident X-ray beam and the fluorescence signal (I_f) was detected using a Si drift detector placed 90° to the incident X-ray beam. An ionization chamber detector was used to measure the incident X-ray flux (I_0) and the sample absorbance ($m=I_f/I_0$) as a function of energy obtained by scanning the monochromator over a specified energy range. EXAFS oscillations were extracted from the XAS spectra following the standard procedure.³¹ The EXAFS oscillations, $\chi(k)$ were weighted by k to amplify the oscillation at high k . The $\chi(k)$ k functions were Fourier transformed using a k range of 2-9 \AA^{-1} to generate the $\chi(r)$ versus r (or FT-EXAFS) spectra in terms of the real distances from the center of the absorbing atom. The Demeter software package was used for EXAFS data analysis by the reduction and fitting of the experimental EXAFS data.³² The EXAFS data fitting parameters were bond distance (r), coordination number (N), and Debye–Waller factor (σ^2), which give the static and thermal disorder of the system. The k range for Fourier transform and the R range for data fitting were chosen in such a way that in each case during fitting, the number of free variables was always kept below the upper limit set by the Nyquist theory ($N_{\text{free}}=2\Delta k\Delta r/\pi+1$).³³ The goodness of the fit in the above process is generally expressed by the R_{factor} [Eq. (1)] below:

$$R_{\text{factor}} = \sum \frac{[\text{Im}(\chi_{\text{dat}}(r_i) - \chi_{\text{th}}(r_i))]^2 + [\text{Re}(\chi_{\text{dat}}(r_i) - \chi_{\text{th}}(r_i))]^2}{[\text{Im}(\chi_{\text{dat}}(r_i))]^2 + [\text{Re}(\chi_{\text{dat}}(r_i))]^2}$$

in which χ_{dat} and χ_{th} refer to the experimental and theoretical $\chi(r)$ values, respectively, and Re and Im refer to the real and imaginary parts of the respective quantities. The R_{factor} of all the fitting is less than 0.01, which indicates the good fitting of the data.

2A.2.4 Catalytic Activity Test

Liquid-phase cyclohexane oxidation was performed in a two-necked round-bottomed flask equipped with a condenser and charged with cyclohexane (1 mmol), acetonitrile (5 mL) as the solvent, catalyst (50 mg), and TBHP (1.2 mmol) as the oxidant. The reaction was performed at 70 °C for 24 h with continuous stirring. After the reaction, the catalyst was separated by simple centrifugation, and the products were analyzed using GC (Agilent 7890 connected with HP5 column and flame ionization detector; FID) and confirmed by using GC-MS (Varian connected

with an HP5 column). The products were determined by comparison with authentic samples by using GC and GC-MS. HPLC with a Rezex ROA H+ column was used to analyze acid products. To test reusability, after each cycle, the catalyst was washed repeatedly with acetonitrile and pretreated at 120 °C for 12 h.

2A.3 Results and Discussion

2A.3.1 X-ray Diffraction

The powder XRD patterns of the CrO_x-MCM-41 catalysts were collected in two different 2θ regions. In the small-angle X-ray diffraction (SAXRD) pattern (Figure 2A.1a), a peak at 2θ=2.5 corresponds to the d₁₀₀ reflection in agreement with the XRD pattern of the MCM-41-type materials.^{27, 34} As the Cr loading in the catalyst increases from 0.5 to 10 wt %, the intensity

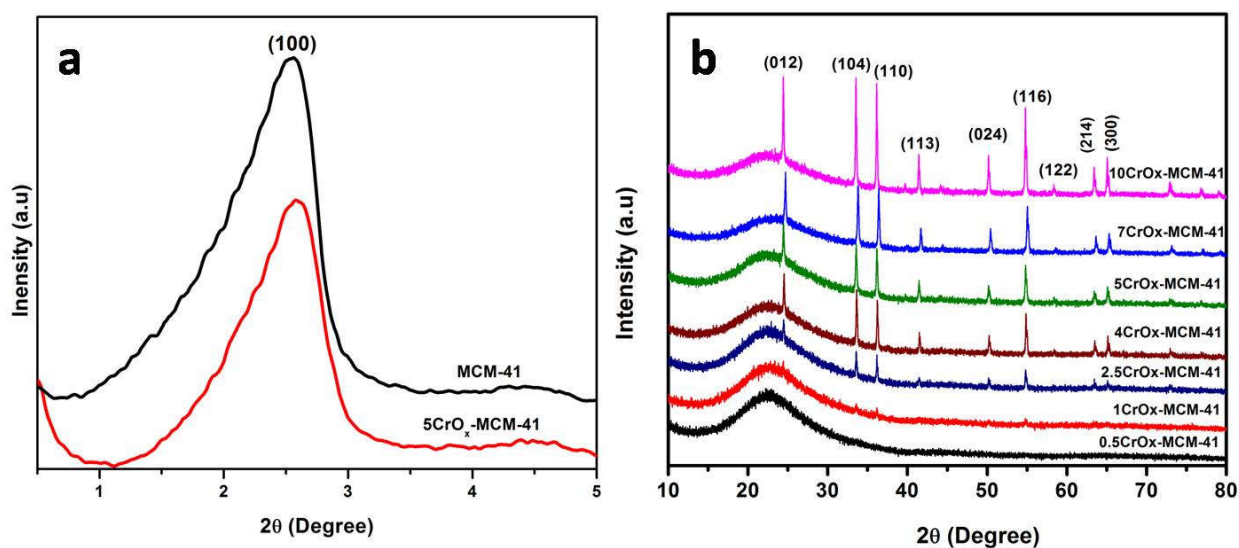


Figure 2A.1: XRD plots of CrO_x-MCM-41 catalysts (a) small-angle XRD and (b) wide-angle XRD.

of the (100) peak becomes weak. Nevertheless, the peak is still detectable, indicating that the mesoporous structure was preserved even after impregnation, followed by calcination. A decrease in the peak intensity with an increase of the Cr loading also infers the anchoring of Cr in the MCM-41 pores. If we compare the unit cell parameter (a_0) for pristine MCM-41 ($a_0=39.4$ Å) and 5CrO_x-MCM-41 ($a_0=40.1$ Å), no clear incorporation of Cr into the silica framework can be inferred. From the wide-angle XRD patterns (Figure 2A.1b), the diffraction lines are attributable to the rhombohedral phase of Cr₂O₃ (JCPDS No: 84-1616) with a clear increase in intensity with metal loading.

2A.3.2 N₂ Porosimetry

The textural properties of catalysts were explored using N₂ adsorption-desorption analysis, and the results are summarized in Table 2A.1. The chromium oxide supported MCM-41 catalysts 0.5CrO_x-MCM-41, 5CrO_x-MCM-41, and 10CrO_x-MCM-41 show typical type-IV isotherms with H1 hysteresis (Figure 2A.2), which indicate that the overall mesoporous structure of the catalysts

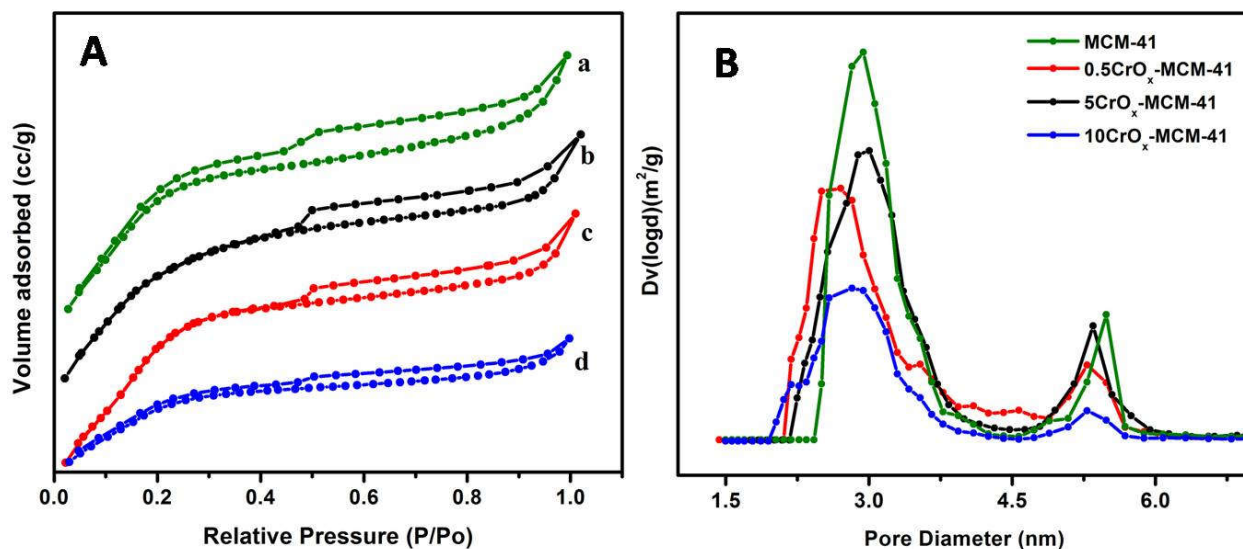


Figure 2A.2: (A) N₂ adsorption-desorption isotherm (a) MCM-41, (b) 0.5CrO_x-MCM-41, (c) 5CrO_x-MCM-41, and 10CrO_x-MCM-41 and (B) pore size distribution of CrO_x-MCM-41 catalysts.

Table 2A.1: The textural properties of MCM-41 and nCrO_x-MCM-41^[a] catalysts

Catalyst	BET Surface area (m ² /g)	Pore diameter (nm)	Pore Volume (cc/g)
MCM-41	957	2.9 & 5.4	0.53
0.5CrO _x -MCM-41	926	2.9 & 5.4	0.52
5CrO _x -MCM-41	859	2.7 & 5.2	0.50
10CrO _x -MCM-41	535	2.8 & 5.3	0.27

[a] nCrO_x-MCM-41, where n indicates wt % of Cr loading with respect to support was retained. The pure MCM-41 material exhibits a high surface area (957 m²g⁻¹), large pore volume (0.529 ccg⁻¹), and a bimodal distribution (Figure 2A.2B) with pore radii of 2.9 and 5.4

nm. After MCM-41 was loaded with Cr species, the surface area, pore diameter, and pore volume of the material decreased, which indicates that chromium oxide was anchored on the MCM-41 mesoporous channels (Table 2A.1).

2A.3.3 Electron Microscopy

Electron microscopy techniques like TEM and SEM were utilized to monitor the synthesized materials' surface morphology and pore structures. From Figure 2A.3, the spherical morphology of synthesized MCM-41 material with an average particle size of ~ 70 nm was confirmed, and the hexagonal mesoporous nature of the catalyst is found to be in good agreement

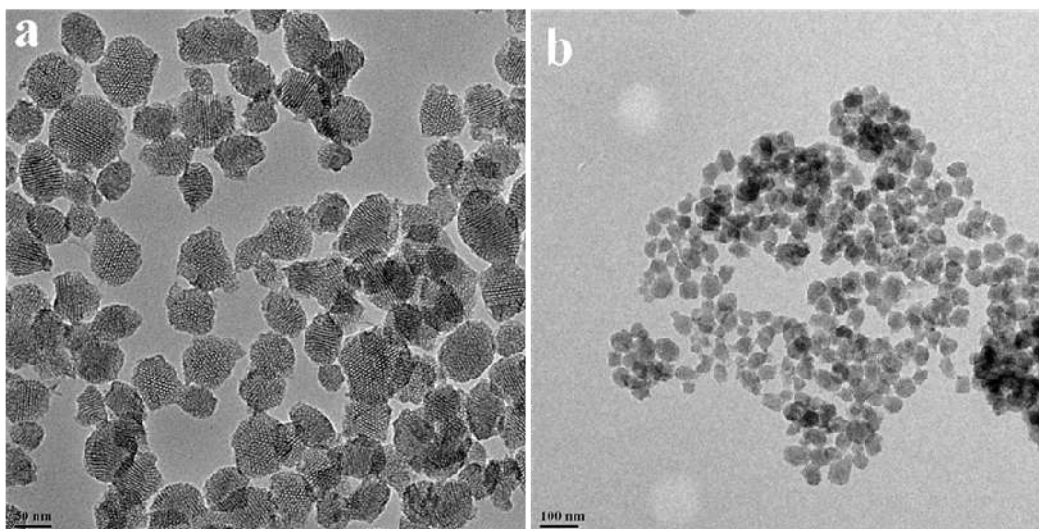


Figure 2A.3: TEM images of (a) pure MCM-41 and (b) $5\text{CrO}_x\text{-MCM-41}$.

with SA-XRD results. The TEM image of 5 wt % Cr loaded catalyst, $5\text{CrO}_x\text{-MCM-41}$, in Figure 2A.3b, shows spherical morphology as well as the mesoporous nature of the material even after the calcination treatment. EDAX analysis from TEM for $5\text{CrO}_x\text{-MCM-41}$ catalyst showed the presence of chromium (~ 4.6 wt %) in the spherical MCM-41 sample. SEM image for $5\text{CrO}_x\text{-MCM-41}$ catalyst clearly shows the spherical surface morphology of the synthesized catalyst (Figure 2A.4).

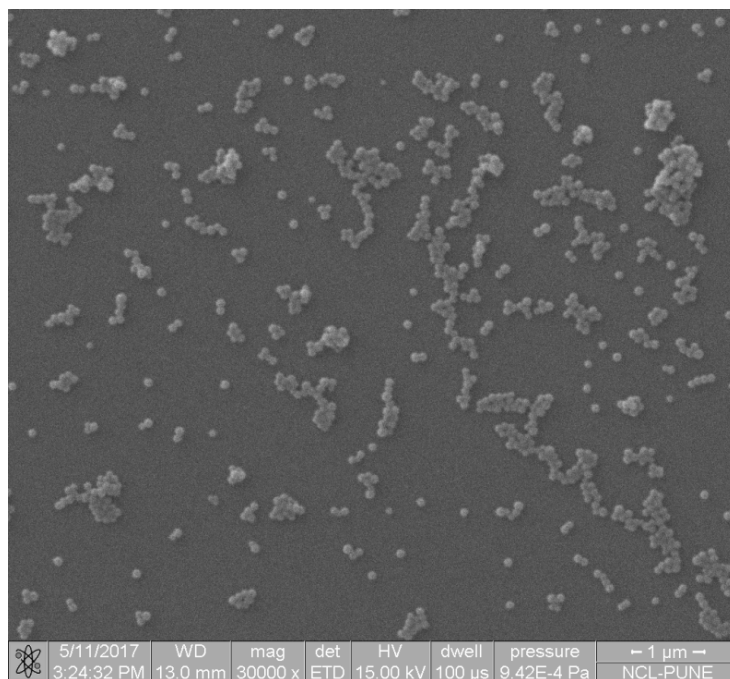


Figure 2A.4: SEM image for 5CrO_x-MCM-41.

2A.3.4 Solid-state NMR Spectroscopy

²⁹Si cross-polarization magic-angle spinning (CPMAS) NMR spectra of pure MCM-41 and 5CrO_x-MCM-41 are shown in Figure 2A.5. Three distinct peaks exist at $\delta = -92$, -102 , and -112 ppm, corresponding to the Q², Q³, and Q⁴ sites on the silica framework, respectively. There is no noticeable difference in the intensity and width of these distinct peaks observed in both pure MCM-41 and the 5CrO_x-MCM-41 catalysts. Zhang and Pinnavaia proposed that a broadening of the peak width and increase in the intensity of the Q⁴ sites along with a decrease in the intensity of the Q² and Q³ sites is mainly caused by isomorphous transition metal substitution into the Si framework.³⁵ Thus, the retention of three sites in silica indicates that isomorphous Cr metal substitution into the silica framework was improbable in this case.

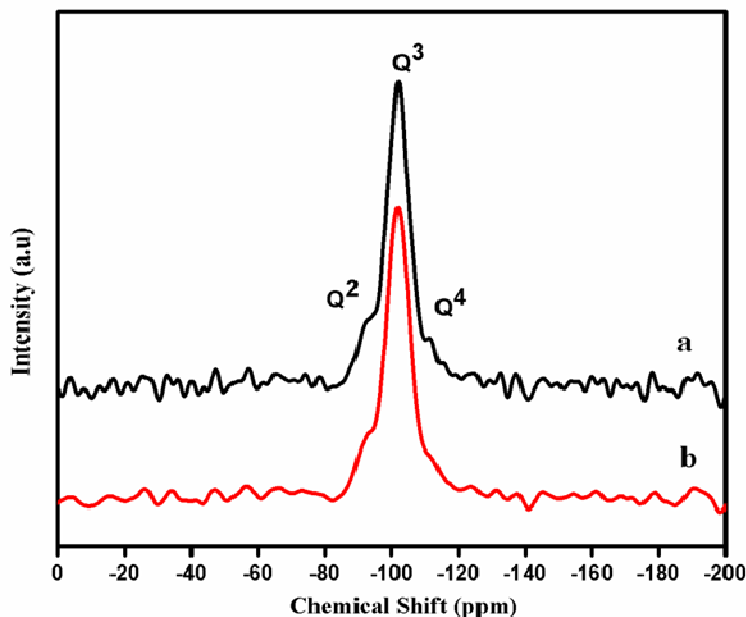


Figure 2A.5: ^{29}Si CPMAS NMR spectra (a) pure MCM-41 and (b) 5CrO_x-MCM-41.

2A.3.5 DRUV-visible Spectroscopy

In order to investigate the oxidation state and coordination environment of Cr in CrO_x-MCM-41 catalysts, UV-Visible DRS experiments were carried out. In Figure 2A.6, two absorption bands centered at 275 nm and 365 nm are observed in all synthesized catalysts and are assigned to tetrahedrally coordinated isolated Cr oxide species O→Cr(VI). These bands are typical due to the transitions of ${}^1T_2 \leftarrow {}^1A_1$ (${}^1t_1 \rightarrow {}^7t_2$ and ${}^6t_2 \rightarrow 2e$) and ${}^1T_2 \leftarrow {}^1A_1$ (${}^1t_1 \rightarrow 2e$), respectively.³⁶ A peak at 467 nm is mainly assigned to Cr³⁺ transition having a distorted octahedral symmetry (${}^4T_{1g} \leftarrow {}^4A_{2g}$),^{36, 37} which increased with increase in Cr content. This peak's intensity is weaker than the charge transition bands in the lower Cr containing catalysts. An additional broad band located at 600 nm due to the d-d transitions related to Cr³⁺ species in octahedral coordination indicates the presence of Cr₂O₃ clusters. As we move to higher wt %, Cr loaded catalysts, synthesized materials exhibit a gradual increase in peak intensity at 275 nm due to the overlapping of charge transfer band of Cr³⁺ with Cr⁶⁺ signal.³⁶ In contrast, a rise in peak intensity at 600 nm corresponds to the agglomeration of Cr³⁺ species to inactive crystalline α -Cr₂O₃ at higher Cr content.

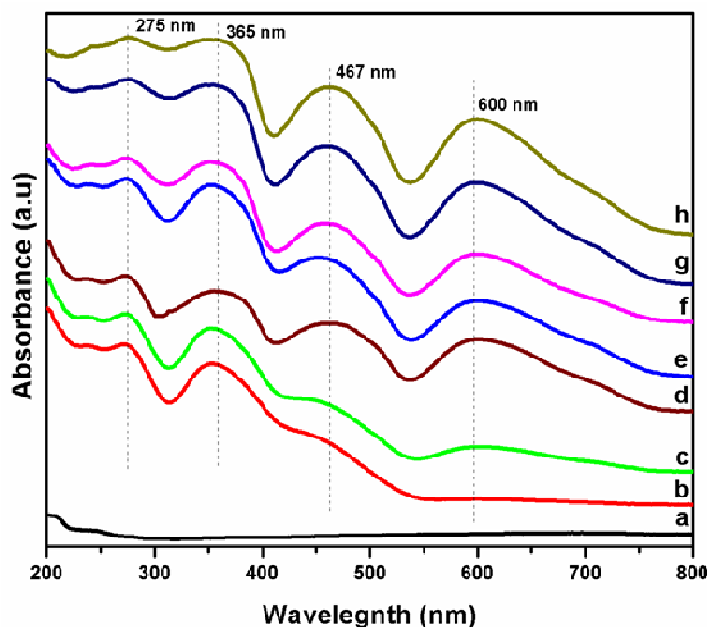


Figure 2A.6: UV- Visible spectra of (a) pure MCM-41, (b) 0.5CrO_x-MCM-41, (c) 1CrO_x-MCM-41, (d) 2.5CrO_x-MCM-41, (e) 4CrO_x-MCM-41, (f) 5CrO_x-MCM-41, (g) 7CrO_x-MCM-41, and (h) 10CrO_x-MCM-41.

2A.3.6 IR Spectroscopy

FT-IR spectroscopy is a convenient technique to study the nature of Cr species present in porous CrO_x-MCM-41 catalysts (Figure 2A.7). The IR bands at 800 cm⁻¹, 950 cm⁻¹, and 1105 cm⁻¹ correspond to Si-O-Si symmetric stretching, Si-OH stretching, and Si-O-Si asymmetric stretching vibrations in silica framework, respectively.³⁸ The IR band for O-Cr(VI) species³⁹ in CrO_x-MCM-41 material occurs at 950 cm⁻¹, and its peak is not measurable quantitatively due to the merging of Si-OH stretching band in the same region. Meanwhile, a distinct band is observed at 623 cm⁻¹ which corresponds to chromium oxide species,⁴⁰ and it can be taken as an indicator for the presence of CrO_x species in MCM-41 channels.

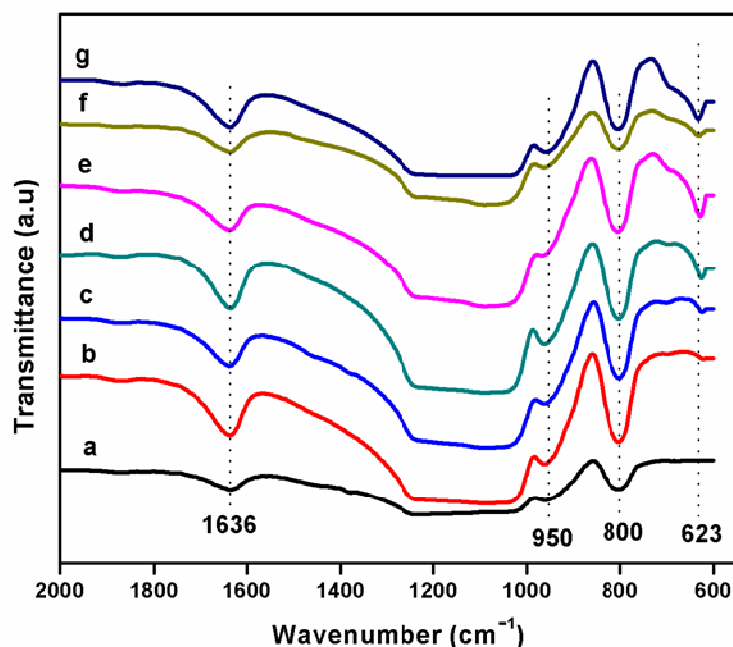


Figure 2A.7: FT-IR spectra of (a) 0.5CrO_x-MCM-41, (b) 1CrO_x-MCM-41, (c) 2.5CrO_x-MCM-41, (d) 4CrO_x-MCM-41, (e) 5CrO_x-MCM-41, (f) 7CrO_x-MCM-41 and (g) 10CrO_x-MCM-41.

2A.3.7 Raman Spectroscopy

Raman spectroscopic technique was used to probe the molecular nature of supported Cr species in all solid catalysts. In Raman spectra (Figure 2A.8), a series of synthesized catalysts with increased chromium loading exhibited bands corresponding to different Cr surface species. A peak at 350 cm⁻¹ is assigned to monochromatic Cr⁶⁺ surface species, which increases the intensity above 5 wt % Cr loaded catalyst.⁴¹ It is observed that the intensity of two bands centered at 553 cm⁻¹ and 609 cm⁻¹, characteristic of crystalline Cr₂O₃ and distorted octahedral Cr³⁺ species, respectively, rises with an increase in Cr content.^{15, 42} Moreover, the two broad bands located at 868 cm⁻¹ and 980 cm⁻¹, observed only at the higher Cr loaded catalysts are evident and confirm the existence of polymeric Cr⁶⁺ species.⁴¹ The peaks at 305 cm⁻¹ and 525 cm⁻¹, which are absent in lower loading, confirm the absence of crystalline α -Cr₂O₃ species, visible in higher chromium loaded catalysts, i.e., above monolayer coverage. As metal loading increases, the mono- and dichromate species tend to agglomerate to form trichromate species, leading to the formation of crystalline Cr₂O₃ clusters in good agreement with UV-Vis and XRD results.

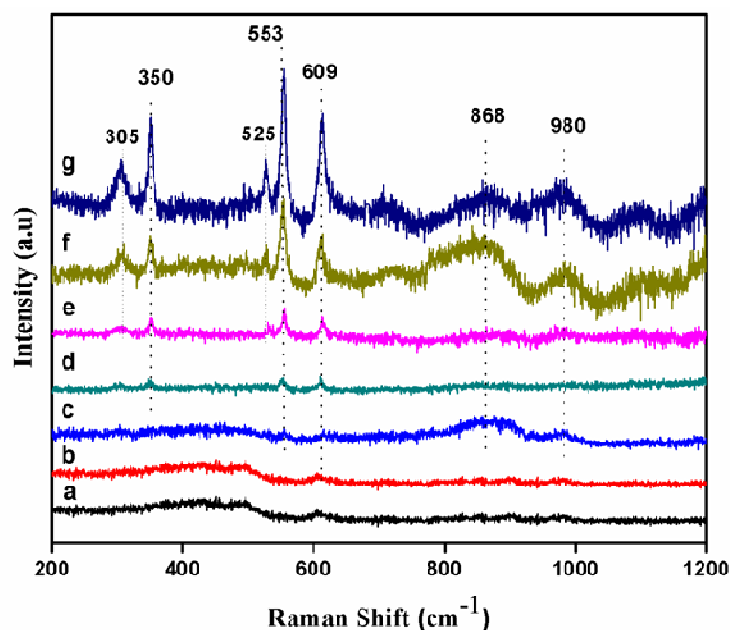


Figure 2A.8: Raman spectra of (a) 0.5CrO_x-MCM-41, (b) 1CrO_x-MCM-41, (c) 2.5CrO_x-MCM-41, (d) 4CrO_x-MCM-41, (e) 5CrO_x-MCM-41, (f) 7CrO_x-MCM-41 and (g) 10CrO_x-MCM-41.

2A.3.8 X-ray Absorption Spectroscopy (XAS)

To garner further insight into the structure and coordination environment of the Cr species, synchrotron XAS was done. Figure 2A.9a shows the XANES spectra at Cr K edge of the Cr oxide supported on MCM-41 catalyst samples along with Cr metal, Cr₂O₃, and CrO₃ standards. CrO₃ shows a strong pre-edge peak near 5991 eV, which is due to the dipole forbidden 1s-3d transition. This forbidden transition is allowed when Cr cations exist in the non-centrosymmetric environment. In CrO₃, Cr(VI) cations exist in tetrahedral coordination, which facilitates the hybridization of the 3d and 4p orbitals. Therefore the 1s-3d transition becomes allowed resulting in a strong pre-edge. In Cr₂O₃, the Cr(III) cations exist in octahedral coordination, forbidding the 1s-3d transition resulting in no pre-edge.⁴³⁻⁴⁵ Linear combination fitting (LCF) of the XANES spectra of the samples have been performed using Cr₂O₃ and CrO₃ standard XANES spectra to determine the molar percentage Cr(III) and Cr(VI) species.

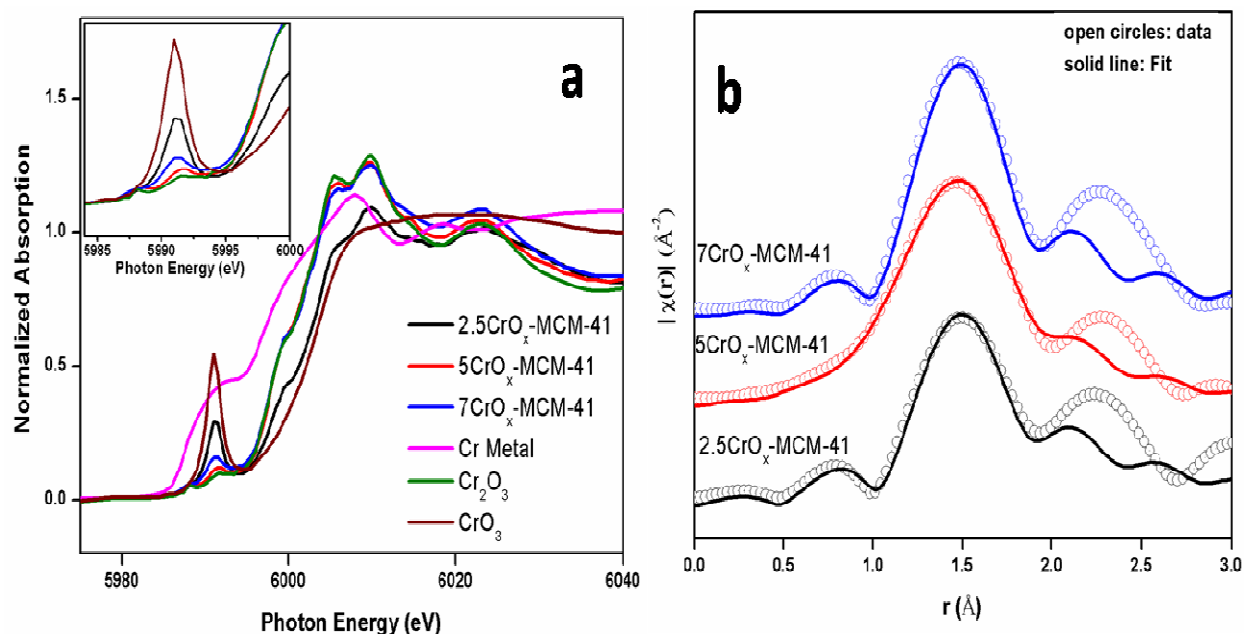


Figure 2A.9: (a) XANES and (b) EXAFS spectra of $n\text{CrO}_x\text{-MCM-41}$ catalysts.

The results of the linear combination fitting have been tabulated (Table 2A.2). From the LCF results, it can be concluded that in the $5\text{CrO}_x\text{-MCM-41}$ and $7\text{CrO}_x\text{-MCM-41}$ samples, Cr cations mostly exist as octahedral Cr (III) species, where above 5 wt % loading most of the Cr^{3+} species may occur as $\alpha\text{-Cr}_2\text{O}_3$. However, in the $2.5\text{CrO}_x\text{-MCM-41}$ sample, Cr cations exist as both octahedral Cr (III) species and tetrahedral Cr (VI) species with Cr(III):Cr(VI) molar percentage ratio of 55:45. The LCF results corroborate with the intensity variation of the pre-edge peaks, as shown in Figure 2A.9a on an enlarged scale.

Table 2A.2: Result of linear combination fitting of the Cr K edge XANES spectra.

Samples	Cr(III)	Cr(VI)
$2.5\text{CrO}_x\text{-MCM-41}$	54.9 %	45.1 %
$5\text{CrO}_x\text{-MCM-41}$	99.3 %	0.7 %
$7\text{CrO}_x\text{-MCM-41}$	92.6 %	7.4 %

Figure 2A.10 shows the experimental EXAFS ($\mu(E)$ versus E) spectra of the Cr oxide supported on MCM-41 catalyst samples measured at Cr K edge and the experimental $\chi(r)$ versus r plots of

the Cr oxide supported on MCM-41 catalyst samples at Cr K edge have been fitted from 1-2 Å assuming a Cr-O ($\times 6$) shell. Figure 2A.9b shows the experimental $\chi(r)$ versus r plots of the Cr oxide supported on MCM-41 catalyst samples at Cr K edge along with best fit theoretical plots carried out as above, and the fitting results have been tabulated (Table 2A.3).

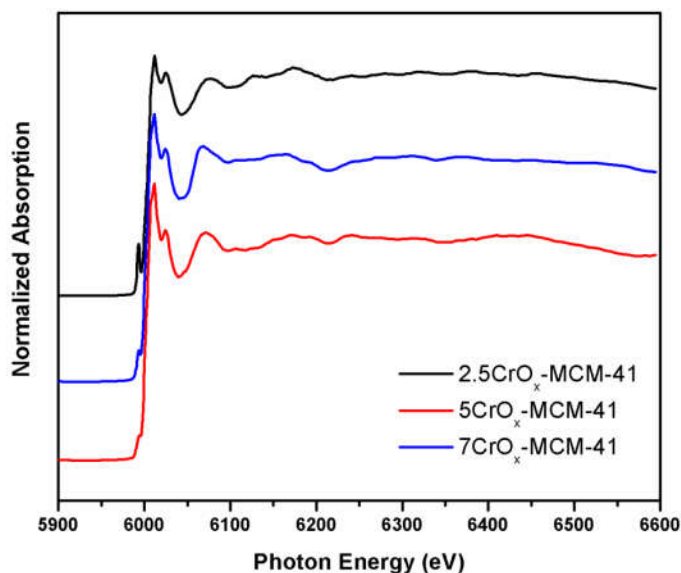


Figure 2A.10: Experimental EXAFS ($\mu(E)$ versus E) spectra of $n\text{CrO}_x$ -MCM-41 catalysts

From the EXAFS analysis results, it can be observed that for the samples 5CrO_x -MCM-41 and 7CrO_x -MCM-41, six oxygen atoms exist around Cr cations at a distance of around 1.95 Å. This local environment resembles the Cr_2O_3 structure suggesting the presence of octahedral Cr (III) species. However, for the 2.5CrO_x -MCM-41 sample, the Cr-O bond length decreases to 1.89 Å with coordination number 5. This decrease in bond length and coordination number may be attributed to the presence of tetrahedral Cr(VI) cations in this sample.

Table 2A.3: Cr K edge EXAFS fitting results

Samples	Cr-O Shell		
	$r(\text{Å})$	N	$\sigma^2 (\text{Å}^{-2})$
2.5CrO_x -MCM-41	1.89	4.9	0.003
5CrO_x -MCM-41	1.95	5.9	0.007
7CrO_x -MCM-41	1.93	5.8	0.001

From XANES analysis, the Cr(III):Cr(VI) molar percentage ratio is 55:45 in this sample, giving an average coordination number of $0.55 \times 6 + 0.45 \times 4 = 5.1$. Therefore, the EXAFS analysis results corroborate with the XANES LCF results. Thus from XANES LCF and EXAFS analysis, it can be concluded that Cr cations mostly exist as octahedral Cr (III) in $5\text{CrO}_x\text{-MCM-41}$ and $7\text{CrO}_x\text{-MCM-41}$ samples with a significant portion of Cr(III) existing in crystalline $\alpha\text{-Cr}_2\text{O}_3$ phase in the latter. In the $2.5\text{CrO}_x\text{-MCM-41}$ sample, Cr cations exist as both octahedral Cr (III) species and tetrahedral Cr (VI) species with Cr(III):Cr(VI) molar percentage ratio of 55:45.

2A.3.9 X-ray Photoelectron Spectroscopy

Figure 2A.11 shows the Cr 2p XPS plot for $n\text{CrO}_x\text{-MCM-41}$ samples, which provides evidence for the oxidation state of surface Cr species. Calibration of all the peak positions was done by considering C 1s standard value at 284.6 eV. The broad nature of Cr $2p_{3/2}$ and Cr $2p_{1/2}$ regions of the Cr-oxide catalysts indicate the existence of more than one Cr species on the surface. Through XPS peak fitting program, the Cr $2p_{3/2}$ region could be deconvoluted into two peaks centered at 576 eV and 579 eV attributed to the Cr^{3+} and Cr^{6+} species, respectively.⁴⁶

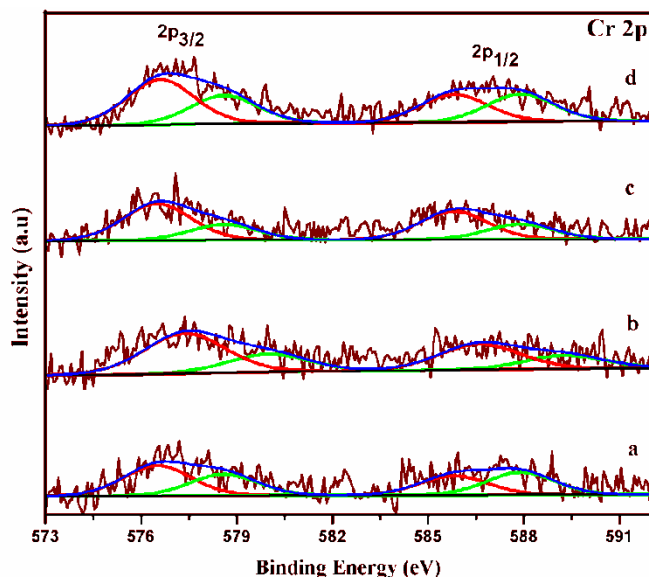


Figure 2A.11: Cr 2p XPS plot for (a) $2.5\text{CrO}_x\text{-MCM-41}$, (b) $4\text{CrO}_x\text{-MCM-41}$, (c) $5\text{CrO}_x\text{-MCM-41}$ and (d) $10\text{CrO}_x\text{-MCM-41}$.

2A.3.10 Cyclohexane oxidation activity

The catalytic performance of the 0.5, 1, 2.5, 4, 5, 7, and 10 wt % Cr loaded catalysts (CrO_x-MCM-41) was investigated in a liquid phase cyclohexane oxidation reaction. The reaction was carried out under mild conditions (70 °C) where acetonitrile was used as the solvent and TBHP as both oxidizer and radical initiator to overcome the induction period.

Table 2A.4: Catalytic oxidation of cyclohexane to cyclohexanone^[a]

Entry	Catalyst	Conv. ^[b] (%)	Selectivity (%) ^[c, d]		Ref.
			Cy-one	Cy-ol	
1	Without catalyst	0	0	0	This work
2	Pure MCM-41	0	0	0	''
3	Bulk Cr ₂ O ₃	9	91	9	''
4	CrO ₃	6	83	17	''
5	0.5CrO _x -MCM-41	14	99	-	''
6	1CrO _x -MCM-41	18	99	-	''
7	2.5CrO _x -MCM-41	36	99	-	''
8	4CrO _x -MCM-41	54	99	-	''
9	5CrO _x -MCM-41	72	99	-	''
10	7CrO _x -MCM-41	12	99	-	''
11	10CrO _x -MCM-41	8	99	-	''
12*	(Cr)MCM-41 [TBHP]	61	81	-	5
13*	(Cr)MCM-41 [H ₂ O ₂]	99	1	89	14
14*	(Cr)PMO [TBHP]	12	70	22	13
15*	Cr-MCM-41 [air]	7	66	26	47
16*	Cr-Co-TUD-1[TBHP]	43	84	5	48

[a] Reaction conditions: catalyst (50 mg); cyclohexane (1 mmol); 70 % TBHP (1.2 mmol); CH₃CN (5 ml); reaction temperature: 70 °C; time: 24 h; [b] [initial con. of C₆H₁₂ - con. of C₆H₁₂

at time t / initial con. of C_6H_{12}] $\times 100$; [c] [moles of individual product / moles of total products] $\times 100$; [d] include trace amounts of adipic acid; * from comparable literature reports.

Table 2A.4 (entries 5-11) shows the catalytic activity trend of different catalysts in oxidation reaction to achieve the direct production of cyclohexanone from cyclohexane. It is remarkably noted that the 5 wt % Cr loaded catalyst showed a conversion of 72 % and 99 % selectivity towards cyclohexanone. To validate the performance of our CrO_x -MCM-41 catalysts for higher selectivity towards cyclohexanone from cyclohexane with comparable conversion, activity results were compared with previous literature reports on Cr-based silica catalysts where TBHP, H_2O_2 , and air were used as oxidants (Table 2A.4, entries: 12-16). It is generally observed that cyclohexanone was the major product obtained when TBHP was used as the oxidant, which agrees with previous reports.^{5, 22, 49} From the literature, the nature of the active site for cyclohexane oxidation on Cr-MCM-41 catalysts was dictated to be the tetrahedral Cr species in the silica framework.⁵

A volcano-type trend in activity was observed from the conversion plot as the Cr wt % increases in the catalyst (Figure 2A.12 green line) was found to agree with the XPS and XAS data. It is observed that the conversion of cyclohexane over Cr catalysts grows sharply with the increase in total Cr content up to 5 wt%, and a further increase of metal content (7 and 10 wt %) shows a decline in cyclohexane conversion. Interestingly, all synthesized catalysts exhibit 99 % selectivity towards cyclohexanone. This unfavorable drop in conversion could be explained either by the decrease in dispersed Cr^{3+} species or due to the formation of inactive crystalline α - Cr_2O_3 on the surface, which results in pore blocking and limits the diffusion of reactant molecules. A plot of the ratio of Cr^{3+} to Cr^{6+} threw more light into the nature of Cr species active for this reaction. The Cr^{3+}/Cr^{6+} ratio of different Cr loaded catalysts was determined from the fitted peaks of XPS and XANES spectra, and the results revealed that as the Cr content increases, the ratio of Cr^{3+}/Cr^{6+} species increases up to 5 CrO_x -MCM-41 catalyst and decreases with further loading (Figure 2A.12).

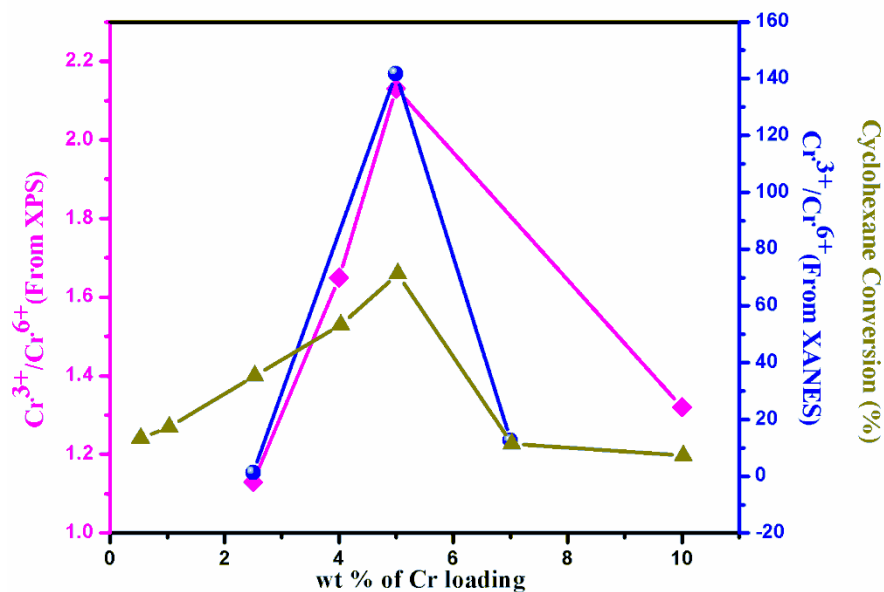


Figure 2A.12: Plot showing the relative effectiveness of $\text{Cr}^{3+}/\text{Cr}^{6+}$ in catalyzing the oxidation of cyclohexane over different wt % $n\text{CrO}_x$ -MCM-41 catalysts.

The formation of crystalline $\alpha\text{-Cr}_2\text{O}_3$ and polymeric Cr-oxide species were significant in 7CrO_x -MCM-41 and 10CrO_x -MCM-41 samples. Cr exists at lower loading in both isolated Cr^{3+} and Cr^{6+} species, whereas in 5 %, the catalyst exclusively consists of dispersed Cr^{3+} oxide sites. Further increase in metal showed the presence of polymeric Cr^{6+} along with Cr^{3+} species, where the significant Cr^{3+} contribution is from the crystalline $\alpha\text{-Cr}_2\text{O}_3$ and was detected by XRD, Raman analysis, and UV-Vis measurements. This confirms that crystalline $\alpha\text{-Cr}_2\text{O}_3$ and polymeric Cr^{6+} species passivates the activity of amorphous Cr^{3+} species on the silica surface at higher loadings. Even though a small amount of Cr_2O_3 cluster peaks were observed in all solid catalysts except 0.5CrO_x -MCM-41, the increase in the conversion of cyclohexane by using the less metal loaded catalysts clearly reveals that these clusters are not blocking the accessible Cr active sites. The present characterization and activity results point out the existence of two different types of Cr^{3+} species like crystalline $\alpha\text{-Cr}_2\text{O}_3$ and amorphous or micro-crystalline phase of non-framework Cr^{3+} oxide sites. The cyclohexane oxidation reaction was also carried out without catalyst, bare MCM-41, bulk Cr_2O_3 and CrO_3 (Table 2A.4, entries: 1-4), which exhibited lower conversion. In controlled experiments, the absence of oxidized products or lower conversion from cyclohexane evidence that isolated amorphous Cr^{3+} species in the supported

MCM-41 catalyst plays a key role in transferring oxygen from the oxidant to cyclohexane during the reaction.

To check the leaching of Cr ions from the MCM-41 channels in the catalyst, a recycling study of the active 5CrO_x -MCM-41 catalyst was performed by charging the spent catalyst continuously for the successive two cycles of the catalytic oxidation reaction. The regenerated catalyst was pretreated at $120\text{ }^\circ\text{C}$ for 12 h to remove the physisorbed moisture molecules before charging the spent catalyst for each cycle. In this step, the catalyst was recovered by centrifugation, repeatedly washed with acetonitrile, and dried at $120\text{ }^\circ\text{C}$ for 12 h.

Table 2A.5: Recycling study of 5CrO_x -MCM-41 catalyst in the cyclohexane oxidation reaction.

Entry	Catalyst	Conv. (%)	Selectivity (%)	
			Cy-one	Cy-ol
1	5CrO_x -MCM-41(fresh)	72	99	-
2	First cycle	60	99	-
3	Second cycle	49	99	-
4	Spent (after calcination)	70	99	-

Reaction conditions: catalyst (50 mg); cyclohexane (1 mmol); 70 % TBHP (1.2 mmol); CH_3CN (5 ml); reaction temperature: $70\text{ }^\circ\text{C}$; time: 24 h.

The catalyst showed a gradual loss in its activity in each successive run (Table 2A.5). To investigate the cause for the decline in the activity after each cycle, XPS analysis of the spent catalyst was carried out. Comparing the ratio of $\text{Cr}^{6+}/\text{Cr}^{3+}$ in fresh (0.47) and spent (0.40) 5CrO_x -MCM-41 catalysts indicates that non-framework Cr^{6+} species was majorly leached out during the reaction along with a small amount of Cr^{3+} species. UV-Vis measurements for the spent catalyst were also carried out (Figure 2A.13). A decrease in peak intensity at 275 nm, 365 nm, and 467 nm was observed in spent catalyst compared to the fresh, which indicates the leaching of Cr ions from the catalysts during the reaction. The 600 nm peak was intact, showing that Cr^{3+} species from crystalline Cr_2O_3 are not affected during the recycling experiment and are not the likely

reason for catalyst deactivation. Thus, the UV-Vis data also correlate well with the XPS analysis, which showed Cr^{3+} species to be unaffected during the reaction.

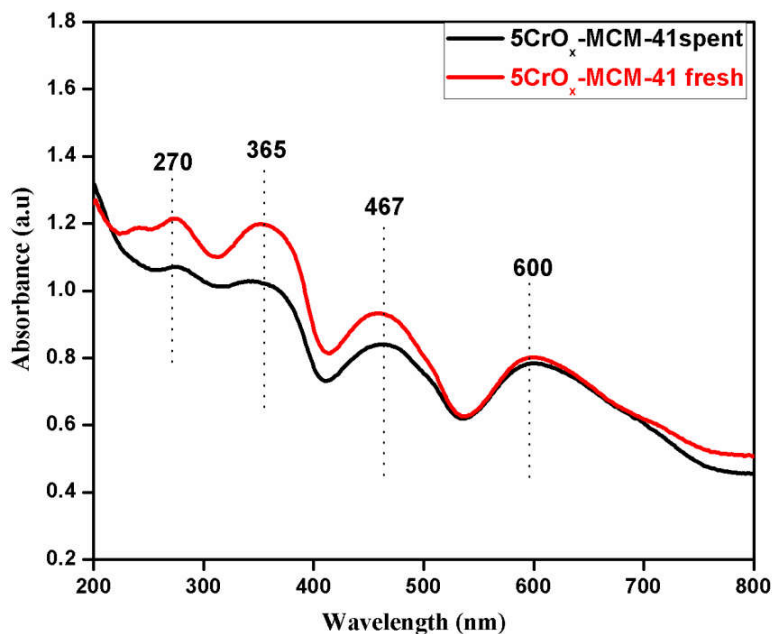


Figure 2A.13: Diffuse reflectance UV-Vis spectra of fresh and spent 5CrO_x-MCM-41 catalyst.

The Cr content in the spent 5CrO_x-MCM-41 catalyst was confirmed using ICP analysis (Spectro Across ICP-OES) and was found to be ~ 4 % with respect to the catalyst. Since the Cr^{3+} species are nearly intact in the catalyst, the loss in catalytic activity during the second and third cycles was intriguing. To probe this, the used catalyst was pretreated by calcining at 600 °C for 8 h and used for the cyclohexane oxidation reaction. The pretreated used catalyst showed similar activity (~ 70 % conversion) like that of fresh 5CrO_x-MCM-41 catalyst which points out that non-framework Cr^{3+} species in the catalyst is active under reaction conditions, and the deactivation might be caused due to the blocking of active sites by carbonaceous species.

Part 2B. Phenol hydrogenation reaction over Ru-oxide supported MCM-41 catalyst

2B.1 Introduction

Catalytic transformations of biorenewable aromatics to value-added chemicals and fuels through the economic and energy-efficient process have currently attracted considerable attention. Global demand for polymers like nylon-6, nylon-6,6, and the depletion in the products derived from non-renewable energy sources has forced to identify a renewable feedstock that replaces the existing materials.⁵⁰⁻⁵² Lignocellulosic biomass is considered as the most accessible renewable feedstock for a variety of fine chemicals and biofuels.⁵³ Among which, lignin accounts for the second most abundant biomass in nature,⁵⁴ which after depolymerization yields highly oxygenated aromatic monomers mainly, phenolic compounds.⁵⁵ By utilizing both heterogeneous and homogeneous catalysts of transition metals, including Pd,⁵⁶ Ru,⁵⁷ Pt,⁵⁸ biomass-derived phenolic bio-oil components (phenols, guaiacols, and syringols) are transformed to their corresponding cycloalkanes with high selectivity. Selective hydrogenation of phenols is a desirable strategy to yield various products involving cycloketones, cycloalcohols, arenes, cycloalkanes, and methane, which are key intermediates to higher-value commodities.

Generally, the phenol hydrogenation reactions are carried out in the vapor phase at elevated temperatures and pressures over supported Pd catalysts, but they suffer deactivation due to coke formation.⁵⁹ Later on, many researchers have contributed to the liquid phase hydrogenation reaction of phenol using Pd,⁶⁰ Pt,⁶¹ Rh⁶² catalysts on different supports for improving the activity. Previous investigations suggest that the metal sites facilitate the activation of H₂ and basic sites in support adsorb phenol during hydrogenation reactions. Depending on the geometry of phenol adsorption on different sites on the support, the product selectivity can be tuned.⁶³ Designing a heterogeneous catalyst using ruthenium nanoparticles is of great interest due to its excellent intrinsic ability for hydrogenation reactions⁶⁴⁻⁶⁶ and cost-effectiveness compared to other noble metals. A detailed insight into the literature reveals that, to date, there are very few efforts to utilize ruthenium as a catalyst to selectively hydrogenate phenolic entities. In the recent past, studies on ruthenium catalysts have been a subject of great interest to hydrogenate arenes,⁵⁵ hydrodeoxygenation of lignin-derived phenols,⁵⁷ and selective hydrogenolysis of phenols,⁶⁷ since they contribute to the concept of chemicals from nature. The main shortcoming with Ru-based

catalysts is the metal detachment from the support resulting in leaching, which reduces the efficiency of the catalyst in liquid phase phenol hydrogenation. Hence it is challenging to develop a stable, highly efficient, and selective catalyst for phenol hydrogenation in a liquid phase. By tuning the nanoparticles' size and shape and the support properties, the catalytic performance can be improved by achieving better physical and chemical reactivity.⁶⁸ Somorjai et al. have proved the remarkable size dependence of Ru NP on the CO oxidation reactivity where 6 nm catalyst showed 8-fold higher activity compared to 2 nm particles.⁶⁹ The catalytic activity trend by nanoparticles with different size has been subject of interest due to its practical and fundamental perspective. It can predict the structure sensitivity of catalytic reaction since particle size alters the surface atomic structure, oxidation state, metal-support interaction and the electronic state which influences the nature of active sites that tunes the product selectivity and conversion.⁷⁰

Identification of suitable solvent is significant in catalytic activity as it drastically influences the rate and selectivity in the hydrogenation of phenolic compounds. The solvent for phenol hydrogenation should be stable to the catalyst and reaction conditions, dissolve and transport of H₂, retain reactants and products in solution.⁷¹ Generally, halogenated organic compounds,⁷² ScCO₂,⁷³ cyclohexane,⁷⁴ ionic liquids,⁷⁵ and water⁷⁶ are used as solvents for phenol hydrogenation. Green solvent water has attracted much attention due to the non-polluting nature of the environment. Recently, Yong Wang et al. have found that hydrogenation of phenol on Pd@mpg-C₃N₄ catalyst proceeds more effectively in water than in organic solvents. Further, DFT calculations showed that water molecules could lower the activation energy for the reaction and will accelerate the proton transfer involved in the hydrogenation of phenol and cyclohexanone to cyclohexanol.⁷⁷ The complete aqueous solubility of phenol could be achieved by an increase in temperature, and the low aqueous solubility of products favors easy separation.

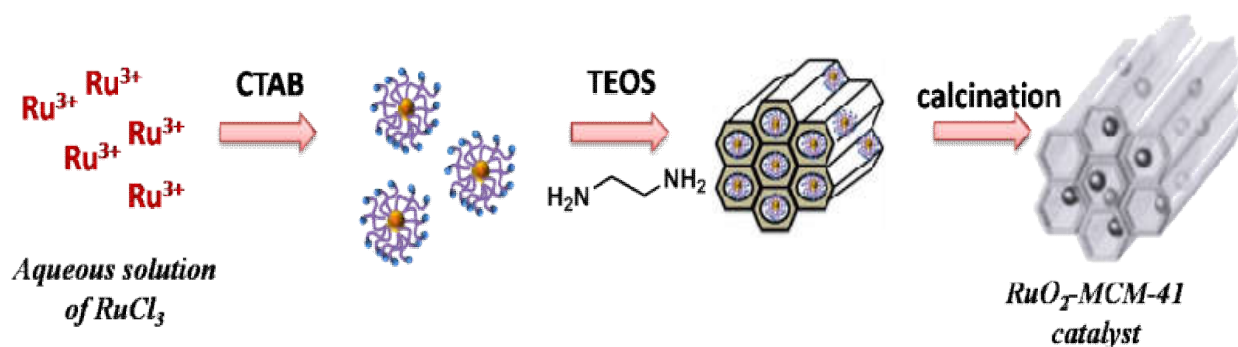
In this present work, a one-pot approach to synthesize finely dispersed nanostructured RuO₂ immobilized on MCM-41 with different amounts of ruthenium with the goal of engineering Ru active sites is attempted. All the Ru-oxide catalysts have been well characterized, and the reaction conditions will be optimized systematically. The optimized RuO₂-MCM-41 catalyst has been utilized for the hydrogenation of phenol, and its substrates, including biomass-derived phenolic compounds, to give corresponding cycloalcohols selectively with high activity under

mild conditions in the aqueous medium. The heterogeneous behavior and stability of RuO₂-MCM-41 catalyst were studied under a reducing reaction environment.

2B.2 Experimental

2B.2.1 One-pot synthesis of RuO₂ nanoparticles supported on MCM-41

Typically, 8 mmol of CTAB was dissolved in 60 mL of water under stirring at 95 °C for 15 min, and a calculated amount of RuCl₃ was added. Simultaneously, in another beaker, 2.5 mL of TEOS was added to 20 mL of ethanol mixed thoroughly, and 1.5 mL of ethylenediamine was added in drops and stirred at RT for 30 min to get a clear solution. The resulting clear solution was added drop-wise into the above metal precursor solution, which is maintained at 75 °C and kept for stirring for the next 2 h. The resulting reaction mixture was cooled to room temperature and aged overnight. The residue was filtered, washed thoroughly with water and ethanol to remove excess ethylenediamine and CTAB. The obtained powder was dried at 80 °C for 12 h and calcined at 400 °C for 6 h (at a ramp rate of 2°C/min). The Ru loading on MCM-41 was controlled to 0.5, 1, 2.5, 4, 5, and 10 wt % by changing the amount of metal precursor to explore the effect of metal content and particle size. Compared to the dry synthesis method,⁷⁸ one-pot approach provides better uniform dispersion and controllable particle size of RuO₂ nanoparticles supported on silica materials like MCM-41. The steps followed for the synthesis of RuO₂-MCM-41 catalyst has been represented in scheme 2B.1.



Scheme 2B.1: One-pot synthesis of RuO₂-MCM-41 catalyst using ethylenediamine.

2B.2.2 Catalytic aqueous phase hydrogenation of phenols

The hydrogenation of phenol over RuO₂-MCM-41 catalysts was investigated in a Parr 4842 autoclave (100 mL) equipped with a mechanical stirrer and temperature controller. The reaction pot was charged with phenol (1.6 mmol), water (10 mL), and catalyst (50 mg), and the autoclave was sealed and purged twice with H₂ to exclude air. A range of experiments was carried out to optimize the reaction conditions by varying temperature, pressure, solvent, amount of catalyst, and time. After the reaction, the catalyst was separated by centrifugation, and the product extraction was done using chloroform. The phenol conversion and selectivity were determined using GC (Agilent 7890 connected with HP5 column and FID detector) and confirmed by GC-MS (Varian connected with HP5 column). The crude product in chloroform was purified using column chromatography and analyzed by ¹H NMR. To check reusability, after each cycle, the separated catalyst was washed repeatedly with water and acetone and dried at 100 °C for 12 h.

2B.3 Results and Discussion

2B.3.1 X-ray Diffraction

The PXRD patterns of the synthesized RuO₂-MCM-41 catalysts were carried out in two different 2θ regions. To evaluate the regularity and formation of the mesoporous MCM-41 silica material by one-pot synthesis strategy was confirmed by the small-angle XRD spectrum. A peak at 2.5° in Figure 2A.1A corresponds to the d₁₀₀ reflection, which is in accordance with the previously reported MCM-41 material.^{27, 34} Intensity of the (100) peak has decreased gradually with ruthenium loading, which could be due to the anchoring of Ru on the MCM-41 mesoporous channels. The wide-angle XRD analysis (Figure 2B.1B) of different wt % of Ru loaded catalysts exhibited the typical reflections attributable to the tetragonal structure of RuO₂ (JCPDS No: 00-018-1139). The reflections from RuO₂ increased sharply with an increase in metal content, indicating the growth of particle size.

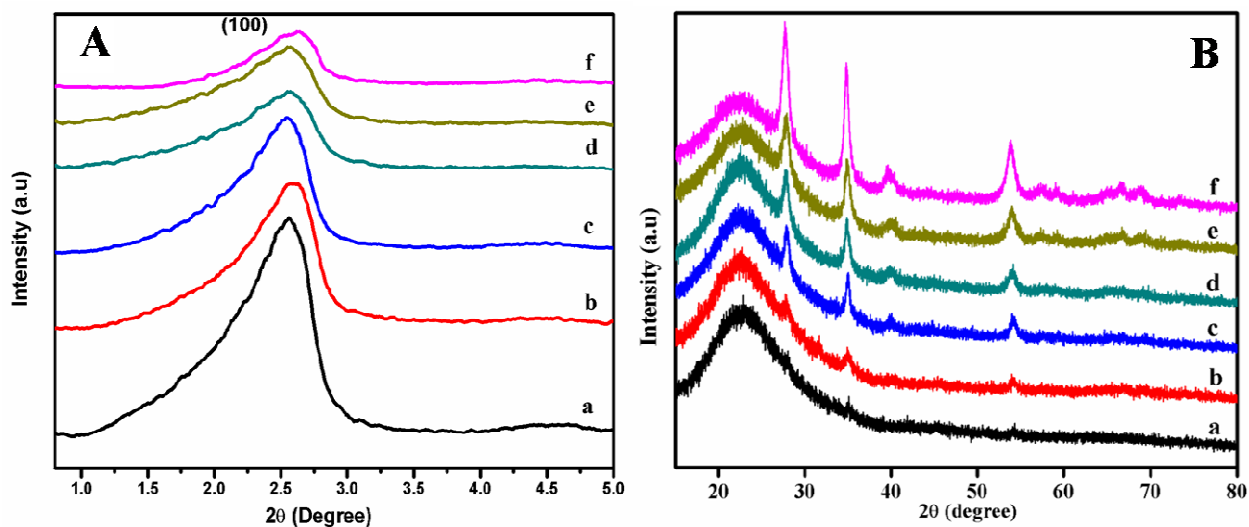


Figure 2B.1: Powder XRD patterns of RuO₂-MCM-41 catalysts in two different 2θ regions. A) Small angle-XRD and B) Wide angle-XRD: (a) 0.5RuO₂-MCM-41, (b) 1RuO₂-MCM-41, (c) 2.5RuO₂-MCM-41, (d) 4RuO₂-MCM-41, (e) 5RuO₂-MCM-41 and (f) 10RuO₂-MCM-41

2B.3.2 N₂ Adsorption and ICP-AES Analysis

The textural properties of the synthesized material were analyzed using the N₂ adsorption-desorption method, and the results are outlined in Table 2B.1. All RuO₂-MCM-41 catalysts showed typical type-IV isotherms with H1 hysteresis (Figure 2B.2) and the pore size distribution (inset) with a unimodal pore diameter of ~3.8 nm, which indicates the mesoporous nature of the

Table 2B.1: The textural properties of nRuO₂-MCM-41^a catalysts

Catalyst	BET Surface area (m ² /g)	Pore diameter (nm)	Pore Volume (cc/g)
MCM-41	983	3.9	0.28
0.5RuO ₂ -MCM-41	971	3.8	0.28
5RuO ₂ -MCM-41	844	3.8	0.25
10RuO ₂ -MCM-41	768	3.7	0.21

^anRuO₂-MCM-41, where n indicates wt % of Ru loading with respect to support.

support. The surface area and pore volume were found to decrease with an increase in metal loading. The Ru content in the fresh 5RuO₂-MCM-41 catalyst was confirmed using ICP analysis (Spectro Acros ICP-OES) and was found to be ~ 4.8 % with respect to the catalyst (theoretical loading 5 wt %).

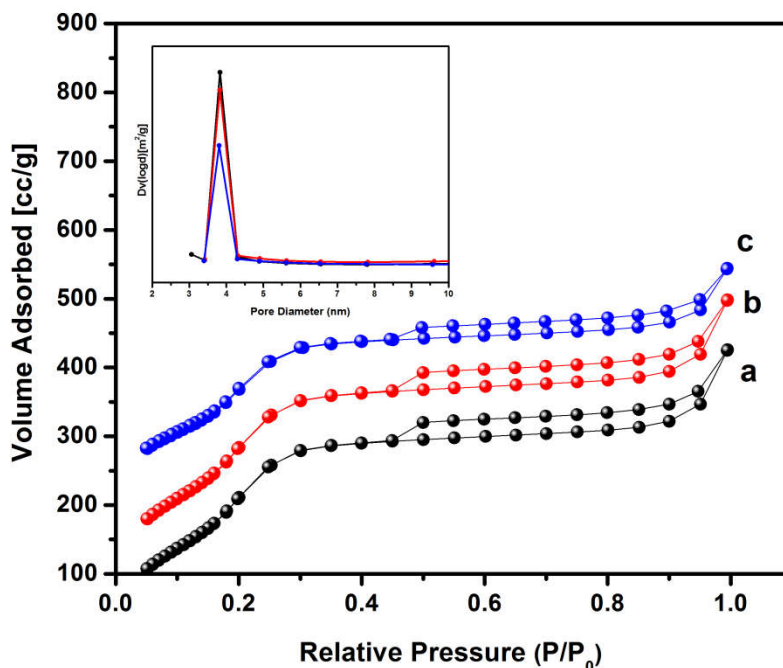


Figure 2B.2: N₂ adsorption-desorption isotherms and pore size distributions (inset) of (a) 0.5RuO₂-MCM-41, (b) 5RuO₂-MCM-41 and (c) 10RuO₂-MCM-41.

2B.3.3 Electron Microscopy

To gain more insight into the size and morphology of the RuO₂-MCM-41 catalysts, transmission electron microscopy analysis was carried out. The TEM images of the catalysts shown in Figure 2B.3 reveal that RuO₂ nanoparticles were well dispersed on mesoporous MCM-41 support and the corresponding average particle size distributions of the catalysts, which increase from 3 nm to 15 nm for 2.5RuO₂-MCM-4, 5RuO₂-MCM-41, and 10RuO₂-MCM-41, respectively. In the higher metal loaded catalyst (10 wt %), the RuO₂ particle size was found to be < 15 nm, which portrays the advantage of the one-pot synthesis strategy using ethylenediamine as a ligand which acts as the metal coordination site to stabilize and tune the particle size, and also maintains the basic pH for the formation of MCM-41 silica material. The mesoporous nature of the MCM-41 material from TEM images agrees with the N₂ sorption and the PXRD results.

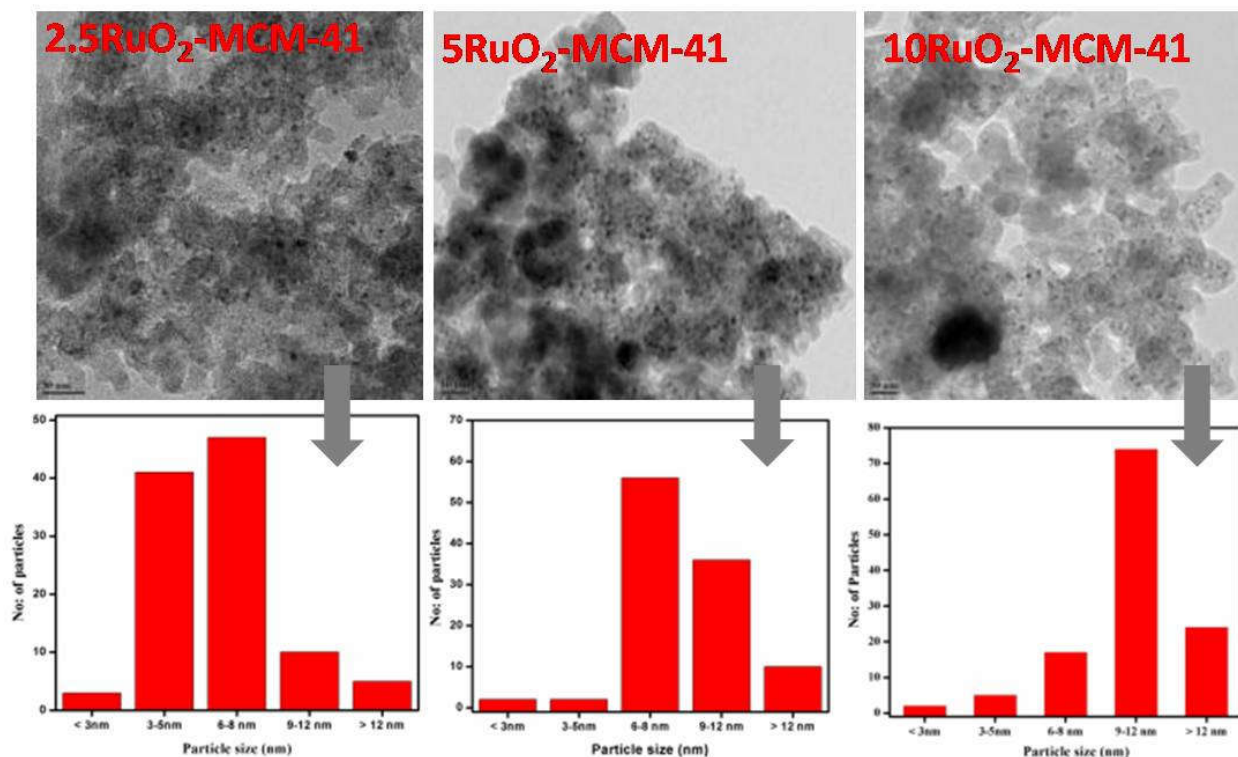


Figure 2B.3: TEM images and corresponding particle size distributions of RuO₂-MCM-41 catalyst.

2B.3.4 Solid-state NMR Spectroscopy

In ²⁹Si CPMAS NMR spectra for RuO₂-MCM-41 catalysts shown in Figure 2B.4, a gradual decrease in the intensity was observed for the three distinct peaks centered at -92 ppm, -102 ppm, and -112 ppm correspond to the Q², Q³, and Q⁴ sites on silica framework, respectively, as the metal loading increased. This may be due to the interference of the silica and Ru precursor in the one-pot synthesis to form the metal-supported silica system. This loss of siloxane framework architecture can also tend to the growth of Ru particle size, which can be confirmed from the TEM images for the 10RuO₂-MCM-41 catalyst.

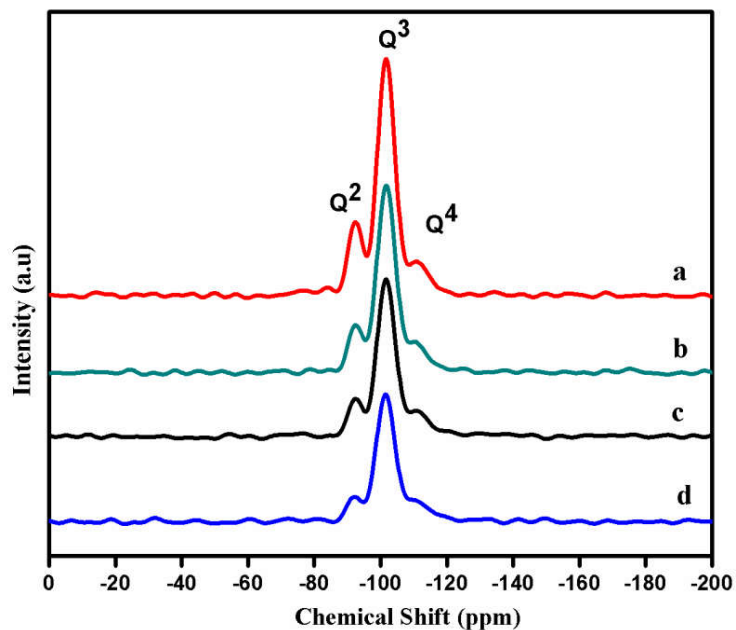


Figure 2B.4: ^{29}Si CPMAS NMR spectra of (a) $2.5\text{RuO}_2\text{-MCM-41}$, (b) $4\text{RuO}_2\text{-MCM-41}$, (c) $5\text{RuO}_2\text{-MCM-41}$ and $10\text{RuO}_2\text{-MCM-41}$.

2B.3.5 H_2 -TPR analysis

Figure 2B.5 shows the H_2 -TPR profile of RuO_2 loaded MCM-41 catalysts. All the supported Ru oxide catalysts were completely reduced below 150°C . This sharp reduction peak at low

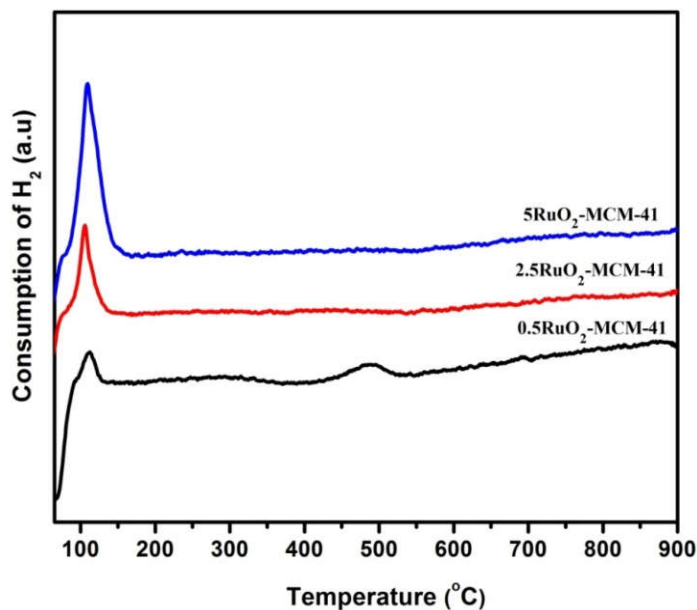


Figure 2B.5: TPR profiles for various metal loading on MCM-41 catalysts.

temperature suggests that the supported Ru-oxide can be easily reduced to metallic Ru NPs on an MCM-41 silica support, which denotes a weak metal-support interaction.

2B.3.6 X-ray Photoelectron Spectroscopy

To better understand the oxidation state and chemical composition of RuO₂, XPS analysis was carried out. Figure 2B.6a shows the Ru 3d and C 1s spectra of the 5RuO₂-MCM-41 catalyst. Typically, the Ru 3d_{5/2} spectrum is considered for identifying the electronic states of Ru. Unfortunately, the Ru 3d_{3/2} spectrum are generally overlapped with C 1s spectrum, which is

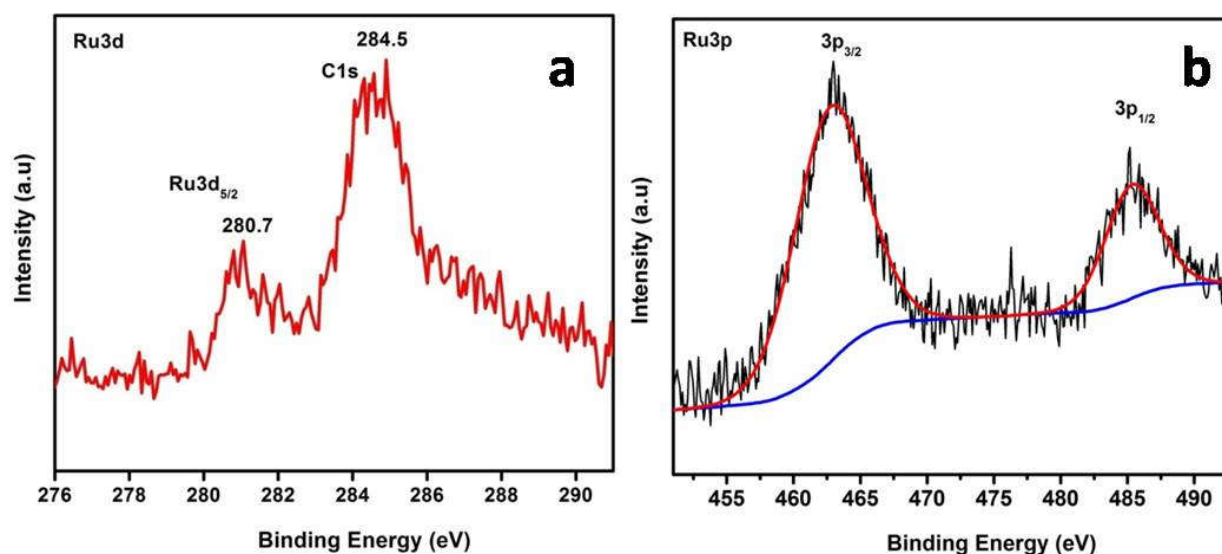


Figure 2B.6: Ru XPS spectra of 5RuO₂-MCM-41 catalyst. (a) Ru 3d and (b) Ru 3p.

observed at 284.5 eV. The Ru 3d_{5/2} peak of the Ru-oxide catalyst, which is located at 280.9 eV, shows that the metal is in a +4 oxidation state.⁷⁹ In order to avoid the intervention from carbon, Ru 3p_{3/2} of the Ru-oxide catalyst was performed, and the peak at 462.5 eV confirms that the metal is in a +4 oxidation state with the successful deposition of RuO₂ on MCM-41 (Figure 2B.6b).⁸⁰

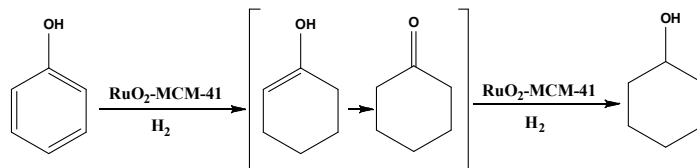
2B.4 Catalytic Activity

The catalytic performances of the heterogenized RuO₂-MCM-41 catalysts were screened in a liquid-phase phenol hydrogenation reaction. In order to check the role of Ru metal in

Exploring the Chemical Modifications in Periodic Mesoporous Silica Materials for Heterogeneous Catalytic Applications

hydrogenation, we controlled the metal loading to 0.5, 1, 2.5, 4, 5, and 10 wt % by varying the amount of Ru precursor. The phenol conversion over RuO₂-MCM-41 catalysts increased sharply

Table 2B.2: Aqueous- phase phenol hydrogenation with nRuO₂-MCM-41^a catalysts



Entry	Catalyst	Conv. (%)	Selectivity (%)		Ref.
			Cy-ol	Cy-one	
1	Without catalyst	3	100	0	this work
2	Pure MCM-41	5	92	8	„
3	0.5RuO ₂ -MCM-41	24	73	27	„
4	1RuO ₂ -MCM-41	33	75	25	„
5	2.5RuO ₂ -MCM-41	47	90	10	„
6	4RuO ₂ -MCM-41	88	96	4	„
7	5RuO ₂ -MCM-41	100	100	0	„
8	10RuO ₂ -MCM-41	100	100	0	„
9*	Ru/Al ₂ O ₃	95	52	48	74
10*	Ru/ACC	89	99	1	81

Reaction conditions: phenol- 1.6 mmol, H₂O-10 mL, Cat- 50 mg, T- 100 °C, P H₂- 1 MPa, t- 12 h. ^anRuO₂-MCM-41, where n indicates wt % of Ru loading with respect to support. * by the use of state-of-the-art catalysts.

with the increase in total Ru content and showed 100 % activity for 5 wt % loaded system, further increase in metal content did not show any decline in activity. It is worth mentioning that the selectivity also increased linearly towards cyclohexanol with metal loading. This activity

trend in phenol hydrogenation reaction could be correlated with the Ru particle size, which increased with the metal loading in the catalyst. The enhanced activity for larger RuO₂ particles compared to the smaller ones in low metal content may be due to the formation of well-defined facets, which acts as an active site for phenol hydrogenation reaction, or due to easily reducible surface Ru oxide in larger particle size.^{69, 82} To confirm the activity of the 5RuO₂-MCM-41 catalyst, the reaction was compared with pure MCM-41 (5 %) and blank reaction (3 %), and further control experiments were carried out using the optimal 5RuO₂-MCM-41 catalyst.

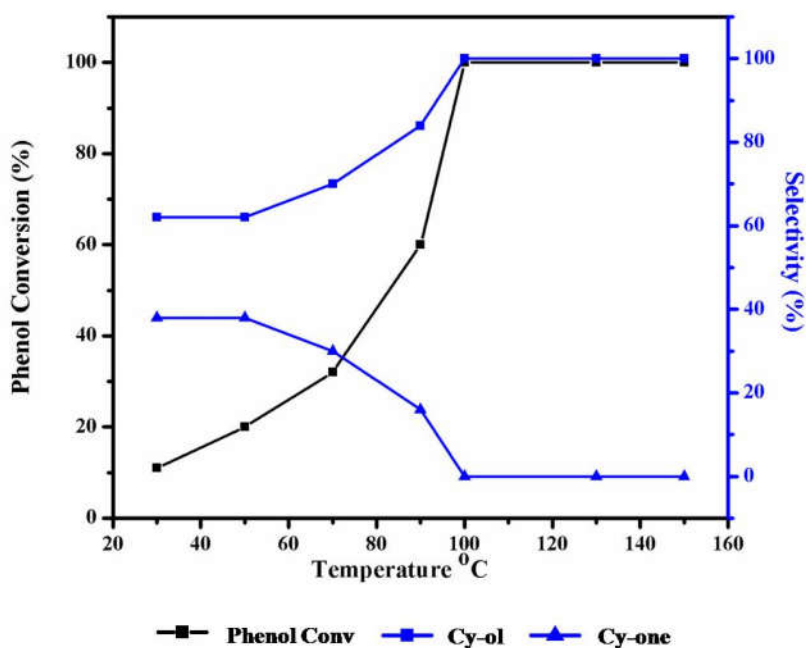


Figure 2B.7: Influence of reaction temperature on phenol conversion over 5RuO₂-MCM-41 catalyst. Reaction conditions as mentioned in the footnote of Table 2B.2.

Figure 2B.7 depicts the effect of reaction temperature on the conversion of phenol and the product selectivity on 5RuO₂-MCM-41 catalyst. Cyclohexanol was found to be the major product with an increase in temperature along with the increase in phenol conversion. As the reaction temperature was lowered to room temperature, the phenol conversion rate was found to decrease along with the formation of a mixture of cyclohexanol and cyclohexanone, which shows that the formation of cyclohexanol occurs at the expense of cyclohexanone. Complete conversion of phenol was attained at 100 °C with 100 % selectivity towards cyclohexanol within 12 h. Further increase in temperature did not show any effect on conversion and selectivity. The

increased rate at higher temperature may attribute to the augmentation of the diffusion rate of phenol in the catalyst channels.

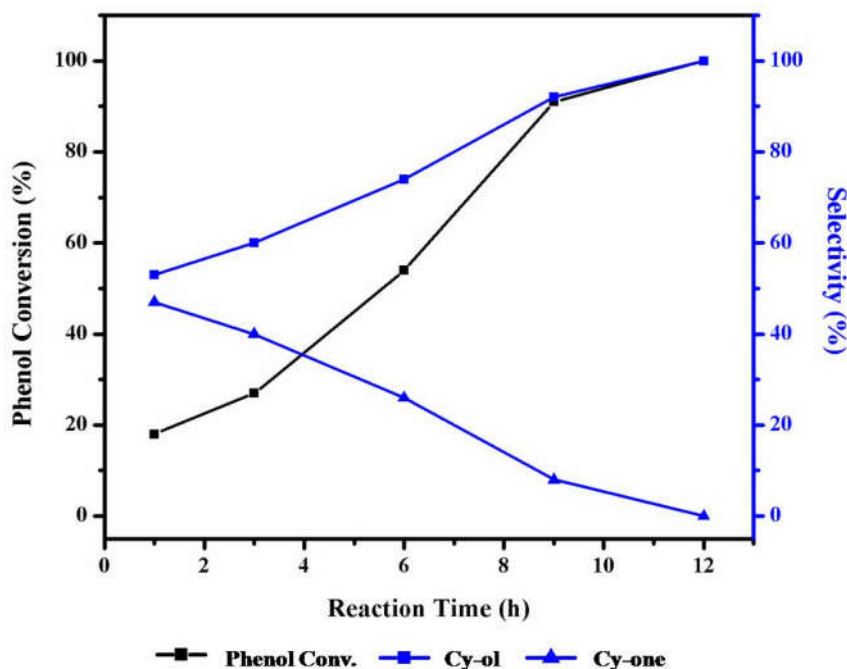


Figure 2B.8: Effect of reaction time on phenol conversion over 5RuO₂-MCM-41 catalyst. Reaction conditions as mentioned in the footnote of Table 2B.2.

The time-dependent study of phenol hydrogenation reaction using 5RuO₂-MCM-41 catalyst performed at 100 °C (Figure 2B.8) also points to the fact that cyclohexanone may be the intermediate for cyclohexanol formation. The conversion of phenol increased almost linearly with time and reached 50 % within 6 h, and full conversion was attained by 12 h with full selectivity for cyclohexanol. This result shows that the reaction time influenced the phenol conversion and the cyclohexanol selectivity to a great extent. To explore the impact of solvent on the reaction rate and selectivity, phenol hydrogenation is carried out in different polar organic solvents with different polarity. In all the organic solvents studied like toluene, cyclohexane, ethanol, chloroform, and ethyl acetate, only a marginal conversion was observed (Table 2B.3). Interestingly, the conversion and selectivity of phenol hydrogenation in an aqueous medium with strong polarity (dielectric constant $\epsilon = 80.4$) attained 100 % in 12 h. To further illustrate the

influence of water, a physical mixture of water ($\epsilon = 80.4$) and ethanol ($\epsilon = 24.3$) is used as a solvent for the reaction.⁸³

Table 2B.3: Effect of solvent in the aqueous-phase phenol hydrogenation reaction.

Entry	solvents	Conversion (%)	Selectivity (%)	
			Cy-ol	Cy-one
1.	Water	100	100	0
2.	Chloroform	10	75	25
3.	Ethyl acetate	0	0	0
4.	Ethanol	0	0	0
5.	Toluene	7	33	67
6.	Cyclohexane	5	47	53

Reaction conditions: phenol- 1.6 mmol, Solvent-10 mL, Cat- 50 mg, T- 100°C, P H₂- 1 MPa, t- 12 h.

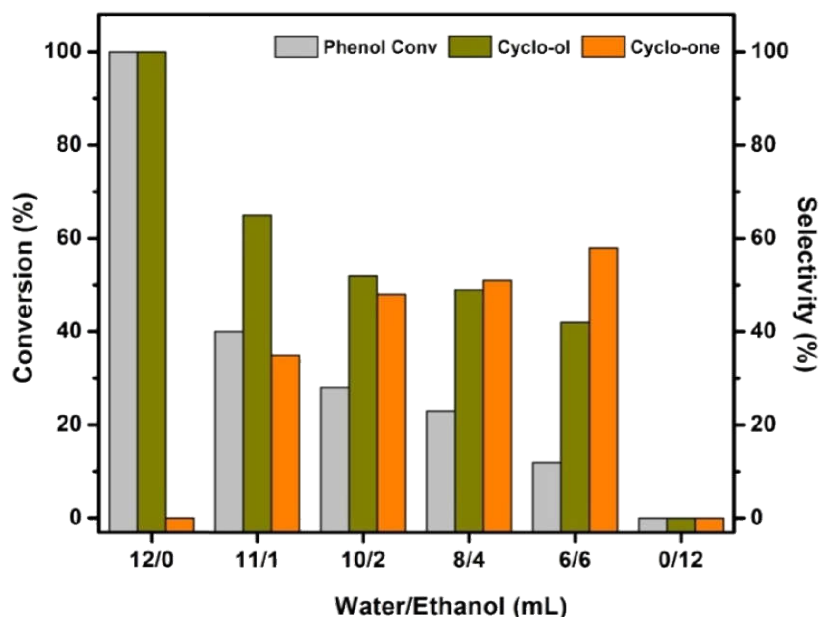
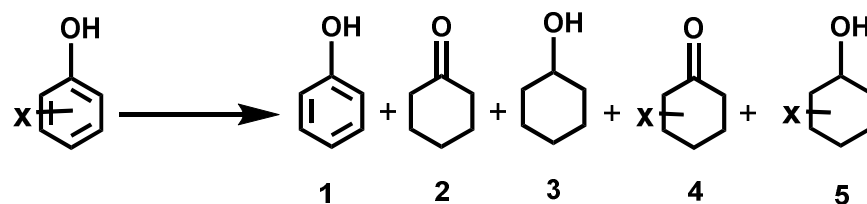


Figure 2B.9: Effect of the bi-solvent system on phenol conversion over 5RuO₂-MCM-41 catalyst.

As illustrated in Figure 2B.9, upon increasing the amount of ethanol, a sudden decrease in the conversion and selectivity is observed, in agreement with the previous literature. The absolute chemical inertness of phenol in ethanol is due to the competitive adsorption of solvent on the Ru surface, along with less interaction between the phenol and ethanol. Less polar solvents like chloroform, toluene, and cyclohexane, displayed much better selectivity for cyclohexanone than the over hydrogenation product cyclohexanol. This result demonstrates that the solvent effect can control the product selectivity. It is worthy to note that the selectivity to cyclohexanone increases as the amount of ethanol increases with a drastic drop in catalytic activity. This decreased activity could be attributed to the strong adsorption and solvation of Ru surface sites and phenol with ethanol. This strong adsorption limits the hydrogenation of phenol and cyclohexanone in ethanol, making the active sites non-accessible compared to water.

To extend the scope of the 5RuO₂-MCM-41 catalyst, we have investigated the hydrogenation reactivity of various phenol derivatives that contain electron-donating and electron-withdrawing groups. According to the results shown in Table 2B.4, all phenolic substrates exhibited > 90 % conversion with higher selectivity. Phenolic substrates with electron-donating substituents exhibited higher activity than the electron-withdrawing system and lower conversion for ortho-substitution (entries 3, 6, 8) compared to para- (entries 2, 4, 5, 7) due to higher steric effect. In short, cyclohexanol and substituted cyclohexanol are found to be the major products for these reactions using Ru-oxide catalysts. In halophenols (entries 2-4), hydrodehalogenation occurs with elimination of mineral acids such as HCl and HBr to form cyclohexanol with phenol as intermediate via. hydrogenolysis of C-X bond (X= -Cl and -Br) and further hydrogenation to form cyclohexanol.⁸⁴ Out of these halophenols, chlorophenols reduction rate is higher than bromophenol due to its less bulky effect and geometrical position in the phenolic ring.⁸⁵ Moreover, it is worthy to note that hydrogenation of guaiacol, generally obtained from lignin depolymerization, showed 95 % conversion with selectivity to cycloalcohols (entry 6). In addition, the hydrogenolysis pathway of guaiacols favours the formation of cyclohexanol which diminishes product selectivity (entries 5, 6). However, in the case of alkyl-substituted phenols (entries 7 and 8), hydrogenolysis reaction is inhibited due to the higher dissociation energy of the -CH₃ group, which adopts a low-energy hydrogenation pathway to form substituted cyclohexanols.

Table 2B.4: Substrate scope study on 5RuO₂-MCM-41 catalyst



Entry	Phenolic substrate	Conversion (%)	Selectivity (%)				
			1	2	3	4	5
1		100	-	-	100	-	-
2		95	8	6	86	-	-
3		90	11	9	80	-	-
4		93	53	8	39	-	-
5		100	-	3	31	31	35
6		95	-	5	20	20	55
7		98	-	-	-	-	100
8		91	-	-	-	8	92

Reaction conditions: phenol- 1.6 mmol, H₂O-10 mL, 5RuO₂-MCM-41- 50 mg, T- 100 °C, P H₂- 1 MPa, t- 24 h

The reusability test of 5RuO₂-MCM-41 catalyst for selective hydrogenation of phenols in an aqueous medium was performed as it represents an integral part of the economic evaluation of the catalyst for various chemical transformations. After each reaction, the catalyst was recovered by centrifugation, washed, dried, and reused for the next run. As shown in Figure 8, 5RuO₂-MCM-41 catalyst was stable, highly reusable in phenol hydrogenation where both phenol conversion and cyclohexanol selectivity remain the same even after five successive runs.

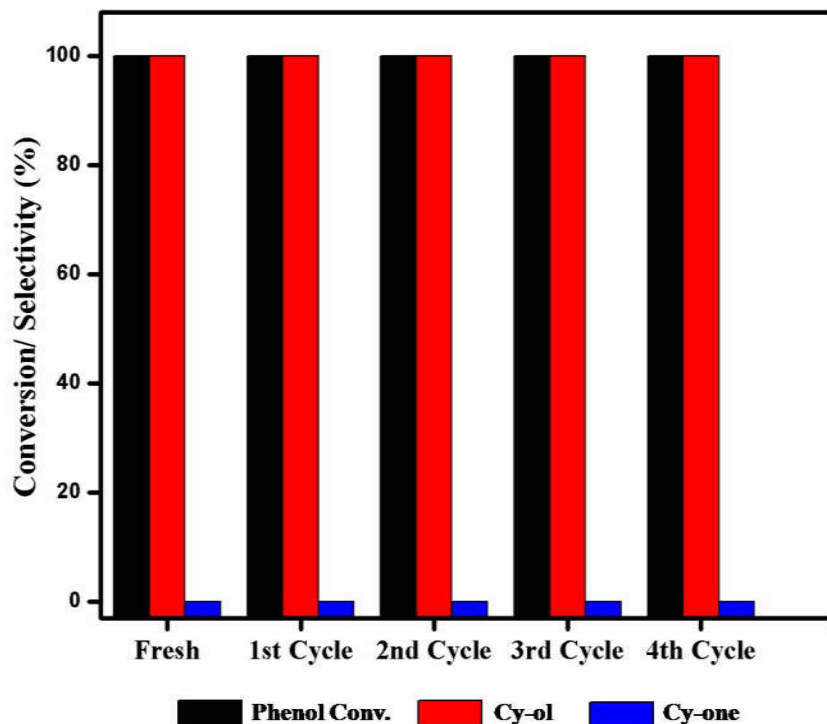


Figure 2B.10: Reusability of 5RuO₂-MCM-41 catalyst in aqueous phase phenol hydrogenation reaction. Reaction conditions as mentioned in the footnote of Table 1.

The ICP analysis of the spent 5RuO₂-MCM-41 catalyst was ~ 4.6 %, indicating negligible metal leaching from the catalyst during the reaction. This retention of activity clearly reveals that RuO₂-MCM-41 catalysts synthesized by the one-pot approach are purely heterogeneous as no metal loss was observed under the reaction conditions for five cycles. No apparent deactivation of the catalyst was realized from XRD and TEM analysis of the spent catalyst (Figure 2B.11). The morphology and particle size of RuO₂ were maintained in the range of 6-10 nm even after several cycles of the hydrogenation reaction, which supports the experimental results.

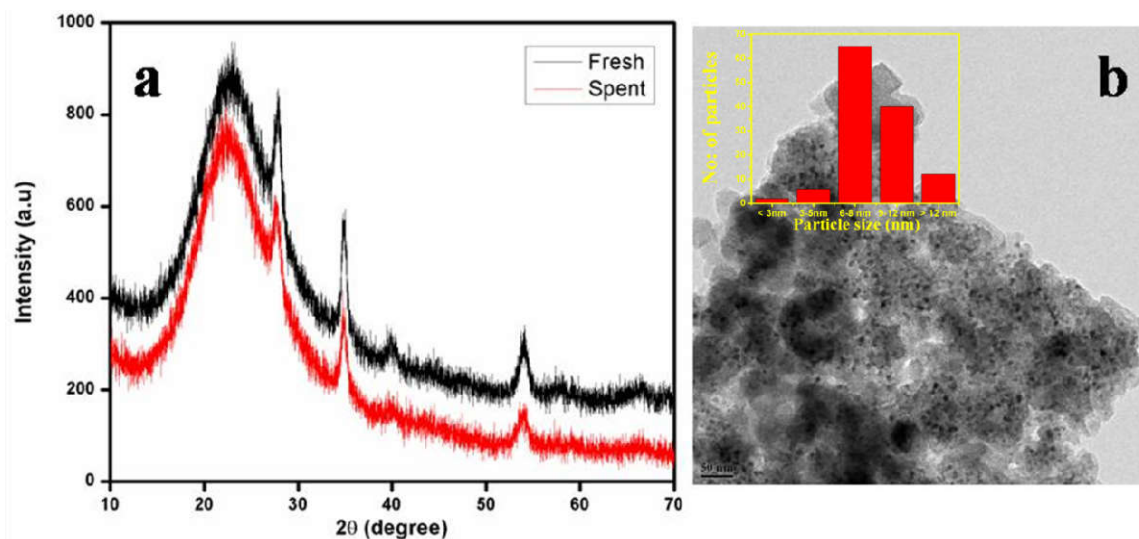


Figure 2B.11: Spent catalyst analysis of 5RuO₂-MCM-41 catalyst (a) XRD and (b) TEM.

2.1 Conclusions

To probe the nature of catalytically active Cr sites in the cyclohexane oxidation reaction, chromium oxide-supported MCM-41 nanosphere catalysts were synthesized by facile wet impregnation method. Among the different wt % of Cr loaded catalysts, 5 wt % metal loaded catalysts were found to show unprecedentedly high activity with 72 % cyclohexane conversion and 99 % selectivity for cyclohexanone. A better understanding of the active Cr species was obtained by correlating the catalytic and characterization results for the cyclohexane oxidation reaction. The volcano-type catalytic performance could be attributed to the interplay between the surface Cr⁶⁺ and Cr³⁺ species in the material, which varies with the Cr content. From our results, the excellent activity towards the cyclohexanone product under mild reaction conditions can be attributed to the initial concentration of the extra-framework amorphous Cr³⁺ species in the MCM-41 supported catalyst. Efforts are on identifying the root cause for deactivation using spectroscopic techniques.

In the second part of this chapter, one-pot approach to synthesize size-controlled RuO₂ nanostructures supported MCM-41 catalysts was accomplished. Under mild conditions, the optimum RuO₂ loaded catalyst exhibited excellent activity in selective aqueous phase hydrogenation of phenol and lignin-derived phenols. The RuO₂ nanoparticle size of the optimum

catalyst was found to be around 6-8 nm. The combination of different characterization techniques and activity results showed that RuO₂-MCM-41 catalysts are highly active, stable, and reusable and are a better candidate to hydrogenate bio-renewable aromatics to beneficial platform chemicals.

2.5 References

1. M. T. Musser, in *Ullmann's Encyclopedia of Industrial Chemistry*, Wiley-VCH Verlag GmbH & Co. KGaA, 2000, DOI: 10.1002/14356007.a08_217.
2. R. A. Sheldon and J. K. Kochi, in *Adv.Catal.A*, eds. H. P. D.D. Eley and B. W. Paul, Academic Press, 1976, vol. Volume 25, pp. 272-413.
3. K. Wu, B. Li, C. Han and J. Liu, *Appl. Catal. A-Gen*, 2014, **479**, 70-75.
4. H. X. Yuan, Q. H. Xia, H. J. Zhan, X. H. Lu and K. X. Su, *Appl. Catal. A-Gen*, 2006, **304**, 178-184.
5. A. Sakthivel and P. Selvam, *J. Catal.*, 2002, **211**, 134-143.
6. S. A. C. Carabineiro, L. M. D. R. S. Martins, A. J. L. Pombeiro and J. L. Figueiredo, *ChemCatChem*, **0**.
7. S. A. C. Carabineiro, L. M. D. R. S. Martins, M. Avalos-Borja, J. G. Buijnsters, A. J. L. Pombeiro and J. L. Figueiredo, *Appl. Catal. A-Gen*, 2013, **467**, 279-290.
8. M. P. de Almeida, L. M. D. R. S. Martins, S. A. C. Carabineiro, T. Lauterbach, F. Rominger, A. S. K. Hashmi, A. J. L. Pombeiro and J. L. Figueiredo, *Catal.Sci.Technol*, 2013, **3**, 3056-3069.
9. M. Dias Ribeiro de Sousa Martins Luísa, C. Carabineiro Sónia Alexandra, J. Wang, M. Rocha Bruno Gonçalo, J. Maldonado-Hódar Francisco and J. Latourrette de Oliveira Pombeiro Armando, *ChemCatChem*, 2016, **9**, 1211-1221.
10. L. M. D. R. S. Martins, M. P. d. Almeida, S. A. C. Carabineiro, J. L. Figueiredo and A. J. L. Pombeiro, *ChemCatChem*, 2013, **5**, 3847-3856.
11. A. P. C. Ribeiro, L. M. D. R. S. Martins, S. A. C. Carabineiro, J. G. Buijnsters, J. L. Figueiredo and A. J. L. Pombeiro, *ChemCatChem*, **0**.
12. D. Tsukamoto, A. Shiro, Y. Shiraishi and T. Hirai, *J. Phys. Chem. C*, 2011, **115**, 19782-19788.
13. S. Shylesh, C. Srilakshmi, A. P. Singh and B. G. Anderson, *Microporous Mesoporous Mater.*, 2007, **99**, 334-344.
14. S. E. Dapurkar, A. Sakthivel and P. Selvam, *New J. Chem.*, 2003, **27**, 1184-1190.
15. B. M. Weckhuysen, I. E. Wachs and R. A. Schoonheydt, *Chem.Rev.*, 1996, **96**, 3327-3350.
16. J.-M. Jehng, I. E. Wachs, B. M. Weckhuysen and R. A. Schoonheydt, *J. Chem. Soc., Faraday Trans.*, 1995, **91**, 953-961.
17. L. M. Baker and W. L. Carrick, *J. Org. Chem.*, 1968, **33**, 616-618.
18. H. E. B. Lempers and R. A. Sheldon, *J. Catal.*, 1998, **175**, 62-69.
19. E. V. Spinacé, U. Schuchardt and D. Cardoso, *Appl. Catal. A-Gen*, 1999, **185**, L193-L197.
20. P. Michorczyk, J. Ogonowski, P. Kuśtrowski and L. Chmielarz, *Appl. Catal. A-Gen*, 2008, **349**, 62-69.
21. A. P. Singh and T. Selvam, *J. Mol. Catal. A: Chem.*, 1996, **113**, 489-497.

22. K. Li, D. Zhou, J. Deng, X. Lu and Q. Xia, *J. Mol. Catal. A: Chem.*, 2014, **387**, 31-37.
23. N. Ulagappan and C. N. R. Rao, *Chem. Commun.*, 1996, DOI: 10.1039/CC9960001047, 1047-1048.
24. T. J. Pinnavaia, M. S. Tzou and S. D. Landau, *J. Am. Chem. Soc.*, 1985, **107**, 4783-4785.
25. D. L. Myers and J. H. Lunsford, *J. Catal.*, 1986, **99**, 140-148.
26. J. S. Beck, J. C. Vartuli, W. J. Roth, M. E. Leonowicz, C. T. Kresge, K. D. Schmitt, C. T. W. Chu, D. H. Olson, E. W. Sheppard, S. B. McCullen, J. B. Higgins and J. L. Schlenker, *J. Am. Chem. Soc.*, 1992, **114**, 10834-10843.
27. Q. Cai, Z.-S. Luo, W.-Q. Pang, Y.-W. Fan, X.-H. Chen and F.-Z. Cui, *Chem. Mater.*, 2001, **13**, 258-263.
28. X. Zhang, Y. Yue and Z. Gao, *Catal. Lett.*, 2002, **83**, 19-25.
29. A. K. Poswal, A. Agrawal, A. K. Yadav, C. Nayak, S. Basu, S. R. Kane, C. K. Garg, D. Bhattacharyya, S. N. Jha and N. K. Sahoo, *AIP Conference Proceedings*, 2014, **1591**, 649-651.
30. S. Basu, C. Nayak, A. K. Yadav, A. Agrawal, A. K. Poswal, D. Bhattacharyya, S. N. Jha and N. K. Sahoo, *Journal of Physics: Conference Series*, 2014, **493**, 012032.
31. D. C. Koningsberger and R. Prins, *X-ray absorption: principles, applications, techniques of EXAFS, SEXAFS, and XANES*, John Wiley and Sons, New York, NY; None, 1988.
32. B. Ravel and M. Newville, *Journal of Synchrotron Radiation*, 2005, **12**, 537-541.
33. S. Kelly, D. Hesterberg and B. Ravel, *Methods of soil analysis. Part*, 2008, **5**, 387-463.
34. H. I. Meléndez-Ortiz, L. A. García-Cerda, Y. Olivares-Maldonado, G. Castruita, J. A. Mercado-Silva and Y. A. Perera-Mercado, *Ceram. Int.*, 2012, **38**, 6353-6358.
35. W. Zhang and T. J. Pinnavaia, *Catal. Lett.*, 1996, **38**, 261-265.
36. F. Cavani, M. Koutyrev, F. Trifirò, A. Bartolini, D. Ghisletti, R. Iezzi, A. Santucci and G. Del Piero, *J. Catal.*, 1996, **158**, 236-250.
37. M. Roy, S. Ghosh and M. K. Naskar, *Mater. Chem. Phys.*, 2015, **159**, 101-106.
38. S. Musi, N. Filipovi -Vincekovi and L. Sekovani *Brazilian Journal of Chemical Engineering*, 2011, **28**, 89-94.
39. X. Zhao and X. Wang, *J. Mol. Catal. A: Chem.*, 2007, **261**, 225-231.
40. T. Ivanova, K. Gesheva, A. Cziraki, A. Szekeres and E. V্লাikova, *Journal of Physics: Conference Series*, 2008, **113**, 012030.
41. P. Michorczyk, P. Pietrzyk and J. Ogonowski, *Microporous Mesoporous Mater.*, 2012, **161**, 56-66.
42. M. Cherian, M. S. Rao, A. M. Hirt, I. E. Wachs and G. Deo, *J. Catal.*, 2002, **211**, 482-495.
43. Y. Wang, Y. Ohishi, T. Shishido, Q. Zhang, W. Yang, Q. Guo, H. Wan and K. Takehira, *J. Catal.*, 2003, **220**, 347-357.
44. M. L. Peterson, G. E. Brown, G. A. Parks and C. L. Stein, *Geochimica et Cosmochimica Acta*, 1997, **61**, 3399-3412.

45. K. Takehira, Y. Ohishi, T. Shishido, T. Kawabata, K. Takaki, Q. Zhang and Y. Wang, *J. Catal.*, 2004, **224**, 404-416.
46. L. F. Liotta, A. M. Venezia, G. Pantaleo, G. Deganello, M. Gruttadauria and R. Noto, *Catal.Today*, 2004, **91-92**, 231-236.
47. A. P. Singh, N. Torita, S. Shylesh, N. Iwasa and M. Arai, *Catal.lett.*, 2009, **132**, 492-499.
48. A. A. Alshehri, A. M. Alhanash, M. Eissa and M. S. Hamdy, *Appl. Catal. A-Gen*, 2018, **554**, 71-79.
49. S. Samanta, N. K. Mal and A. Bhaumik, *J. Mol. Catal. A: Chem.*, 2005, **236**, 7-11.
50. A. Corma, S. Iborra and A. Vely, *Chemical Reviews*, 2007, **107**, 2411-2502.
51. J. Zakzeski, P. C. A. Bruijninx, A. L. Jongerius and B. M. Weckhuysen, *Chemical Reviews*, 2010, **110**, 3552-3599.
52. R. D. Perlack, S. United, E. Department of, S. United, A. Department of and L. Oak Ridge National, 2005.
53. C. Xu, R. A. D. Arancon, J. Labidi and R. Luque, *Chemical Society Reviews*, 2014, **43**, 7485-7500.
54. B. M. Upton and A. M. Kasko, *Chemical Reviews*, 2016, **116**, 2275-2306.
55. X. Cui, A.-E. Surkus, K. Junge, C. Topf, J. Radnik, C. Kreyenschulte and M. Beller, *Nature Communications*, 2016, **7**, 11326.
56. C. Zhao, Y. Kou, A. A. Lemonidou, X. Li and J. A. Lercher, *Angewandte Chemie International Edition*, 2009, **48**, 3987-3990.
57. K. L. Luska, P. Migowski, S. El Sayed and W. Leitner, *Angewandte Chemie*, 2015, **127**, 15976-15981.
58. D.-Y. Hong, S. J. Miller, P. K. Agrawal and C. W. Jones, *Chemical Communications*, 2010, **46**, 1038-1040.
59. L. M. Sikhwivhilu, N. J. Coville, D. Naresh, K. V. R. Chary and V. Vishwanathan, *Applied Catalysis A: General*, 2007, **324**, 52-61.
60. H. Liu, T. Jiang, B. Han, S. Liang and Y. Zhou, *Science*, 2009, **326**, 1250.
61. A. K. Talukdar, K. G. Bhattacharyya and S. Sivasanker, *Applied Catalysis A: General*, 1993, **96**, 229-239.
62. S.-i. Fujita, T. Yamada, Y. Akiyama, H. Cheng, F. Zhao and M. Arai, *The Journal of Supercritical Fluids*, 2010, **54**, 190-201.
63. Y. Wang, J. Yao, H. Li, D. Su and M. Antonietti, *Journal of the American Chemical Society*, 2011, **133**, 2362-2365.
64. S. Galvagno, G. Capannelli, G. Neri, A. Donato and R. Pietropaolo, *Journal of Molecular Catalysis*, 1991, **64**, 237-246.
65. J. Ning, J. Xu, J. Liu and F. Lu, *Catalysis Letters*, 2006, **109**, 175-180.

66. R. Marcos Esteban, K. Schütte, D. Marquardt, J. Barthel, F. Beckert, R. Mülhaupt and C. Janiak, *Nano-Structures & Nano-Objects*, 2015, **2**, 28-34.
67. Y.-B. Huang, L. Yan, M.-Y. Chen, Q.-X. Guo and Y. Fu, *Green Chemistry*, 2015, **17**, 3010-3017.
68. B. F. Machado, M. Oubenali, M. Rosa Axet, T. Trang Nguyen, M. Tunckol, M. Girleanu, O. Ersen, I. C. Gerber and P. Serp, *Journal of Catalysis*, 2014, **309**, 185-198.
69. S. H. Joo, J. Y. Park, J. R. Renzas, D. R. Butcher, W. Huang and G. A. Somorjai, *Nano Letters*, 2010, **10**, 2709-2713.
70. A. Aho, S. Roggan, O. A. Simakova, T. Salmi and D. Y. Murzin, *Catalysis Today*, 2015, **241, Part B**, 195-199.
71. J. He, C. Zhao and J. A. Lercher, *Journal of Catalysis*, 2014, **309**, 362-375.
72. H. Liu, T. Jiang, B. Han, S. Liang and Y. Zhou, *Science*, 2009, **326**, 1250-1252.
73. H. Yoshida, S. Narisawa, S.-i. Fujita and M. Arai, *Journal of Molecular Catalysis A: Chemical*, 2013, **379**, 80-85.
74. A. N. Raut, S. U. Nandanwar, Y. R. Suryawanshi, M. Chakraborty, S. Jauhari, S. Mukhopadhyay, K. T. Shenoy and H. C. Bajaj, *Kinetics and Catalysis*, 2016, **57**, 39-46.
75. A. Chen, G. Zhao, J. Chen, L. Chen and Y. Yu, *RSC Advances*, 2013, **3**, 4171-4175.
76. Y. Xiang, L. Ma, C. Lu, Q. Zhang and X. Li, *Green Chemistry*, 2008, **10**, 939-943.
77. Y. Li, X. Xu, P. Zhang, Y. Gong, H. Li and Y. Wang, *RSC Advances*, 2013, **3**, 10973-10982.
78. M. Gopiraman, S. Ganesh Babu, Z. Khatri, W. Kai, Y. A. Kim, M. Endo, R. Karvembu and I. S. Kim, *The Journal of Physical Chemistry C*, 2013, **117**, 23582-23596.
79. K. S. Kim and N. Winograd, *Journal of Catalysis*, 1974, **35**, 66-72.
80. P. Wang, H. Liu, Q. Tan and J. Yang, *RSC Advances*, 2014, **4**, 42839-42845.
81. Z. Li, M. Garedew, C. H. Lam, J. E. Jackson, D. J. Miller and C. M. Saffron, *Green Chemistry*, 2012, **14**, 2540-2549.
82. J. Jae, W. Zheng, A. M. Karim, W. Guo, R. F. Lobo and D. G. Vlachos, *ChemCatChem*, 2014, **6**, 848-856.
83. H. Xia, H. Tan, H. Cui, F. Song, Y. Zhang, R. Zhao, Z.-N. Chen, W. Yi and Z. Li, *Catalysis Science & Technology*, 2021, **11**, 1881-1887.
84. T. T. Bovkun, Y. Sasson and J. Blum, *Journal of Molecular Catalysis A: Chemical*, 2005, **242**, 68-73.
85. T. Tsukinoki, T. Kakinami, Y. Iida, M. Ueno, Y. Ueno, T. Mashimo, H. Tsuzuki and M. Tashiro, *Journal of the Chemical Society, Chemical Communications*, 1995, DOI: 10.1039/C39950000209, 209-210.

CHAPTER-3

Confinement of Single Au Nanoparticles inside Titanium Doped Hollow Structured Mesoporous Organosilica for Alkene Oxidation

This chapter is based on:

1) **K. J. Betsy**, and C. P. Vinod; Confinement of single Au nanoparticles inside titanium doped hollow structured mesoporous organosilica nanoreactors for alkene oxidation (Manuscript under preparation).

3.1 Introduction

Architectural designs of nanoscale hollow or yolk-shell structured mesoporous functional materials having internal spaces or voids along with unique morphology have achieved great interest in the field of catalysis, nanofabrication, drug storage and delivery, energy storage in Li-ion batteries, etc. due to its captivating properties like available high surface area, low density, and permeable shells.¹⁻⁵ Among the various porous materials, silica-based materials are most frequently studied in the field of catalysis. The fabrication of hollow/ yolk-shell nanostructures is usually limited to conventional hydrophilic mesoporous silica formation. One way of revising the physical and chemical properties of the mesoporous silica-based materials is through the integration of organic moieties, either as part of the silica framework or onto the silica surface.^{6,7} The evolution of organic-inorganic hybrid mesoporous siliceous materials display improved stability, activity, and selectivity in a variety of catalytic reactions.⁸ In contrast to the conventional silica materials, periodic mesoporous organosilica (PMO) hybrid materials has the merits from the molecular-scale mixing of both organic and inorganic components, which are homogeneously distributed over the framework.^{9, 10} By tuning the pore wall chemistry through the bridging of organic moieties inside the network impose specific features capable of enhancing the catalysis by varying the degree of hydrophobicity, structure rigidity along with the refined accessibility of task-specific sites due to their open structure.¹¹

Titanium containing porous solids have been extensively studied to synthesize industrially important chemical intermediates through selective oxidation catalysis.^{12, 13} Both Ti-containing zeolites and mesoporous materials are active for the oxidation of many organic transformation reactions using oxidants like H₂O₂ and other organic peroxides.¹⁴⁻¹⁷ In contrast to the microporous zeolites, mesoporous molecular sieves were more effective in diffusing the bulky organic substrates and oxidants, among which Ti-SBA-15 and Ti-MCM-41 materials were well exploited in such reactions.^{18, 19} The inorganic-mesostructured Ti-containing silica was proven to be a promising candidate for epoxidation catalysis using peroxides as oxidizing agents. However, some associated disadvantages exist like low activity and selectivity due to the amorphous pore wall structure and the ample amount of surface silanol groups resulting in increased hydrophilicity.¹⁷ This can be overcome either through the silylation of the surface silanol groups or by the integration of the organic segments into the silicate framework, which helps to improve

the hydrophobicity of titanosilicate materials.^{11, 20, 21} The bridging of organic linkers into the Ti-containing silicate framework through the one-pot hydrothermal synthesis is an effective strategy to boost hydrophobicity. Here comes the applicability of PMO materials where the organic groups are uniformly distributed throughout the silica framework, which tunes the adsorption-desorption properties of the reactant and product species in oxidation catalysis.^{20, 22-24} Previous experimental reports recommend precise tetrahedral framework Ti centers as a requisite for epoxidation catalysis and such isolated tetrahedral Ti sites are crucial for a stable and active catalyst.²⁵ In contrast, the extra-framework Ti species in titanosilicate is observed to spoil the catalytic activity.^{26, 27} Hence it is challenging to stabilize Ti active species inside the PMO hybrid silica framework selectively, especially in yolk-shell and core-shell nanostructures.

Heterogeneous catalysis by gold nanoparticles has been intensely investigated and demonstrated in the literature; still, the silica-supported gold-based catalysts exhibit some paramount issues like low dispersion and sintering due to the reduced intimacy with the silica material.²⁸ One alternative approach to tackle this issue is to encapsulate the small gold nanoparticles inside the porous dielectric materials like silica either in the form of yolk-shell or core-shell nanostructures.²⁹⁻³³ This becomes an attractive strategy since there are no neighbouring accessible metal nanoparticles for the process of sintering even under harsh reaction conditions. Among these two configurations, the yolk-shell structures become more remarkable in the liquid-phase catalysis due to the associated diffusion constraints with the core-shell nanostructures.³⁴⁻³⁷ These hollow spherical shells can act as the physical barrier to protect the active noble metal components from deactivation during the catalytic process. The quest for designing functional materials for catalysis with exciting properties and composition became a driving force for the evolution of these yolk-shell structured metal nanoparticle encapsulated nanoreactors. This work reports the confinement of small-sized single gold nanoparticles inside the titanium incorporated hollow structured periodic mesoporous organosilica nanospheres (Au@Ti-HPMO). The one-pot synthesis of Ti-HPMO hollow spheres was achieved through our optimized reaction conditions. All the synthesized catalysts were thoroughly characterized, and these nanoreactors were found to serve as stable and recyclable catalysts for liquid phase alkene oxidation reactions.

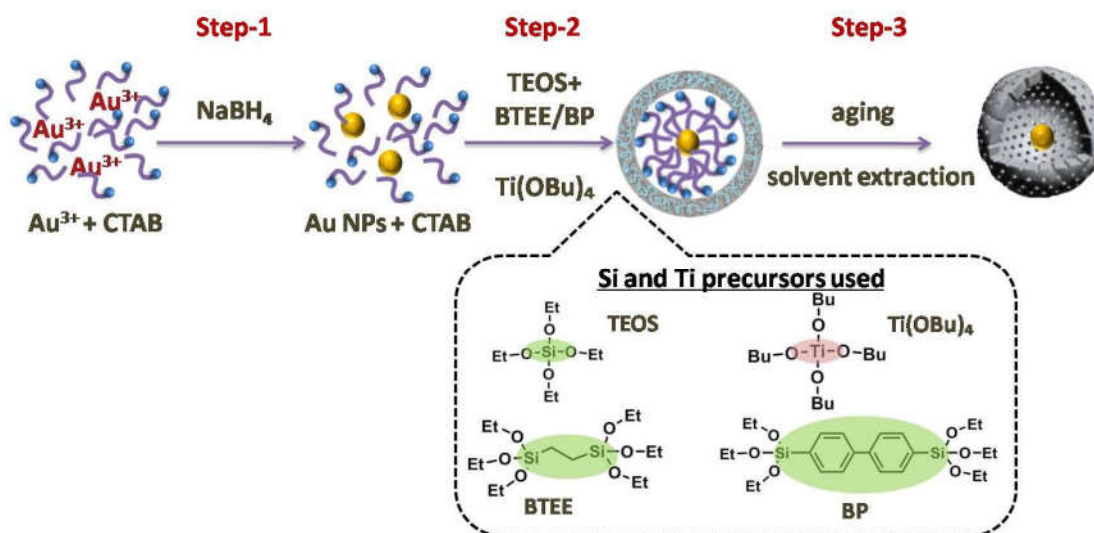
3.2 Experimental Section

3.2.1 Synthesis of gold colloid

The colloidal solution of gold nanoparticles was synthesized by reducing the gold precursor HAuCl_4 using NaBH_4 as a reducing agent at room temperature. Typically, 0.2 g of CTAB was dissolved in 10 mL of water to which 400 μL of 75 mM HAuCl_4 was added and stirred for 15 min. 2 mL of 10 mM NaBH_4 solution was added in drops, stirred for another 15 min at RT. A brownish-red coloured solution was obtained, which was further used for the encapsulation with titanium-containing organosilica material.

3.2.2 Encapsulation of single gold nanoparticles inside the Ti-incorporated hollow structured spherical periodic mesoporous organosilica nano hybrid (Au@Ti-HPMO).

Synthesis of nano hybrid Ti-HPMO was carried out using surfactant-assisted sol-gel procedure followed by hydrothermal treatment. Typically, 0.5 g of CTAB was dissolved in a mixture of water and ethanol in a 2:1 ratio and 3 mL of ammonia solution (25 wt%). To make the solution homogeneous, the mixture was vigorously stirred for 1 h at room temperature. The pre-synthesized gold colloid solution was added in drops and stirred for 15 min. A solution of titanium butoxide in 5 mL of ethanol containing 1.2 mL of 1,2-Bis(triethoxysilyl)ethane (BTEE) and 300 μL TEOS was added in drops forming a pinkish-red slurry, where the Si/Ti ratio varied from 25 to 150. After 24 h stirring, the solution was transferred into Teflon lined stainless-steel autoclave and hydrothermally treated at 150 °C for 12 h. The obtained residue was centrifuged and washed thoroughly with water and ethanol, followed by drying at 60 °C for 12 h. Finally, the solvent extraction of the template CTAB was carried out in 30 mL of ethanol acidified with con. HCl at 60 °C for 6 h, washing was repeated twice to remove the surfactant completely, and the pinkish-red colored residue was dried at 60 °C for 12 h to obtain Au@Ti-HPMO_e . Instead of BTEE, 4,4'-bis(triethoxysilyl)1,1'-biphenyl (BP) was added for synthesizing Au@Ti-HPMO_{bp} . Bare hollow structured Ti-HPMO catalysts were synthesized by removing the gold colloid solution step during the synthesis.



Scheme 3.1: Synthesis of gold encapsulated mesoporous Ti-incorporated hollow structured spherical periodic mesoporous organosilica nanohybrid (Au@Ti-HPMO).

In the one-pot synthesis of organic-bridged Ti-HPMO, the Si/Ti ratio was varied from 25 to 150 to optimize the catalyst framework components. The incorporation of Ti species inside the organosilica framework was achieved through the co-hydrolysis, followed by the co-condensation of Ti precursor and the silica precursors. The Ti incorporation simultaneously occurs with the co-assembly with CTAB micelles, as illustrated in Scheme 1, step-2. The evolution of the hollow spherical nanostructures involves the hydrolysis of Si and Ti precursors in the basic medium containing water-ethanol mixture with the CTAB as the sacrificial template (See section 3.2.2). The final morphology of the Ti-HPMO is obtained through the hydrothermal treatment of the residue at 150 °C. As a control experiment, the bridging organic moiety inside the silica framework was changed from ethane to biphenyl (See section 3.2.2), and the obtained hybrid HPMO was labeled as Ti-HPMO_{bp}-100, where the Si/Ti ratio =100 was maintained. Confinement of Au nanoparticles inside Ti-HPMO_{bp}-100 was carried out similarly and denoted as Au@Ti-HPMO_{bp}-100.

3.2.3 Analytical equipment

UV-visible analysis was performed on Shimadzu 2700 spectrophotometer with a dual-beam source of He lamp and tungsten lamp as UV and visible light source, respectively. DRUV

analysis was done for powder samples using a dual-beam source with diffuse reflectance attachment by taking BaSO₄ as the standard. Powder X-ray Diffraction was recorded on Rigaku D MAX with a Cu K α source of wavelength 1.54 Å with an operational voltage of 40 mV and 15 mA current. N₂ adsorption-desorption analysis was done using Autosorb 1C Quantachrome, USA. The sample was first degassed at 300 °C for 3 hr. After degassing, the samples were cooled down to room temperature, and analysis was done by adsorbing/desorbing liquid N₂ at different pressures. BET model calculated the surface area. Pore size distribution was calculated using the BJH method. TEM analysis was carried out by the JOEL JEM F-200 instrument working at a voltage of 200kV. The samples for TEM analysis were prepared in isopropyl alcohol and dried completely before analysis. XPS measurements were carried out using a Thermo Kalpha+ spectrometer using micro-focused and monochromated Al K α radiation with energy 1486.6 eV. The peak fitting of the individual core levels was done using CASA XPS software with a Shirley-type background.

3.2.4 Catalytic screening for liquid phase olefin oxidation

The liquid phase olefin oxidation was carried out in a two-necked round bottom flask by attaching one neck to the condenser and the other neck sealed with a rubber septum for the addition of the oxidant. Typically 25 mg of the catalyst was mixed with 5 mL of acetonitrile (solvent) and 0.5 mmol of olefin and kept in the oil bath set at 70 °C. The mixture was stirred at this temperature for 15-20 min to attain a homogeneous condition. After this, 1mmol TBHP (70%) was added slowly under stirring. The reaction mixture was taken out at regular intervals to obtain the conversion and selectivity. The reactant and products were analyzed by GC equipped with FID and HP5 column.

3.3 Results and Discussion

3.3.1 UV-Visible (DRUV) Spectroscopy

The coordination environment of the Ti inside the ethane bridged organosilica materials were examined through the diffuse reflectance UV-vis spectroscopy (Figure 3.1a). All ratios of Ti-HPMO_e showed a strong absorption band at 215-225 nm, which is designated to the isolated tetrahedral Ti centers due to the LMCT charge transfer from oxygen to Ti.³⁸ As we increased the Ti loading inside the silicate framework, a shoulder peak was observed at 260 nm, suggesting the higher Ti coordination along with the water-coordinated Ti species. For higher Ti loaded

material Ti-HPMO_e-25 (Si/Ti ratio 25), absorption at 330 nm was observed, which is indicative of the presence of extra-framework Ti species.³⁹

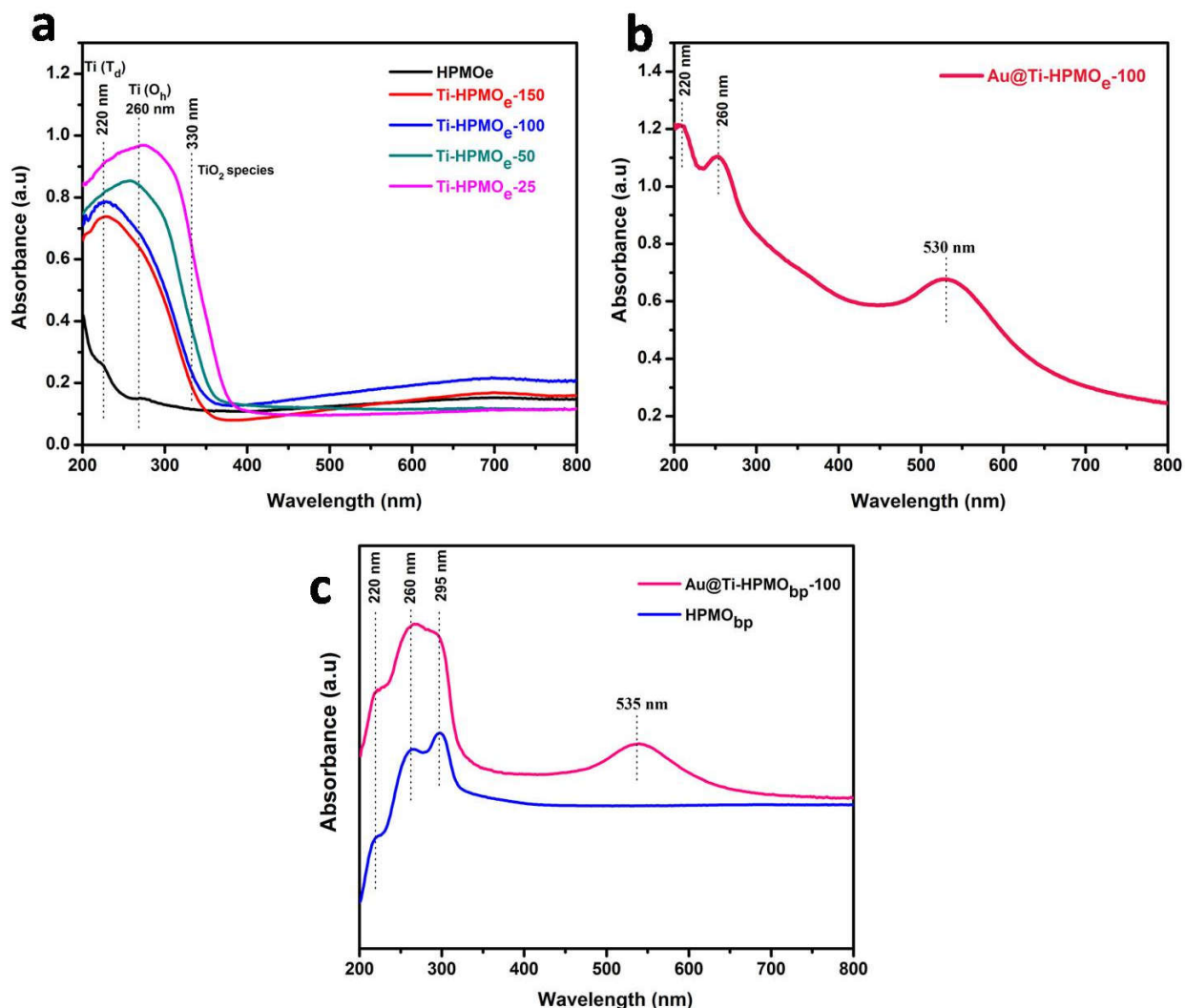


Figure 3.1: UV-Vis spectra of Ti-HPMOs and Au@Ti-HPMO catalysts.

The synthesized Au@Ti-HPMO_e-100 catalyst was used for UV-Vis analysis (Figure 3.1b), confirming the presence of gold nanoparticles showing the surface plasmon resonance absorbance band at 530 nm. A sharp absorption band at 220 nm evidenced isolated tetrahedral Ti centers and a peak at 260 nm, suggesting higher Ti coordination. No absorption at 330 nm confirms the absence of the extra-framework Ti species (Figure 3.1b). Similarly, the UV-Vis analysis was carried out on Au@Ti-HPMO_{bp}-100 where the SPR band for Au NPs was seen at 535 nm, but the different Ti species inside the framework was not conclusive from the UV

spectra because the absorption from the biphenyl group inside the framework was also observed in the same region (Figure 3.1c).

3.3.2 X-ray Diffraction

In the wide-angle XRD (Figure 3.2a), all Ti-HPMO_e samples displayed a broad peak at 23° indicates the amorphous nature of hybrid silica. At lower Si/Ti molar ratios, no diffraction peaks from the crystalline TiO₂ phase were observed, whereas, for molar ratios, 50 and 25 samples showed the peaks corresponding to the TiO₂ anatase phase.²⁷ The XRD results were well

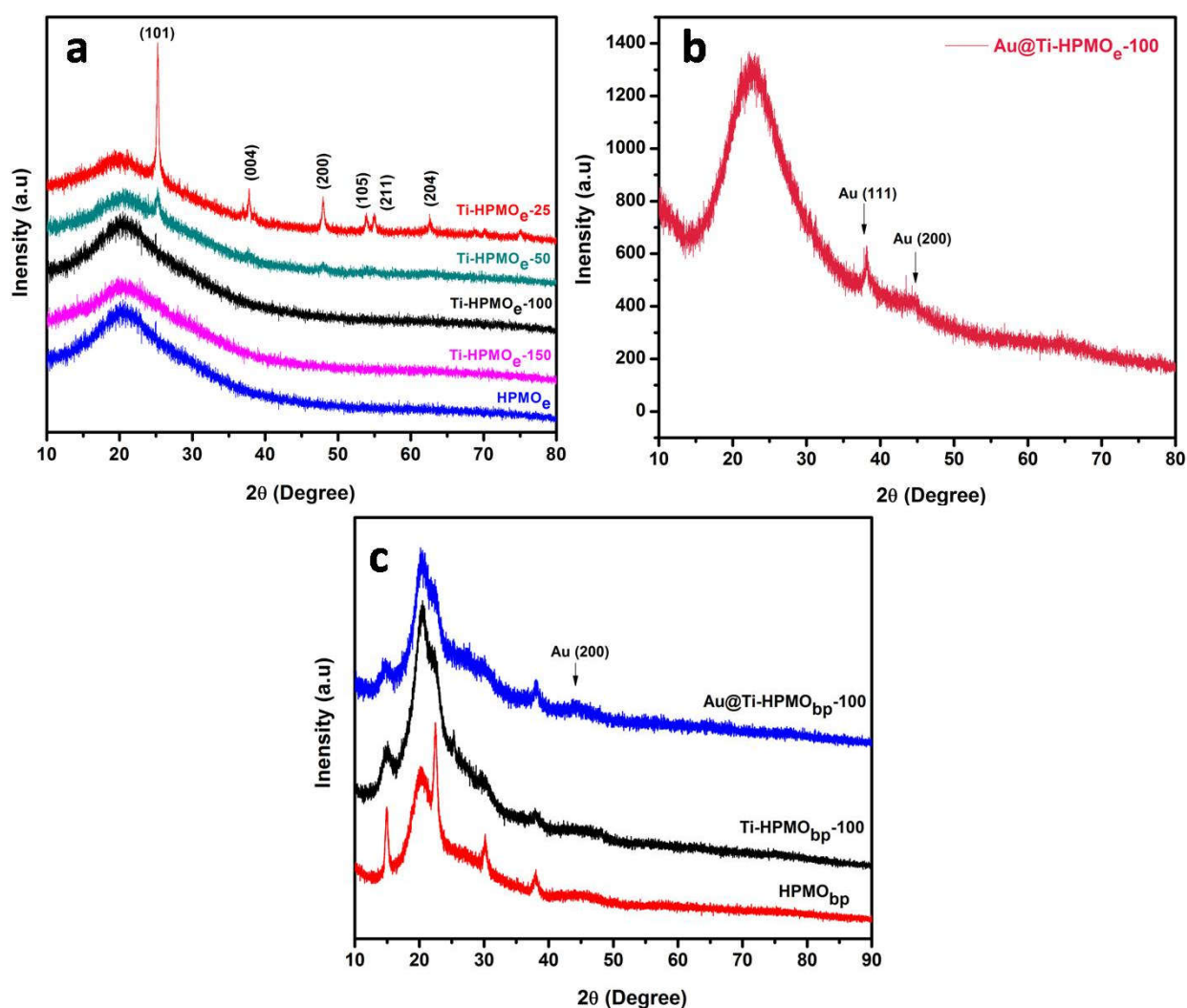


Figure 3.2: XRD pattern for Ti-HPMOs and Au@Ti-HPMO catalysts.

matching with the observation from UV-Vis analysis. The optimum Si/Ti ratio 100 was used to encapsulate the Au NPs, and the corresponding wide-angle XRD is given in Figure 3.2b. The

FCC crystal structure of the Au NPs was detected from the XRD pattern of the Au@Ti-HPMO_e-100 catalyst. Even in the presence of gold nanoparticles during the synthesis of Au@Ti-HPMO_e-100, no peaks were detected in XRD, proving the absence of extra-framework titania, which supported the UV results. The XRD pattern for the Ti-HPMO_{bp}-100 and Au@Ti-HPMO_{bp}-100 was carried out, and the reflection from the molecular scale ordering from the biphenyl bridging was observed for both Ti and Au loaded catalyst (Figure 3.2c). The XRD spectrum of Au@Ti-HPMO catalysts confirms the FCC crystal structure of the Au nanoparticles inside the hollow spheres from the visible Au (200) diffraction plane (Figure 3.2 b and c).

3.3.3 N₂ Porosimetry

The surface analysis by N₂ adsorption analysis showed a type IV isotherm for filling of mesopores (Figure 3.3a). The textural properties of all these catalysts have been tabulated in Table 3.1. All the catalysts showed very high surface area, and the surface area was found to decrease with an increase in the titanium content. Among all the ethane-bridged catalysts, Ti-HPMO_e-25 showed the least surface area and less pore volume (0.25 cc/g), which might be due to the pore-blocking from the extra-framework TiO₂ species in the higher Ti loaded catalyst. The appearance of larger pores along with the pores of 3.8 nm in the Ti-HPMO_e-25 catalysts can be due to the incorporation of titanium in the silica matrix. Since the ionic radius of Ti⁴⁺ is greater

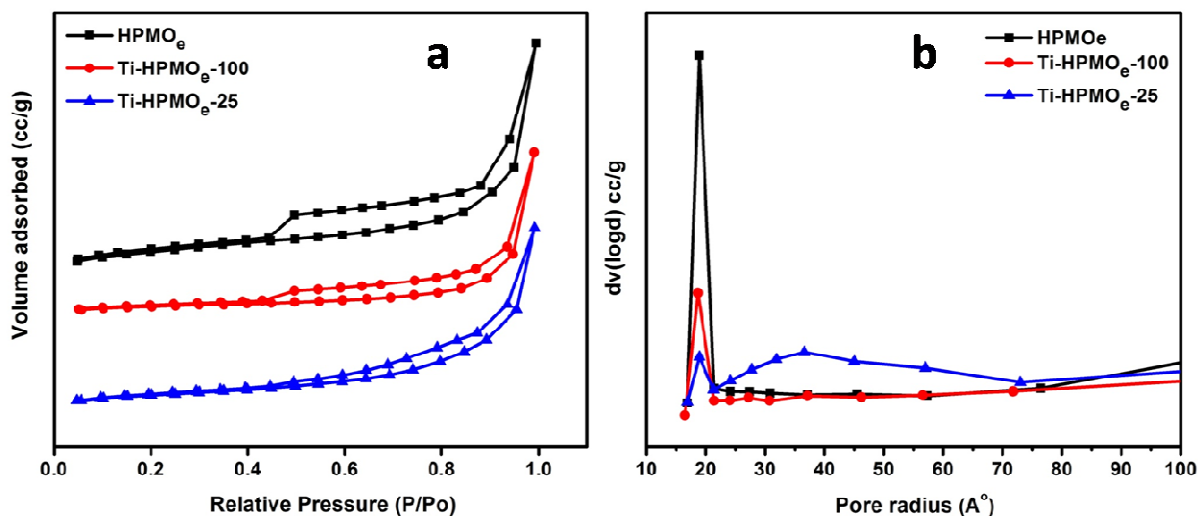


Figure 3.3: (a) N₂ adsorption-desorption isotherms and (b) pore size distribution of Ti-HPMO_e catalysts

than Si^{4+} ($\text{Si}^{4+}=0.48 \text{ \AA}$ and $\text{Ti}^{4+}=0.68 \text{ \AA}$), the exchange of some Si^{4+} ions by Ti^{4+} in the silica matrix caused the pore enlargement. The pore diameter for all the catalysts was in the range of 3-4 nm, indicating the generated mesoporosity from the CTAB soft template. The biphenyl-bridged Ti-HPMO_{bp}-100 catalyst showed a very high surface area (654 m²/g) compared to the ethane framework along with the formation of mesopores.

Table 3.1: Textural properties of different Ti-HPMO catalysts.

Catalyst	BET Surface area (m ² /g)	Pore diameter (nm)	Pore Volume (cc/g)
HPMO _e	396	3.8	0.47
Ti-HPMO _e (Si/Ti = 100)	329	3.7	0.40
Ti-HPMO _e (Si/Ti = 25)	256	3.8	0.25
Ti-HPMO _{bp} (Si/Ti = 100)	654	4.1	0.44

3.3.4 Solid State NMR Spectroscopy

The solid-state ¹³C cross-polarization (CP) MAS NMR spectra of HP MO_e and Ti-HPMO_e-100 shows one resonance peak at 5.4 ppm for the ethylene (-Si-(CH₂)₂-Si-) bridging inside the titanosilicate framework (Figure 3.4a).⁴⁰ Similarly, the ²⁹Si CP-MAS NMR spectra (Figure 3.4b) for those samples features significant resonance signals at -57 and -67 ppm attributed to the framework Si coordination T² [CSi(OSi)₂OH] and T³ [CSi(OSi)₃], respectively.⁴⁰

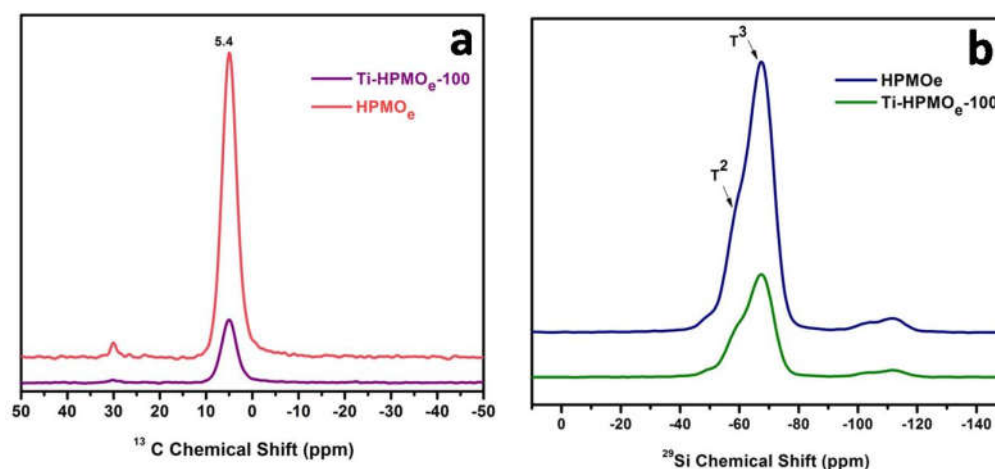


Figure 3.4: Solid-state NMR spectra of Ti-HPMOe (a) ¹³C and (b) ²⁹Si

The integration of biphenyl moiety inside the Ti-containing siloxane framework was confirmed from solid-state ^{13}C and ^{29}Si NMR measurements (Figure 3.5 a and b, respectively). The ^{13}C -MAS solid-state NMR spectrum showed the four aromatic resonances and side bands from the biphenyl bridging, consistent with the reported biphenyl-PMO system.²⁵ No other carbon peaks confirmed the complete removal of surfactant from the Ti-HPMO material through the solvent extraction method. In the ^{29}Si NMR spectrum, the strong resonance from the T^n sites attributed to T^1 -silicon [$\text{CSi}(\text{OSi})(\text{OH})_2$] species at -61 ppm, T^2 -silicon species [$\text{CSi}(\text{OSi})_2(\text{OH})$] at -71 ppm, and T^3 species [$\text{CSi}(\text{OSi})_3$] at -81 ppm.

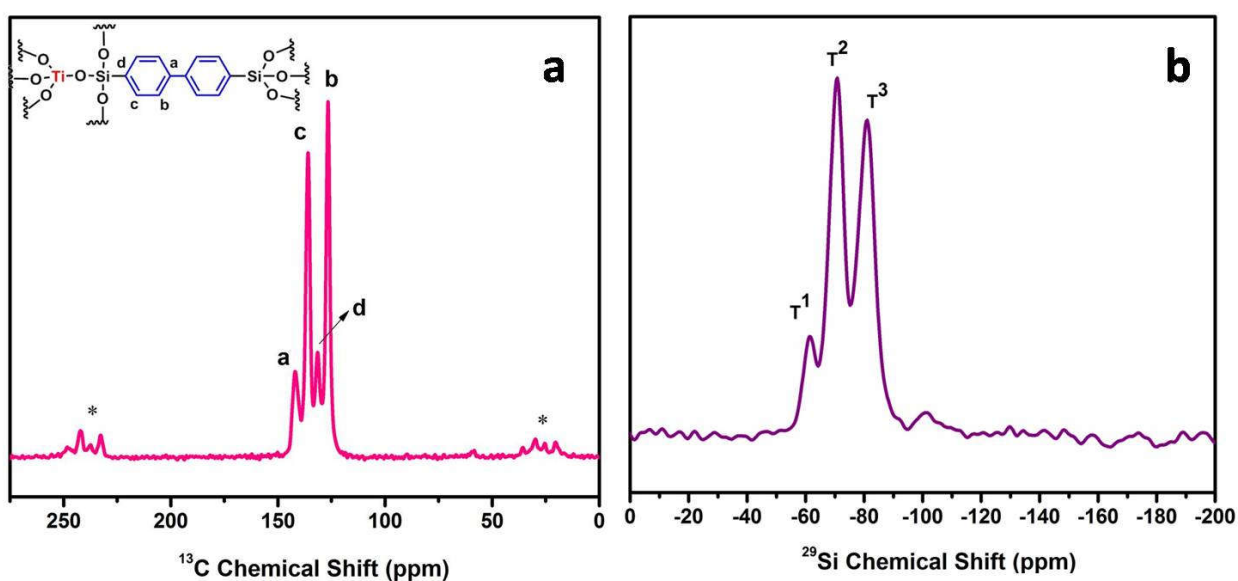


Figure 3.5: Solid-state NMR spectrum for Ti-HPMO_{bp} (a) ^{13}C (* spinning side bands) and (b) ^{29}Si .

3.3.5 X-ray Photoelectron Spectroscopy

To elucidate the chemical composition of Ti species on the surface of hybrid hollow nanospheres, XPS measurements were carried out on Ti-HPMO_e samples with varying Si/Ti molar ratios (Figure 3.6a). The XPS spectra of Ti 2p exhibit two peaks corresponding to $2p_{3/2}$ and $2p_{1/2}$, which, after deconvolution, confirmed the existence of two different coordination environments for titanium inside the material. Titanium tetrahedral (Td) and octahedral (Oh) coordination was observed in Ti-HPMO_e-100 and Ti-HPMO_e-50, whereas only octahedrally coordinated Ti was detected in Ti-HPMO_e-25, agreed with previous experimental results. The relative percentage fraction of surface $\text{Ti}^{4+}(\text{Oh})$ and $\text{Ti}^{4+}(\text{Td})$ species were determined from the

fitted peak areas, which varied according to the hollow nanostructures' Si/Ti molar ratio. From Figure 3.6b, it can be observed that the Ti-HPMO_e-100 catalyst shows the maximum amount of Ti⁴⁺(Td) species (35 %) whereas, further increasing the Ti loading inside the organosilica framework showed a decrease in tetrahedrally coordinated Ti species. In contrast, no characteristic for tetrahedral coordination was noticed in the Ti-HPMO_e-25 catalyst. From these characterization results, the optimized Si/Ti molar ratio in Ti-HPMO_e was found to be 100, and the Ti-HPMO_e-100 was further used to encapsulate gold nanoparticles. No prominent peak at the gold 4f region was measured, which may be due to the hybrid silica encapsulation with a shell thickness of ~25 nm (as determined from TEM).

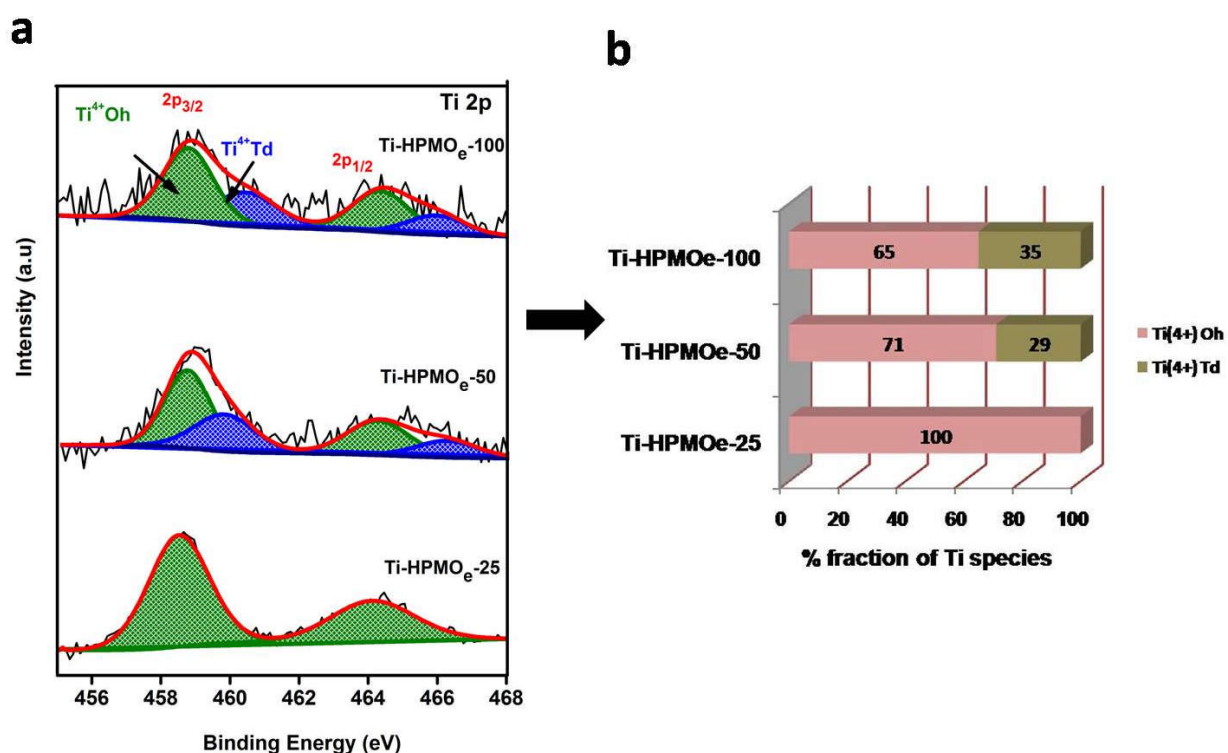


Figure 3.6: (a) Ti 2p XPS spectra of Ti-HPMO_e-(Si/Ti) catalysts and (b) percentage fraction of different Ti species on the surface of hollow hybrid titanosilicate catalysts.

3.3.6 Scanning Electron Microscopy (SEM)

SEM analyzed the morphology of synthesized Ti-containing HPMO catalysts. All ratios of Si/Ti showed spherical morphology using the optimized synthesis methodology, while Si/Ti = 25 (Ti-HPMO_e-25) resulted in the partial destruction of spherical architecture, which can be seen from

Figure 3.7. This can be due to the change in the rate of hydrolysis for the formation of extra-framework TiO_2 at higher Ti loading. The average particle size of spheres was ~ 70 nm.

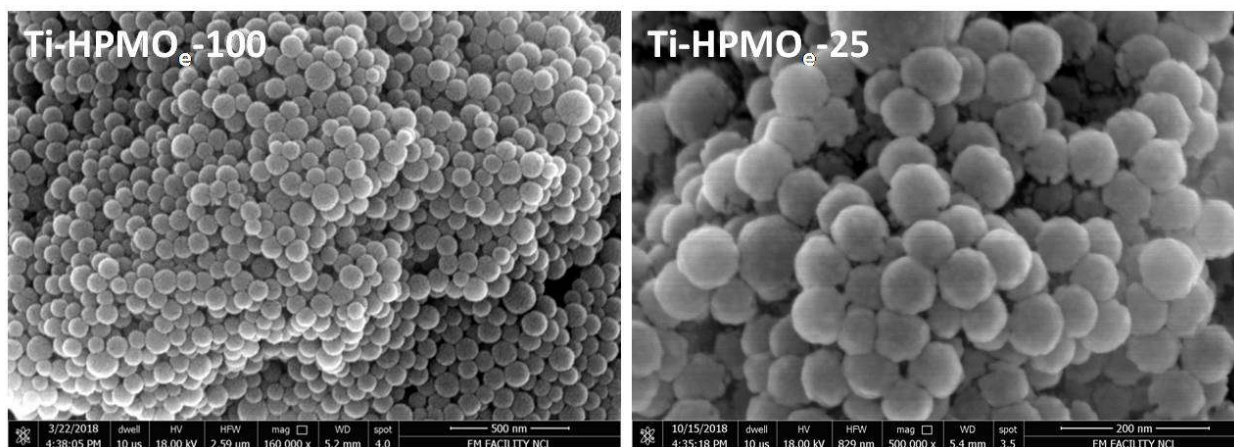


Figure 3.7: SEM images of Ti-HPMO_e-100 (scale 500 nm) and Ti-HPMO_e-25 (scale 200 nm)

3.3.7 Transmission Electron Microscopy (TEM)

Figure 3.8a and 3.8b show the representative images of surfactant removed Ti-HPMO_e with the Si/Ti ratios 100 and 25, respectively. Apparent changes were observable from the TEM images of both the Si/Ti ratios, where the uniform thickness of shell (~ 20 nm) was formed in Ti-HPMO_e-100, but in the case of Ti-HPMO_e-25 (higher Ti loading) formation of irregularly shaped hollow spheres of varying shell thickness was noticed. This irregularity was caused due to the simultaneous growth of extra-framework TiO_2 , which alters the rate of hydrolysis and condensation reactions. Further, these architectures were used for the compartmentalization of single Au NPs.

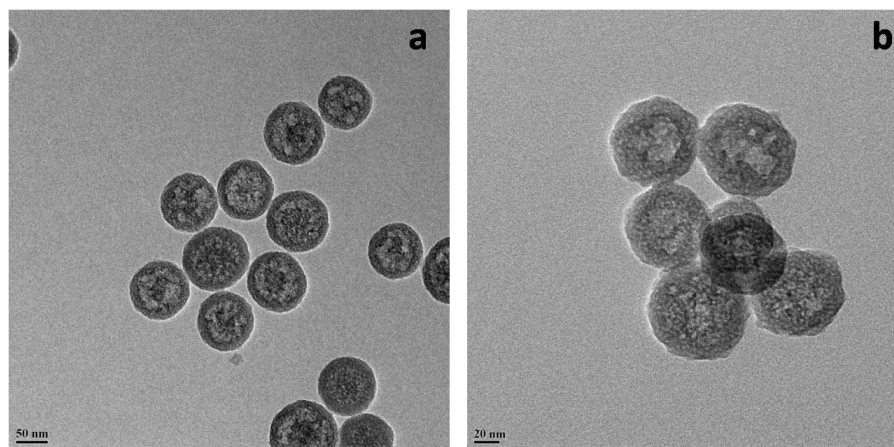


Figure 3.8: TEM images of (a) Ti-PMO_e-100 (scale 50 nm) and (b) Ti-PMO_e-25 (scale 20 nm).

The successful formation of yolk-shell spherical morphology having an average shell thickness of ca. 25 nm carrying a single gold nanoparticle of an average size of ca. 3-5 nm as the yolk can be observed from the TEM images (Figure 3.9). The mesostructured hybrid organo-titanosilicate hollow spherical shell was clearly visible from the TEM images. Not many hybrid spheres were spotted encapsulating more than one Au NPs in the overall analysis. Even by varying Au loading from 1 wt % to 5 wt %, we could not notice many multiple occupancies of Au NPs in a single sphere.

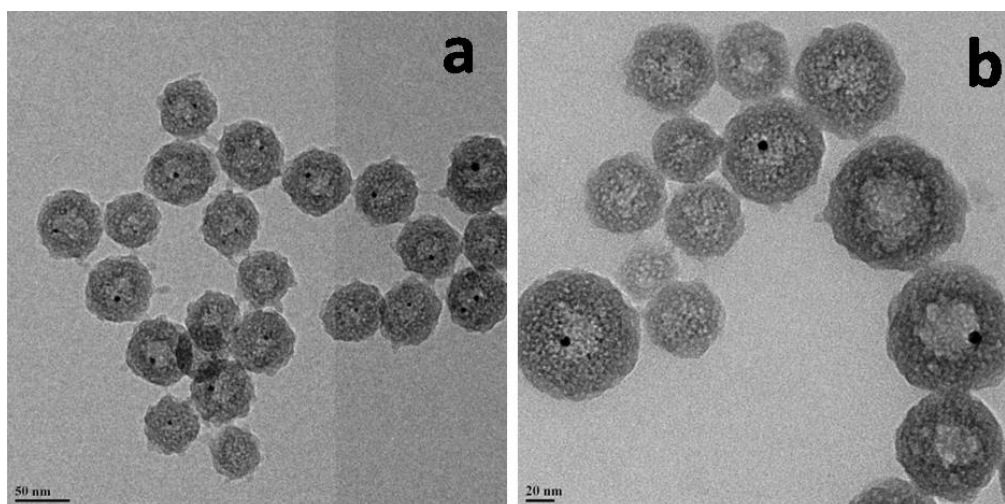


Figure 3.9: TEM images of Au@Ti-PMOe-100 (a) scale 50 nm and (b) 20 nm.

The hollow cavity spaces along with fine Au nanoparticles was confirmed from the HAADF-STEM image, which clearly shows the spatial proximity between the Au and Ti-HPMO_e hollow support inside the confined nanospace (Figure 3.10a). As indicated from the STEM elemental mappings (Figure 3.10b-d) for Si, O, and Ti atoms are homogeneously distributed on the hollow structured particle. The single Au NP was encapsulated by the hollow shell resulted in a yolk-shell morphology (Figure 3.10e, f). Elemental EDX line scan across the selected Au@Ti-HPMO_e particle along with the shown direction in Figure 3.10g confirms the formation of confined Au nanoparticles inside Ti-HPMO_e, resulting in a yolk-shell structure with uniformly distributed atoms (Figure 3.10h). This confirmed that the shell is enriched with the uniform distribution of the Si, Ti, O, and the yolk is majorly made by the single Au NP.

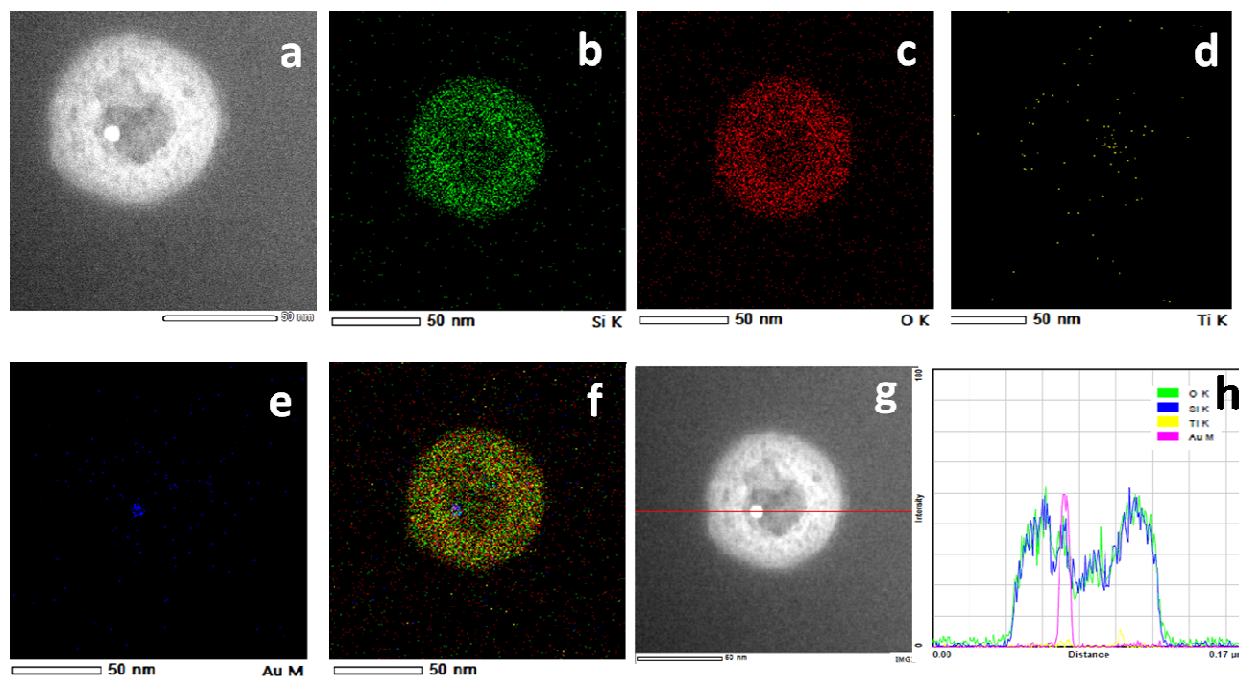


Figure 3.10:(a) HAADF-STEM image of Au@Ti-HPMO_e-100 (scale 50 nm), (b-f) STEM-EDX elemental mapping of (b) Si K, (c) O K, (d) Ti K, (e) Au M edges, and (f) overlay image, line scan profile of Au@Ti-HPMO_e-100 (g) line scan region and (h) line scan profile image.

The TEM analysis of the Au NP encapsulated biphenyl bridged hybrid Ti-containing HP MO (Au@Ti-HPMO_{bp}-100) synthesized using a similar synthesis procedure is shown in Figure 3.11. The TEM images of the surfactant removed Au@Ti-HPMO_{bp}-100 samples in Figure 3.11a, b showed the successful encapsulation of single Au NPs inside the Ti-HPMO_{bp} spheres, but the formation of hollow architecture was not successful while using the biphenyl PMO precursor (BP) in the synthesis. The only difference in the synthesis is the change in the organic bridging siloxane precursor. The possible reason for the difference in the structural evolution can be the difference in the rate of hydrolysis and polycondensation of BP under the hydrothermal treatment in the optimized basic reaction conditions.⁴¹ Generally, while using the CTAB assisted synthesis of silica particles, the core etching occurs due to the lower stability of the inside silica compared to the surfactant attached peripheral silica in basic reaction medium. The difference in the organic functional moieties in the silica core and periphery can alter the etching rate.⁴² The hydrothermal stability of biphenyl bridged silica is higher than the ethane bridging. Hence the core etching under these optimized synthesis conditions are not facile in biphenyl bridged

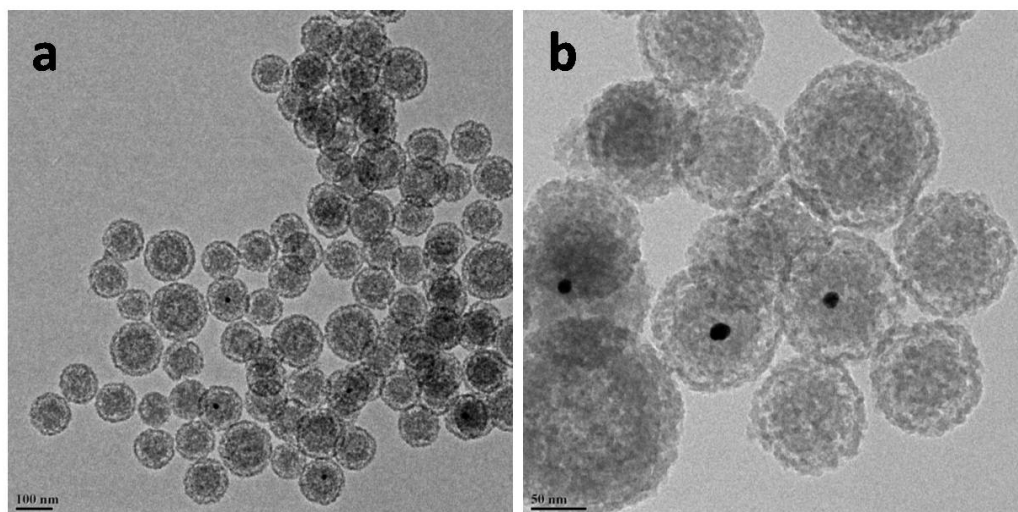


Figure 3.11: TEM images for Au@Ti-HPMO_{bp}-100, scale (a) 100 nm and (b) 50 nm Ti-HPMO_{bp}, which can be clearly seen from the TEM studies (Figure 3.11). Still, we can observe the less dense or hollow formation near the layers below the periphery of silica spheres suggests the partial construction of hollow silica. But further internal core etching may take prolonged time. The average particle size of Ti-HPMO_{bp} spheres was calculated to be ~120 nm, and the average Au NP size was determined to be ~ 5 nm.

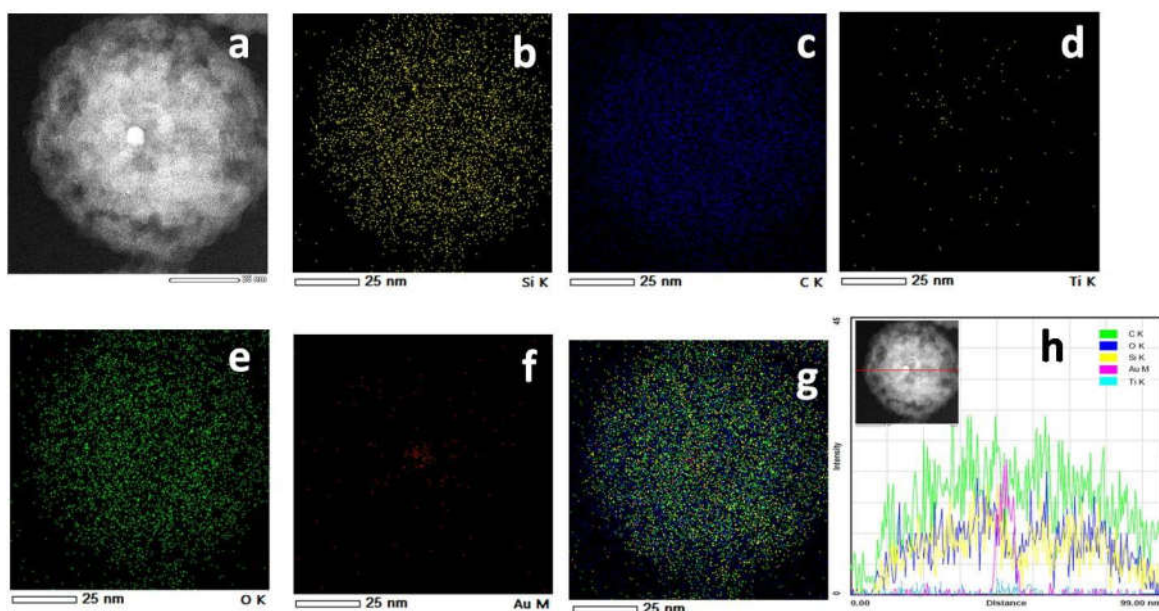


Figure 3.12: (a) HAADF-STEM image of Au@Ti-HPMO_{bp}-100 (scale 25 nm), (b-g) STEM-EDX elemental mapping of (b) Si K, (c) C K, (d) Ti K, (e) O K, (f) Au M edges and (g) overlay image, (h) line scan profile of Au@Ti-HPMO_{bp}-100 (inset: line scan region).

For Au@Ti-HPMO_{bp}, the density of the silica periphery compared to the core is significantly less, which can be seen from the HAADF-STEM image (Figure 3.12a), which also supports the TEM analysis. As indicated from the STEM elemental mappings (Figure 3.12b-e) for Si, C, Ti, and O, atoms are homogeneously distributed on the spherical structured hybrid silica particle. The single Au NP was encapsulated by the silica shell resulting in core-shell morphology (Figure 3.12f, g). The elemental EDX line scan across the selected Au@Ti-HPMO_{bp} particle and the shown direction in Figure 3.12h (inset) confirm the formation of confined Au nanoparticles inside Ti-HPMO_{bp}, resulting in a core-shell structure with uniformly distributed atoms (Figure 3.12h). This confirmed that the shell is enriched with the uniform distribution of the Si, Ti, O, and the core is majorly by the single Au NP.

3.3.8 Catalytic Activity for Olefin Epoxidation

Generally, the mesoporous titanosilicates made of purely inorganic bridging are frequently utilized as catalysts for the liquid phase epoxidation reactions.⁴³ Here, we carried out the reaction using the synthesized inorganic-organic hybrid titanosilicate catalysts for the liquid-phase oxidation of alkenes where acetonitrile was used as the solvent and TBHP as the oxidant. Figure 3.13 shows the results of the oxidation of cyclooctene as the model reaction. All ratios of Si/Ti in the ethane bridged Ti-HPMO_e catalysts showed more than 75 % selectivity for the cyclooctene oxide irrespective of the alkene conversion. This may be due to the less ring strain of the alkene in the bulky cyclooctene substrate. A volcano-type activity trend was observed as we increased the Ti loading in the HP MO_e, and the maximum conversion (63 %) was obtained for the Ti-HPMO_e-100 (Si/Ti = 100). A further increase in the Ti loading showed a decline in the activity. As a control experiment, TS-1 catalyst was used for the reaction. The conversion was measured less than 50 % due to the microporous nature of the material, which restricts the diffusion of the bulky molecules like cyclooctene in the liquid phase reaction, but the selectivity for the cyclooctene oxide (79 %) was maintained. The XPS studies on the Ti-HPMO_e-x (x= Si/Ti ratio) catalysts for quantifying the different Ti coordination species showed that Ti-HPMO_e-100 catalysts have maximum tetrahedral Ti centers (35 %), which was in trend with the activity results. The mesoporous nature of the hybrid material and the optimum concentration of tetrahedral Ti sites are responsible for the obtained activity. The effect of ethane organic bridging was not much prominent in the cyclooctene epoxidation catalysis using TBHP. Hence we used

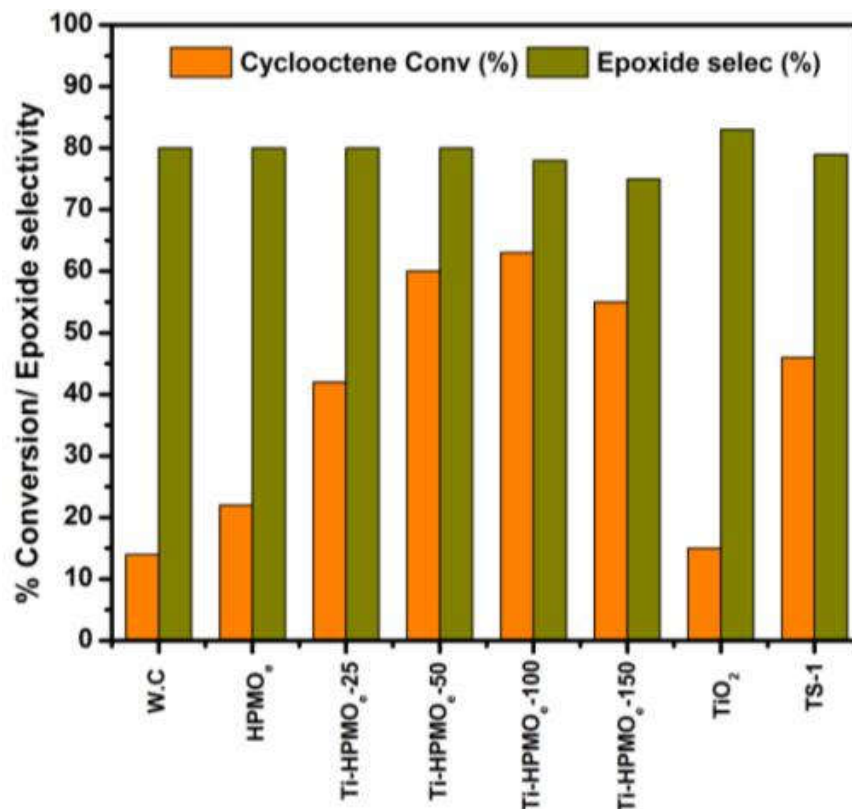


Figure 3.13: Catalytic oxidation of cyclooctene over Ti-HPMO_e-x (x= Si/Ti) catalysts. Reaction conditions: cyclooctene (0.5 mmol), TBHP (1 mmol), CH₃CN (5 mL), T (70 °C), and t (16 h). Other products include diol, enol and enone.

the biphenyl bridged Ti-HPMO_{bp}-100 catalyst for the reaction and could see an enhancement in the conversion (69 %) and the epoxide selectivity (92 %) compared to the ethane bridging (Ti-HPMO_e-100) and the inorganic TS-1 and TiO₂ material. This improvement can be attributed to the weak interaction of the epoxide with the surface-active species, which was effortlessly desorbed and prevented the ring-opening of the epoxide from forming the diols. In the Ti-HPMO_{bp}-100 catalyst, the activity was derived from the highly dispersed isolated Ti centers and the surface characteristics of organic-inorganic hybrid materials. The oxidant effect was checked by using H₂O₂ (30 %) on the Ti-HPMO_e-100 catalyst, where low conversion (55 %) of cyclooctene was observed with 83 % selectivity for epoxide. Similarly, the Ti-HPMO_{bp}-100 catalyst was used with H₂O₂, and lower conversion (58 %) and selectivity (86 %) were measured. Hence the oxidant was optimized to be TBHP for further studies. These hybrid Ti-silicates have been utilized as the nanoreactors for the encapsulation of the Au NPs and have

been tested for catalysis to investigate the enhanced activity by the synergy of Au and Ti sites. The gold NP encapsulated hybrid systems have been tested for the cyclooctene epoxidation reaction. However, no noticeable improvement was observed due to the bulkiness of cyclooctene to encounter the encapsulated Au NPs, which are buried inside the silicate shell of larger thickness. Hence the substrate was changed to styrene for the study since it is an industrially significant molecule, and the Au@Ti-HPMO_e-100 and Au@Ti-HPMO_{bp}-100 catalysts were tested for liquid phase styrene oxidation using TBHP as an oxidant. The primary selective product obtained for the reaction was styrene oxide.

Table 3.2: Liquid-phase catalytic oxidation of styrene.

Sl No.	Catalyst (Si/Ti= 100)	Conversion (%)	Selectivity (%)		
			SO	BA	PA
1.	Ti-HPMO _e	48	66	22	10
2.	Au@Ti-HPMO _e	64	69	21	9
3.	Ti-HPMO _{BP}	69	71	18	8
4.	Au@Ti-HPMO _{BP}	71	77	15	5
5.	Au-TiO ₂	31	62	23	15
6.	Au@Ti-HPMO _e (spent)	63	63	20	5
7.	Au@Ti-HPMO _{BP} (spent)	67	73	19	3

Reaction conditions: Styrene- 0.1 mmol, CH₃CN- 3 mL, TBHP -0.2 mmol, Cat- 20 mg (Au 2.5 wt%), T- 80 °C, t- 24 h. SO = styrene oxide, BA = benzaldehyde, PA = phenylacetaldehyde

The catalytic results for styrene oxidation are tabulated in Table 3.2. Compared to Ti-HPMO_e catalyst (conversion 48 %), Ti-HPMO_{bp} (conversion 69 %) showed better conversion of styrene, confirming the effect of organic bridging with Ti dispersion and mesoporosity for the enhanced activity. These systems with Au NPs were tested for the reaction under similar conditions. The Au NPs inside ethane bridged Ti-HPMO_e material displayed enhanced styrene conversion (64 %) in comparison to Ti-HPMO_e alone (Table 3.2, entries 1 and 2). Similarly, Au NPs inside

biphenyl bridged Ti-HPMO_{bp} material was utilized for the reaction. Still, no noticeable change in the conversion and selectivity was observed (Table 3.2, entries 3 and 4) in comparison to bare Ti-HPMO_{bp}. This difference in activity can be explained with respect to the morphological differences in both Au@Ti-HPMO_e and Au@Ti-HPMO_{bp} catalysts. As evidenced from the TEM analysis, Au@Ti-HPMO_e exists in hollow structured yolk-shell morphology, which has a mesoporous shell of hybrid Ti-silicate having a thin shell (~20 nm). Due to the reduced diffusion constraints, the Au NPs inside the shell are easily accessible to the alkene and bulky oxidants in the liquid phase. The Au NPs inside the yolk-shell architectures are mobile inside the thin shell, which favours mass transfer to the active catalytic centers.⁴⁴ In the case of Au@Ti-HPMO_{bp}, the core-shell morphology was achieved, restricting the facile interaction of alkene with the Au NPs embedded inside the porous Ti-silicate shell of thickness ~ 50 nm. Owing to the morphological and physicochemical attributes of the hybrid Ti-silicates collectively contributed to the alkene oxidation catalysis and the Au@Ti-HPMO_e catalyst with Si/Ti ratio 100 was found to be the more active catalyst in the present study.

The heterogeneity of Au@Ti-HPMO_e catalyst was studied by reusability experiment, where the spent catalyst was utilized for the subsequent catalytic run, and no apparent change in both conversion and selectivity was noticed (Table 3.2, entries 6 and 7). The study confirmed that no active species was lost into the solution phase and this was further confirmed through the ICP-OES measurements. Leaching of Au or Ti was not detected in the solution after the reaction suggesting the heterogeneous behaviour of active moieties on the hybrid silica. The TEM analysis of the spent Au@Ti-HPMO_e catalyst was carried out (Figure 3.14a) which showed that the Au NP size was maintained even after the reaction. This points out the significant role of the encapsulation strategy of Au in Ti-modified hybrid silica shell. To study the nature of surface Ti species in the catalyst after reaction, XPS analysis was carried out. From Figure 3.14b, it can be observed that Au@Ti-HPMO_e spent catalyst showed the existence of Ti⁴⁺(Td) and Ti⁴⁺(Oh) species, where the former is considered the active site for the oxidation catalysis.

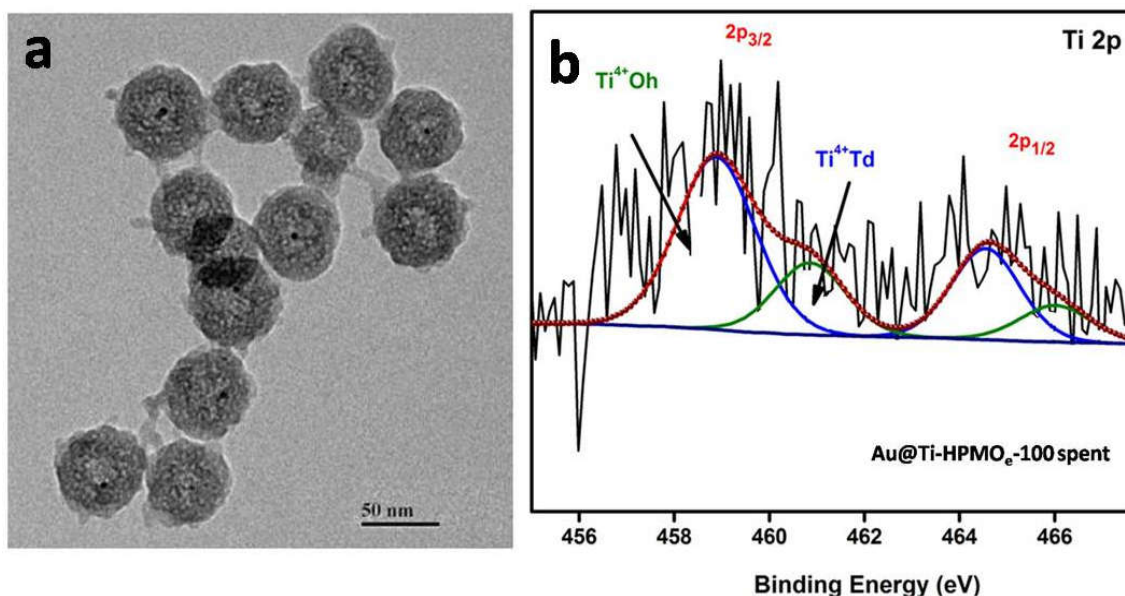


Figure 3.14: Au@Ti-HPMO_e spent catalyst analysis (a) TEM image and (b) Ti 2p XPS plot.

3.4 Conclusions

In conclusion, mesoporous titanium-modified organic-inorganic hybrid silica nanostructures (yolk-shell and core-shell) were synthesized using the sol-gel hydrothermal method. The ethane and biphenyl organic motif incorporated inside the Ti-modified silica with the aid of a structure-directing agent to form spherical morphology. The use of ethane silane precursor resulted in a hollow spherical architecture, whereas the biphenyl silane precursor yielded hybrid silica spheres with no void space. The liquid-phase oxidation of cyclooctene over these nanoarchitectures with varying Ti content showed that the best Si/Ti ratio is 100 with almost 35 % Ti⁴⁺(Td) sites (determined from XPS) gave a better catalytic performance. The Au NP encapsulated Ti-HPMO acts as nanoreactors for the styrene epoxidation reaction in the liquid phase. Among the yolk-shell and core-shell morphologies, the enhanced catalytic performance in terms of conversion was observed for the Au@Ti-HPMO_e catalyst with a hollow structure with a thin porous shell facilitating a favourable mass transfer compared to core-shell morphology. This encapsulation strategy with porous hybrid silica shell was found to prevent the leaching and sintering of small Au NPs during the liquid-phase catalysis.

3.5 References

1. F. Caruso, R. A. Caruso and H. Möhwald, *Science*, 1998, **282**, 1111.
2. X. Fang, Z. Liu, M.-F. Hsieh, M. Chen, P. Liu, C. Chen and N. Zheng, *ACS Nano*, 2012, **6**, 4434-4444.
3. Y. Li and J. Shi, *Advanced Materials*, 2014, **26**, 3176-3205.
4. J. Liu, S. Z. Qiao, J. S. Chen, X. W. Lou, X. Xing and G. Q. Lu, *Chemical Communications*, 2011, **47**, 12578-12591.
5. A. Pan, T. Zhu, H. B. Wu and X. W. Lou, *Chemistry – A European Journal*, 2013, **19**, 494-500.
6. J. A. Melero, R. van Grieken and G. Morales, *Chemical Reviews*, 2006, **106**, 3790-3812.
7. B. Karimi and F. K. Esfahani, *Advanced Synthesis & Catalysis*, 2012, **354**, 1319-1326.
8. A. Lazar, S. C. George, P. R. Jithesh, C. P. Vinod and A. P. Singh, *Applied Catalysis A: General*, 2016, **513**, 138-146.
9. S. Inagaki, S. Guan, T. Ohsuna and O. Terasaki, *Nature*, 2002, **416**, 304-307.
10. Q. Yang, M. P. Kapoor and S. Inagaki, *Journal of the American Chemical Society*, 2002, **124**, 9694-9695.
11. J. A. Melero, J. Iglesias, J. M. Arsuaga, J. Sainz-Pardo, P. de Frutos and S. Blazquez, *Journal of Materials Chemistry*, 2007, **17**, 377-385.
12. E. Klemm, E. Dietzsch, T. Schwarz, T. Kruppa, A. Lange de Oliveira, F. Becker, G. Markowz, S. Schirrmeister, R. Schütte, K. J. Caspary, F. Schüth and D. Hönicke, *Industrial & Engineering Chemistry Research*, 2008, **47**, 2086-2090.
13. A. Corma, *Chemical Reviews*, 1997, **97**, 2373-2420.
14. A. Corma, P. Esteve, A. Martinez and S. Valencia, *Journal of Catalysis*, 1995, **152**, 18-24.
15. P. Wu, T. Tatsumi, T. Komatsu and T. Yashima, *Journal of Catalysis*, 2001, **202**, 245-255.
16. W. Zhang, M. Fröba, J. Wang, P. T. Tanev, J. Wong and T. J. Pinnavaia, *Journal of the American Chemical Society*, 1996, **118**, 9164-9171.
17. Z. Wang and K. J. Balkus, *Microporous and Mesoporous Materials*, 2017, **243**, 76-84.
18. K. Lin, P. P. Pescarmona, K. Houthoofd, D. Liang, G. Van Tendeloo and P. A. Jacobs, *Journal of Catalysis*, 2009, **263**, 75-82.
19. F. Bérubé, F. Kleitz and S. Kaliaguine, *The Journal of Physical Chemistry C*, 2008, **112**, 14403-14411.
20. Y. Huang, P. Yuan, Z. Wu and X. Yuan, *Journal of Porous Materials*, 2016, **23**, 895-903.
21. J. Silvestre-Alberó, M. E. Domine, J. L. Jordá, M. T. Navarro, F. Rey, F. Rodríguez-Reinoso and A. Corma, *Applied Catalysis A: General*, 2015, **507**, 14-25.
22. Y. Wei, G. Li, J. Liu, Y. Yi and H. Guo, *Microporous and Mesoporous Materials*, 2021, **310**, 110668.

23. Y. Wei, G. Li, C. Wang and H. Guo, *Journal of Colloid and Interface Science*, 2021, **586**, 233-242.
24. A. Modak, M. Nandi and A. Bhaumik, *Catalysis Today*, 2012, **198**, 45-51.
25. M. Du, G. Zhan, X. Yang, H. Wang, W. Lin, Y. Zhou, J. Zhu, L. Lin, J. Huang, D. Sun, L. Jia and Q. Li, *Journal of Catalysis*, 2011, **283**, 192-201.
26. J. Zhuang, D. Ma, Z. Yan, X. Liu, X. Han, X. Bao, Y. Zhang, X. Guo and X. Wang, *Applied Catalysis A: General*, 2004, **258**, 1-6.
27. S. Gupta, C. P. Vinod and D. Jagadeesan, *RSC Advances*, 2015, **5**, 92371-92377.
28. M. Sankar, Q. He, R. V. Engel, M. A. Sainna, A. J. Logsdail, A. Roldan, D. J. Willock, N. Agarwal, C. J. Kiely and G. J. Hutchings, *Chemical Reviews*, 2020, **120**, 3890-3938.
29. A. C. Sunil Sekhar, K. Ziyad, Y. Soni and C. P. Vinod, *ChemCatChem*, 2015, **7**, 1222-1230.
30. I. Lee, J. B. Joo, Y. Yin and F. Zaera, *Angewandte Chemie International Edition*, 2011, **50**, 10208-10211.
31. S.-H. Wu, C.-T. Tseng, Y.-S. Lin, C.-H. Lin, Y. Hung and C.-Y. Mou, *Journal of Materials Chemistry*, 2011, **21**, 789-794.
32. Y. Chen, S. Lerch, Z. Say, C. Tiburski, C. Langhammer and K. Moth-Poulsen, *RSC Advances*, 2021, **11**, 11642-11650.
33. L. Luo, L. Bock, Y. Liang and R. Anwender, *European Journal of Inorganic Chemistry*, 2020, **2020**, 3967-3976.
34. J. Han, R. Chen, M. Wang, S. Lu and R. Guo, *Chemical Communications*, 2013, **49**, 11566-11568.
35. J. Han, M. Wang, R. Chen, N. Han and R. Guo, *Chemical Communications*, 2014, **50**, 8295-8298.
36. J. C. Park and H. Song, *Nano Research*, 2011, **4**, 33-C49.
37. Y. Yao, X. Zhang, J. Peng and Q. Yang, *Chemical Communications*, 2015, **51**, 3750-3753.
38. G. N. Vayssilov, *Catalysis Reviews*, 1997, **39**, 209-251.
39. J. Huang, C. Liu, D. Sun, Y. Hong, M. Du, T. Odum-Wubah, W. Fang and Q. Li, *Chemical Engineering Journal*, 2014, **235**, 215-223.
40. Y. Liang, M. Hanzlik and R. Anwender, *Journal of Materials Chemistry*, 2005, **15**, 3919-3928.
41. Y. Chen, H. Chen, L. Guo, Q. He, F. Chen, J. Zhou, J. Feng and J. Shi, *ACS Nano*, 2010, **4**, 529-539.
42. W. Li, Y. Tian, C. Zhao, B. Zhang, H. Zhang, Q. Zhang and W. Geng, *Journal of Nanoparticle Research*, 2015, **17**, 480.
43. H.-S. Cheong, K.-K. Kang and H.-K. Rhee, *Catalysis Letters*, 2003, **86**, 145-149.
44. H. Sun, X. Shen, L. Yao, S. Xing, H. Wang, Y. Feng and H. Chen, *Journal of the American Chemical Society*, 2012, **134**, 11243-11250.

CHAPTER-4

Hydrogenation Catalysis by Fine Pd-nanoparticles on N-incorporated Periodic Mesoporous Organosilica (NPMO)

Part 4A. Pd-NPMO Catalyzed Low-temperature and Atmospheric Pressure Phenol Hydrogenation Reaction

Part 4B. Aqueous-phase Hydrogenation of CO₂ to Formate on Pd-NPMO Catalyst

This chapter is adapted from:

- 1) **K. J. Betsy**, and C. P. Vinod; Pd nanoparticles in multifunctional N-incorporated hybrid organosilica and the impact on room temperature phenol hydrogenation (Manuscript ready for submission).
- 2) **K. J. Betsy**, Anish Lazar, Anjuna Pavithran and C. P. Vinod, CO₂ Hydrogenation to Formate by Palladium Nanoparticles Supported on N-Incorporated Periodic Mesoporous Organosilica, *ACS Sustainable Chem. Eng.* **2020**, 8, 39, 14765–14774.

4.1 Introduction

Periodic mesoporous organosilica (PMOs) have become the state-of-the-art advanced silica material over the past few years. Their high surface area, tunable porosity, and structural diversity make them a suitable scaffold for a myriad of applications, including gas sorption, drug delivery, and catalysis.¹ The seemingly unlimited possibilities of PMOs offered through the judicious choice of bridging functional framework linkers and preparation conditions.^{2,3} Among the various nanoporous materials, mesoporous silica-based materials generally contain amorphous framework. In contrast, a molecular-scale ordering has been observed within the pore walls of periodic mesoporous organosilica (PMOs) constructed using the bridged organosilane precursors.^{4,5} The crystal-like ordering in the PMO pore walls has been achieved in the recent decades using several hydrophobic bridging organic functionalities, where the organosilane precursor undergo self-assembly in water through hydrophobic and hydrophilic interactions to form lamellar structures with the molecular scale ordering induced by the π - π stacking, H-bonding, etc.⁵⁻⁸ Hybrids of nanostructured PMOs with covalently incorporated organic groups in the pore walls of silica framework without destructing the mesopores induce unique properties.⁹ Several organic framework bridges starting from organic π -systems to metal complexes are reported for implementing framework functionality carrying unique properties like introducing electro-active centers, modulating HOMO-LUMO levels, and generating reactive catalytic sites.¹⁰⁻¹⁵ The ability to alter the pore size, surface area, and topology and incorporate task-specific functional groups into the framework make them a potential material for fine chemical synthesis.

Synergistic effect achieved by the use of catalyst support as an active component along with metal nanoparticles (NPs) is an attractive strategy in catalysis.^{16,17} Compared to redox-active supports like CeO₂, TiO₂ which acts as an electronic and structural promoter in heterogeneous catalysis, silica behaves inert and inactive component which can merely hold the metal NPs with the aid of surfactants, expensive dendrimers or polymers, and structure-directing agents.^{18,19} Synthesis and stabilization of downsized metal NPs on silica without any aiding reagents is challenging due to the weak interaction of the metal precursors with the silica surface.²⁰ Incorporation of N-containing organic domains inside the host silica framework achieved by the rational design of bridged organosilane precursor for organic-inorganic hybrid support or the

surface decorated silyl functionality is an effective protocol that can stabilize and electronically modify the fine metal NP sites responsible for boosting the catalyst performance.²¹⁻²³ Compared to the simple surface anchored functionality, covalently bridged N-containing organic moieties in the silica framework helps to create well-dispersed active centers that are more stable and leach proof under the catalytic reaction conditions.²⁴⁻²⁶

The first part of this chapter, i.e., 4A, describes the synthesis and detailed characterization of Pd NPs supported on a new framework incorporating nitrogen-containing hybrid PMO silica material (Pd@NPMO). This material has been screened for selective hydrogenation of phenol and its derivatives at room temperature under atmospheric hydrogen pressure. The catalytic performance of hybrid material has been compared with unmodified Pd@SBA-15 catalysts. Based on the experimental and literature reports, a possible reaction mechanism is proposed for the low-temperature phenol hydrogenation explaining the role of nitrogen-containing organic domains in the silica framework. In the second part of this chapter 4B, the Pd@NPMO hybrid catalyst has been tested for the selective aqueous phase CO₂ hydrogenation reaction. To validate the superior performance of the Pd@NPMO catalyst, we compared the activity with Pd-SBA-15 catalysts and the crucial role of nitrogen sites in our catalyst to boost the CO₂ valorization to formate has been studied using various optimization reactions.

4.2 Experimental

Synthesis of 1,3,5-triformylphloroglucinol²⁷ and SBA-15 silica²⁸ was carried out using the reported procedure. All other chemicals, reagents, and solvents were used as received without any further purification.

4.2.1 Synthesis of N-incorporated organo-silane precursor: The synthesis was done using the Schiff-base reaction of a trialdehyde and amine. Typically, 0.47 mmol of 1,3,5-triformylphloroglucinol (TFPG) was loaded in a 50 mL, two-neck round-bottom flask equipped with a condenser and magnetic stirrer. An inert atmosphere was achieved by applying a vacuum and flushing using N₂ gas. Anhydrous dichloromethane (DCM, 20 mL) was injected and allowed for complete dissolution by stirring at 40 °C. After adding 1.43 mmol of (3-aminopropyl)trimethoxysilane, the mixture was allowed to stir for 20 h to obtain an orange-red

solution. DCM was removed after the reaction by rota-evaporation to get crude semi-liquid product and used as organosilica precursor.

4.2.2 Synthesis of N-incorporated mesoporous hybrid organosilica nanospheres (NPMO):

Typically, 0.5 g of CTAB was dissolved in a mixture of water and ethanol in the ratio of 2:1 in the presence of 2.5 mL of aqueous ammonia solution (25 wt%) and stirred for two hours. A premixed solution of organosilica precursor and TEOS in the ratios varied from 1:0, 1:1, 1:3, 1:5, and 1:10, in ethanol obtained after 0.5 h stirring was added in a drop-wise manner under stirring. After addition, the mixture was allowed for 24 h stirring at RT, a pale-orange colored residue was obtained, which was transferred into a Teflon-lined stainless-steel autoclave after dispersing in 15 mL of MQ water. The autoclave was hydrothermally heated at 100 °C for two days. The product obtained was filtered, washed, and dried at 60 °C for 12 h. The removal of surfactant CTAB was done by three repetitive solvent extractions using acidified ethanol at 60 °C. The final powder obtained after filtration, washing, and drying was labeled as NPMO support.

4.2.3 Pd nanoparticles supported NPMO nanosphere catalyst (Pd@NPMO): Palladium nanoparticles were supported on NPMO support through simple wet chemical reduction using NaBH₄ as a reducing agent. 100 mg of NPMO support was dispersed in water at RT, to which the calculated amount of Na₂PdCl₄ solution in water was added and stirred for one hour. Freshly prepared 3 mL, 1 M NaBH₄ solution was added slowly, and the reaction was allowed to stir for another 2 h. The obtained material was filtered, washed, and dried at 60 °C for 12 h to obtain Pd@NPMO catalysts. The Pd loading was controlled by varying the amount of Na₂PdCl₄ precursor. Pd@SBA-15 catalyst was also synthesized using the same protocol for control experiments, only changing the support NPMO with SBA-15. Small-sized, highly dispersed Pd nanoparticles on SBA-15 catalyst were used, labeled as Pd@SBA-15(DP), and synthesis was carried out using a reported modified deposition-precipitation protocol.²⁹

4.2.4 Catalysts Characterization

Powder X-ray diffraction (PXRD) analysis of all the synthesized materials was carried out on PANalytical X'pert Pro diffractometer with Cu K α radiation ($\lambda = 1.5406 \text{ \AA}$) operated at 40 kV and 30 mA. Fourier transform infrared (FTIR) spectra for the samples were collected on a Bruker Optics ALPHA-E spectrometer with universal Zn-Se attenuated total reflection accessory (ATR) with a Diamond ATR (Golden Gate) in 600 to 4000 cm⁻¹ range. Autosorb 1C Quantachrome,

USA, instrument was used to study the N₂ isotherms and pore-size distribution of the material. The analyses of the degassed samples at 100 °C for 4 h were run at liquid N₂ temperature. BET multipoint model was used to calculate the surface area at P/P₀=0.06–0.3 and BJH desorption model for pore size distribution. Thermogravimetric analyses were carried out under N₂ atmosphere on a TG50 analyzer (Mettler-Toledo) or SDT Q600 TG-DTA analyzer at a heating rate of 10 °C/min within 30–900 °C temperature range. XPS measurements for the catalyst were done on a Thermo Kalpha+ spectrometer using Al K α radiation with an energy of 1486.6 eV. All the spectra were charge corrected with reference to C1s at 284.6 eV. The peak fitting was carried out using CasaXPS software with Shirley-type background. The TEM images of the samples were recorded by FEI Tecnai TF-20 electron microscope, operating at 200 kV with LaB6 filament. SEM images obtained by dual-beam scanning electron microscope (FEI company, model Quanta 200 3D) operating at 30 kV with a tungsten filament. The solid-state NMR spectra for ¹³C and ¹⁵N nuclei were recorded on Jeol ECX-400 MHz spectrometer (100.6 MHz on solid 4 mm MAS probe). Magic-angle spinning (MAS) NMR spectra for ²⁹Si nuclei was recorded on BRUKER DSX300 spectrometer at 7.05 T (resonance frequencies 59.595 MHz, rotor speed 10000 Hz and 75.43 MHz, rotor speed 10000 Hz).

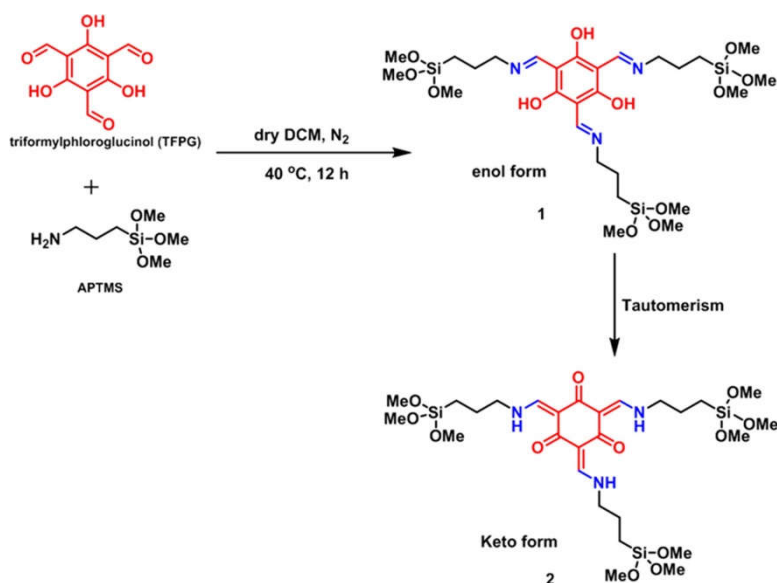
4.2.5 Catalytic studies on the hydrogenation of phenol: Typically, Pd catalyst (0.7 mol % Pd relative to phenol) was placed into a 20 mL Schlenk flask equipped with a magnetic bar and was purged with H₂ gas to exclude air. The catalyst was activated by heating at 100 °C under H₂ for 1 h. A mixture of phenol (0.53 mmol) and water (2 mL) was injected, and the reaction was conducted at 40 °C under 1 atm H₂ pressure for 16 h. H₂ gas was continuously supplied to maintain the pressure during the course of the reaction. After the reaction, the catalyst was filtered off, and the mixture was extracted with chloroform, and the products were analyzed by GC (Agilent 7890 connected with HP5 column and FID detector). The catalyst was collected by filtration for the recycling studies, washed, dried, and then reused in the next runs. A variety of phenol derivatives were used to examine the substrate scope for the aqueous phase hydrogenation under atmospheric H₂ pressure.

4.2.6 Aqueous phase catalytic hydrogenation of CO₂: The hydrogenation of CO₂ over Pd@NPMO catalysts was investigated in a high-pressure Parr 4848 autoclave (50 mL) equipped

with a mechanical stirrer and temperature controller. The reaction pot was charged with catalyst (20 mg) in aqueous KOH solution (0.5 M, 20 mL), and the autoclave was sealed and purged twice with CO₂ and H₂ gas mixture (1:3) to exclude air and pressurized to 4 MPa, and the reaction was carried out at 100 °C for 20 h. A range of experiments was carried out to optimize the reaction conditions by varying the reaction parameters. After the reaction, the catalyst was separated by simple filtration, and the product determination and quantification were carried out using HPLC (equipped with RID detector and a Rezex ROA-organic acid H⁺ column) by injecting authentic samples followed by standard calibration method and confirmed by liquid state ¹H and ¹³C NMR of the reaction mixture in D₂O. Gas effluents after the catalytic run were injected in the offline GC (equipped with TCD detector and carbosphere column) in order to detect the presence of any gaseous products. The reusability was checked after each run, where the separated catalyst was washed repeatedly with water and dried at 60 °C for 12 h.

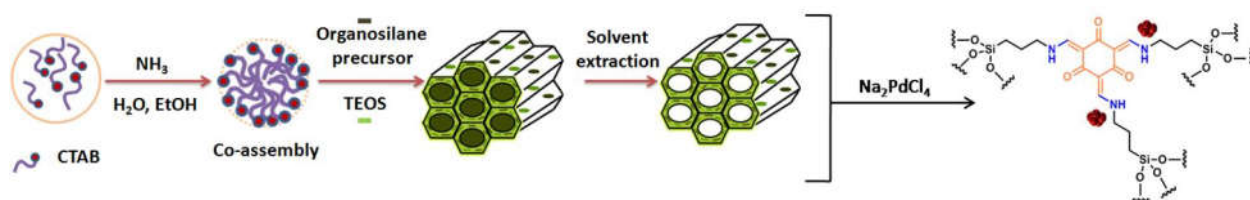
4.3 Results and Discussion

The N-containing tris-organosilane precursor was prepared by the silylation of trialdehyde, (1,3,5-triformylphloroglucinol) with (3-aminopropyl)trimethoxysilane through the Schiff-base reaction to yield enol-imine (Scheme 4.1, precursor-1), which can undergo tautomerism to the keto-enamine form (Scheme 4.1, precursor-2).²⁷ Synthesis of NPMO (Scheme 4.2) was done by the surfactant templated sol-gel strategy using the organosilane precursor-2 and tetraethyl orthosilicate (TEOS) by varying the molar ratio (organic silane precursor to TEOS ratio used 1:0, 1:1, 1:3, 1:5, and 1:10). The hydrolysis followed by the polycondensation of the methoxy groups in the silanes under basic conditions leads to forming an organic-inorganic hybrid silica framework. Uniformly distributed functionalities were obtained with the aid of a structure-directing agent, cetyltrimethylammoniumbromide (CTAB), and the powdered material was further extracted with an acidified ethanolic solution. In order to preserve the Si-C linkage during the condensation process, the precipitate obtained was centrifuged to remove the supernatant solution and was aged by dispersing in fresh Millipore water under moderate conditions.



Scheme 4.1: Synthesis of N-containing tris-organic silane precursor by reaction of 1,3,5-triformylphloroglucinol (TFPG) with (3-aminopropyl)trimethoxysilane.

In order to explore the hybrid NPMO material in catalysis, it was chosen as a platform for the stabilization of small, well-dispersed Pd nanoparticles. However, silica-based supports often suffer from weak nanoparticle interactions, leading to low metal loading and agglomerated particles due to sintering. Stabilization of monodispersed fine Pd nanoparticles on NPMO was achieved successfully through simple chemical reduction with NaBH₄ without any surfactant, expensive dendrimers, precipitating agents, or ligands. Using a similar synthesis methodology Pd was also supported over unmodified SBA-15 silica for the control experiment.



Scheme 4.2: Synthesis of Pd@NPMO hybrid silica catalyst.

4.3.1 N₂ Adsorption and Micro-elemental Analysis

The porosity and surface area of the hybrid silica was estimated by N₂ gas sorption analysis and carried out on the activated NPMO. The results showed a type-IV isotherm which is typical for mesoporous materials (Figure 4.1a). Using the BET model, the surface area for hybrid NPMO was calculated to be 823 m²/g, and the pore size distribution was calculated using the BJH desorption method, showing a peak maxima at a pore diameter of 2.6 nm.

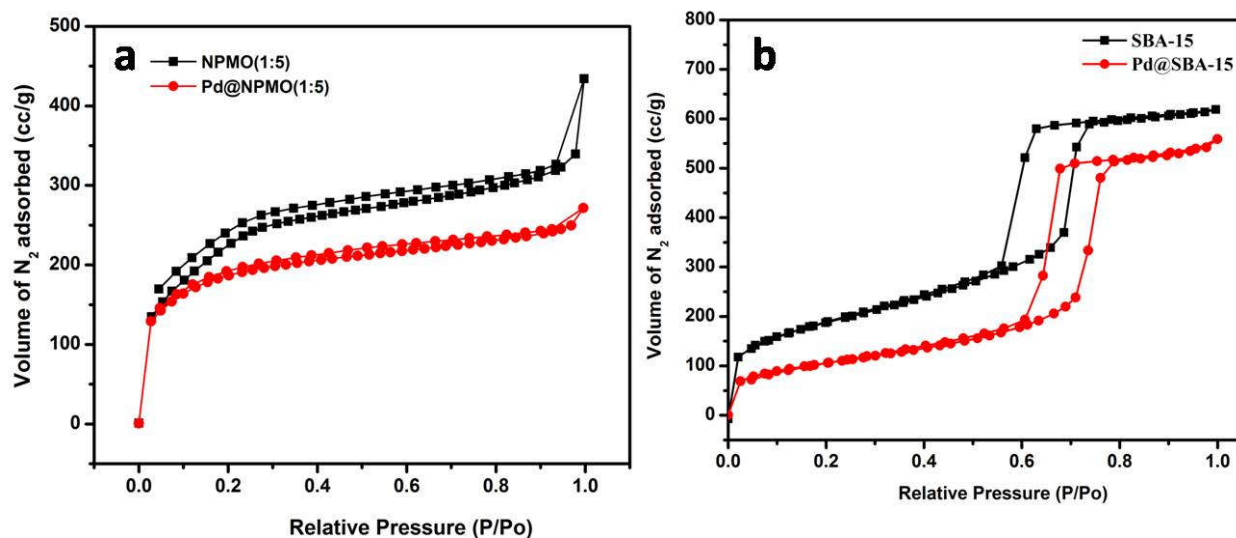


Figure 4.1: N₂ adsorption-desorption isotherms of Pd supported silica catalysts.

The extent of Pd loading on NPMO support was reflected in BET surface area measurements where the Pd@NPMO(1:5) (489 m²/g) decreased compared to pristine NPMO(1:5) (823 m²/g).

Table 4.1: Textural properties of different NPMO(x:y) hybrid silica supports. *determined from CHN elemental analysis.

Catalyst support	BET Surface area (m ² /g)	Pore diameter (nm)	N content* (%)
NPMO(1:0)	47	2.1	6.6
NPMO(1:1)	116	2	6
NPMO(1:3)	547	2.8	5.4
NPMO(1:5)	823	2.6	4.8
NPMO(1:10)	1149	2.5	3.1
SBA-15	710	6.2	-

This decrease in surface area is justified as the pore surface (fully or partially) in the NPMO is occupied by small Pd nanoparticles.³⁰ The N-content in the NPMO obtained was calculated to be 4.6 % from the CHN elemental analysis (see Table 4.1).

4.3.2 Thermogravimetric Analysis

Thermal stability of hybrid NPMO materials with varying amounts of organic moieties inside the hybrid silica framework was studied using thermogravimetric analysis (TGA). The organic bridging in the framework showed to be stable up to 300 °C under O₂

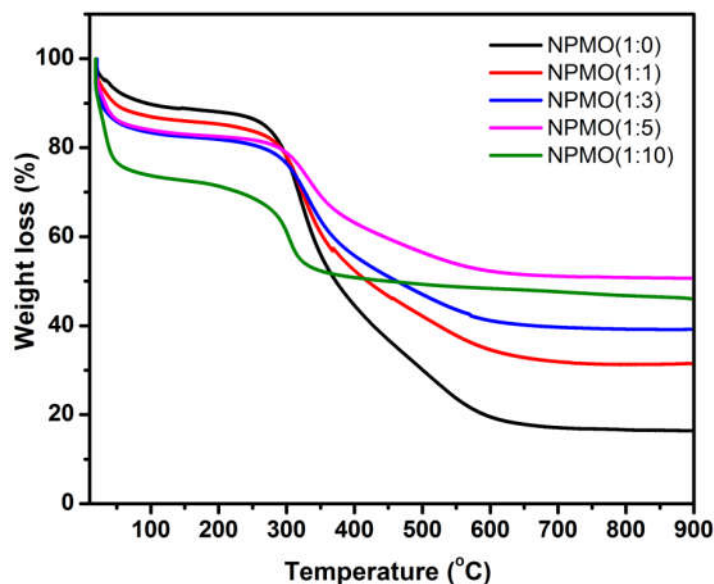


Figure 4.2: TGA study on various NPMO catalysts under O₂ atmosphere.

atmosphere and a considerable weight loss were observed at temperatures above 300 °C (Figure 4.2). The weight-loss trend observed from TGA goes well with the amount of organic silane loading in the support. The observed weight loss below 100 °C can be attributed to the adsorbed water molecules. As we increased the organic linker loading, a considerable decrease in the material affinity towards the water was observed, and a minimum was noticed for NPMO(1:0).

4.3.3 X-ray Diffraction

Small-angle XRD of Pd@NPMO catalyst with the high surface area is presented in Figure 4.3a, which reveals the diffraction peak at 2.5° due to a mesoscale periodicity of the NPMO material was retained even after the loading of Pd nanoparticles. The wide-angle PXRD (Figure 4.3b) patterns of Pd supported NPMO and SBA-15 catalysts showed a broad peak at 23°, indicating

the amorphous nature of the silica material, and the rest of the peaks are assigned to Pd (111), (200), and (220) planes. The particle size from Debye-Scherrer calculation showed crystallite size to be ~ 3 nm for Pd on NPMO hybrids and 7 nm on SBA-15. The PXRD profile confirms the ability of NPMO support to stabilize small-sized, uniformly dispersed Pd nanoparticles compared to Pd supported SBA-15 material.

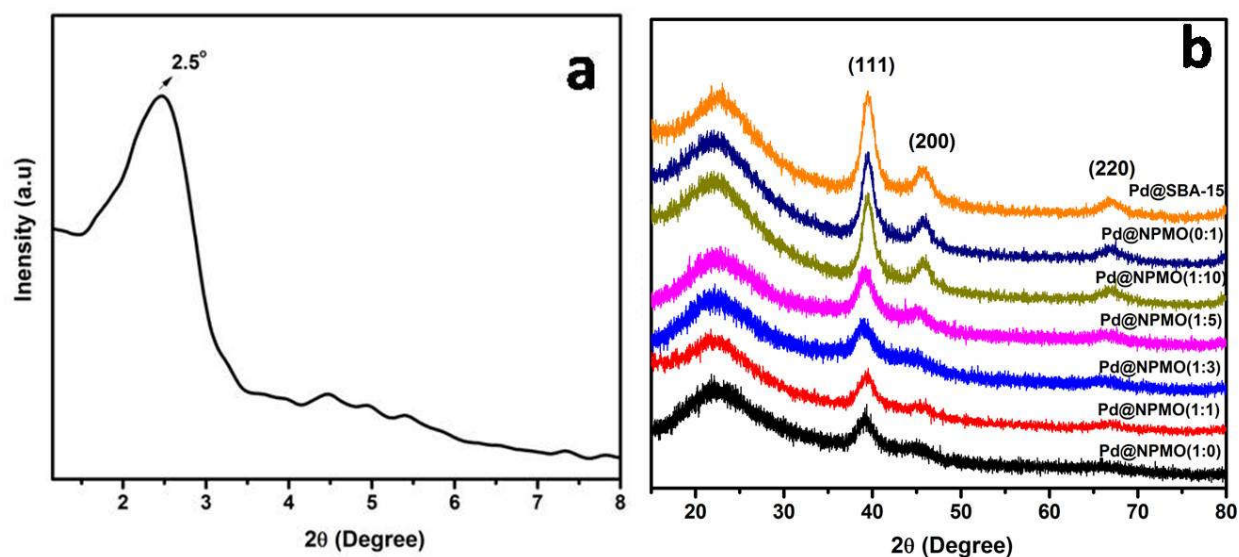


Figure 4.3: PXRD plots of Pd@NPMO catalysts (a) small-angle XRD of Pd@NPMO(1:5) and (b) wide-angle PXRD of Pd loaded NPMO catalysts.

4.3.4 FTIR- Spectroscopy

The formation of a keto-enamine framework in the hybrid NPMO was confirmed by FTIR spectroscopy. The FTIR spectra for the starting material trialdehyde (TFPG) showed the carbonyl stretching (C=O) band at 1642 cm^{-1} (Figure 4.4a).³¹ Most of the peaks in the FTIR spectrum of the NPMO silica (Figure 4.4c) matched well with the organic silane precursor-2 (NPMO precursor), which exists in the keto-form (Figure 4.4b). The C=O peak was observed at 1616 cm^{-1} and a strong peak at 1548 cm^{-1} from the C=C bond. The absence of a peak at 1642 cm^{-1} in the synthesized silane precursor and NPMO confirms the complete utilization of aldehyde during the Schiff-base reaction, which corroborated with the NMR results. The IR band for C–N at 1298 cm^{-1} in the silica framework showed the retention of the keto-form after the hydrolysis and polycondensation reaction at basic conditions while forming hybrid silica. The

band at 1075 cm^{-1} shows the Si–O–Si vibration from the framework, confirming a siliceous network formation in the material.

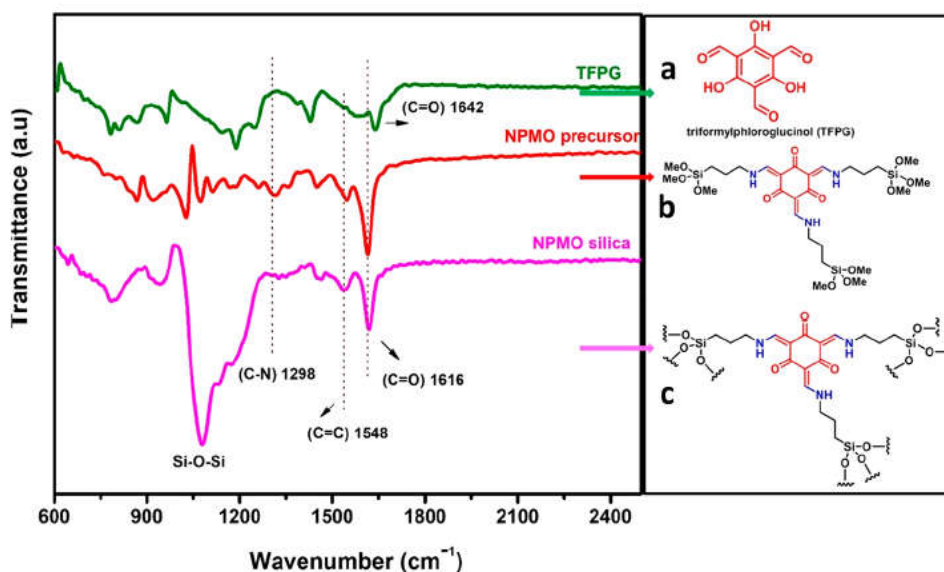


Figure 4.4: FTIR spectra of hybrid NPMO silica.

The presence of all the prominent peaks of NPMO in all ratios of organic precursor to TEOS in FTIR spectra confirmed that the chemical composition in the NPMO framework remained intact even after the strong treatment with NaBH_4 . The keto-enamine hybrid silica framework in all systems was confirmed from FTIR spectroscopy (Figure 4.5). As we increased the organic silane precursor concentration in the synthesis protocol, we observed the prominence of the Si-O-C ($\sim 1125\text{ cm}^{-1}$) vibrations compared to the Si-O-Si (1075 cm^{-1}), which confirmed the successful integration of the N-containing organic spacer inside the siloxane framework. Even after the immobilization of Pd nanoparticles on the NPMO support, the existence of the stretching vibrations for C=C ($\sim 1548\text{ cm}^{-1}$) and C-N ($\sim 1298\text{ cm}^{-1}$) confirmed that the high metal loading was occurred without hampering the initial NPMO architecture.

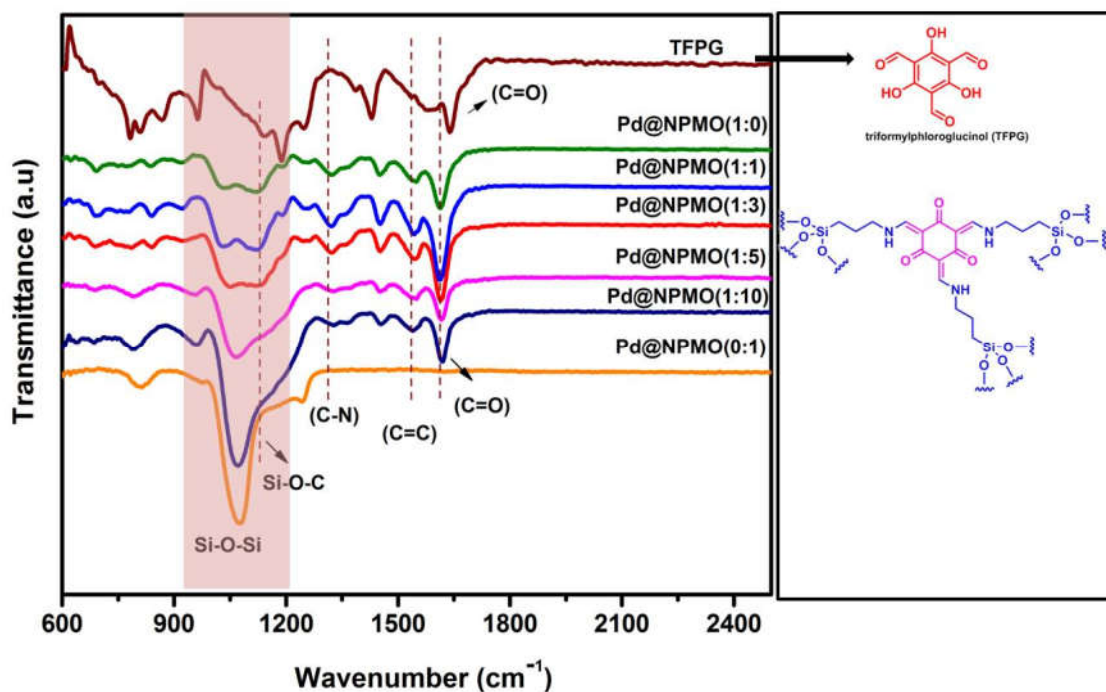


Figure 4.5: FTIR spectra of all Pd@NPMO hybrid catalysts.

4.3.5 Solid-state NMR Spectroscopy

The organic functionality in the mesoporous silica framework of NPMO material was confirmed by ^{13}C , ^{29}Si , and ^{15}N cross-polarization (CP) magic-angle spinning (MAS) NMR spectroscopy. The keto-form in the organic hybrid silica was established from solid-state ^{13}C NMR spectroscopy (Figure 4.6a). The resonance peak for the carbonyl carbon of the aldehyde in the starting material (TFGP) was observed at 192 ppm and was absent in the final NPMO silica material (Figure 4.6a), which indicates the complete consumption of the starting material during the Schiff-base reaction. The N-incorporated PMO clearly showed the signal corresponding to the carbonyl group at 184 ppm, which unambiguously confirmed the existence of keto-form. ^{13}C NMR of all ratios of the NPMO catalysts showed the carbon resonances from the organic moiety in the keto-form. In ^{29}Si NMR spectra (Figure 4.6b), the presence of two different types of Si environments in the framework was observed in the ranges from -90 to -113 ppm and -50 to -65 ppm corresponding to the Q^n sites and T^n sites, respectively.³² The peaks at -55 and -66 ppm in the T^n region represent the $\text{T}^2[\text{SiC}(\text{OSi})_2\text{OH}]$ and $\text{T}^3[\text{SiC}(\text{OSi})_3]$ linkages from the organic spacer bridge in the siliceous framework. The signals from the Q^n sites at -91, -100, and -110

ppm from $[\text{Si}(\text{OSi})_2(\text{OH})_2]$, $[\text{Si}(\text{OSi})_3(\text{OH})]$, and $[\text{Si}(\text{OSi})_4]$, respectively, were observed from the inorganic bridge in the framework. As we introduced TEOS in the hybrid NPMO synthesis showed the appearance of Q^n sites from the inorganic bridge in the framework, which increased gradually with the increase in TEOS loading (Figure 4.6b), which was well accordance with the FT-IR analysis.

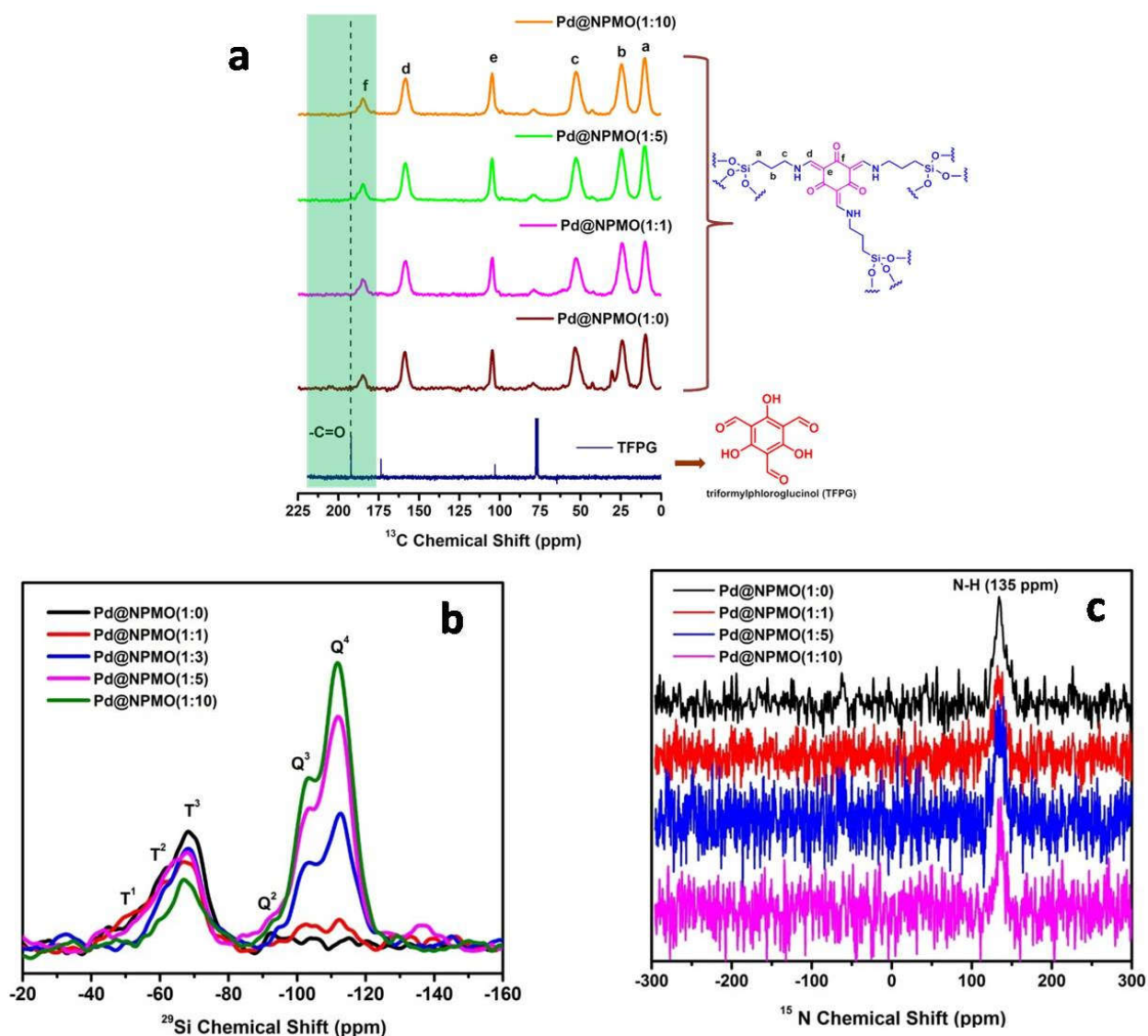


Figure 4.6: Solid-state NMR spectra of all Pd@NPMO catalysts (a) ^{13}C , (b) ^{29}Si , and (c) ^{15}N . Both ^{13}C and ^{29}Si NMR showed the successful integration of the keto-form of the organic silane into the hybrid silica through our optimized synthesis methodology. ^{15}N CP-MAS NMR spectra

of NPMO hybrid silica displayed a peak at 135 ppm chemical shift assigned to the N-H species in the organic bridging functionality (Figure 4.6c).³³ The N-H peak was visible due to the efficient ¹H cross-polarization effects. The absence of other peaks in Figure 4.6c further confirmed the absence of the NH₂ group from the starting APTMS. Thus, the Pd metal loading and NaBH₄ reduction did not destruct the framework architecture as confirmed from solid-state NMR studies (Figure 4.6c).

4.3.6 Electron Microscopy

The TEM images (Figure 4.7(a-d)) and Pd particle size distribution histogram (Figure 4.7(e-h)) of Pd supported hybrid silica materials confirm the spherical morphology of the NPMO hybrid silica support where the small-sized Pd NPs were stabilized. From the TEM image of Pd@NPMO(1:5), uniformly distributed Pd nanoparticles with an average particle size of ca. 2-5 nm was spotted on the spherical NPMO hybrid support. This was in line with XRD results. The NPMO support synthesized using 100 % organic tris-silica precursor [Pd@NPMO(1:0), Figure 4.8a)] showed poor metal dispersion and low surface porosity, which was per the surface area results.

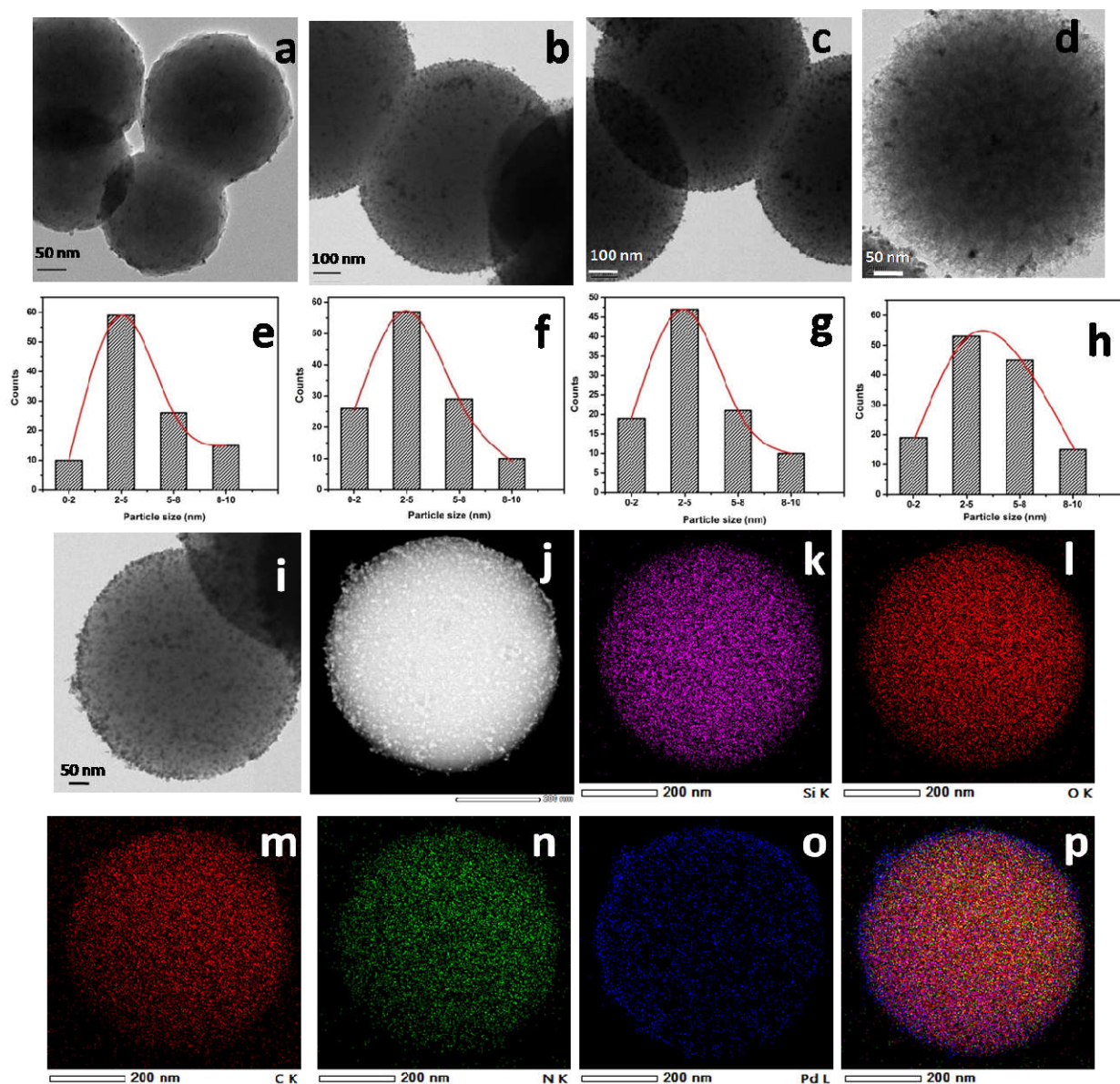


Figure 4.7: Characterizations of the Pd@NPMO(x:y) catalysts. TEM images of (a) Pd@NPMO(1:0) (scale 50 nm), (b) Pd@NPMO(1:3) (scale 100 nm), (c) Pd@NPMO(1:5) (scale 100 nm) and (d) Pd@NPMO(1:10) (scale 50 nm), Histogram showing the particle-size distribution from the TEM of (e) Pd@NPMO(1:0), (f) Pd@NPMO(1:3), (g) Pd@NPMO(1:5), and (h) Pd@NPMO(1:10). (i) High-resolution TEM image for Pd@NPMO(1:5) (scale 50 nm), (j) HAADF-STEM image of Pd@NPMO(1:5) (scale 200 nm). (k–p) STEM-EDX elemental mapping of the (k) Si K, (l) O K, (m) C K, (n) N K, (o) Pd L, and (p) overlay image.

The TEM image of the Pd@NPMO(1:10) (Figure 4.7d) also justifies the highly porous hybrid silica support, but the particle size of Pd was increased with the loss of metal dispersion (Figure 4.7h). STEM-HAADF analysis along with the EDX elemental mapping was carried out on Pd@NPMO(1:5) to confirm the well-dispersed small-sized Pd nanoparticles (Figure 4.7j) and organic bridging moieties in the hybrid silica support with extensive coverage. The narrow size distribution of Pd nanoparticles (2-5 nm) can be seen in hybrid NPMO material, along with the uniform distribution of C and N throughout the material were confirmed from the obtained color maps (Figure 4.7k-p).

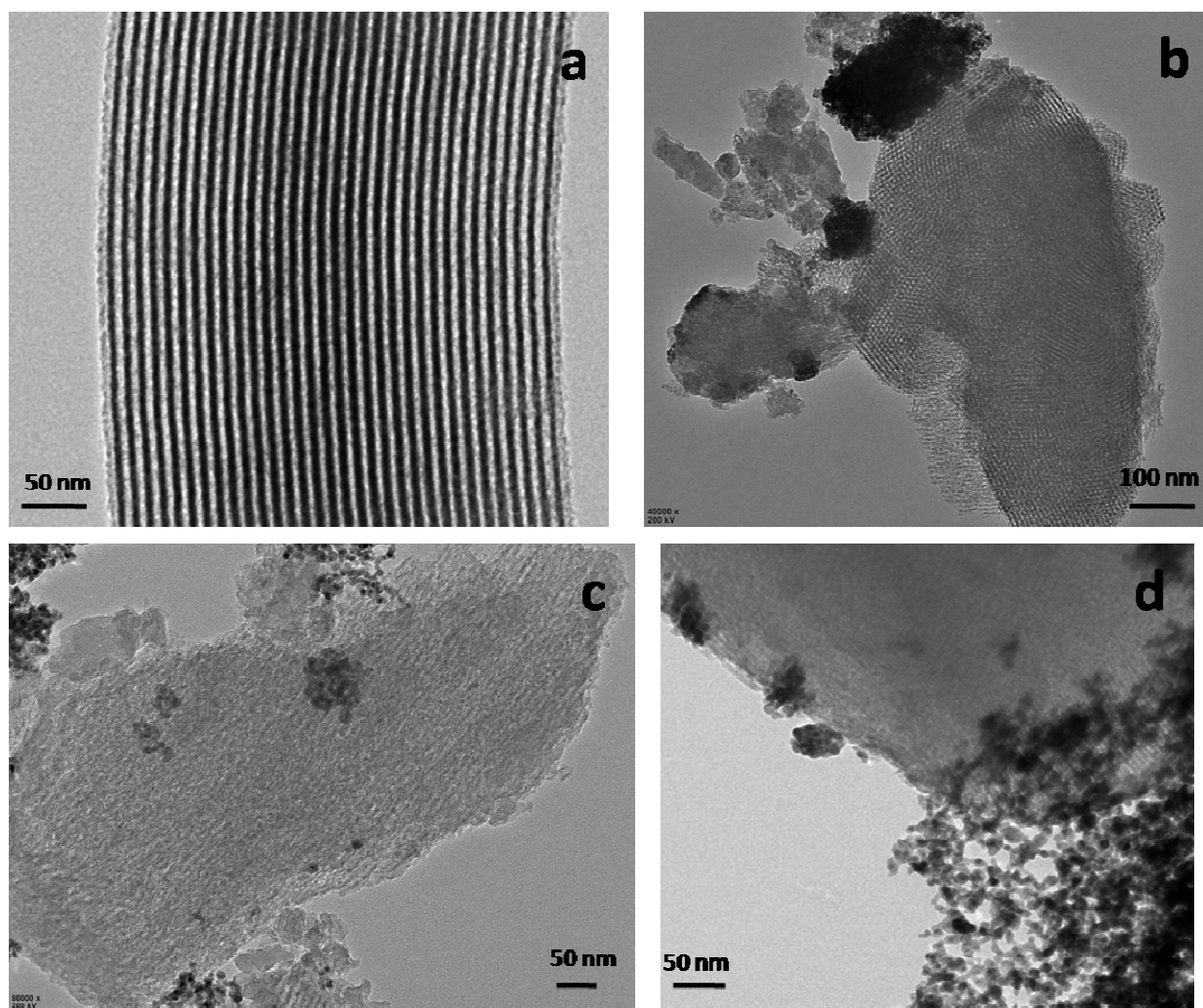


Figure 4.8: Transmission electron microscopy images of (a) SBA-15 (scale 50 nm) and (b-d) 5Pd@SBA-15 catalyst (scale 100, 50 and 50 nm, respectively).

From the TEM images of the 5Pd@SBA-15 catalyst (Figure 4.8), poor dispersion of Pd on the SBA-15 support due to agglomeration was visible, which clearly demonstrates the role of nitrogen in acting as a pseudo-ligand on the PMO matrix for stabilizing metal nanoparticles. Unsupported Pd NPs can also see clearly from Figure 4.8d, confirming the poor affinity of the bare silica for NPs. As a control experiment, well-dispersed small Pd nanoparticles on SBA-15 (Pd@SBA-15(DP)) were synthesized using a modified deposition–precipitation protocol and examined. The TEM results (Figure 4.9) showed the uniform-sized Pd nanoparticles (~ 3 nm) homogeneously dispersed on the long hexagonal channels of SBA-15.

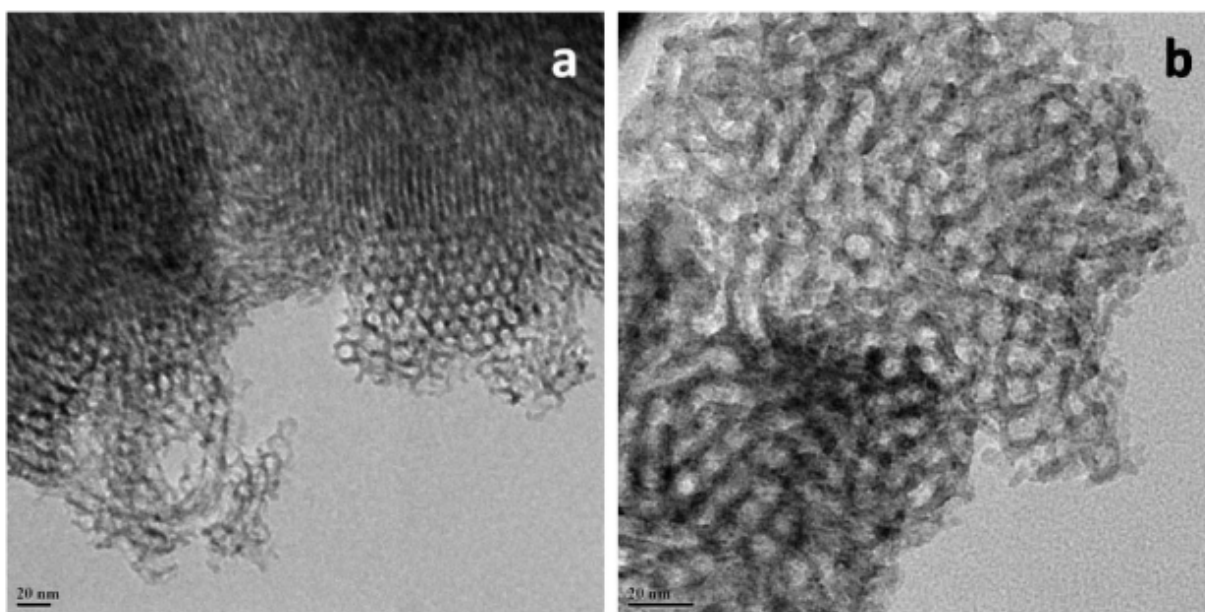


Figure 4.9: Transmission electron microscopy images of Pd@SBA-15(DP) catalyst show small, well-disposed Pd nanoparticles inside the SBA-15 channels.

From the FE-SEM image shown in Figure 4.10, Pd@NPMO samples with varying quantities of organic linker inside the framework majorly consist of spheres having an average particle size of ca. 250 nm.

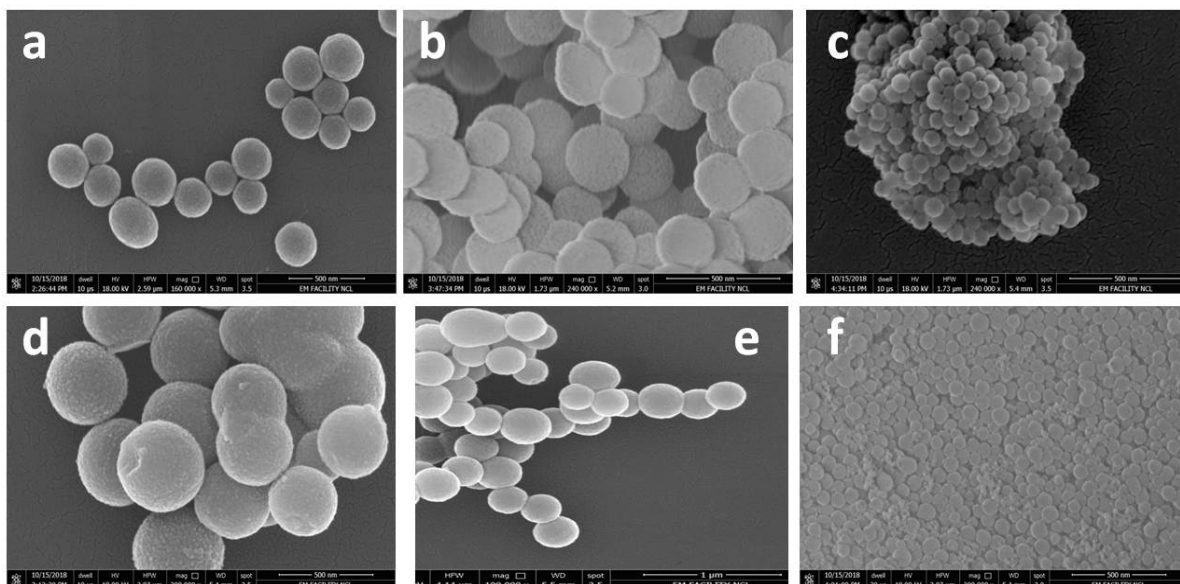


Figure 4.10: SEM images for Pd catalysts. (a) Pd@NPMO(1:0), (b) Pd@NPMO(1:1), (c) Pd-NPMO(1:3), (d) Pd-NPMO(1:5), (e) Pd-NPMO(1:10) and (f) Pd-SiO₂(0:1)

4.3.7 ICP-AES

ICP-AES analysis was done to estimate the loading of palladium in the Pd@NPMO and Pd@SBA-15 catalysts. The theoretical 5 and 7 wt % loading of Pd on NPMO catalysts was estimated from ICP to be 4.8 % and 6.9%, respectively. However, Pd on SBA-15 catalysts showed the Pd loading of 4.4 % for 5Pd@SBA-15 and 6.1 % for 7Pd@SBA-15, respectively. ICP analysis confirmed almost complete loading of Pd over NPMO support, whereas unmodified SBA-15 showed a weak affinity for Pd which resulted in the lower loading over SBA-15.

4.3.8 X-ray Photoelectron Spectroscopy

To garner insight into the nature of surface Pd species on the different ratios of NPMO hybrid silica support, XPS analysis has been carried out along with its quantification analysis (Figure 4.11). The XPS spectra of Pd in all supported NPMO catalysts showed two different peaks corresponding to 3d_{5/2} and 3d_{3/2}, which, after deconvolution, gave two different Pd components centered at 335 and 337 eV, which corresponds to metallic Pd and oxidized Pd states, respectively. It was observed that after the reduction of Pd with the same amount of NaBH₄ solution in all the hybrid catalysts showed different quantities of Pd⁰/Pd²⁺ species. This clearly

indicates the ability of hybrid NPMO support to influence the electronic states of surface Pd species. The relative percentage of Pd (0) and Pd (2+) species in the hybrid silica was found from the fitted peak area, which varied according to the concentration of bridged organic loading inside the framework.

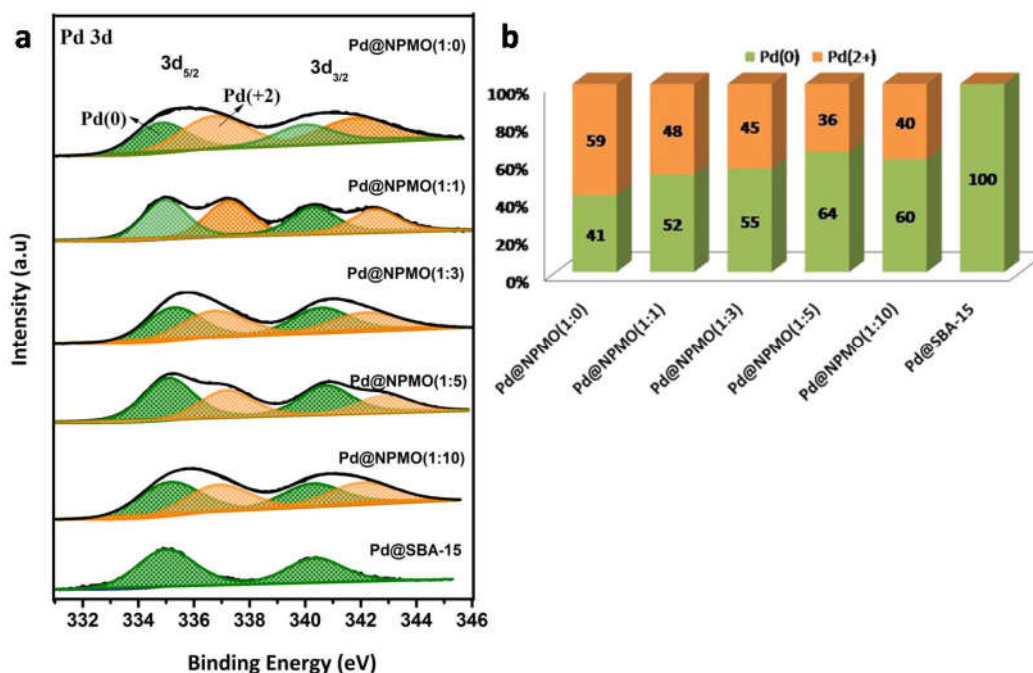


Figure 4.11: (a) Comparative XPS plots of (a) Pd@NPMO(x:y) and (b) comparison of % Pd species in Pd@NPMO(x:y) catalysts as calculated from XPS.

The Pd supported NPMO(1:0), 100 % organosilane bridged, showed a higher percentage of Pd(2+) species (59 %) which had higher N content (6.6 %). The predominance of the Pd (2+) species in catalyst points at the N-induced charge transfer from Pd to the NPMO hybrid silica.³⁴ As we dilute the tris-organosilane precursor with TEOS, we could observe a gradual switching in the surface Pd species from Pd(2+) to Pd(0). The Pd-supported SBA-15 material showed 100 % Pd (0) species compared to the hybrid silica system due to the absence of N sites. The deconvolution of N 1s spectra determined the chemical nature of N species in the hybrid silica and the major existence in N-H species (Figure 4.12).

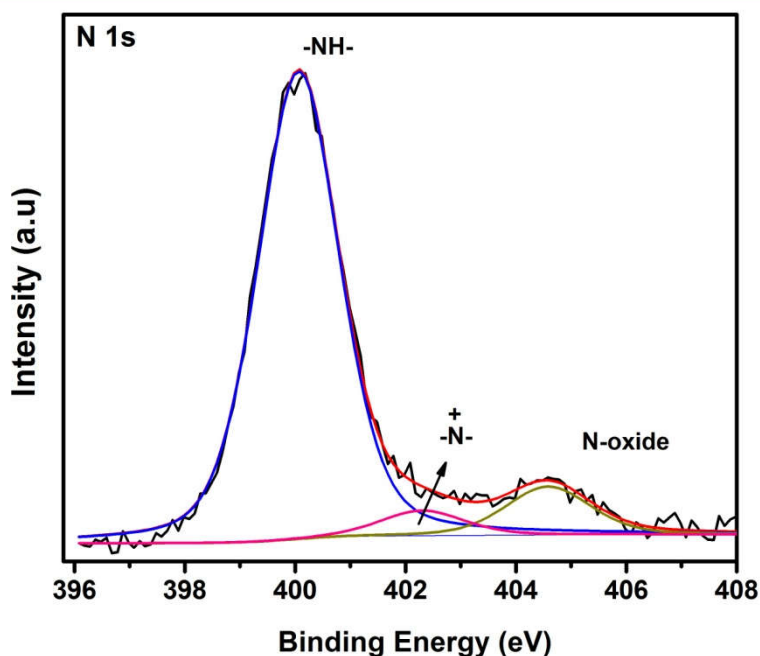


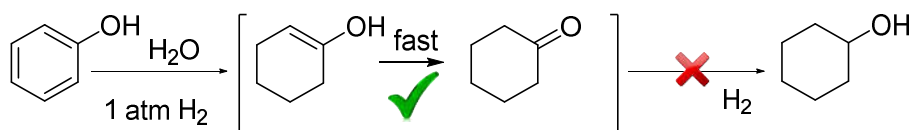
Figure 4.12: N1s spectrum of Pd@NPMO(1:5) catalyst.

4.3.10 Catalytic Activity

The synthesized Pd nanocatalysts were tested for aqueous phase phenol and CO₂ hydrogenation reactions. The details of the reaction procedures have been provided in the experimental section of this chapter. The catalytic performance of Pd on hybrid silica catalyst has been discussed in the two sections of this chapter as 4A and 4B for phenol hydrogenation and CO₂ hydrogenation reactions, respectively.

Part 4A: Pd-NPMO catalyzed low-temperature and atmospheric pressure phenol hydrogenation reaction.

Phenol hydrogenation is an industrially crucial catalytic process due to the formation of compounds like cyclohexanone. Typically cyclohexanone is used in the synthesis of caprolactam and adipic acid to produce nylon-6 and nylon-66, respectively, whereas cyclohexanone derivatives were utilized for chiral tacrine and cyclohexanone imines.^{35, 36} Generally, a commercial preparation of cyclohexanones has done either via cyclohexane oxidation or phenol hydrogenation which requires very harsh reaction conditions and also suffers from low yield and low selectivity.^{37, 38} Hence the selective synthesis of cyclohexanone and its derivatives through the hydrogenation of phenolics is a highly appreciated industrial process through the utilization of biomass-derived renewable feedstocks like lignin. For this purpose, many homo- and hetero-tagged catalysts have been developed in the past and screened for liquid phase phenol hydrogenation in order to offer cost and energy assets.³⁹⁻⁴⁴ Improved phenol conversion can be achieved at the higher reaction temperature; however, thermodynamically favored cyclohexanol formation occurs through the over hydrogenation of cyclohexanone. Hence, pausing the reaction at high cyclohexanone selectivity with an adequate phenol conversion within a single step is challenging. Tailoring of new Pd catalysts for the low-temperature liquid-phase hydrogenation of phenol was remarkably exemplified by Liu and co-workers displaying high conversion and cyclohexanone selectivity on a dual-supported Pd Lewis acid catalyst at 50 °C and 10 bar H₂ pressure.⁴⁵ However, the use of soluble Lewis acids such as AlCl₃ for hydrogenation reactions imposes severe limitations in the catalytic process technology. Later, notably, some researchers developed very few Pd-based catalysts promising phenol hydrogenation catalysis even at room temperature and atmospheric H₂ pressure in an environmentally green solvent like water (Scheme 4A.1).⁴⁶



Scheme 4A.1: Reaction pathway for atmospheric pressure selective hydrogenation of phenol to cyclohexanone in water.

Notably, some previous research activity on the catalytic hydrogenation of phenol have shown the key role of the surface chemistry of the support, which majorly influences the product distribution, mainly the chemisorbed phenol on the support reacts with the metal activated hydrogen, usually on Pd sites, yielding the products.⁴⁷ Generally suggested that the non-planar mode of phenol adsorption over basic sites lead to yield cyclohexanone whereas the coplanar adsorption on acidic sites results in the cyclohexanol and cyclohexane formation.^{16, 48-50}

4 A.1 Catalytic Hydrogenation of Phenol

Phenol was chosen as a model substrate to estimate the catalyzing ability of Pd@NPMO hybrid silica catalysts. Requisite quantities of the synthesized Pd catalysts were charged, and the reaction parameters were optimized accordingly. Table 4A.1 summarizes the activity profile on various Pd@NPMO materials under similar reaction conditions. The conversion of phenol over Pd@NPMO(1:0) catalyst displayed much lower activity (32 % conversion) with the cyclohexanone selectivity (99 %). A gradual increase in phenol conversion was observed on the Pd supported hybrid NPMO catalysts as we increased the dilution with TEOS precursor and reached a maximum for Pd@NPMO(1:5) (100 % conversion) and further increase showed a decline in the catalytic activity. A complete conversion was observed on the Pd@NPMO(1:5) catalyst without compromising cyclohexanone selectivity at 40 °C and 1 atm H₂ pressure in water. As a control experiment, we compared the activity with the Pd@SBA-15 catalyst, where Pd loading was carried out using a similar synthesis procedure. Under the optimized reaction conditions, Pd@SBA-15 having the larger Pd nanoparticles (TEM analysis) with 100 % metallic Pd species (XPS analysis) showed only 6 % phenol conversion with good selectivity towards cyclohexanone. To further emphasize the role of hybrid NPMO support in low temperature and atmospheric H₂ pressure phenol hydrogenation reaction in water, we used small-sized Pd nanoparticles stabilized on SBA-15, [Pd@SBA-15(DP)], which was synthesized using a previously reported modified deposition-precipitation method and employed for phenol hydrogenation catalysis.²⁹ Results showed a conversion of 32 % with a cyclohexanone selectivity of 80 %, along with the formation of an over hydrogenation product, cyclohexanol (20 %).

Table 4A.1: Hydrogenation of phenol on Pd supported silica catalysts in water.

Entry	Catalyst	Phenol Conversion (%)	Cy-one (%)	Cy-ol (%)
1	Pd@NPMO(1:0)	32	99	1
2	Pd@NPMO(1:1)	39	99	1
3	Pd@NPMO(1:3)	83	99	1
4	Pd@NPMO(1:5)	100	99	1
5	Pd@NPMO(1:10)	90	98	2
6	Pd@SBA-15	6	92	8
7	Pd@SBA-15(DP)	30	80	20
8	Pd/C	23	96	4

Reaction conditions: Substrate (0.53 mmol), catalyst (0.7 mol % Pd relative to substrate), H₂ (1 bar pressure), water (2 mL), T (40 °C) and t (16 h).

To optimize the reaction process, a detailed reaction parameter study was carried out (Figure 4A.1). The temperature scan on Pd@NPMO(1:5) catalyst demonstrated the role of a hybrid organosilica framework in stabilizing Pd nanoparticles and enhancing the hydrogenation catalysis. The catalyst was active even at a low temperature (40 °C), showing conversion of 48 % and complete selectivity towards cyclohexanone within 6 h under the atmospheric H₂ pressure. Further increasing the reaction temperature increased the rate of hydrogenation catalysis and reached full conversion at 100 °C within 6 h along with the formation of the side product cyclohexanol. The reaction at >100 °C showed a drop in cyclohexanone selectivity and the formation of an over hydrogenated cyclohexanol product. The kinetics of the phenol hydrogenation reaction through time-on-stream analysis (Figure 4A.1b) was studied on Pd@NPMO(1:5) at 40 °C and 1 atm H₂ pressure. It was found that 16 h of reaction was enough for the complete conversion of phenol to yield cyclohexanone selectively.

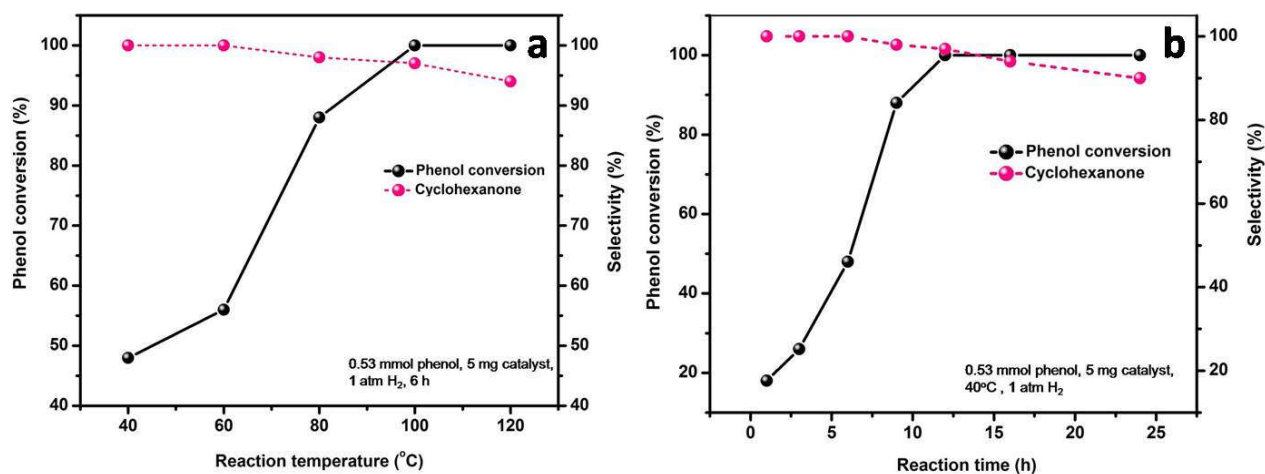
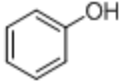
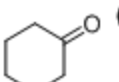
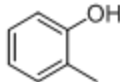
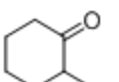
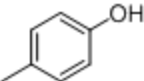
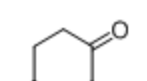
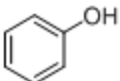
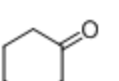
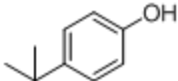
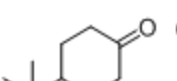
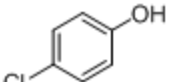
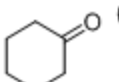


Figure 4A.1: Optimization of reaction parameters for the reduction of phenol. (a) the reaction temperature and (b) reaction time.

A substrate scope study was carried out to extend the applicability of Pd@NPMO(1:5) hybrid catalyst in hydrogenation catalysis, and the results are tabulated in Table 4A.2. As expected, all the phenolic substrates gave both excellent conversion and selectivity to corresponding cyclohexanone products in the aqueous medium. It was methyl phenol (Table 4A.2, entry 2) that showed a comparatively lower hydrogenation rate of reaction due to the steric-hindrance effect of methyl group on the phenol ring. Similar trend was also observed for p-tertiary phenol (Table 2, entry 5), whereas all other substrates showed above 90 % conversion with very high selectivity for cyclohexanone derivatives under atmospheric H₂ pressure.

Table 4A.2: Hydrogenation of phenol derivatives on Pd@NPMO(1:5) catalyst in water.

Entry	Reactant	T (°C)	t (h)	Conv. (%)	Product sel. (%)
1.		40	12	100	 (99 %)
2.		85	16	72	 (93 %)
3.		85	16	90	 (98 %)
4.		85	16	92	 (92 %)
5.		95	24	64	 (86 %)
6.		85	16	96	 (79 %)

Reaction conditions: Substrate (0.53 mmol), Pd@NPMO(1:5) (1.4 mol % relative to substrate), H₂ (1 bar pressure), water (2 mL).

A recycling study was carried out to assess the stability of Pd@NPMO(1:5) in the aqueous phase selective hydrogenation of phenol, and the results are given in Figure 4A.2a. The catalyst showed no loss in activity even after the four consecutive catalytic runs, and the separated catalyst was examined using TEM (Figure 4A.2b). No noticeable change was observed in the TEM image of the recycled catalyst compared to the fresh Pd@NPMO(1:5) catalyst, along with the retention of small Pd nanoparticles (2-5 nm) on the spent catalyst.

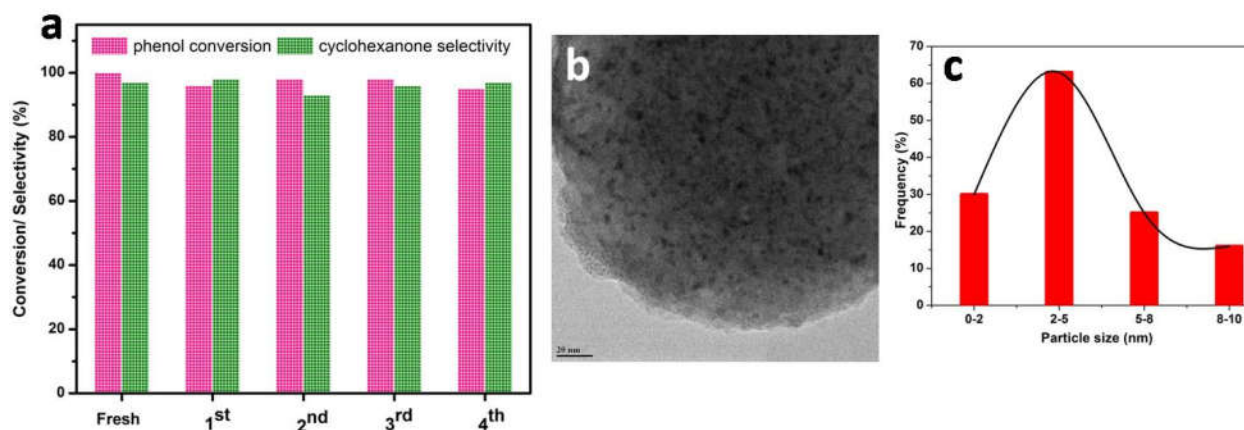


Figure 4A.2: (a) catalytic activity plot showing the recycling study on the Pd@NPMO(1:5) catalyst (b) TEM of spent Pd@NPMO(1:5) catalyst after three cycles of the catalytic run, (c) histogram showing the Pd particle-size distribution over the spent Pd@NPMO(1:5) catalyst.

From XPS, the quantity of Pd(0) species on the spent catalyst has increased to 78 % after the three cycles of the catalytic run at 40 °C and 1 atm H₂ pressure (Figure 4A.3). Hence the Pd 3d XPS measurements on the Pd@NPMO(1:5) spent catalyst confirmed the significant Pd species on the active surface exists as Pd(0), which retains the catalytic cycle even after three cycles.

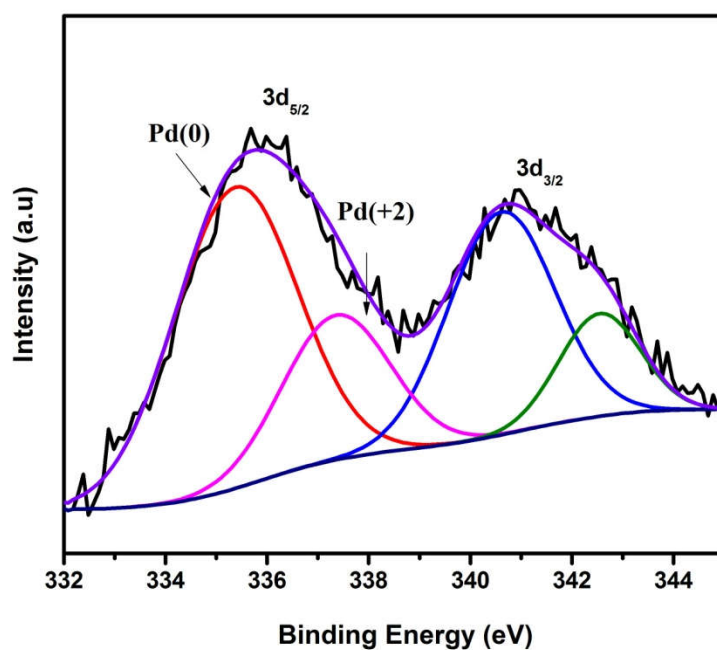
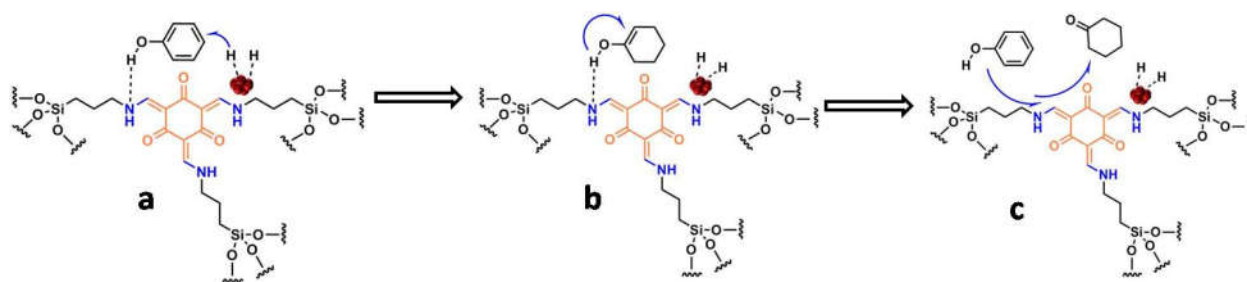


Figure 4A.3: Pd 3d XPS spectrum for spent Pd@NPMO(1:5) catalyst.

A plausible reaction pathway was depicted in Scheme 4A.2, showing the sequence of events involved during the Pd@NPMO mediated phenol hydrogenation to selectively synthesize cyclohexanone. One noticeable property of the hybrid NPMO support is that it carries an in-built framework N-H group, which acts as basic centers on the catalyst surface, which may be employed for the selective adsorption of phenol molecules by an acid-base interaction. Amine functionalized mesoporous silica has been reported to be an efficient adsorbent for phenols in aqueous media compared to bare silica material.^{51, 52} Hence the synergy between the hybrid organosilica support and small-sized Pd(0) active centers play a crucial role in the enhanced hydrogenation catalysis of phenol to selectively yield cyclohexanone under mild conditions in an aqueous medium.



Scheme 4A.2: Proposed reaction mechanism explaining the role of bridged N-containing organic moiety in Pd@NPMO catalyst for low-temperature selective hydrogenation of phenol to cyclohexanone.

Depending on the nature of the catalytically active surface, the mode of interaction of phenol can vary, and in this case, it may occur through the O-H---N interactions. As reported and proved in the previous literature, a non-planar mode of adsorption is preferred by phenol over basic sites.⁴⁹ Initially, the phenol can be certainly adsorbed on the Pd@NPMO surface in a non-planar fashion, and the gaseous H₂ can get activated on the support induced small Pd nanoparticles (Scheme 4A.2a). The partially hydrogenated enol form from phenol rapidly isomerized to cyclohexanone (Scheme 4A.2b). The weakly bonded cyclohexanone will be quickly replaced from the Pd@NPMO surface, which hinders the over hydrogenation of cyclohexanone to cyclohexanol (Scheme 4A.2c). The adsorption-desorption strength of molecules on hybrid NPMO materials determines hydrogenated phenol products selectivity over conventional supported catalysts.

Part 4B: Aqueous-phase hydrogenation of CO₂ to formate on Pd-NPMO catalysts

Catalytic chemical transformation of CO₂ is an excellent alternative for producing fuels and platform chemicals that minimize our huge dependence on carbon-rich fossil fuels. Among the various approaches for CO₂ valorization, catalytic hydrogenation has been regarded as the most promising route to achieve this goal. Industrially, CO₂ has been converted at elevated temperatures (200-300 °C) and pressures (50-100 bar) using a conventional Cu/ZnO/Al₂O₃ catalyst to produce methanol.⁵³⁻⁵⁵ Such harsh reaction conditions are required because of the chemically inert and thermodynamically stable nature of the CO₂ molecule.⁵³ Out of the several platform compounds from CO₂, the most targeted molecules are methanol,⁵⁶ formate/formic acid,⁵⁷ and dimethyl ether,⁵⁸ due to the value addition of these molecules in the energy sector worldwide. Formic acid (FA) with a 4.4 wt % theoretical hydrogen content and volumetric storage density of 53 g H₂/L is regarded as a promising liquid organic hydrogen carrier (LOHC). The other advantages are stable, less toxic, biodegradable, and easy to store and transport.⁵⁹ Currently, the requirement for HCOOH is industrially met via carbonylation of CH₃OH to HCOOCH₃ followed by its hydrolysis.⁶⁰ Furthermore, the consumption of HCOOH and its salts in the direct formic acid fuel cells (DFAFCs)⁶¹ makes their production more pronounced from a C1 carbon source like gaseous CO₂ making the approach green and cyclic.

In the past decades, a variety of homogeneous and heterogeneous catalysts were designed and examined for the catalytic reduction of CO₂ to formate/formic acid.⁶²⁻⁶⁴ One among the strategies to overcome the exergonic thermodynamic limitations ($\Delta G^0 = -9.5 \text{ kJmol}^{-1}$ in water and at room temperature) in liquid phase CO₂ hydrogenation is the use of suitable bases.⁶⁵ A variety of heterogeneous catalysts containing nitrogen atoms either in the form of metal nitrides⁶⁶ or in supports have been reported to improve the activity. Similarly, N-heterocyclic carbenes,⁶⁷ ionic liquids,⁶⁸ carbon nitride,⁶⁹ and amine-functionalized silica⁷⁰ combined with noble and non-noble metals such as Co, Ir, and Ru bimetallic PdAg have been reported. Recently, Liu et al. reported a urea-derived framework (PMO-UDF) exhibiting an enhanced CO₂ capture property with its catalytic conversion to cyclic carbonates by reacting with epoxides under mild conditions.⁷⁰ The photocatalytic CO₂ reduction using modified PMO containing immobilized ruthenium complexes as photosensitizing sites was also reported recently.⁷¹

4 B.1 Aqueous phase catalytic hydrogenation of CO₂

The catalytic properties of synthesized Pd@NPMO material and other control samples were evaluated for the aqueous phase CO₂ hydrogenation reaction. When the reaction was carried out with 5Pd@NPMO under 4 MPa, (CO₂/H₂ = 1:3) at 100 °C, 6.3 mmol of formate was generated after 20 h in 0.5 M KOH aqueous solution. The ¹H and ¹³C NMR analyses of the reaction mixture after 20 h evidenced the formation of formate as the only liquid product under our optimized reaction conditions. Interestingly, no gaseous CO₂ hydrogenation products like CO and methane were detected during the catalytic run, which implies the complete selectivity for the direct synthesis of formate on 5Pd@NPMO, making separation of products effortless. To the best of our knowledge, this is the first time demonstrating the catalytic utilization of Pd nanoparticles on chemically modified PMO in the selective CO₂ reduction to formate with a good yield under mild conditions. In order to highlight the role of N-incorporation in a periodic mesoporous hybrid silica matrix in CO₂ catalysis, reactions were also performed under similar conditions using Pd on SBA-15 (5Pd@SBA-15), which produced only 0.9 mmol of formate.

Table 4B.1: CO₂ hydrogenation catalyzed by Pd@NPMO^a

Entry	Temp (°C)	Formic acid^[e]/ mmol	TOF^[f] (h⁻¹)
1	60	2.2	38
2	80	4.1	71
3	100	6.3	108
4	150	4.8	83
5 ^[b]	100	8.2	140
6 ^[c]	100	n.d	-
7 ^[d]	100	n.d	-

^a Reaction conditions: 5Pd@NPMO catalyst (20 mg), aqueous KOH solution (20 mL, 0.5 M), CO₂:H₂ (1:3, 4 MPa), time (20 h). ^b Aqueous KOH (20 mL, 1 M). ^c Only using H₂ (4 MPa). ^d Without catalyst. ^e Determined by HPLC. ^f Determined from [moles of formate formed]/[mole of active Pd sites in catalyst per hour]. The number of moles of active Pd sites was determined from ICP OES and CO chemisorption.

TOF was calculated for 5Pd@NPMO and 5Pd@SBA-15 catalysts and gave 108 and 9.4 h⁻¹, respectively. The active metal exposed for the reaction obtained using the ICP-OES and percentage metal dispersion from CO chemisorption was used for calculation. To confirm the positive effect of the N moiety from the PMO framework on enhancing the CO₂ hydrogenation to formate, we carried out the reaction using the Pd@SBA-15(DP) catalyst, which had a narrow particle size distribution (~ 3 nm) along with an excellent dispersion on the SBA-15 support. This catalyst showed a TOF of only 25.6 h⁻¹, emphasizing the importance of N incorporation. Even under a reaction temperature of 60 °C, using a 5Pd@NPMO catalyst yielded 2.2 mmol of formate with a TOF of 38 h⁻¹ showing the ability of the material to activate the reactants at a much lower temperature. Further, increasing the CO₂ reduction temperature from 100 to 150 °C resulted in the decline of activity to TOF 83 h⁻¹. This can be attributed to the structural deformation of the hybrid framework during the reaction under a 0.5 M KOH aqueous solution, which led to the Pd particle agglomeration (Figure 4B.1).

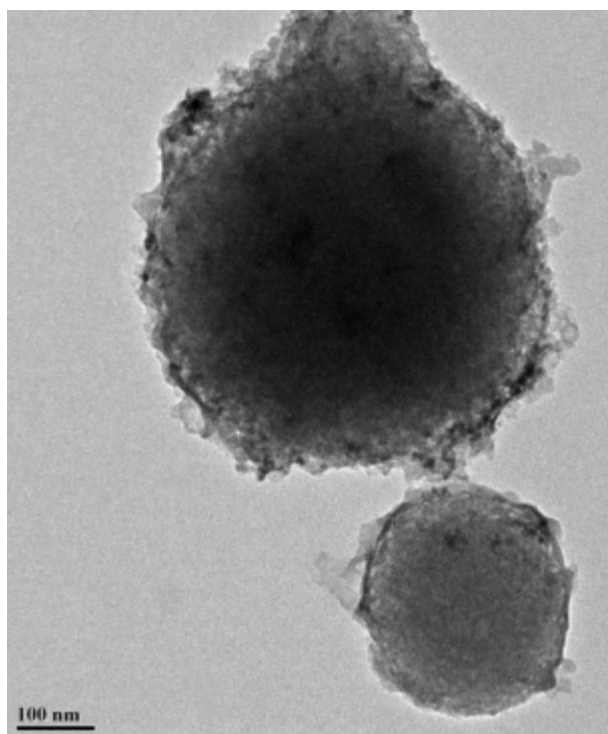


Figure 4B.1: Transmission electron microscopy images of spent 5Pd@NPMO catalyst after reaction at 150 °C for 20 h in 0.5 M aqueous KOH solution.

The control experiments confirmed no formate being produced in the absence of a catalyst (Table 4B.1, entry 7), and also no carbon moiety from the hybrid catalyst framework was utilized in the formate formation as ensured by carrying the reaction only in H₂ pressure (4 MPa) (Table 4B.1, entry 6). The effect of the base concentration on CO₂ hydrogenation was studied, and the results showed that by increasing 0.5 M KOH aqueous solution to 1 M, the TOF for formate on the 5Pd@NPMO catalyst increased from 108 to 140 h⁻¹ (Table 4B.1, entry 5 and Figure 4B.2) confirming the role of base in the reaction. The reaction in the absence of base did not yield appreciable formic acid from CO₂ under our reaction conditions, implying the vital role of a basic medium to improve the reaction by stabilizing HCOOH in the form of formate salts well as the solubility of gaseous reactants in water.^{72, 73}

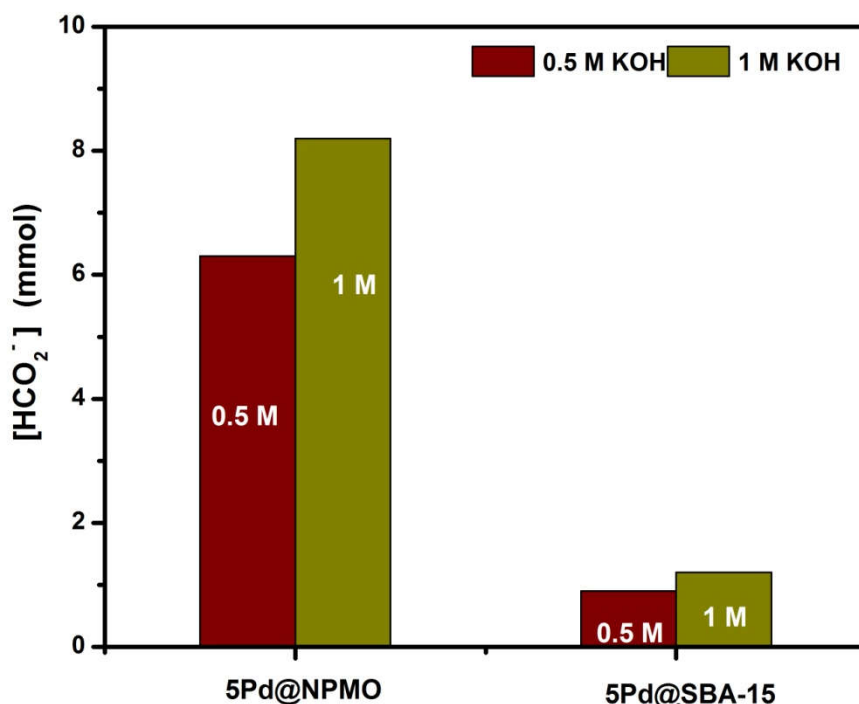


Figure 4B.2: Effect of KOH conc. in CO₂ hydrogenation on Pd catalysts. Reaction conditions: Catalyst (20 mg), aqueous KOH solution (20 mL, 0.5/1 M), CO₂:H₂ (1:3, 4 MPa), time (20 h), and temperature (100 °C).

Screening of different Pd catalysts on both NPMO and SBA-15 for CO₂ hydrogenation was carried out, and the results showed the promising effect of NPMO support for the reaction (Figure 4B.3a). Even the 2 % Pd loaded NPMO (2Pd@NPMO) catalyst showed 3.1 mmol of

formate formation, which is much higher compared to the Pd@SBA-15 catalysts. During the course of the reaction (Figure 4B.3b), the 5Pd@NPMO catalyst showed a linear increase in formate (6.9 mmol) production, where the TOF increased up to 108 h^{-1} in 20 h and decreased to 99 h^{-1} by further increasing the reaction time to 24 h. Hence, the reaction time was optimized to 20 h for further studies, and the heterogeneous nature of the Pd@NPMO catalyst was studied by the hot-filtration method under the optimized reaction conditions. After 12 h (3.5 mmol formates produced), the catalyst was filtered off, and the filtrate was allowed to proceed further for the CO_2 hydrogenation reaction for the remaining 12 h under identical conditions. No increase in the formate yield was observed, maintaining the 3.5 mmol in the reaction medium, suggesting that the catalysis is purely heterogeneous (Figure 4B.4a).

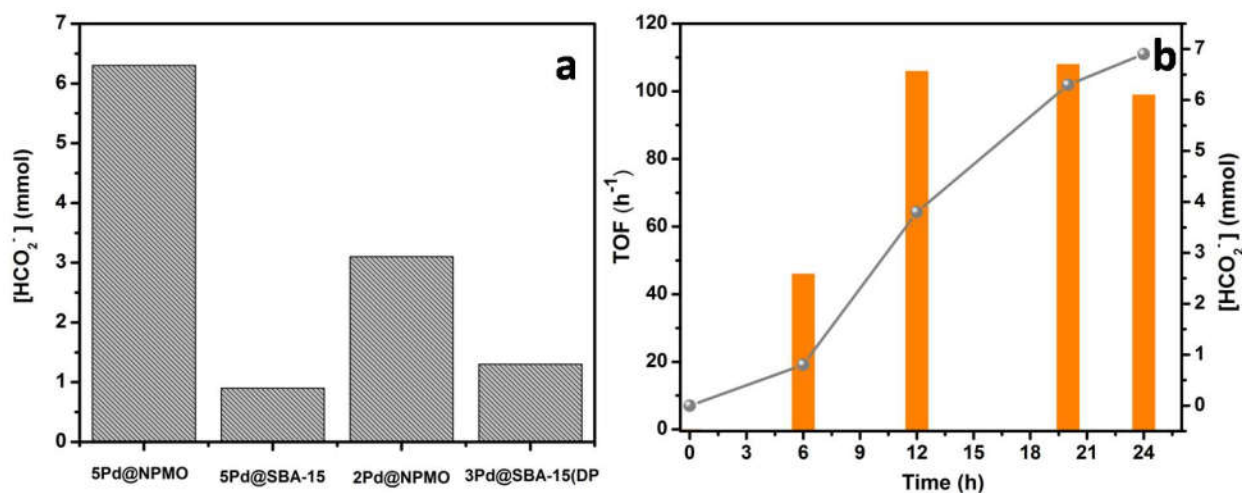


Figure 4B.3: (a) Screening of CO_2 reduction to formate on various Pd catalysts to highlight the effect of N-incorporation in the hybrid PMO. (b) Time courses of CO_2 hydrogenation to formate catalyzed by 5Pd@NPMO. Reaction conditions: Catalyst (20 mg), aqueous KOH solution (20 mL, 0.5 M), $\text{CO}_2:\text{H}_2$ (1:3, 4 MPa), temperature (100°C), and time (20 h).

In order to confirm the reusability and stability of the Pd@NPMO catalyst, the reaction was performed for two consecutive runs by using the recovered catalyst after the fresh run. As shown in Figure 4B.4b, the first run of the recovered 5Pd@NPMO catalyst produced 5.8 mmol of formate, indicating a negligible decrease in the yield compared to the fresh reaction. But the consecutive second cycle showed a dip in the formate production to 3.8 mmol. Further, spent

catalyst analysis was carried out to investigate the cause for a decrease in activity after the second run.

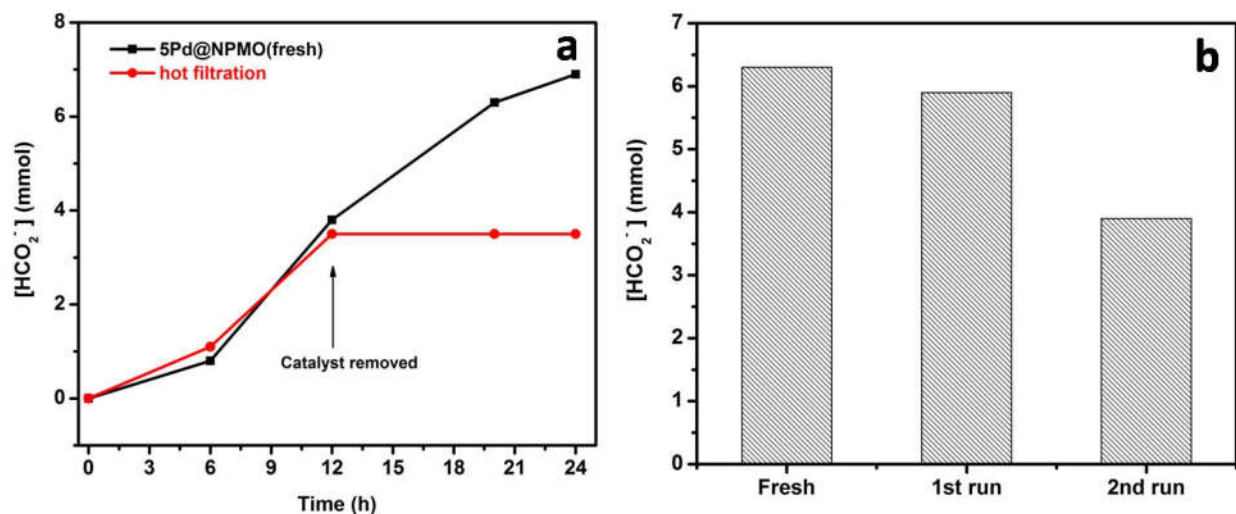


Figure 4B.4: (a) Heterogeneity study of Pd@NPMO catalyst by hot-filtration test (catalyst removed after 12 h reaction and further reaction carried in the absence of catalyst). (b) Recycling experiment to study reusability. Reaction conditions: 5Pd@NPMO (20 mg), aqueous KOH solution (20 mL, 0.5 M), $\text{CO}_2:\text{H}_2$ (1:3, 4 MPa), temperature (100 °C), and time (20 h).

The high-resolution TEM images of the spent 5Pd@NPMO catalyst after the second cycle (Figure 4B.5) revealed that during the reaction under 0.5 M KOH solution and at a boiling reaction temperature for a prolonged time resulted in the partial destruction of the silica support morphology generating islands of agglomerated Pd nanoparticles along with well-dispersed small particles. It is true that complete dissolution of silica was not observed even under our reaction conditions. The well-dispersed small Pd nanoparticles were also observed and those are likely the ones protected inside the N sites of mesopores that prevented agglomeration.

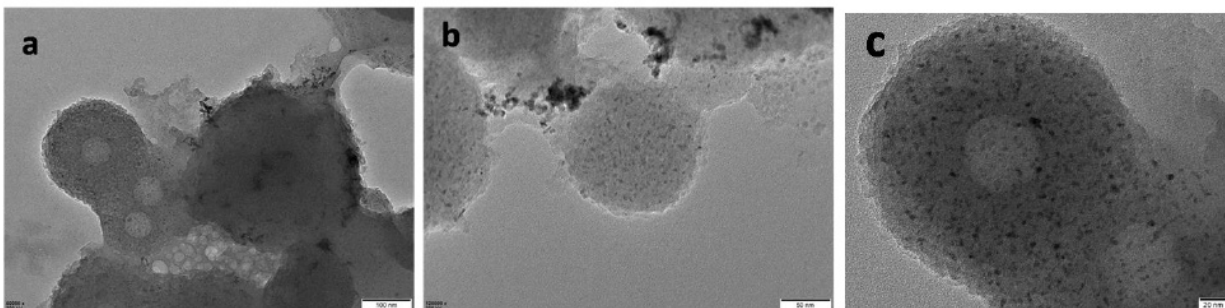


Figure 4B.5: Transmission electron microscopy images of spent 5Pd@NPMO catalyst after 2 cycles (a, b, and c with scale 100, 50, and 20, respectively).

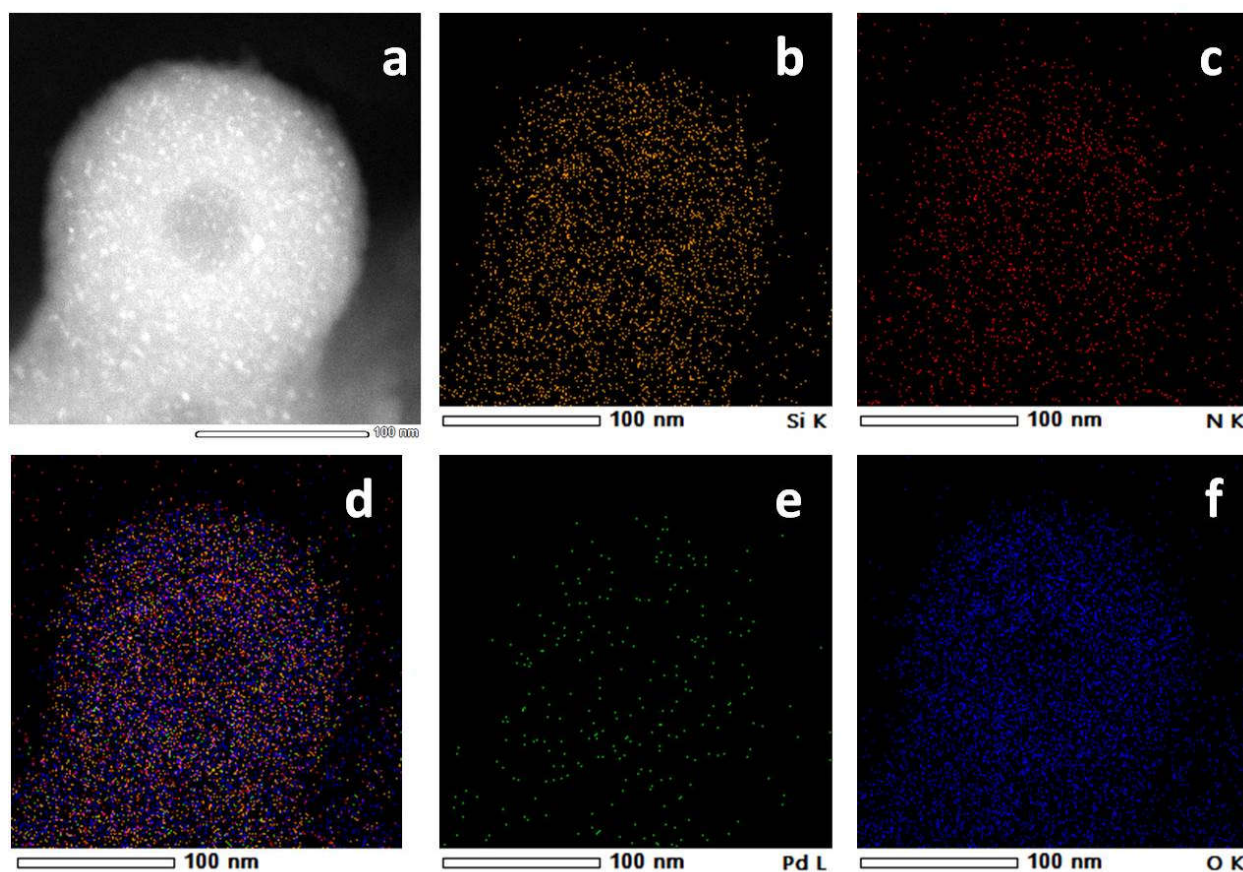


Figure 4B.6: Structural characterization of 5Pd@NPMO spent catalyst (after 2 cycles). (a) HAADF-STEM image (scale 100 nm) and (b-f) STEM-EDX elemental mapping of the (b) Si K, (c) N K, (e) Pd L, (f) O K edges and (d) overlay image.

HAADF-STEM elemental mapping of the spent 5Pd@NPMO catalyst (Figure 4B.6) showed the presence of nitrogen on the PMO, which in combination with small Pd nanoparticles yielded 3.8 mmol of formate after the second cycle. The formation of large voids in hybrid NPMO spheres after the reaction may be due to the etching of silica under the basic reaction conditions.⁷⁴ A similar result was observed with the 3Pd@SBA-15(DP) catalyst after the reaction, where the ordered SBA-15 channels were collapsed with concomitant agglomeration of Pd nanoparticles producing 0.46 mmol formate in the second run (Figure 4B.7).

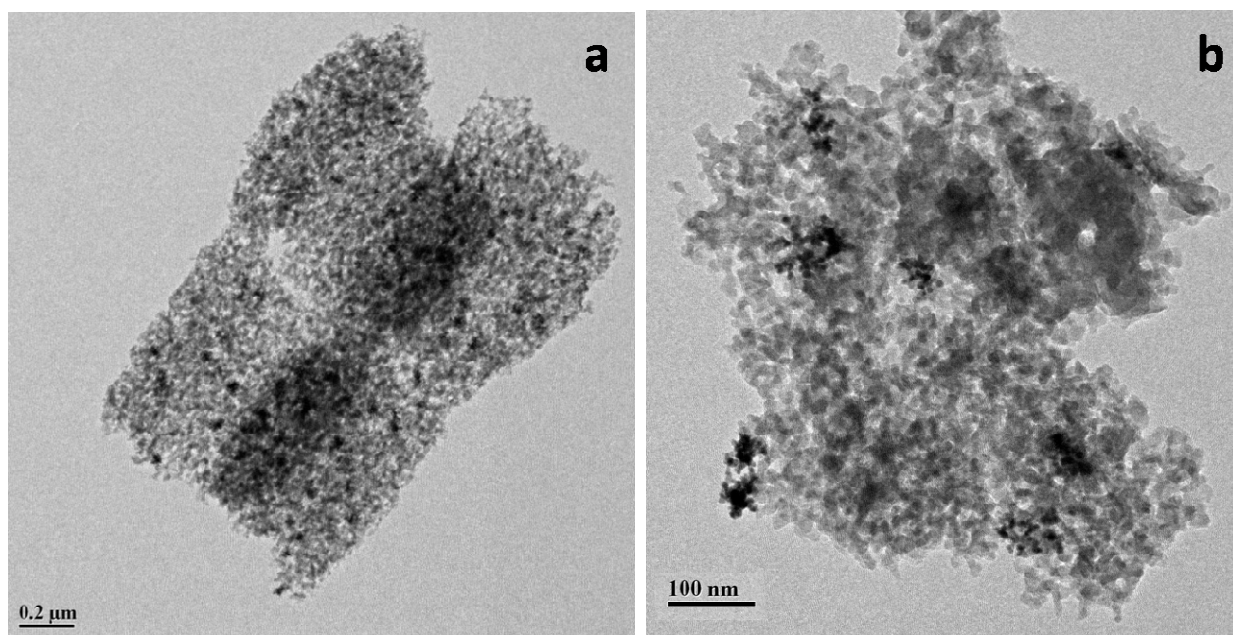


Figure 4B.7: Transmission electron microscopy images of spent 3Pd@SBA-15 (DP) catalyst after 2 cycles.

The XPS measurements of the spent 5Pd@NPMO catalyst showed the existence of both Pd(0) and Pd(+2) species (Figure 4B.8), and the relative percentage was found to be 78:22. The XPS peak intensities for Pd 3d in the spent 5Pd@NPMO had decreased considerably along with the reduction of oxidized Pd(+2) species, indicating Pd nanoparticles' growth with concomitant loss in dispersion, a result in good agreement with the TEM results. The N 1s spectrum for the spent 5Pd@NPMO showed similar species compared to the fresh catalyst, and the major peak at 400 eV corresponding to N–H species confirmed no structural change in the keto-form in the organic moiety in the framework under the CO₂ hydrogenation reaction environment (Figure 4B.9).

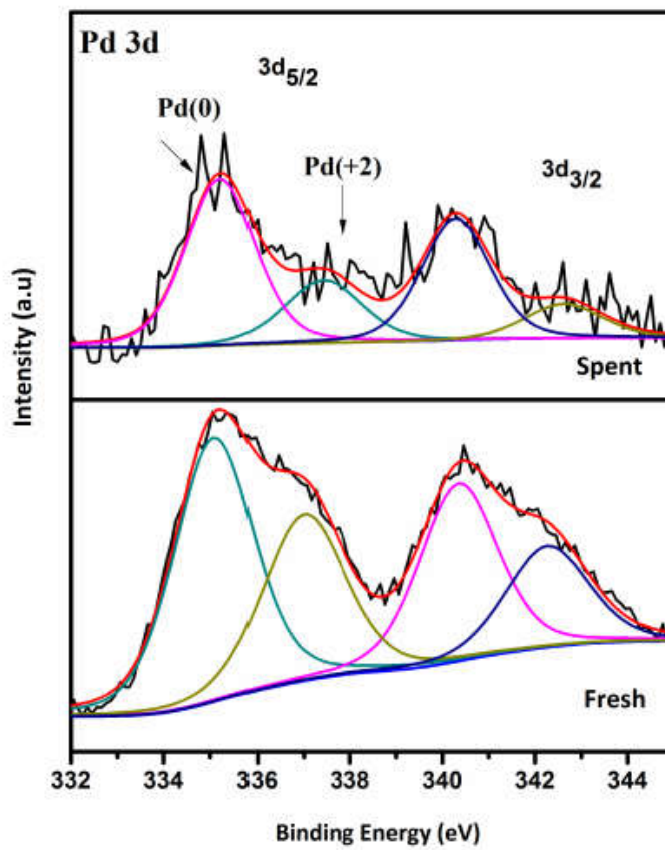


Figure 4B.8: Comparison of XPS plot of fresh and spent Pd@NPMO catalyst.

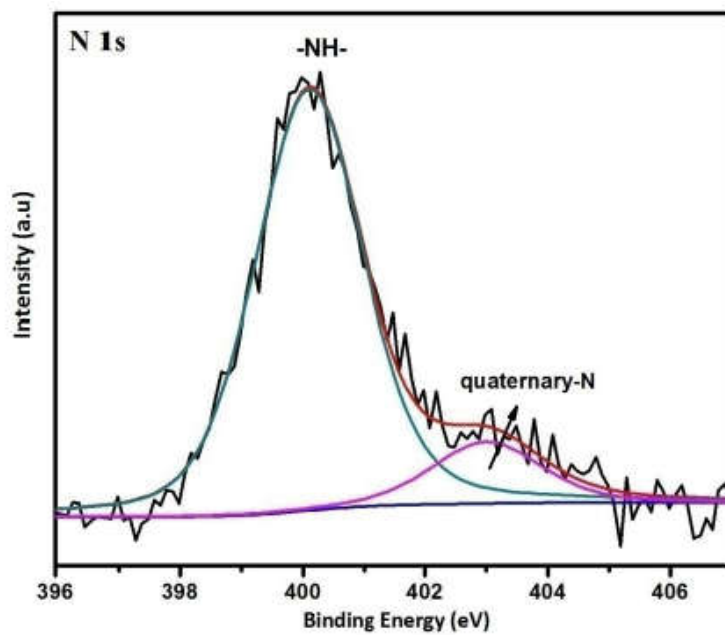


Figure 4B.9: N1s XPS spectrum for spent Pd@NPMO catalyst

The Pd content in the spent 5Pd@NPMO was calculated from ICP-OES and found to be ~4.8 % with respect to the support, which showed no metal leaching from the catalyst under our reaction conditions, confirming that the catalyst behaves purely heterogeneously in nature. The N content in the spent catalyst was determined as 2.8 % from the CHN elemental analysis. The plausible reason for the drop in activity after the second run may be the combination of agglomerated Pd nanoparticles and a decrease in N content under the basic reaction conditions.

4.4 Conclusions

The results from both sections of Chapter 4 (4A and 4B) show that Pd supported chemically modified hybrid silica synthesized by sol-gel hydrothermal method demonstrates a potential heterogeneous hydrogenation catalyst for phenol and CO₂. The main agenda is to stabilize the active metal species on the catalytically inactive supports like silica to improve the activity/selectivity in catalysis. As discussed in part 4A, the hybrid silica-supported metal catalyst mediated phenol hydrogenation opens up the possibility of utilizing the framework chemistry in the silica materials. The catalysis performed on such metal-supported periodic mesoporous organosilica helps to bring down the operation conditions yielding good catalytic efficiency. The optimized reaction conditions from part 4A concluded that the N-containing hybrid organosilica-supported Pd catalyst is more reactive towards the phenol hydrogenation reaction at 40 °C and 1 atm H₂ pressure in a water medium. The Pd@NPMO catalyst is completely reusable without prior activation treatments, indicating the heterogeneity of the material. The present study clearly emphasizes the role of nitrogen centers in the silica framework to facilitate the synthesis of small-sized Pd nanoparticles (2-5 nm) with high metal loading without any stabilizing agents followed by the selective conversion phenol to cyclohexanone compared to the SBA-15 supported catalysts. From part 4B, an efficient heterogeneous Pd-based aqueous phase CO₂ hydrogenation catalyst was developed using a new N-incorporated periodic mesoporous organosilica in the framework (Pd@NPMO). The catalytic activity of the NPMO catalyst (TOF 108 h⁻¹) was superior compared to Pd@SBA-15 (9.4 h⁻¹), demonstrating the role of nitrogen sites on NPMO supports for boosting the CO₂ reduction with complete selectivity to formate under mild reaction conditions. A combination of characterization and catalytic results confirmed the CO₂ hydrogenation catalysis on Pd@NPMO to be purely heterogeneous.

Finally, it can be concluded that employing the new chemically modified silica bridging framework with small-sized Pd NPs behaves as an effective catalyst for liquid-phase hydrogenation reaction of phenol and CO₂ molecule. Future developments in supported metal nanoparticle catalysts based on N-containing PMOs for sustainable catalysis can find several insights from the present study.

4.5 References

1. W. Li, J. Liu and D. Zhao, *Nature Reviews Materials*, 2016, **1**, 16023.
2. Y. Maegawa and S. Inagaki, *Dalton Transactions*, 2015, **44**, 13007-13016.
3. P. Van Der Voort, D. Esquivel, E. De Canck, F. Goethals, I. Van Driessche and F. J. Romero-Salguero, *Chemical Society Reviews*, 2013, **42**, 3913-3955.
4. N. Mizoshita and S. Inagaki, *Angewandte Chemie International Edition*, 2015, **54**, 11999-12003.
5. M. Waki, Y. Maegawa, K. Hara, Y. Goto, S. Shirai, Y. Yamada, N. Mizoshita, T. Tani, W.-J. Chun, S. Muratsugu, M. Tada, A. Fukuoka and S. Inagaki, *Journal of the American Chemical Society*, 2014, **136**, 4003-4011.
6. M. Waki, N. Mizoshita, T. Ohsuna, T. Tani and S. Inagaki, *Chemical Communications*, 2010, **46**, 8163-8165.
7. M. Waki, N. Mizoshita, T. Tani and S. Inagaki, *Angewandte Chemie International Edition*, 2011, **50**, 11667-11671.
8. K. Okamoto, Y. Goto and S. Inagaki, *Journal of Materials Chemistry*, 2005, **15**, 4136-4140.
9. T. Yui, H. Takeda, Y. Ueda, K. Sekizawa, K. Koike, S. Inagaki and O. Ishitani, *ACS Applied Materials & Interfaces*, 2014, **6**, 1992-1998.
10. N. Mizoshita, T. Tani, H. Shinokubo and S. Inagaki, *Angewandte Chemie International Edition*, 2012, **51**, 1156-1160.
11. M. Cornelius, F. Hoffmann, B. Ufer, P. Behrens and M. Fröba, *Journal of Materials Chemistry*, 2008, **18**, 2587-2592.
12. M. A. Wahab, S. Sudhakar, E. Yeo and A. Sellinger, *Chemistry of Materials*, 2008, **20**, 1855-1861.
13. T. P. Nguyen, P. Hesemann, P. Gaveau and J. J. E. Moreau, *Journal of Materials Chemistry*, 2009, **19**, 4164-4171.
14. S. Ishikawa, Y. Maegawa, M. Waki and S. Inagaki, *ACS Catalysis*, 2018, **8**, 4160-4169.
15. V. Dufaud, F. Beauchesne and L. Bonneviot, *Angewandte Chemie International Edition*, 2005, **44**, 3475-3477.
16. J. Zhong, J. Chen and L. Chen, *Catalysis Science & Technology*, 2014, **4**, 3555-3569.
17. J. Chen, W. Zhang, L. Chen, L. Ma, H. Gao and T. Wang, *ChemPlusChem*, 2013, **78**, 142-148.
18. A. Trovarelli, *Catalysis Reviews*, 1996, **38**, 439-520.
19. M. Cargnello, N. L. Wieder, P. Canton, T. Montini, G. Giambastiani, A. Benedetti, R. J. Gorte and P. Fornasiero, *Chemistry of Materials*, 2011, **23**, 3961-3969.
20. A. C. S. Sekhar, C. J. Meera, K. V. Ziyad, C. S. Gopinath and C. P. Vinod, *Catalysis Science & Technology*, 2013, **3**, 1190-1193.
21. N. Ishito, K. Nakajima, Y. Maegawa, S. Inagaki and A. Fukuoka, *Catalysis Today*, 2017, **298**, 258-262.

22. C. A. Didó, C. D. G. Caneppele, A. C. Schneid, M. B. Pereira, T. M. H. Costa and E. V. Benvenuti, *Microporous and Mesoporous Materials*, 2018, **270**, 48-56.
23. M. H. Lim and A. Stein, *Chemistry of Materials*, 1999, **11**, 3285-3295.
24. A. Lazar, S. C. George, P. R. Jithesh, C. P. Vinod and A. P. Singh, *Applied Catalysis A: General*, 2016, **513**, 138-146.
25. C. Baleizão, B. Gigante, D. Das, M. Alvaro, H. Garcia and A. Corma, *Chemical Communications*, 2003, DOI: 10.1039/B304814D, 1860-1861.
26. E. Gu, W. Zhong and X. Liu, *RSC Advances*, 2016, **6**, 98406-98412.
27. J. H. Chong, M. Sauer, B. O. Patrick and M. J. MacLachlan, *Organic Letters*, 2003, **5**, 3823-3826.
28. A. Lazar, C. P. Vinod and A. P. Singh, *Microporous and Mesoporous Materials*, 2017, **242**, 173-181.
29. Y. Soni, S. Pradhan, M. K. Bamnia, A. K. Yadav, S. N. Jha, D. Bhattacharyya, T. S. Khan, M. A. Haider and C. P. Vinod, *Applied Catalysis B: Environmental*, 2020, **272**, 118934.
30. P. Pachfule, S. Kandambeth, D. Díaz Díaz and R. Banerjee, *Chemical Communications*, 2014, **50**, 3169-3172.
31. S. Kandambeth, A. Mallick, B. Lukose, M. V. Mane, T. Heine and R. Banerjee, *Journal of the American Chemical Society*, 2012, **134**, 19524-19527.
32. A. Lazar, K. J. Betsy, C. P. Vinod and A. P. Singh, *Catalysis Communications*, 2018, **104**, 62-66.
33. Y. Hu, Y. Shim, J. Oh, S. Park, S. Park and Y. Ishii, *Chemistry of Materials*, 2017, **29**, 5080-5089.
34. Y. Zhou, T. Holme, J. Berry, T. R. Ohno, D. Ginley and R. O'Hayre, *The Journal of Physical Chemistry C*, 2010, **114**, 506-515.
35. M. Liu, X. Lu, L. Shi, F. Wang and J. Sun, *ChemSusChem*, 2017, **10**, 1110-1119.
36. M. Saidi, F. Samimi, D. Karimipourfard, T. Nimmanwudipong, B. C. Gates and M. R. Rahimpour, *Energy & Environmental Science*, 2014, **7**, 103-129.
37. K. J. Betsy, C. Nayak, A. Lazar, A. Krishnan, D. Bhattacharyya, S. N. Jha and C. P. Vinod, *ChemCatChem*, 2018, **10**, 3291-3298.
38. R. A. Sheldon and J. K. Kochi, in *Adv.Catal.A*, eds. H. P. D.D. Eley and B. W. Paul, Academic Press, 1976, vol. Volume 25, pp. 272-413.
39. P. Makowski, R. Demir Cakan, M. Antonietti, F. Goettmann and M.-M. Titirici, *Chemical Communications*, 2008, DOI: 10.1039/B717928F, 999-1001.
40. K. J. Betsy, A. Lazar and C. P. Vinod, *Nano-Structures & Nano-Objects*, 2018, **13**, 36-43.
41. J.-F. Zhu, G.-H. Tao, H.-Y. Liu, L. He, Q.-H. Sun and H.-C. Liu, *Green Chemistry*, 2014, **16**, 2664-2669.
42. D. Kong, J. Z. Y. Tan, F. Yang, J. Zeng and X. Zhang, *Applied Surface Science*, 2013, **277**, 105-110.

43. G. Porwal, S. Gupta, S. Sreedhala, J. Elizabeth, T. S. Khan, M. A. Haider and C. P. Vinod, *ACS Sustainable Chemistry & Engineering*, 2019, **7**, 17126-17136.
44. C. Tian, H. Fang, H. Chen, W. Chen, S. Zhou, X. Duan, X. Liu and Y. Yuan, *Nanoscale*, 2020, **12**, 2603-2612.
45. H. Liu, T. Jiang, B. Han, S. Liang and Y. Zhou, *Science*, 2009, **326**, 1250.
46. C.-J. Lin, S.-H. Huang, N.-C. Lai and C.-M. Yang, *ACS Catalysis*, 2015, **5**, 4121-4129.
47. N. C. Nelson, J. S. Manzano, A. D. Sadow, S. H. Overbury and I. I. Slowing, *ACS Catalysis*, 2015, **5**, 2051-2061.
48. G. Neri, A. M. Visco, A. Donato, C. Milone, M. Malentacchi and G. Gubitosa, *Applied Catalysis A: General*, 1994, **110**, 49-59.
49. Y. Wang, J. Yao, H. Li, D. Su and M. Antonietti, *Journal of the American Chemical Society*, 2011, **133**, 2362-2365.
50. Y. Z. Chen, C. W. Liaw and L. I. Lee, *Applied Catalysis A: General*, 1999, **177**, 1-8.
51. B. Sedai, J. L. Zhou, N. Fakhri, A. Sayari and R. T. Baker, *ACS Sustainable Chemistry & Engineering*, 2018, **6**, 9716-9724.
52. M. Anbia and S. Amirmahmoodi, *Scientia Iranica*, 2011, **18**, 446-452.
53. M. Behrens, F. Studt, I. Kasatkin, S. Kühl, M. Hävecker, F. Abild-Pedersen, S. Zander, F. Girgsdies, P. Kurr, B.-L. Kniep, M. Tovar, R. W. Fischer, J. K. Nørskov and R. Schlögl, *Science*, 2012, **336**, 893-897.
54. S. Kuld, M. Thorhauge, H. Falsig, C. F. Elkjær, S. Helveg, I. Chorkendorff and J. Sehested, *Science*, 2016, **352**, 969-974.
55. G. C. Chinchin, P. J. Denny, D. G. Parker, M. S. Spencer and D. A. Whan, *Applied Catalysis*, 1987, **30**, 333-338.
56. X. Jiang, N. Koizumi, X. Guo and C. Song, *Applied Catalysis B: Environmental*, 2015, **170-171**, 173-185.
57. S. Moret, P. J. Dyson and G. Laurenczy, *Nature Communications*, 2014, **5**, 4017.
58. S. Wang, D. Mao, X. Guo, G. Wu and G. Lu, *Catalysis Communications*, 2009, **10**, 1367-1370.
59. M. Grasemann and G. Laurenczy, *Energy & Environmental Science*, 2012, **5**, 8171-8181.
60. B. Elvers, *Ullmann's encyclopedia of industrial chemistry*, Verlag Chemie, 1991.
61. X. Ji, K. T. Lee, R. Holden, L. Zhang, J. Zhang, G. A. Botton, M. Couillard and L. F. Nazar, *Nature Chemistry*, 2010, **2**, 286-293.
62. S. Kattel, P. Liu and J. G. Chen, *Journal of the American Chemical Society*, 2017, **139**, 9739-9754.
63. D. B. Lao, B. R. Galan, J. C. Linehan and D. J. Heldebrant, *Green Chemistry*, 2016, **18**, 4871-4874.
64. C. Guan, Y. Pan, E. P. L. Ang, J. Hu, C. Yao, M.-H. Huang, H. Li, Z. Lai and K.-W. Huang, *Green Chemistry*, 2018, **20**, 4201-4205.

65. M. S. Maru, S. Ram, R. S. Shukla and N.-u. H. Khan, *Molecular Catalysis*, 2018, **446**, 23-30.
66. L. Wang, W. Zhang, X. Zheng, Y. Chen, W. Wu, J. Qiu, X. Zhao, X. Zhao, Y. Dai and J. Zeng, *Nature Energy*, 2017, **2**, 869-876.
67. A. Azua, S. Sanz and E. Peris, *Chemistry – A European Journal*, 2011, **17**, 3963-3967.
68. A. Weilhard, M. I. Qadir, V. Sans and J. Dupont, *ACS Catalysis*, 2018, **8**, 1628-1634.
69. C. Mondelli, B. Puértolas, M. Ackermann, Z. Chen and J. Pérez-Ramírez, *ChemSusChem*, 2018, **11**, 2859-2869.
70. K. Mori, S. Masuda, H. Tanaka, K. Yoshizawa, M. Che and H. Yamashita, *Chemical Communications*, 2017, **53**, 4677-4680.
71. Y. Kuramochi, M. Sekine, K. Kitamura, Y. Maegawa, Y. Goto, S. Shirai, S. Inagaki and H. Ishida, *Chemistry – A European Journal*, 2017, **23**, 10301-10309.
72. C. E. Mitchell, U. Terranova, I. Alshibane, D. J. Morgan, T. E. Davies, Q. He, J. S. J. Hargreaves, M. Sankar and N. H. de Leeuw, *New Journal of Chemistry*, 2019, **43**, 13985-13997.
73. Z. Duan and R. Sun, *Chemical Geology*, 2003, **193**, 257-271.
74. Z. Zhu, S. Zhang, C. Li, J. Zhang, J. Yu, X. Du, L. He and X. Zhang, *Physical Chemistry Chemical Physics*, 2018, **20**, 1440-1446.

CHAPTER-5

Pd-supported Bridged Organo-aluminosilicate Hybrid Catalyst for Reductive-amination of Furfural

This chapter is based on:

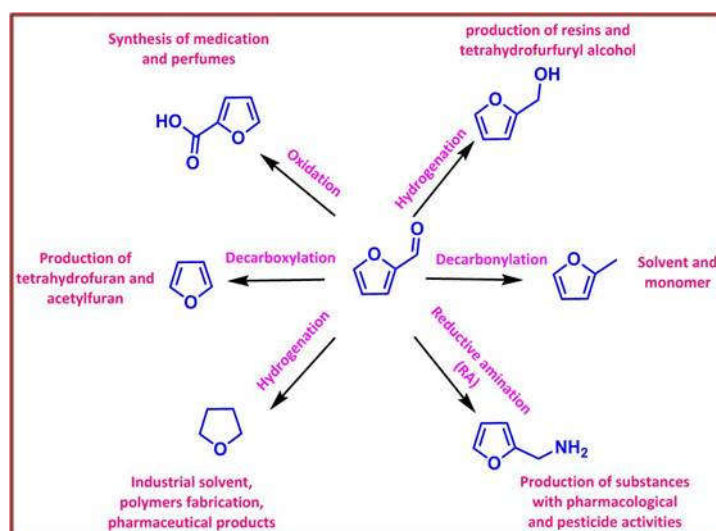
1) **K. J. Betsy**, Anju George and C. P. Vinod; Pd-supported bridged organo-aluminosilicate hybrid catalyst for reductive-amination of furfural (Manuscript under preparation).

5.1 Introduction

The primary source of many valuable chemicals is fossil fuels; however, their reasonable impact on climate change and their considerable depletion have forced intense research to replace them with renewable sources.¹ One such renewable resource that has gained significant attention considering its vast abundance is lignocellulosic biomass.² The selective transformation of biomass-based feedstocks to liquid fuels and commodity chemicals is highly desirable and accounts for one of the prime challenges in catalysis. Among the variety of feedstocks from biomass, furfural can serve as a potential secondary source for synthesizing fine chemicals like furfuryl alcohol, 2-methyl furan, tetrahydrofuran, etc (Scheme 5.1). Enormous efforts have been made to design suitable and adept catalytic reactions where the heterogeneous catalysts play a crucial role due to their practical reasons. Production of a wide range of chemicals from biomass, containing atoms like C, H and O has well explored; nonetheless, fabrication of N-compounds from furfural-derived molecules remains limited, which becomes an important objective of the research.³ Amine-based compounds are valuable in the chemical industry because of their high reactivity and nucleophilic properties.⁴⁻⁶ They serve as flexible key intermediates and feedstocks for the production of life science molecules, advanced chemicals, and polymers.^{7, 8} The aliphatic and aromatic amines of industrial relevance are manufactured from non-renewable resources and, in contrast, owing to the limited efficient amination methods makes the process of biomass transformation into N-containing chemicals less explored.^{9, 10}

Among the various strategies, direct reductive amination (RA) is more preferred due to the associated advantages like high selectivity towards the desired N-containing compounds at comparatively very mild operation conditions. This approach constitutes the cascade reaction of furfural which first converts to imine intermediates followed by the formation of N-containing product through hydrogenation.¹¹⁻¹³ The synthesis of furfurylamines has been studied from furfural (FF) and 5-hydroxymethylfurfural (HMF) using homo- and hetero- tagged catalysts.¹⁴⁻¹⁷ In the literature, research works are dedicated to synthesizing THF-derived amines from furfural by the furan ring deep hydrogenation.¹⁸ THF-derived amines were used as a regulator in the polybutadiene rubber synthesis with precise control of the microstructure, also used for the poly(2-vinyl-4,4-dimethylazlactone) derived (co)polymers synthesis with lower critical solution temperature.^{17, 18}

Generally, both metallic and acidic sites are required for the RA reaction, along with the appropriate choice of reductants.¹⁹⁻²¹ An important step in the cascade reaction is the selective hydrogenation of imines to amines by suppressing the competitive side reactions like direct hydrogenation of furfural.¹⁴ Hence, developing an efficient catalyst capable of enhancing the cascade reaction is crucial for the direct reductive amination of furfural. The reaction selectivity over a heterogeneous catalyst can be controlled by the desired specific reaction sites. Recently, metal (Pt, Ir, Au) stabilized over SO₃H grafted silica was shown to be a bifunctional catalyst active for the RA of furfural with aniline.¹⁹ They specify the influence of the metal sites and the SO₃H group acidic sites in the close proximity affects the hydrogenation step through the transfer of electrons in the bifunctional catalyst.



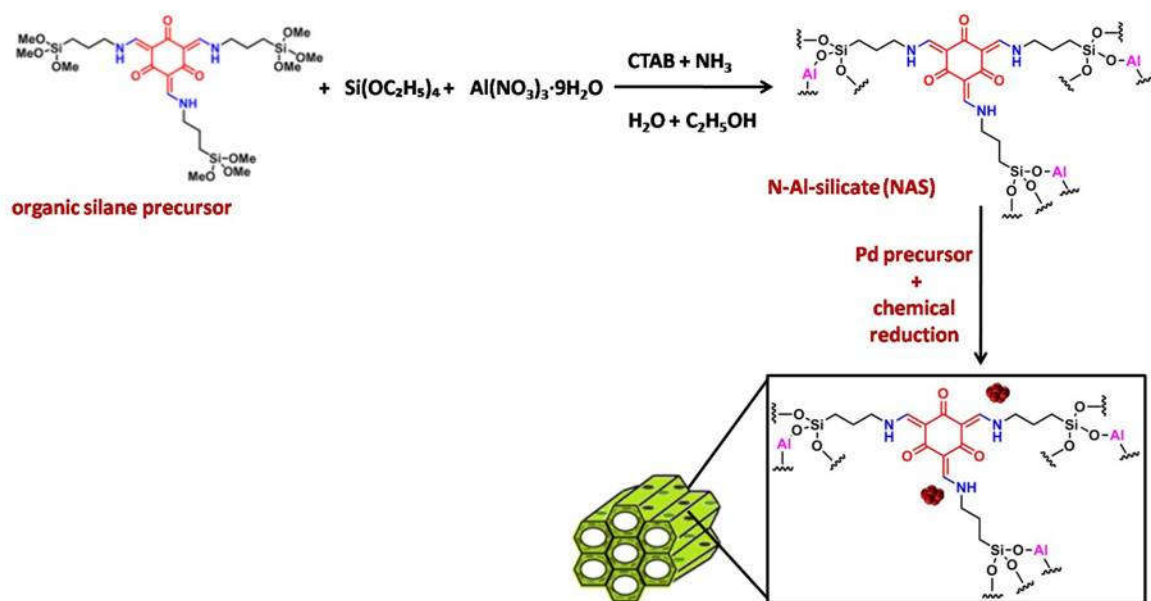
Scheme 5.1: Furfural derivatives and their applications.²²

This chapter has utilized Pd NPs supported over hybrid N-containing organo-aluminosilicate catalyst (Pd-N-Al-silicate) for the liquid-phase, one-pot reductive amination of furfural at mild reaction conditions. The small-sized, well-dispersed Pd NPs were stabilized over the hybrid aluminosilicate framework under the synthesis condition employed in the present work. The material was thoroughly characterized using various physical, spectroscopic, and microscopic techniques. The activity was compared to a Pd-supported conventional Al-silicate catalyst under similar reaction conditions. The effect of the new hybrid bridging and framework aluminium sites on the Pd-N-Al-silicates on RA reaction was well-established compared to the unmodified counterparts.

5.2 Experimental Section

5.2.1 One-pot synthesis of organo-aluminosilicate (N-Al-silicates): The synthesis was carried out using a modified sol-gel process reported in the literature.²³ Briefly, cetyltrimethylammonium bromide (CTAB, 2 g) was dissolved in a water/ethanol solvent mixture (10 mL/ 2 mL) and homogenized by adding ammonia solution (2 mL) through stirring. To this, a premixed solution of N-incorporated organosilane precursor (215 mg, synthesis protocol is described in chapter 4) and TEOS (125 mg) in ethanol (2 mL) was added and stirred for one hour. To this, a solution of aluminium nitrate nonahydrate (40 mg) dissolved in ethanol (6 mL) was added and stirred for the next three hours. The final aluminium modified N-aluminosilicate material was obtained after aging for 12 hours at room temperature followed by centrifugation. Further, the material was dried at 60 °C, and solvent-extracted with acidified ethanol for two times. The final material was collected and dried at 60 °C to obtain the pale orange-colored powder N-Al-silicates. The synthesis of hybrid NPMO silica and inorganic Al-silicates supports used in the control studies was carried out using a similar procedure by avoiding the addition of aluminium and N-organosilane precursors, respectively.

5.2.2 Supported Pd nanoparticles over N-Al-silicate catalyst (Pd-N-Al-silicate): The small palladium nanoparticles were supported on N-Al-silicate support was carried out through simple wet-chemical reduction method using NaBH₄ as a reducing agent as discussed in Chapter 4. Briefly, 100 mg of N-Al-silicate support was dispersed in 10 mL of water at room temperature, to which the calculated amount of Na₂PdCl₄ solution in water was added and stirred for one hour. Freshly prepared 3 mL, 1 M NaBH₄ solution was added slowly, and the reaction was allowed to stir for another 2 h. The obtained material was filtered, washed, and dried at 60 °C for 12 h to obtain Pd-N-Al-silicate catalysts. The Pd loading was controlled by varying the amount of Na₂PdCl₄ precursor. Similarly, Pd NPs were loaded over the supports like NPMO, Al-silicate, and commercial Al₂O₃. Figure 5.2 shows the schematic representation for the synthesis of hybrid catalyst.



Scheme 5.2: Synthesis of Pd-N-Al-silicate hybrid catalyst.

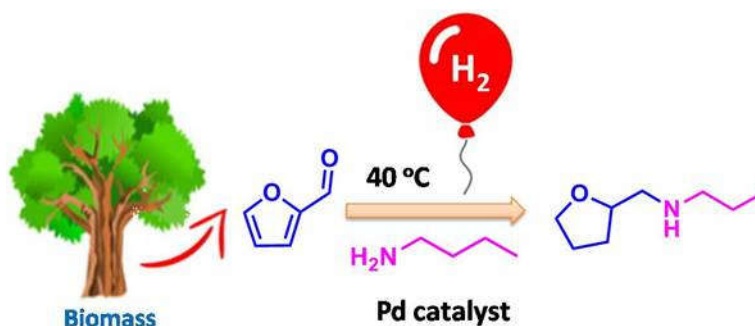
5.2.3 Catalysts characterization

Powder X-ray diffraction (PXRD) analysis of all the synthesised materials were carried out on PANalytical X'pert Pro diffractometer with $\text{Cu K}\alpha$ radiation ($\lambda = 1.5406 \text{ \AA}$) operated at 40 kV and 30 mA at the scan rate of $4^\circ/\text{min}$ from 10 to 90° . Fourier transform infrared (FTIR) spectra for the samples were collected on a Bruker Optics ALPHA-E spectrometer with universal Zn-Se attenuated total reflection accessory (ATR) with a Diamond ATR (Golden Gate) in 600 to 4000 cm^{-1} range. Autosorb 1C Quantachrome, USA, instrument was used to study the N_2 isotherms and pore-size distribution of the material. The analyses of the degassed samples at 100°C for 4 h were run at liquid N_2 temperature. BET multipoint model was used to calculate the surface area at $P/P_0 = 0.06 - 0.3$ and BJH desorption model for pore size distribution. Thermogravimetric analyses were carried out under N_2 atmosphere on a TG50 analyzer (Mettler-Toledo) or SDT Q600 TG-DTA analyzer at a heating rate of $10^\circ\text{C}/\text{min}$ within $30 - 900^\circ\text{C}$ temperature range. XPS measurements for the catalyst were done on Thermo Kalpha+ spectrometer using $\text{Al K}\alpha$ radiation with energy of 1486.6 eV . All the spectra were charge corrected with reference to C1s at 284.6 eV . The peak fitting were carried out using CasaXPS software with Shirley type background. The TEM images of the samples were recorded by FEI Tecnai TF-20 electron microscope, operating at 200 kV with LaB6 filament for TEM images and SEM images obtained

by dual beam scanning electron microscope (FEI company, model Quanta 200 3D) operating at 20 kV with tungsten filament. The solid state NMR spectra for ^{13}C , ^{27}Al , and ^{15}N nuclei were recorded on Jeol ECX-400 MHz spectrometer (frequency of 100.6 MHz on solid 4 mm MAS probe). Magic-angle spinning (MAS) NMR spectra for ^{29}Si nuclei was recorded on BRUKER DSX300 spectrometer at 7.05 T (resonance frequencies 59.595 MHz, rotor speed 10000 Hz and 75.43 MHz, rotor speed 10000 Hz).

5.2.4 Catalytic screening for the liquid phase direct reductive amination of furfural

The furfural liquid phase reductive amination was carried out in a two-necked round bottom flask equipped with the condenser having a hydrogen balloon (1atm), and the other neck was sealed with a rubber septum. Typically, 0.4 mmol of furfural and 0.4 mmol of n-butylamine were dissolved in 2.5 mL of ethanol (solvent), to which 10 mg of the catalyst was added. The reaction was allowed to proceed in the preheated oil bath at 40 °C. The reaction mixture was withdrawn at regular time intervals and injected in GC equipped with HP5 column with FID detector to calculate the conversion and selectivity. The product confirmation was done using GC-MS and NMR (^1H and ^{13}C). The catalytic reductive amination reaction of furfural is shown below (Scheme 5.3).



Scheme 5.3: Catalytic reductive amination of furfural over Pd catalyst.

5.3 Results and Discussion

5.3.1 X-ray Diffraction

Figure 5.1 shows the PXRD patterns of Pd supported hybrid N-Al-silicate and conventional Al-silicate materials. A broad peak at 23° in all the samples indicates the amorphous nature of silicate material, with no peaks matching with the extra-framework crystalline Al₂O₃ observed.

In the case of conventional Pd-Al-silicate, the characteristic reflections at 40.1° , 46.5° , 67.4° which corresponds to (111), (200), and (220) planes, respectively (JCPDS file No.87-0638) for the Pd metallic species in the fcc crystal structure, whereas less intense and broad reflection was obtained for hybrid Pd-N-Al-silicate catalyst which is attributed to the presence of small and highly dispersed Pd metal NPs over the N-Al-silicate hybrid support.

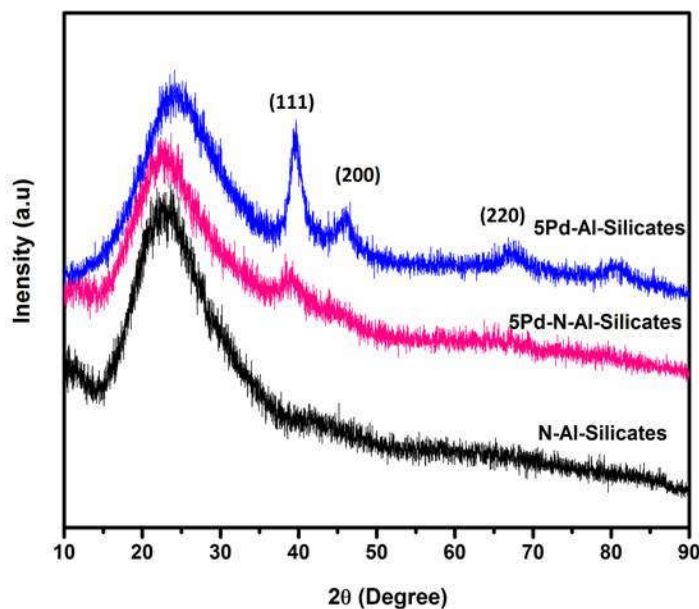


Figure 5.1: XRD pattern of the supported Pd catalysts.

5.3.2 N_2 Porosimetry and Micro-elemental Analysis

The N_2 adsorption-desorption analysis of both N-Al-silicate and Pd-N-Al-silicate material showed type-IV isotherm, which is typical for mesoporous materials (Figure 5.2). The textural properties of the catalyst have been tabulated in Table 5.1. The average pore-size distribution has been estimated to be 3.6 nm through the BJH method, which confirms the mesoporous nature of the hybrid N-Al-silicate support. The BET surface area for Al-silicate and N-Al-silicate materials was $850 \text{ m}^2/\text{g}$ and $425 \text{ m}^2/\text{g}$, respectively. After the 5 wt %, metal loading on N-Al-silicate support showed a decrease in surface area from $425 \text{ m}^2/\text{g}$ to $335 \text{ m}^2/\text{g}$ with no change in the pore diameter (3.6 nm). The nitrogen content in the synthesized catalysts was determined from the CHN microanalysis. It was found that 5.9 % nitrogen has been incorporated inside the framework of hybrid 5-Pd-N-Al-silicates.

Table 5.1: Textural properties of different modified silica supports.

Catalyst	BET surface area (m ² /g)	Pore diameter (nm)	N content (%) [*]
Al-Silicates	850	3.4	-
N-Al-Silicates	425	3.6	6
5Pd-N-Al-Silicates	335	3.6	5.9

*determined from CHN elemental analysis.

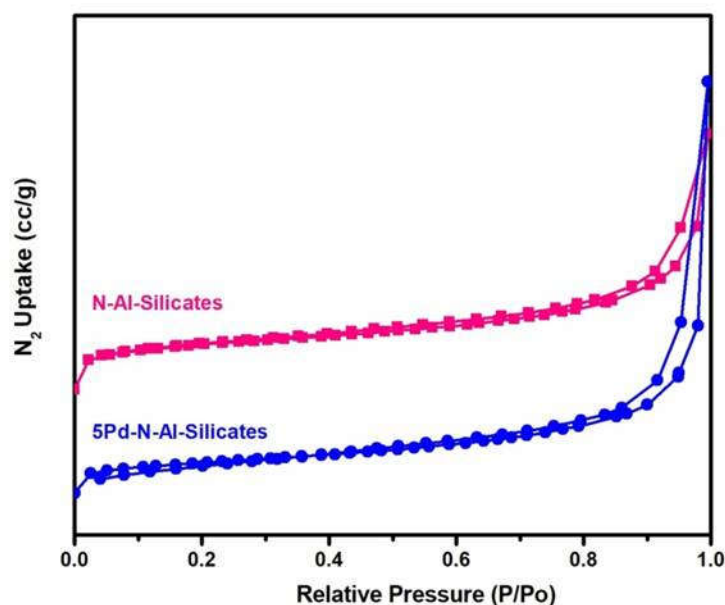


Figure 5.2: N₂ adsorption-desorption isotherms of N-Al-silicate catalysts

5.3.3 Thermogravimetric Analysis

The thermogravimetric (TGA) analysis of Pd-N-Al-silicate samples showed around 40 % weight loss at temperature above 300 °C (Figure 5.3). This weight loss corresponds to the decomposition of bridged organic linkers inside the siloxane framework, indicating the thermal stability of organic-inorganic hybrid aluminosilicates. This also implies the successful integration of ~ 40 % organic functionality in the silicate matrix. Around ~ 10 % weight loss was observed below 100

°C due to the removal of adsorbed water. Further, no weight loss was observed, suggesting the complete removal of the surfactant CTAB during the synthesis.

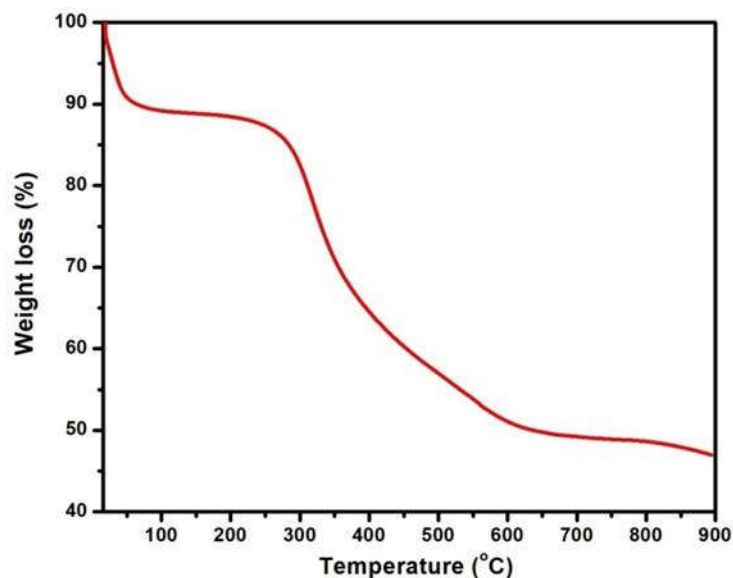


Figure 5.3: The thermogravimetric analysis (TGA) of the Pd-N-Al-silicate sample after the solvent extraction.

5.3.4 Infra-red Spectroscopy

The formation of a keto-enamine framework in the hybrid N-Al-silicate was confirmed by FTIR spectroscopy. As observed in Chapter 4, most of the peaks in the FTIR spectrum of the N-Al-silicate (Figure 5.4) matched well with the organic silane precursor-2 (see chapter 4), which exists in the keto-form. The C=O peak was observed at 1616 cm^{-1} along with a strong peak at 1548 cm^{-1} from the C=C bond from the organic bridging. The IR band for C-N at 1298 cm^{-1} in the silica framework showed the retention of the keto-form after the hydrolysis and polycondensation reaction at basic conditions while forming hybrid organic bridged aluminosilicate. The band at 1075 cm^{-1} shows the Si-O-Si vibration from the framework, confirming a siliceous network formation in the material. The Si-O-C ($\sim 1125\text{ cm}^{-1}$) vibration confirmed the organic motif bridged inside the framework. The framework architecture of the N-Al-silicate support was intact even after the Pd loading and with strong NaBH_4 reduction treatment.

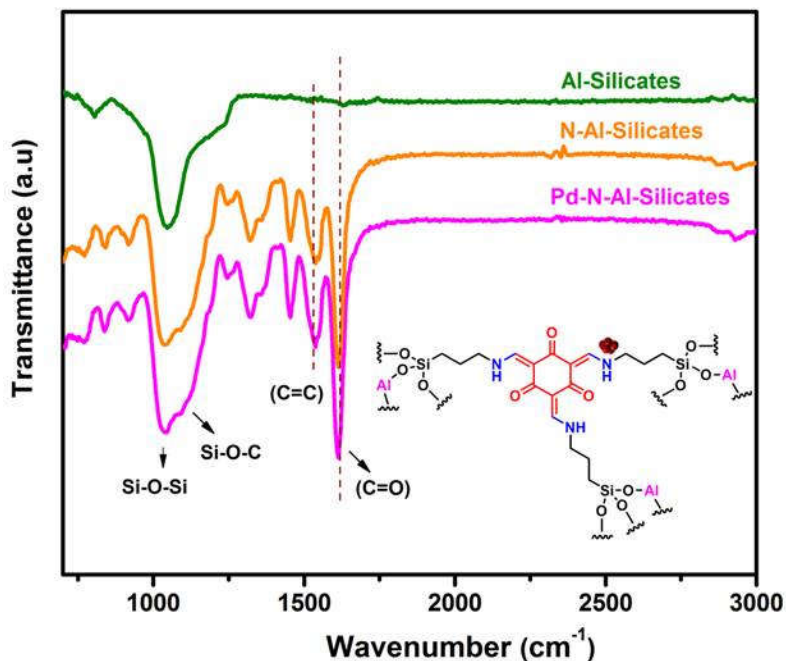


Figure 5.4: FT-IR spectra of Pd-Al-silicate catalysts.

5.3.5 Solid-state NMR Spectroscopy

The organic bridging and aluminium species in the mesoporous aluminosilicate framework were confirmed by the cross-polarization (CP) magic-angle spinning (MAS) NMR for the ^{13}C , ^{29}Si , ^{27}Al , and ^{15}N nuclei. The existence of the keto-form in the organic hybrid aluminosilicate was

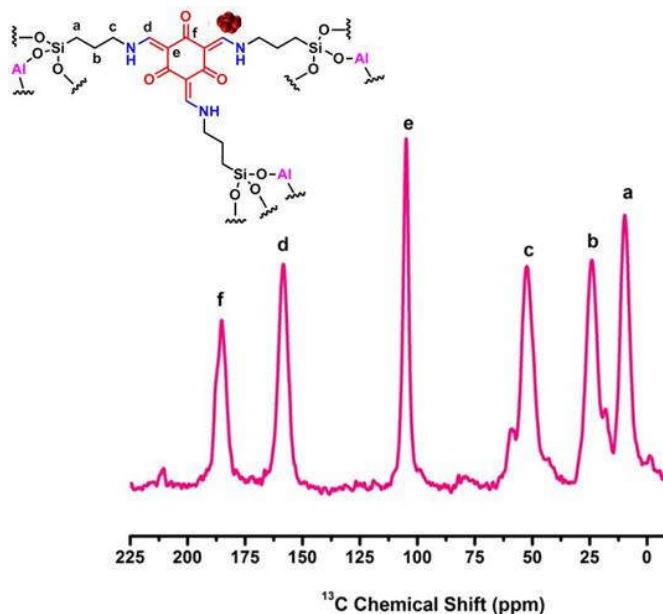


Figure 5.5: Solid-state ^{13}C NMR spectrum of Pd-N-Al-silicate catalyst.

established from ^{13}C CP-MAS solid-state NMR spectroscopy (Figure 5.5). The N-containing organic moiety in the bridging clearly showed the signal corresponding to the carbonyl group at 184 ppm, which unambiguously confirmed the existence of keto-form.

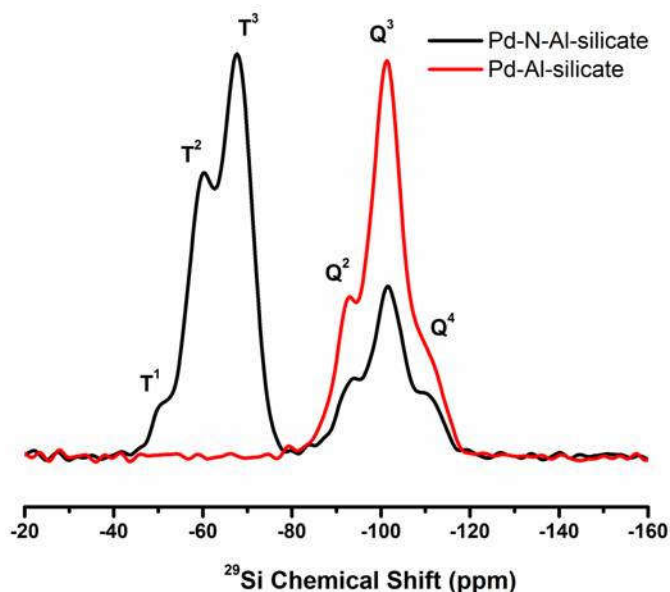


Figure 5.6: Solid-state ^{29}Si NMR spectra of Pd-N-Al-silicate and Pd-Al-silicate catalysts.

In ^{29}Si NMR spectra (Figure 5.6), the presence of two different types of Si environments in the framework were inferred and observed as peaks in the ranges from -90 to -113 ppm and -50 to -70 ppm corresponding to the Q^n sites and T^n sites, respectively.²⁴ The peaks at -50, -60, and -68 ppm in the T^n region represent the $\text{T}^1[\text{SiC}(\text{OSi})(\text{OH})_2]$, $\text{T}^2[\text{SiC}(\text{OSi})_2\text{OH}]$, and $\text{T}^3[\text{SiC}(\text{OSi})_3]$ linkages from the organic spacer bridge in the siliceous framework. The signals from the Q^n sites at -91, -100, and -110 ppm from $[\text{Si}(\text{OSi})_2(\text{OH})_2]$, $[\text{Si}(\text{OSi})_3(\text{OH})]$, and $[\text{Si}(\text{OSi})_4]$, respectively, were observed from the inorganic bridge in the framework. Both ^{13}C and ^{29}Si NMR showed the successful integration of the keto-form of the organic silane into the hybrid silica through our optimized synthesis methodology. The ^{15}N CP-MAS NMR spectra for hybrid Pd-N-Al-silicate displayed a peak at 132 ppm chemical shift assigned to the N-H species in the organic bridging functionality (Figure 5.7).²⁵ The N-H peak was visible due to the efficient ^1H cross-polarization effects. The absence of other peaks further confirmed the absence of the NH_2 group from the starting APTMS. Thus, the intact nature of the framework architecture was further confirmed from solid-state NMR studies.

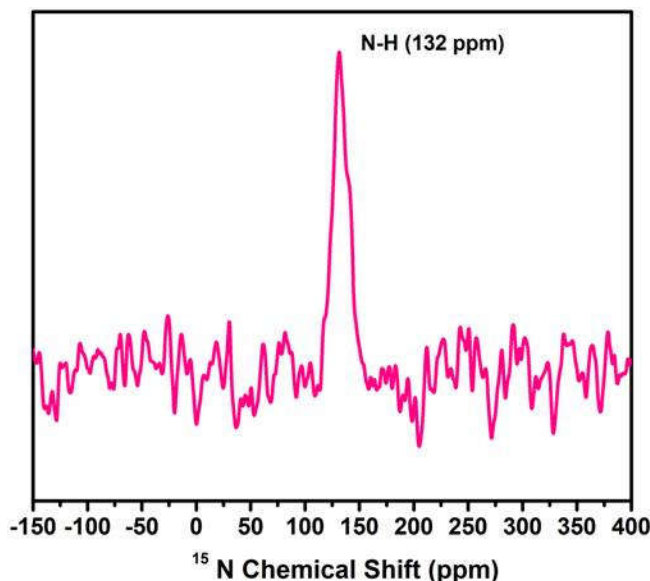


Figure 5.7: Solid-state ^{15}N NMR spectrum of Pd-N-Al-silicate catalyst.

The coordination environment of Al atoms in the Pd-N-Al-silicate hybrid catalyst was characterized by solid-state ^{27}Al NMR (Figure 5.8). The spectra of the hybrid sample (Si/Al =13) show two resonance peaks at 0 and 54 ppm, which can be assigned to octahedrally coordinated extra-framework aluminum and tetrahedrally (Td) coordinated framework aluminum, respectively, which strongly confirms that the majority of Al occupies in the organosilicate framework as Td structure rather than extra-framework Al species.²³

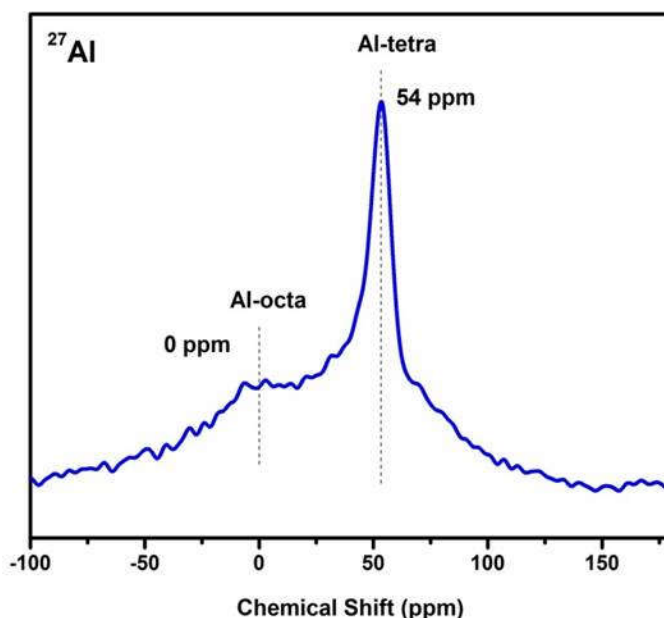


Figure 5.8: Solid-state ^{27}Al NMR spectrum of Pd-N-Al-silicate catalyst.

5.3.6 Electron Microscopy

TEM analysis was performed to investigate the effect of the organic-inorganic hybrid Al-silicate framework stabilizing the Pd NPs and validate the results obtained from PXRD analysis regarding the Pd particle size. The TEM image in Figure 5.9 exhibits the mesoporous nature of the modified silica with aluminium and N-containing organic bridging moieties (Pd-N-Al-silicate). Pd-N-Al-silicate catalyst demonstrates the highly dispersed small Pd NPs of size 3-5 nm on the hybrid support.

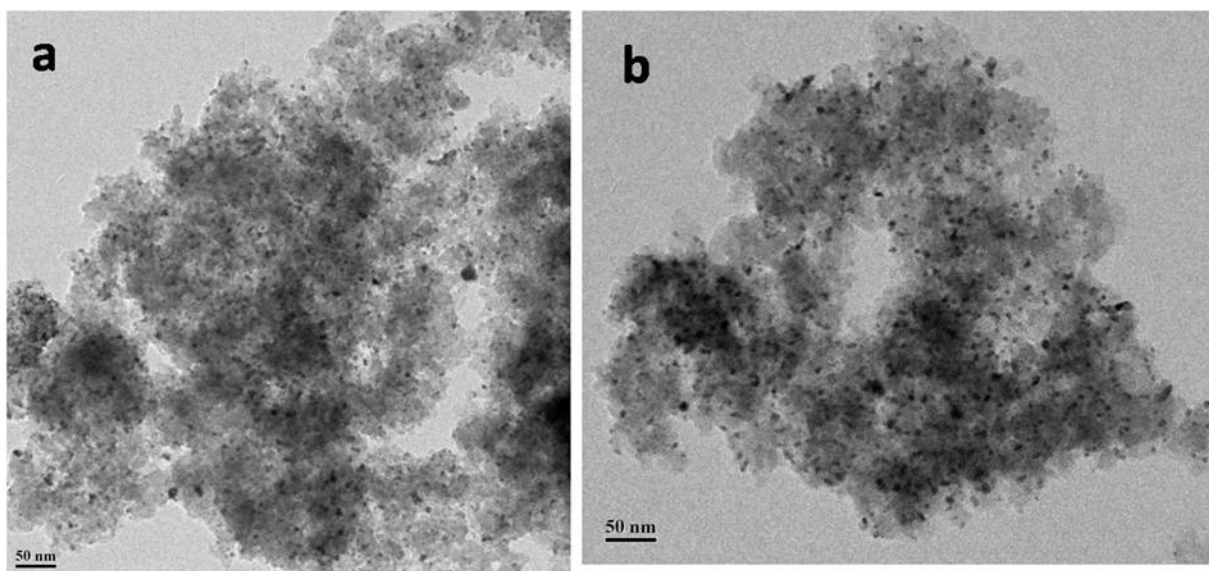


Figure 5.9: TEM images of Pd-N-Al-silicate catalyst.

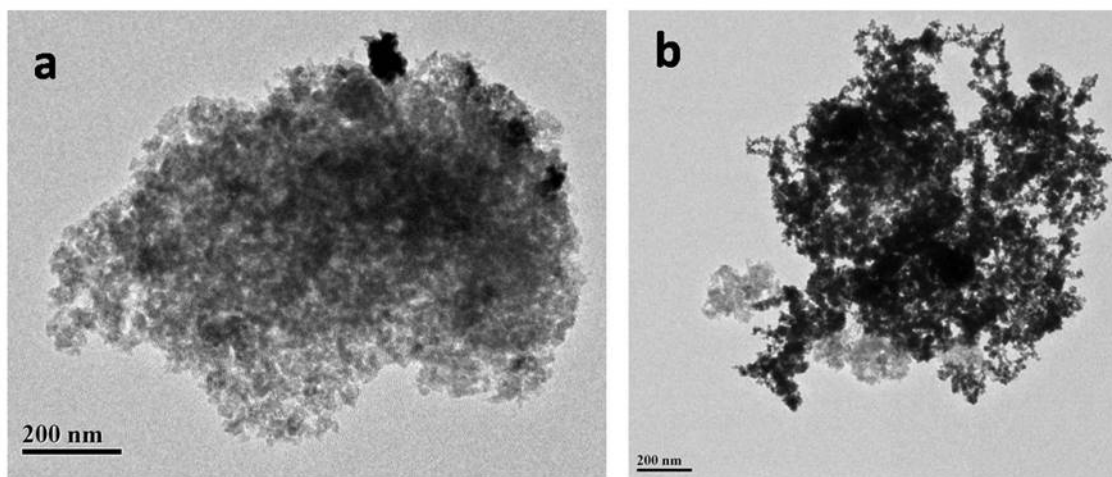


Figure 5.10: TEM images of Pd-Al-silicate catalyst.

From the TEM images (Figure 5.10) of pristine aluminosilicate supported Pd catalyst, the deposition of Pd on the support was observed to be very weak (Figure 5.10 a, b). The images showed the Pd metal nanoparticles to be agglomerated and resulted in poor dispersion. Also, most of the metal nanoparticles were located outside the aluminosilicate support and points to the weak interaction of the Pd NPs on the unmodified inorganic framework. To check the surface morphology of the Pd-N-Al-silicate and Pd-Al-silicate catalyst, SEM analysis was carried out (Figure 5.11). The images show irregularly shaped micron-sized particles in both N-Al-silicate and Al-silicate samples.

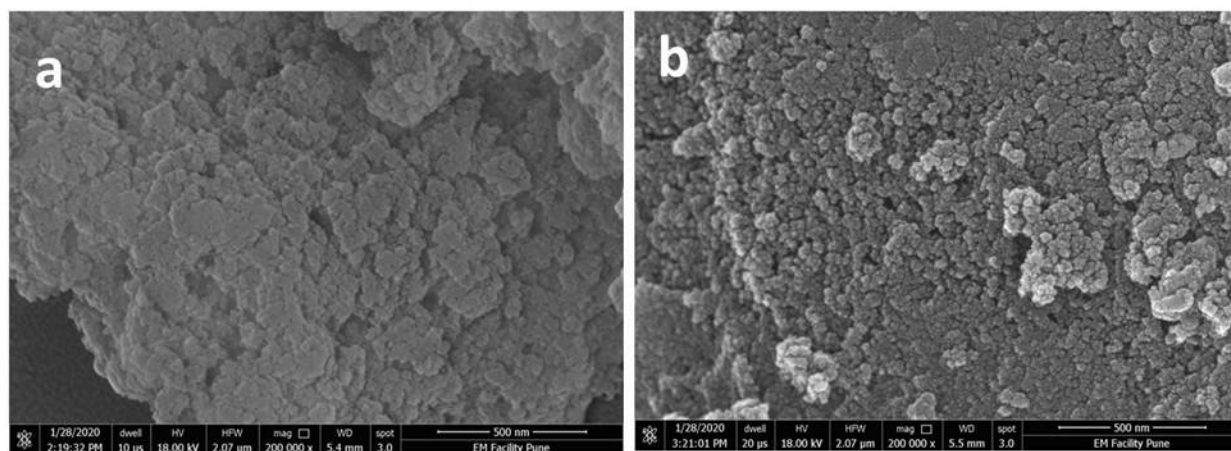


Figure 5.11: SEM images of (a) Pd-N-Al-silicate and (b) Pd-Al-silicate catalyst.

5.3.7 Acidity Measurements

To evaluate the nature and type of acidic sites present in Pd-N-Al-silicates and Pd-Al-silicates having the Si/Al ratio 13, pyridine adsorption experiment were carried out using FT-IR. From Figure 5.12, both Lewis and Bronsted acidic sites were detected in the aluminosilicate sample surfaces with a varying fraction of each site. Among these, Pd-N-Al-silicate catalysts showed a higher amount of acidity in comparison to Pd-Al-silicates. The temperature-programmed desorption (TPD) analysis was carried out using NH_3 as the probe molecule to quantify the acid loading in the catalyst (Figure 5.13). The temperature-induced desorption of chemisorbed NH_3 from the catalyst surface was measured by increasing the temperature from 50 °C to 700 °C. The aluminium incorporated silica catalysts showed two peaks at low-temperature desorption (100 °C) corresponding to the weak acidic sites and at higher temperature desorption (300 to 550 °C) for strong acidic sites.

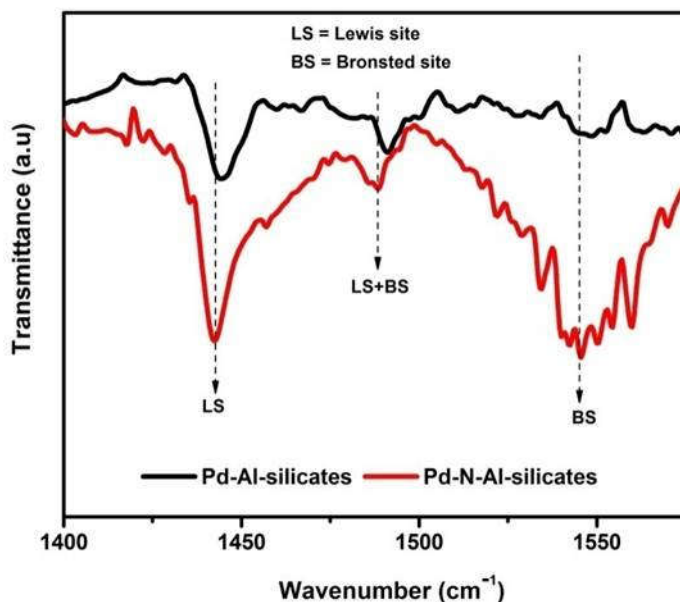


Figure 5.12: FTIR analysis of Pd-N-Al-silicates and Pd-Al-silicates using pyridine as a probe molecule.

The NH₃ desorption at low temperature is ascribed to the Bronsted acid sites and the higher temperature for the Lewis sites, where the NH₃ molecule was coordinatively adsorbed.^{26, 27} A shift in the strong acid site to lower temperature (400 °C) in organic-inorganic hybrid Pd-N-Al-silicate sample compared to that of inorganically

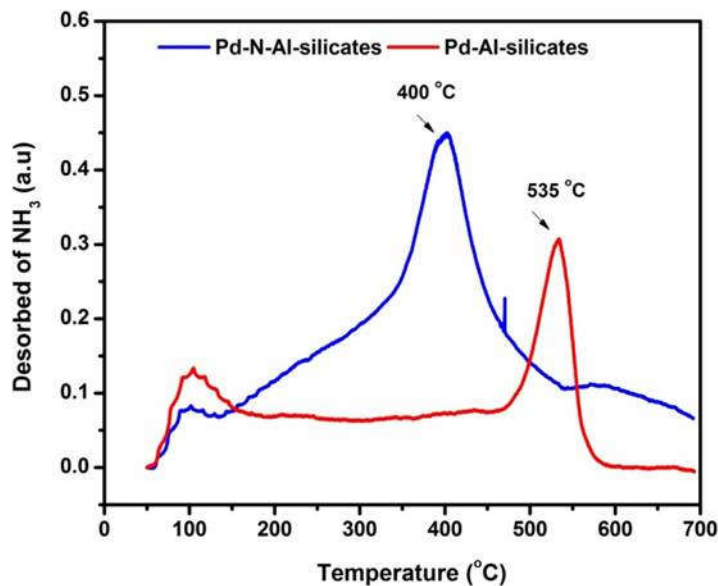


Figure 5.13: NH₃ TPD profile for Pd-N-Al-silicate and Pd-Al-silicate catalysts

bridged Pd-Al-silicate (535 °C) was noted. This can be attributed to the difference in the aluminium bridging environment in the silicate framework, which contributes different acidic strengths to the samples. The overall acidity in the samples was calculated and found to be 1.6 mmol/g for Pd-Al-silicate and 4.3 mmol/g for Pd-N-Al silicate catalyst, which matches well with IR results.

5.3.8 X-ray Photoelectron Spectroscopy

To garner insight into the nature of surface Pd species on the hybrid Pd-N-Al-silicate and Pd-Al-silicate support, XPS analysis has been carried out. The XPS spectra of Pd-N-Al-silicate catalyst showed two different peaks corresponding to $3d_{5/2}$ and $3d_{3/2}$, which gave two different Pd components centered at 335 and 337 eV after deconvolution corresponds to metallic Pd and oxidized Pd states, respectively (Figure 5.14 a). This indicates the ability of hybrid N-Al-silicate support to influence the electronic states of surface Pd species.

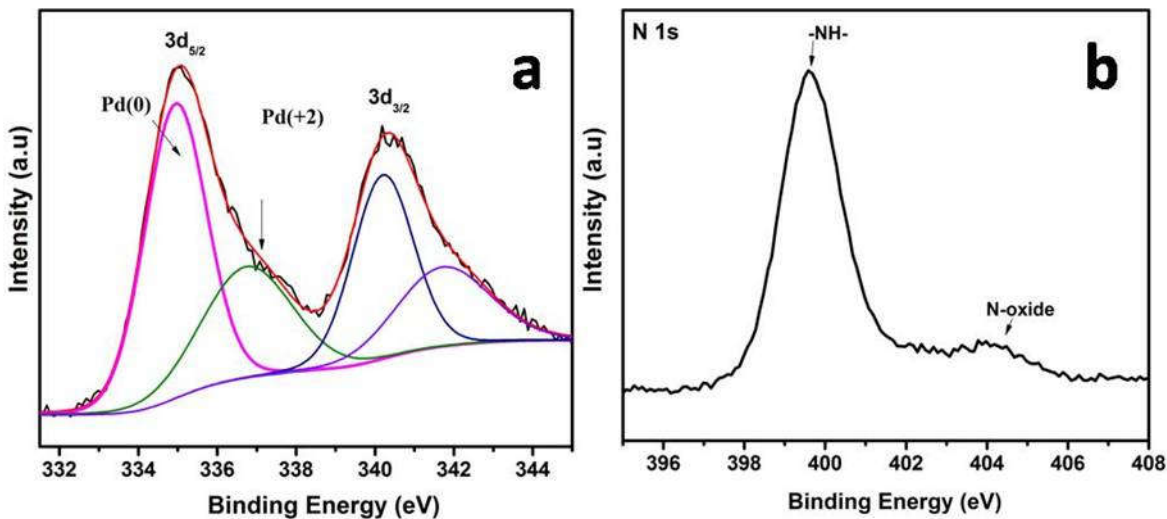


Figure 5.14: XPS plots of Pd-N-Al-silicate catalyst (a) Pd 3d and (b) N 1s.

The Pd supported Al-silicate material showed 100 % Pd (0) species compared to the hybrid silica system owing to the absence of N sites (Figure 5.15). The deconvolution of N1s spectra determined the chemical nature of N species in the hybrid silica and the major existence in N-H species (Figure 5.14 b).

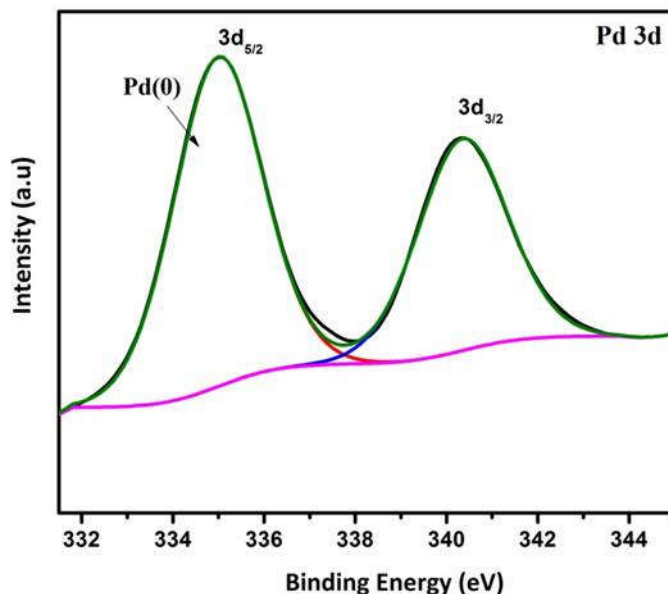
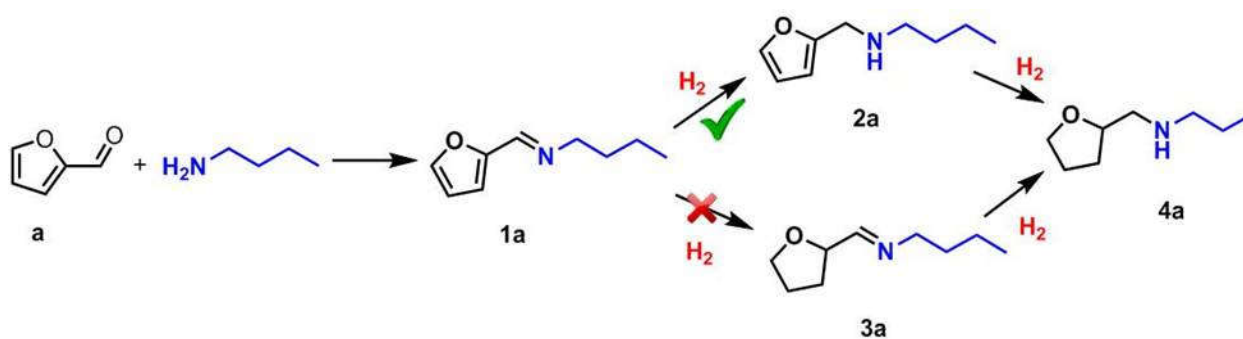


Figure 5.15: Pd 3d XPS plots of Pd-Al-silicate catalyst

5.3.9 Catalytic reductive amination of furfural

The catalysts were tested for the liquid-phase reductive amination of furfural at atmospheric hydrogen pressure and 40 °C. n-Butylamine was the amine used in the study. The reaction pathways involved in the RA reaction of furfural is shown in Scheme 5.4.



Scheme 5.4: Reaction pathways for the reductive amination of furfural with n-BuNH₂ in the presence of H₂ over supported Pd catalyst.

All the synthesized supported Pd catalysts were screened for the direct reductive amination of furfural reaction. All the Pd catalysts showed 100 % furfural conversion, but the selectivity was observed to vary over different supports. Among the tested catalysts, hybrid Pd-N-Al-silicate catalyst displayed maximum selectivity for 4a (86 %) followed by Pd-NPMO (64 %), Pd-SBA-15(DP) (56 %), and the minimum was Pd-Al₂O₃ (39 %) and Pd-Al-silicate (40 %) catalysts during 9 h of reaction. The catalytic activity comparison is represented in Figure 5.16. The

difference in the associated textural properties of the support and the stabilized Pd particle size and dispersion can be the reason for the selectivity variation.

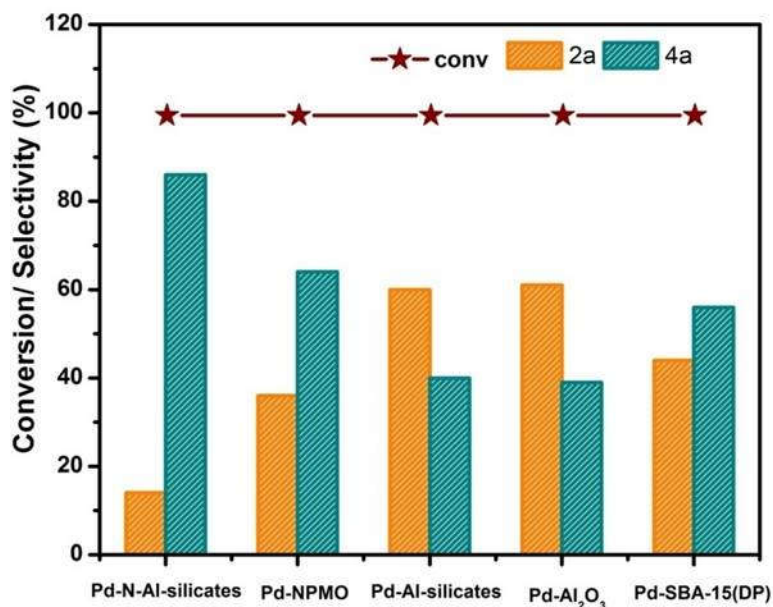


Figure 5.16: Supported Pd catalyst screening for RA of furfural. Reaction conditions: FA (0.4 mmol), EtOH (2.5 mL), n-BuNH₂ (0.4 mmol), catalyst (10 mg), T (40 °C), t (9 h) and H₂ (1 atm).

The optimization of reaction parameters was carried out systematically. The effect of reaction temperature was studied (Figure 5.17) and noted that the 100 % furfural conversion was achieved at 40 °C with product selectivities for 2a (23 %) and 4a (76 %). Increasing the reaction temperature beyond 40 °C showed least difference in the selectivities. Hence the optimized temperature for the direct RA of furfural was 40 °C. The kinetic profile of the furfural RA reaction over Pd-N-Al-silicate was studied at 40 °C and 1 bar H₂ pressure (Figure 5.18 a, b). By analyzing the initial rate of reaction, the 100 % furfural conversion was observed within 15 min of reaction (Figure 5.18 a) with selectivity for 2a (70 %) and 4a (18 %). As the reaction was allowed to proceed, the yield for the product 4a gradually increased at the expense of 2a and reached a maximum of 4a, 86 % within 9 h. Further increase in reaction time did not affect the selectivity. Hence further, all the reactions were studied for 9 h.

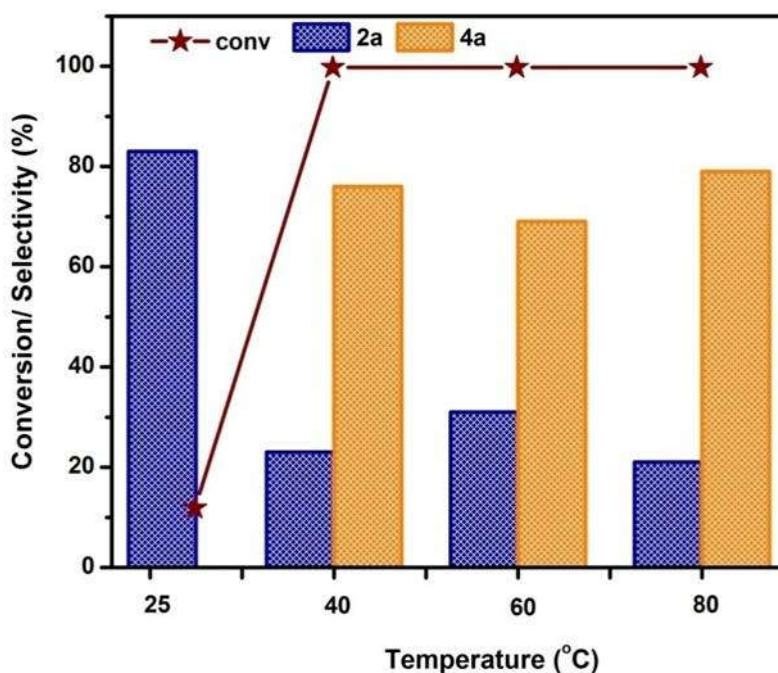


Figure 5.17: Effect of reaction temperature on RA reaction over Pd-N-Al-silicate catalyst. Reaction conditions: FA (0.4 mmol), EtOH (2.5 mL), n-BuNH₂ (0.4 mmol), catalyst (10 mg), T (40 °C), t (6 h) and H₂ (1 atm).

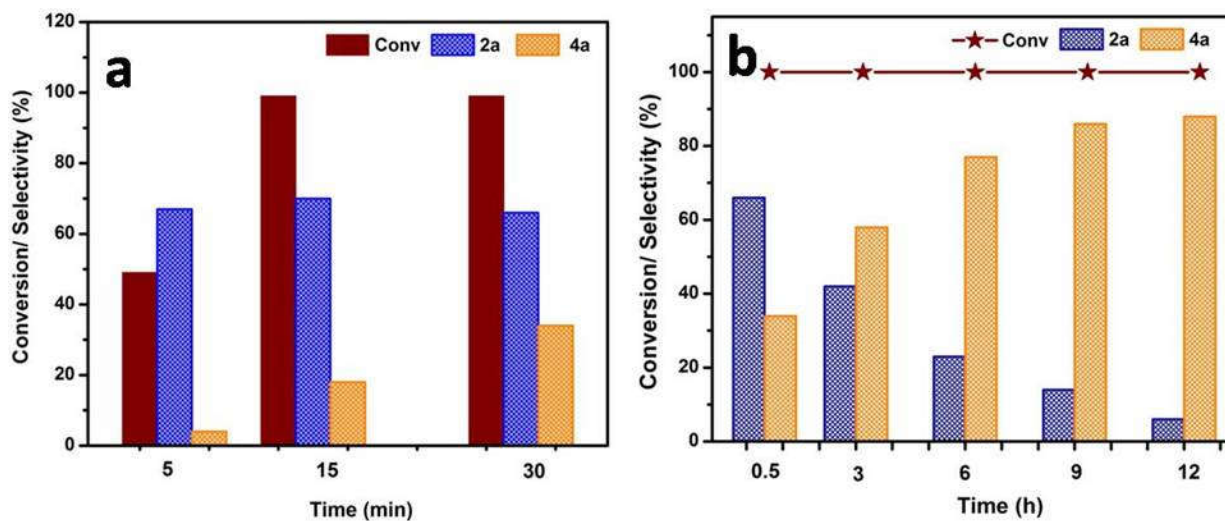


Figure 5.18: Effect of reaction time on RA reaction over Pd-N-Al-silicate catalyst.

The effect of Pd loading on hybrid N-Al-silicate support was tested (Figure 5.19). The percentage of Pd loading with respect to the support was varied from 1 to 10 wt %. All the other

reaction parameters were kept similar to the previous reactions. It was noted that all Pd loaded catalysts showed complete furfural conversion, but the selectivity for the product 4a was found to vary during the reaction for 9 h as can be seen from (Figure 5.19).

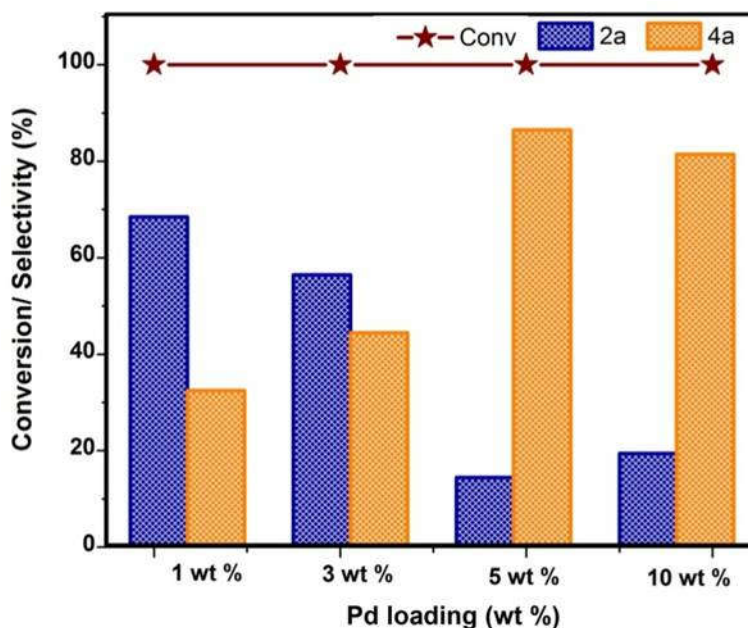


Figure 5.19: Effect of Pd loading on RA reaction over Pd-N-Al-silicate catalyst.

As the metal loading increased from 1 to 5 wt %, the 4a selectivity increased from 32 % to 86 %, and by further increasing the Pd loading to 10 wt %, a noticeable decrease on 4a selectivity was observed. At low Pd loading, sufficient active Pd sites are less in number, which restricts the hydrogenation of 2a to the desired 4a product. As the loading increased to the optimum (5 wt %), maximum selectivity for 4a was achieved. Further increase in the Pd does not show any enhancement; instead, it shows a slight selectivity decrease. From the reported literature, ethanol was the choice of solvent for the reaction.²⁸ The protic solvent like ethanol was reported to be more active than the aprotic polar/non-polar solvents in the reductive amination reaction. Ethanol could decrease the catalyst-solvent interactions, which can help to overcome the side reactions like hydrogenation reaction, and they also promote the furfurylimine formation reaction between furfural and n-BuNH₂.²⁹

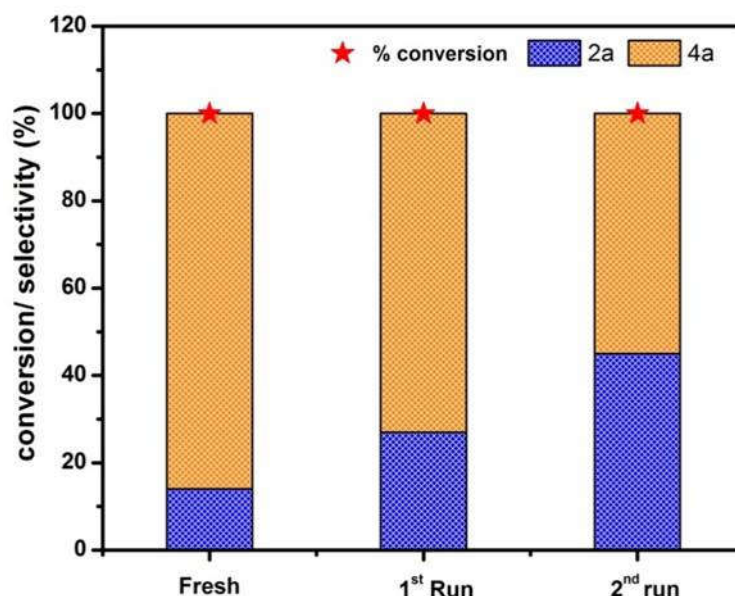


Figure 5.20: Reusability test of Pd-N-Al-silicate catalyst for RA of furfural.

Finally, the heterogeneous nature of the catalyst was tested using recycling studies, where the catalyst was separated after the fresh run and washed thoroughly with ethanol, and dried at 60 °C. The obtained catalyst was loaded for the subsequent two consecutive catalytic runs under similar reaction conditions. The results are given in Figure 5.20, where after each cycle, a gradual decrease in the selectivity for the 4a was observed even though 100 % conversion was achieved in all the repetitive cycles. The possible reason could be the blocking of active sites with the organic residues from each catalytic run. To further confirm, the Pd-N-Al-silicate catalyst was studied by the hot-filtration method under the optimized reaction conditions. After a 3 h reaction (55 % of 4a produced), the catalyst was filtered off, and the filtrate was allowed to proceed further for the RA reaction for the remaining 9 h under identical conditions. No increase in the 4a yield was observed, maintaining the 55 % selectivity in the reaction medium, suggesting that the catalysis is purely heterogeneous (Figure 5.21).

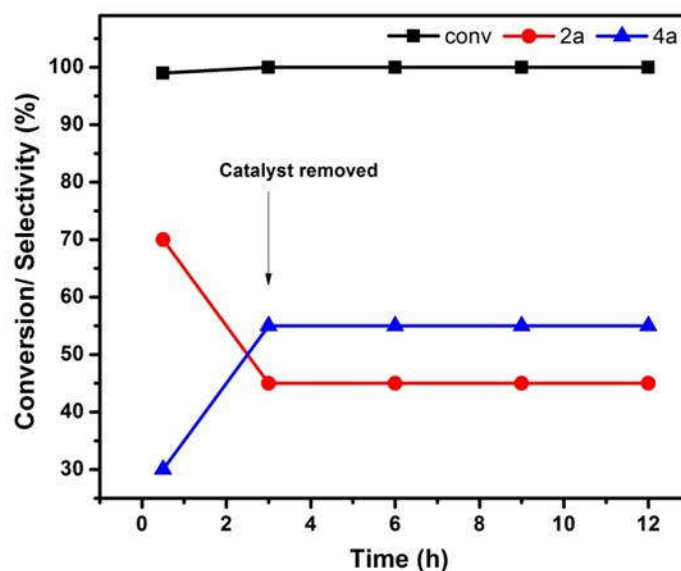


Figure 5.21: Heterogeneity study of Pd-N-Al-silicate catalyst by hot-filtration test (catalyst removed after 3 h reaction, and further reaction carried in the absence of catalyst).

The Pd 3d XPS measurements on the Pd-N-Al-silicate spent catalyst after the catalytic run at 40 °C and 1 atm H₂ pressure confirmed that the significant Pd species on the active surface exists as Pd(0) (Figure 5.22a). No obvious change was observed in the TEM image (Figure 5.22b) of the recycled Pd-N-Al-silicate catalyst compared to the fresh along with the retention of small Pd nanoparticles (2-5 nm) on the spent catalyst with excellent dispersion was maintained even after the liquid-phase reaction.

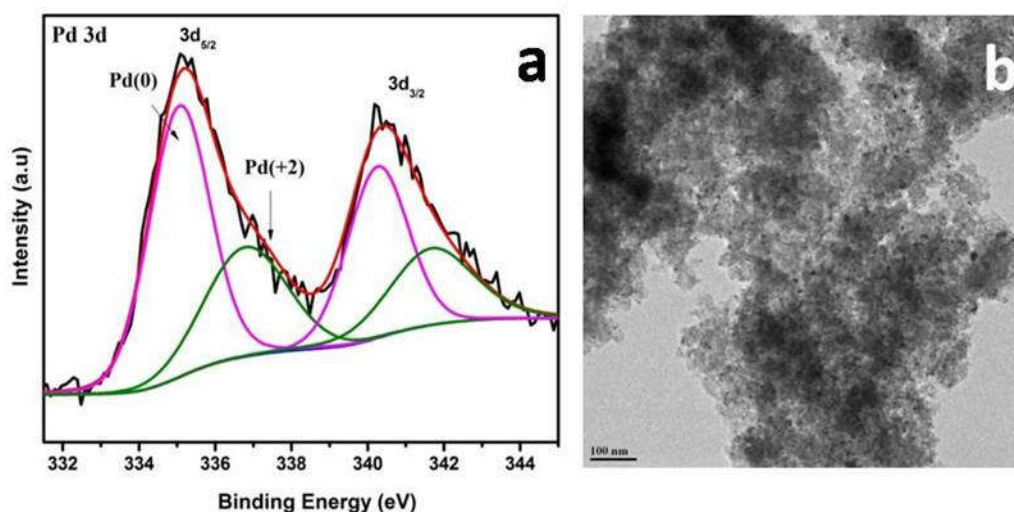


Figure 5.22: Spent Pd-N-Al-silicate catalyst analysis using (a) Pd 3d XPS and (b) TEM

5.4 Conclusions

Organic-inorganic hybrid mesoporous silica with N-containing organo-bridges and aluminium species has been synthesized using a one-pot, cationic surfactant templating method. The integration of aluminium and organic N-moiety inside the hybrid silicate framework was confirmed through various physical, spectroscopic, and microscopic techniques after the template removal using solvent extraction procedure with acidified ethanol. The aluminium predominantly presents in the form of tetrahedral coordination in the organosilica bridges. The aluminium centers on the catalyst provided much higher acidity compared to the inorganic aluminosilicates. The hybrid N-containing bridged organo-aluminosilicates had used as support for the stabilization of Pd NPs. Well dispersed small Pd NPs with an adequate fraction of under-coordination sites were immobilized on the mesoporous hybrid N-Al-silicate support compared to the conventional aluminosilicates using a simple chemical reduction method. This could be attributed to the presence of N-sites in the catalyst framework on which Pd nanoparticles can bind uniformly. This bifunctional (metallic and acidic sites) hybrid supported Pd catalyst was tested for the liquid-phase reductive amination of furfural and displayed enhanced catalysis compared to the conventional system. Pd-N-Al-silicates (86 % 4a) showed better catalytic activity compared to Pd-Al-silicate, Pd-SiO₂, and Pd-Al₂O₃ catalysts, which is due to the high dispersion of Pd nanoparticles and the presence of N sites along with the acidic aluminium centers on the hybrid organo-aluminosilicate framework, which can electronically modify Pd sites responsible for catalysis. The heterogeneity test on the Pd-N-Al-silicate catalyst confirmed that the catalysis is purely heterogeneous in nature.

5.5 References

1. L. Shuai, M. Talebi Amiri and J. S. Luterbacher, *Current Opinion in Green and Sustainable Chemistry*, 2016, **2**, 59-63.
2. C. Li, X. Zhao, A. Wang, G. W. Huber and T. Zhang, *Chemical Reviews*, 2015, **115**, 11559-11624.
3. Z.-Y. Yang, Y.-C. Hao, S.-Q. Hu, M.-H. Zong, Q. Chen and N. Li, *Advanced Synthesis & Catalysis*, 2021, **363**, 1033-1037.
4. A. Gandini, T. M. Lacerda, A. J. F. Carvalho and E. Trovatti, *Chemical Reviews*, 2016, **116**, 1637-1669.
5. I. Delidovich, P. J. C. Hausoul, L. Deng, R. Pfützenreuter, M. Rose and R. Palkovits, *Chemical Reviews*, 2016, **116**, 1540-1599.
6. D. Willcox, B. G. Chappell, K. F. Hogg, J. Calleja, A. P. Smalley and M. J. Gaunt, *Science (New York, N.Y.)*, 2016, **354**, 851-857.
7. V. Froidevaux, C. Negrell, S. Caillol, J.-P. Pascault and B. Boutevin, *Chemical Reviews*, 2016, **116**, 14181-14224.
8. T. Senthamarai, K. Murugesan, J. Schneidewind, N. V. Kalevaru, W. Baumann, H. Neumann, P. C. J. Kamer, M. Beller and R. V. Jagadeesh, *Nature Communications*, 2018, **9**, 4123.
9. P. Roose, K. Eller, E. Henkes, R. Roszbacher and H. Höke, in *Ullmann's Encyclopedia of Industrial Chemistry*, DOI: https://doi.org/10.1002/14356007.a02_001.pub2, pp. 1-55.
10. H. Li, H. Guo, Y. Su, Y. Hiraga, Z. Fang, E. J. M. Hensen, M. Watanabe and R. L. Smith, *Nature Communications*, 2019, **10**, 699.
11. N. Brun, P. Hesemann and D. Esposito, *Chemical Science*, 2017, **8**, 4724-4738.
12. S. Pisiewicz, T. Stemmler, A.-E. Surkus, K. Junge and M. Beller, *ChemCatChem*, 2015, **7**, 62-64.
13. T. Stemmler, A.-E. Surkus, M.-M. Pohl, K. Junge and M. Beller, *ChemSusChem*, 2014, **7**, 3012-3016.
14. M. Chatterjee, T. Ishizaka and H. Kawanami, *Green Chemistry*, 2016, **18**, 487-496.
15. T. Komanoya, T. Kinemura, Y. Kita, K. Kamata and M. Hara, *Journal of the American Chemical Society*, 2017, **139**, 11493-11499.
16. A. Dunbabin, F. Subrizi, J. M. Ward, T. D. Sheppard and H. C. Hailes, *Green Chemistry*, 2017, **19**, 397-404.
17. J. A. T. Caetano and A. C. Fernandes, *Green Chemistry*, 2018, **20**, 2494-2498.
18. Y. Zhu, R. Batchelor, A. B. Lowe and P. J. Roth, *Macromolecules*, 2016, **49**, 672-680.
19. J. J. Martínez, E. Nope, H. Rojas, M. H. Brijaldo, F. Passos and G. Romanelli, *Journal of Molecular Catalysis A: Chemical*, 2014, **392**, 235-240.
20. Annemieke W. Heinen, Joop A. Peters and Herman v. Bekkum, *European Journal of Organic Chemistry*, 2000, **2000**, 2501-2506.

21. A. Srivani, P. S. S. Prasad and N. Lingaiah, *Catalysis Letters*, 2012, **142**, 389-396.
22. A. K. Mathew, A. Abraham, K. K. Mallapureddy and R. K. Sukumaran, in *Waste Biorefinery*, eds. T. Bhaskar, A. Pandey, S. V. Mohan, D.-J. Lee and S. K. Khanal, Elsevier, 2018, DOI: <https://doi.org/10.1016/B978-0-444-63992-9.00009-4>, pp. 267-297.
23. A. C. Sunil Sekhar, A. E. Ashokkumar, C. T. Cygnet, S. Vidhya Lakshmi, F. L. Deepak and C. P. Vinod, *ChemNanoMat*, 2018, **4**, 537-541.
24. A. Lazar, K. J. Betsy, C. P. Vinod and A. P. Singh, *Catalysis Communications*, 2018, **104**, 62-66.
25. Y. Hu, Y. Shim, J. Oh, S. Park, S. Park and Y. Ishii, *Chemistry of Materials*, 2017, **29**, 5080-5089.
26. J. L. Nyalosaso, G. Derrien, C. Charnay, L.-C. de Menorval and J. Zajac, *Journal of Materials Chemistry*, 2012, **22**, 1459-1468.
27. R. Viscardi, V. Barbarossa, R. Maggi and F. Pancrazzi, *Energy Reports*, 2020, **6**, 49-55.
28. S. Song, Y. Wang and N. Yan, *Molecular Catalysis*, 2018, **454**, 87-93.
29. S. Jiang, E. Muller, F. Jérôme, M. Pera-Titus and K. De Oliveira Vigier, *Green Chemistry*, 2020, **22**, 1832-1836.

CHAPTER-6

Summary and Conclusions

The necessity of designing efficient heterogeneous catalysts with well-dispersed, easily accessible catalytically active centres can be achieved by nanocatalysis. The nano-forms of most transition metals are studied for their enhanced heterogeneous catalysis since the small-sized metal nanoparticles interact with the reactants differently, resulting in distinct reactivity compared to the larger nanoparticles. The engineering of catalytically relevant materials with better diffusion properties has interested catalytic research in the recent past. Efforts have been devoted in designing heterogeneously catalytically active materials on silica with improved stability, functionalities, better diffusion property, and sinter resistance under reaction conditions. To avoid or minimize leaching, various strategies are explored, among which immobilizing the active sites on the inorganic oxides like silica is well-established. Nevertheless, silica is considered inert material for catalysis, which can merely hold the active catalytic sites. The work described in the present thesis consolidates the catalyst design, synthesis, characterization, and catalytic applications in various organic transformation reactions. The key focal point in this thesis based on the aforementioned considerations to stabilize small-sized metal nanoparticles on silica using different strategies includes (1) the chemical modifications by altering the silicate framework chemistry with the desired functionality (framework metal sites (Ti and Al) and N-bridged organic hybrid centers), (2) changing the morphological architectures (yolk-shell and core-shell) and (3) supporting active metal oxide centers over silica (Cr and Ru oxides). The major conclusions drawn out of the basic observations are summarized as;

Chapter 1 of the thesis explores a general introduction to the status of heterogeneous catalysis, specifically nanocatalysis, and its progress in recent times. Quantum confinement of nanoparticles alters the physical and chemical properties, which will reflect in the catalytic activity and discussed in this chapter. The role of porous materials in catalysis has been discussed, emphasizing mesoporous materials. Well-established synthesis protocols for synthesizing various silica supports, specifically hybrid porous silica-based materials, have been summarized. Furthermore, a general introduction of various instruments and techniques used for the present thesis work has been elaborated. The applications of these nanocatalysts in various industrially important catalytic reactions and progress made to date have been portrayed with the help of comprehensive literature reports.

Chapter 2: A detailed understanding of the chromium and ruthenium oxide-supported MCM-41 silica catalysts for the industrially significant cyclohexane oxidation and phenol hydrogenation reactions, respectively, was demonstrated in two separate sections 2A and 2B. In chapter 2A, a simple wet-impregnation synthesis method was explored for stabilizing the active Cr species on nano spherical MCM-41 and tested for the liquid-phase cyclohexane oxidation reaction. Further, the optimum catalyst was found to improve the catalytic activity by altering the Cr metal loading. The nature of Cr active species for cyclohexane oxidation reaction has been determined by correlating catalytic activity with characterization results. Under mild reaction conditions, the optimum catalyst (5CrO_x-MCM-41) gave 72 % conversion and 99 % selectivity towards cyclohexanone. The volcano-type catalytic performance could be attributed to the interplay between the surface Cr⁶⁺ and Cr³⁺ species in the material, which varies with the Cr content. The excellent activity towards the cyclohexanone product can be accredited to the initial concentration of the extra-framework amorphous Cr³⁺ species in the MCM-41 supported catalyst. In chapter 2B, one-pot synthesis of RuO₂-MCM-41 catalyst with small-sized RuO₂ (~6 nm) was achieved with the help of ethylenediamine as the ligand to control the ruthenium particle size. The catalyst was well characterized and tested for the aqueous phase hydrogenation of phenol and its derivatives under optimized reaction conditions. The catalyst was found to be highly stable and recyclable without any loss of activity.

Chapter 3 deals with the synthesis of gold-based catalysts for alkene epoxidation. The catalytic activity of gold is critically dependent on NPs size of 3-5 nm. Mesoporous titanium-modified organic-inorganic hybrid silica nanostructures (yolk-shell and core-shell) were synthesized using the sol-gel hydrothermal method to restrict the gold sintering. The ethane and biphenyl organic motif incorporated inside the Ti-modified silica spheres where the ethane bridging silane precursor resulted in a hollow spherical architecture, whereas the biphenyl silane precursor ends up with hybrid silica spheres with no void space. The liquid-phase oxidation of cyclooctene over these nanoarchitectures with varying Ti content was tested. The catalyst with best Si/Ti ratio (100) with a larger fraction of Ti⁴⁺(Td) sites showed a better catalytic performance. The Au NP encapsulated Ti-HPMO catalyst worked as nanoreactors for the industrially important styrene epoxidation reaction. The enhanced catalytic performance in conversion was observed for the Au@Ti-HPMO_e catalyst with a hollow structure with a thin porous shell facilitating a favourable

mass transfer compared to core-shell morphology. This encapsulation strategy with porous hybrid silica shell was found to prevent the leaching and sintering of small Au NPs during the liquid-phase catalysis.

Chapter 4 gives insights on the framework chemistry in fine-tuning the metal nanoparticle size over silica. The Pd nanoparticles supported over a new hybrid N-containing periodic mesoporous organosilica displayed the stabilization of small-sized Pd NPs (3-5 nm) with better dispersion compared to the conventional silica-supported Pd counterparts. The spectroscopic (NMR, IR, etc.) and microscopic studies (HAADF-STEM and elemental mapping) confirmed chemically modified silica framework with the N sites and identified Pd NPs well dispersed over the mesoporous NPMO material. This Pd@NPMO hybrid silica catalyst was tested for the aqueous phase hydrogenation catalysis of phenol and CO₂ molecules. The optimum catalyst was found to show better catalytic performance in both reactions. The phenol hydrogenation at 40 °C and 1 atmospheric H₂ pressure in water showed complete conversion with 99 % selectivity for cyclohexanone. The Pd@NPMO catalyst displayed high stability and recyclability in the phenol hydrogenation reaction, and the substrate scope study also evidences the superior performance of the catalyst for the reaction. Under optimized reaction, the CO₂ hydrogenation in the alkaline aqueous medium at 100 °C and 4 MPa H₂ pressure gave formate with TOF 108 h⁻¹. The conventional Pd@SBA-15 showed only a TOF of 9.4 h⁻¹, demonstrating the role of nitrogen sites on NPMO supports boosting the CO₂ reduction with complete selectivity to formate under mild reaction conditions. A combination of characterization and catalytic results confirmed the CO₂ hydrogenation catalysis on Pd@NPMO to be purely heterogeneous in nature.

Chapter 5, the bifunctional catalytic behaviour of the Pd-supported N-containing hybrid aluminosilicate catalyst is explored. One-pot synthesis of the hybrid aluminosilicate was achieved using the sol-gel method (N-Al-silicates). The N-sites inside the aluminosilicate hybrid framework facilitated the dispersion of the small Pd NPs (3-5 nm) through a simple chemical-reduction method. The unmodified Pd-Al-silicates showed the formation of larger-sized Pd NPs. The new organo-bridged aluminosilicates were characterized and tested for the liquid-phase reductive amination reaction of furfural using n-butylamine as the amine source at 40 °C and 1 atmospheric H₂ pressure. The control experiments proved that the acidic aluminium Td sites and the well-dispersed small-sized Pd NPs in hybrid Pd-N-Al-silicate facilitated the better catalytic

performance with very high selectivity for the targeted THF-derived amine product (86 % 4a) in comparison to Pd-Al-silicate, Pd-SiO₂, and Pd-Al₂O₃ catalysts. The heterogeneity test on the Pd-N-Al-silicate catalyst confirmed that the catalysis is purely heterogeneous.

ABSTRACT

Name of the Student: Betsy K. J

Registration No.: 10CC18A26061

Faculty of Study: Chemical Sciences

Year of Submission: 2022

AcSIR academic centre/CSIR Lab: CSIR- National Chemical Laboratory

Name of the Supervisor(s): Dr. C. P. Vinod

Title of the thesis: Exploring the Chemical Modifications in Periodic Mesoporous Silica Materials for Heterogeneous Catalytic Applications

The dominance of supported metal nanoparticles in heterogeneous catalysis is growing every day, playing a crucial role in catalyzing various industrially important chemical transformations. The characteristics of support and metal nanoparticles (NP's) in heterogeneous catalysts determine the catalytic trends in catalytic reaction. More precisely, the catalytic activity can vary depending upon the strength of metal-support interaction. So the active catalyst must possess metal NPs of optimum size on a support that can extract maximum activity from metal NPs. Periodic mesoporous organosilica (PMOs), the advanced silica material over the past few years owing to their high surface area, tunable porosity, and structural diversity with a myriad of applications including catalysis. Unlimited possibilities of PMOs offer the judicious choice of bridging functional framework linkers through preparation conditions. Hybrids of nanostructured periodic mesoporous silica with covalently incorporated organic groups or heteroatom in the pore walls of silica framework without destructing the mesopores induce unique properties. The ability to alter the pore size, surface area and topology, and incorporate task-specific functional groups into the framework with molecular scale periodicity makes them potential materials for fine chemical synthesis. In order to create active sites for catalysis in the mesoporous silica, organic moieties with functional groups can be anchored onto their surface or framework of silica. Functionalization by incorporating heteroatoms either in the pore wall or on the pore surface. Such homogeneously distributed organic moieties in silica framework and altering the structure, composition, and relative contents of the organic groups can increase its utility in catalysis. Though considerable progress has been made in PMOs, it is still difficult to synthesize PMOs with desired morphology and structure due to its instability in synthesis protocol. Chemical modification in silica by altering the surface characteristics by incorporating task specific organic functionality or dispersion of metal oxides was achieved. The framework modified silica was found to facilitate the stabilization of nano-sized metal NPs without any stabilizing agents. The hollow architectures of gold encapsulated periodic mesoporous silica nanoreactors were found to overcome the sintering during the catalysis making the process sustainable and purely heterogeneous. The new N-bridged periodic mesoporous silica materials were found to stabilize small metal NPs with excellent dispersion and found to be active compared to the conventional silica system. Based on the catalyst design, various industrially important liquid phase oxidation and hydrogenation reactions were performed and the catalytic potential of these materials thoroughly explored. A structure-activity correlation has also been established using multiple spectroscopic techniques.

List of publication(s) emanating from the thesis work:

- ❖ **K. J. Betsy**, Anish Lazar, Anjuna Pavithran and C. P. Vinod, CO₂ Hydrogenation to Formate by Palladium Nanoparticles Supported on N-Incorporated Periodic Mesoporous Organosilica, *ACS Sustainable Chem. Eng.* **2020**, 8, 39, 14765–14774.
- ❖ **K. J. Betsy**, Chandrani Nayak, Anish Lazar, Athira Krishnan, D. Bhattacharyya, S. N. Jha and C. P. Vinod, Selective oxidation of cyclohexane to cyclohexanone using chromium oxide supported mesoporous MCM-41 nanospheres: Probing the nature of catalytically active chromium sites, *ChemCatChem*, **2018**, 10, 3291.
- ❖ **K.J Betsy**, Anish Lazar, and C. P. Vinod, Highly selective aqueous phase hydrogenation of phenols over nanostructured RuO₂ on MCM-41 catalysts, *Nano-structures and Nano-Objects*, **2018**, 13, 36-43.
- ❖ **K. J. Betsy**, and C. P. Vinod; Confinement of single Au nanoparticles inside titanium doped hollow structured mesoporous organosilica nanoreactors for alkene oxidation (Manuscript under preparation).
- ❖ **K. J. Betsy**, and C. P. Vinod; Pd nanoparticles in multifunctional N-incorporated hybrid organosilica and the impact on room temperature phenol hydrogenation (Manuscript under preparation).
- ❖ **K. J. Betsy**, Anju George and C. P. Vinod; Pd-supported bridged organo-aluminosilicate hybrid catalyst for reductive-amination of furfural (Manuscript under preparation).

List of publication(s) not emanating from the thesis:

- ❖ Anish Lazar, **K. J. Betsy**, C.P. Vinod and A.P. Singh, Ru(II)-organofunctionalised SBA-15 as highly chemoselective and acid free catalyst for acetalization of aldehydes and ketones, *Catalysis Communications*. **2018**, 104, 62-66.
- ❖ S. Sreedhala, Shruti Maheshwari, **K. J. Betsy**, C.P. Vinod, Large trisoctahedral Au nanoparticles encapsulated inside porous silica catalyses CO oxidation at room temperature: Probing the effect of encapsulation and the role of step atoms and interfaces, *Applied Catalysis A: General*. **2016**, 524, 1–7.

List of conferences and seminars (presented & attended):

❖ Oral presentation in NCL-RF Annual students' conference 2019 at CSIR-National Chemical Laboratory, Pune on November 28-29, 2019.

Title: Catalytic Boosting of CO₂ Hydrogenation by Fine Palladium Nanoparticles on N-incorporated Periodic Mesoporous Organosilica (PMO)

Abstract: Catalytic transformation of CO₂ to fuels and chemicals are intensely pursued due to the growing demand for energy worldwide and designing an efficient heterogeneous catalyst capable for the selective transformation of CO₂ remains challenging. Even otherwise mitigating CO₂ is a top priority due to the impact this molecule has in contributing to the global warming and climate change. In this contribution, we account a surfactant-directed synthesis of new nitrogen-incorporated periodic mesoporous organosilica nanosphere (NPMO) within the framework. Thoroughly characterized hybrid N-incorporated PMO was utilized as a platform for stabilizing well dispersed accessible Pd nanoparticles (Pd-NPMO) in the absence of any stabilizing agents or expensive dendrimers. Further this bifunctional hybrid catalyst has been demonstrated to show an excellent ligand property in the heterogeneously Pd-catalyzed aqueous phase CO₂ hydrogenation to produce formic acid under our optimized conditions. To validate the significant catalytic performance of Pd-NPMO catalyst, we compared the activity with Pd-SBA-15 catalysts and the results showed a three-fold enhancement which demonstrated the crucial role of nitrogen sites in our catalyst for CO₂ valorization to formic acid.

❖ Participated in the National Conference on Optics Photonics and Synchrotron Radiation for Technological Applications (OPSR-2018) at Raja Ramanna Centre for Advanced Technology, Indore on 29th April to 2nd May, 2018

CO₂ Hydrogenation to Formate by Palladium Nanoparticles Supported on N-Incorporated Periodic Mesoporous Organosilica

K. J. Betsy, Anish Lazar, Anjuna Pavithran, and C. P. Vinod*

Cite This: *ACS Sustainable Chem. Eng.* 2020, 8, 14765–14774

Read Online

ACCESS |



Metrics & More



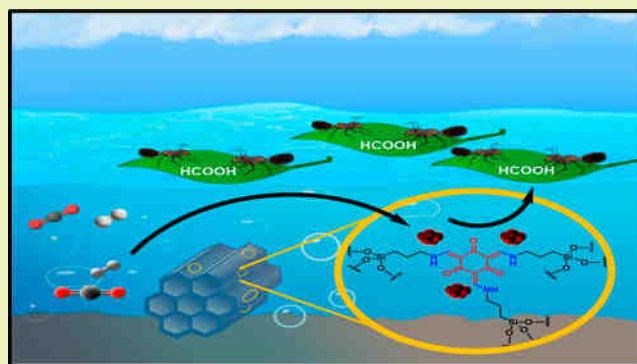
Article Recommendations



Supporting Information

ABSTRACT: Development of a heterogeneous catalyst capable of selective transformation of CO₂ to valuable products still remains a challenge. In this article, we account for the surfactant-directed synthesis of a new framework-incorporated nitrogen-containing periodic mesoporous organosilica nanosphere (NPMO). A thoroughly characterized N-incorporated hybrid PMO was utilized as a platform for stabilizing well-dispersed and easily accessible Pd nanoparticles (Pd-NPMO) without using any stabilizing agents or expensive dendrimers. Further, this bifunctional hybrid catalyst has been demonstrated to heterogeneously catalyze aqueous phase CO₂ hydrogenation (CO₂/H₂ ratio 1:3) for the direct synthesis of formate under 4 MPa pressure and at 100 °C. To validate the superior performance of the Pd-NPMO catalyst, we compared the activity with Pd-SBA-15 catalysts, and the results showed a 10-fold increase in turnover frequency of 108 h⁻¹ using Pd on NPMO which envisaged the crucial role of nitrogen sites in this catalyst to boost the CO₂ valorization to formate.

KEYWORDS: CO₂ hydrogenation, Formic acid synthesis, Hybrid silica, PMO, Pd nanoparticles



■ INTRODUCTION

Catalytic chemical transformation of CO₂ is an excellent alternative for producing fuels and platform chemicals which minimize our huge dependence on carbon-rich fossil fuels. Among the various approaches for CO₂ valorization, catalytic hydrogenation has been regarded as the most promising route to achieve this goal. Industrially, CO₂ has been converted at elevated temperatures (200–300 °C) and pressures (50–100 bar) using a conventional Cu/ZnO/Al₂O₃ catalyst to produce methanol.^{1–3} Such harsh reaction conditions are required because of the chemically inert and thermodynamically stable nature of the CO₂ molecule.¹ Out of the several platform compounds from CO₂, the most targeted molecules are methanol,⁴ formate/formic acid,⁵ and dimethyl ether,⁶ due to the value addition of these molecules in the energy sector worldwide. Formic acid (FA) with a 4.4 wt % theoretical hydrogen content and volumetric storage density of 53 g H₂/L is regarded as a promising liquid organic hydrogen carrier (LOHC). The other advantages are that they are stable, less toxic, biodegradable, and easy to store and transport.⁷ Currently, the requirement for HCOOH is industrially met via carbonylation of CH₃OH to HCOOCH₃ followed by its hydrolysis.⁸ Furthermore, the consumption of HCOOH and its salts in the direct formic acid fuel cells (DFAFCs)⁹ makes their production more pronounced from a C1 carbon source like gaseous CO₂ making the approach green and cyclic.

In the past decades, a variety of homogeneous and heterogeneous catalysts were designed and examined for the catalytic reduction of CO₂ to formate/formic acid.^{10–12} One among the strategies to overcome the exergonic thermodynamic limitations ($\Delta G^0 = -9.5 \text{ kJmol}^{-1}$ in water and at room temperature) in liquid phase CO₂ hydrogenation is the use of suitable bases.¹³ A variety of heterogeneous catalysts containing nitrogen atoms either in the form of metal nitrides¹⁴ or in supports have been reported to improve the activity. Similarly, N-heterocyclic carbenes,¹⁵ ionic liquids,¹⁶ carbon nitride,¹⁷ and amine-functionalized silica¹⁸ combined with both noble and non-noble metals such as Co, Ir, and Ru and bimetallic PdAg have been reported.

Porous solids having a unique accessible pore structure with desired dimensions, distinct reactions, and adsorption sites are well established in the fields of catalysis¹⁹ and adsorption.²⁰ Among the various porous materials like zeolites,²¹ covalent organic frameworks (COFs),²² and metal organic frameworks (MOFs),²³ mesoporous silica is an extensively studied material in catalysis due to its remarkable features like controllable sol–

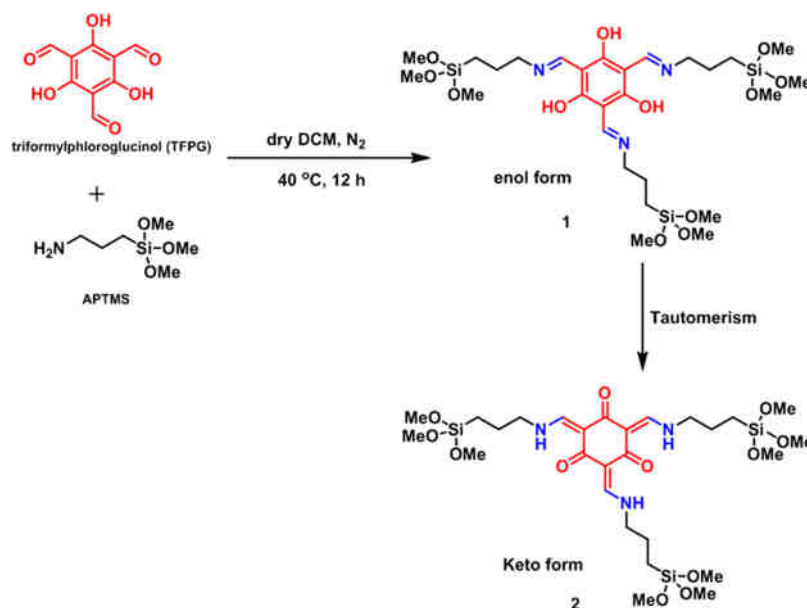
Received: May 23, 2020

Revised: August 7, 2020

Published: September 4, 2020

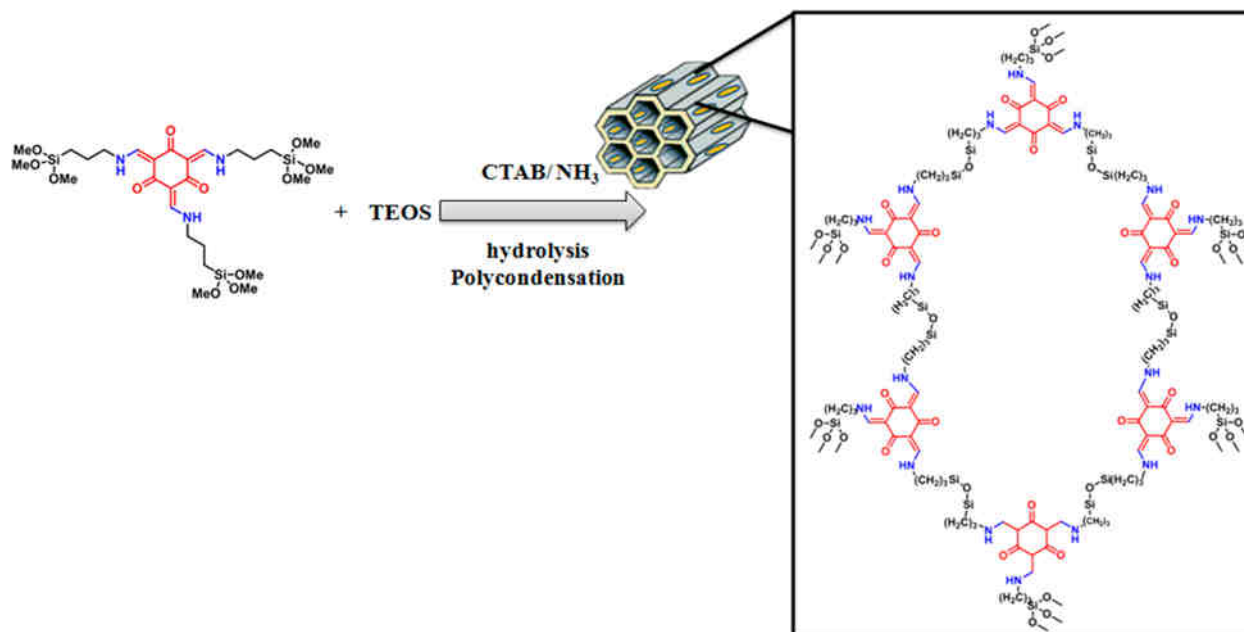


Scheme 1. Schematic Showing Synthesis of N-Containing Tris-Organo Silane Precursor by Reaction of 1,3,5-Triformylphloroglucinol (TFPG) with (3-Aminopropyl)trimethoxysilane^a



^aThe reaction has two steps: Schiff-base reaction followed by enol-to-keto tautomerism of silane precursor.

Scheme 2. Schematic Showing Surfactant-Directed Synthesis of N-Containing Periodic Mesoporous Organosilica (NPMO) by Hydrolysis Followed by Polycondensation under Basic Conditions



gel synthesis process, effortless regulation of silica frameworks, and easy surface functionalization.^{24–26} Creating active centers in inert mesoporous silica through organic functionality in the silica framework or through subsequent functional modification can increase its utility in catalysis.²⁷ After the birth of the periodic mesoporous organosilica (PMO) field in 1999,^{28,29} many reports in the literature are available on the synthesis of organic–inorganic hybrid silica using a variety of organic spacer groups.³⁰ However, the incorporation of multifunctional organic moieties as bridging groups with desired morphologies and structures has been reported in limited capacity for catalysis.³¹ The enhanced CO₂ sorption capacity by PMOs

containing basic functionality either in the framework or on the surface has been investigated by various groups but not extended further to the utilization for catalytic CO₂ transformation.^{20,32,33} Recently, Liu et al. reported a urea-derived framework (PMO-UDF) exhibiting an enhanced CO₂ capture property with its catalytic conversion to cyclic carbonates by reacting with epoxides under mild conditions.³⁴ The photocatalytic CO₂ reduction using modified PMO containing immobilized ruthenium complexes as photosensitizing sites was also reported recently.³⁵

Novel synthetic approaches have been developed for a highly active and sustainable heterogeneous noble metal-based

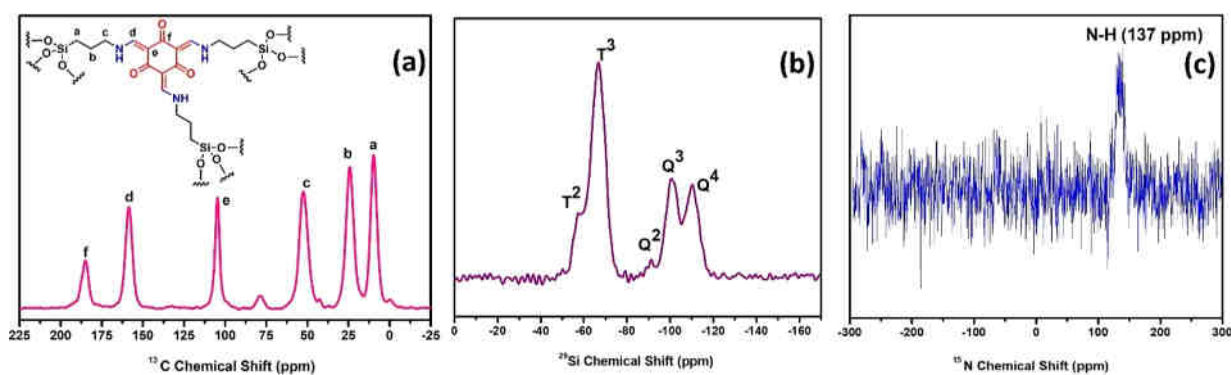


Figure 1. Cross-polarized magic-angle spinning solid-state NMR spectra of NPMO (a) ^{13}C , (b) ^{29}Si , and (c) ^{15}N .

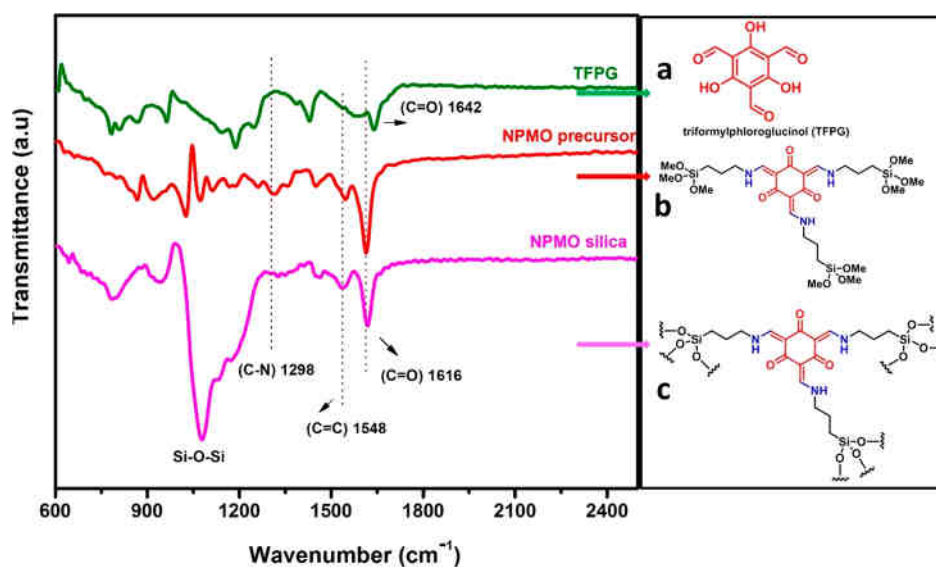


Figure 2. FT-IR spectra of (a) 1,3,5-triformylphloroglucinol (TFPG), (b) organosilane precursor-2 (NPMO precursor), and (c) NPMO silica.

nanocatalysts on inherently inert supports like silica and are employed in various catalysis.³⁶ The deposition and stabilization of small metal nanoparticles without any surfactant or precipitating reagents on silica remains challenging and often results in sintering affecting the catalysis.³⁷ Use of dendrimers on the solid supports through surface functionalization has gained attention to overcome these issues.³⁸ But the tedious synthesis methodology along with the capping of support pores make such catalytic processes less economical.

Herein, we describe a surfactant-directed synthesis of new nitrogen-incorporated periodic mesoporous organosilica (NPMO) within a framework by using a novel N-containing tris-organosilane precursor, synthesized through the Schiff-base reaction, and tetraethyl orthosilicate as the silica precursor in a 1:5 ratio. The N-incorporated hybrid silica has been utilized as the support for stabilizing well-dispersed Pd nanoparticles (Pd-NPMO) in the absence of any stabilizing agents. The bifunctional hybrid catalyst has been demonstrated to show an excellent pseudoligand property in heterogeneous Pd-catalyzed aqueous phase CO_2 hydrogenation to selectively produce formate with best the turn over number reported for a silica-based system.

RESULTS AND DISCUSSION

The N-containing tris-organosilane precursor was prepared by silylating the trialdehyde, (1,3,5-triformylphloroglucinol) with

(3-aminopropyl)trimethoxysilane through the Schiff-base reaction to yield enol-imine (Scheme 1, precursor-1) which can undergo tautomerism to the keto-enamine form (Scheme 1, precursor-2).³⁹ Synthesis of NPMO (Section S2) was done by the surfactant templated sol-gel strategy using the organosilane precursor-2 and TEOS as the inorganic silica precursor. The hydrolysis followed by the polycondensation of the methoxy groups in the silanes under basic conditions leads to the formation of an organic-inorganic hybrid silica framework. Uniformly distributed functionalities were obtained with the aid of a structure directing agent, cetyltrimethylammonium bromide (CTAB) (Scheme 2), and the product was further extracted with an acidified ethanolic solution. In order to preserve the Si-C linkage during the condensation process, the precipitate obtained was centrifuged to remove the supernatant solution and was aged by dispersing in fresh Millipore water under moderate conditions.

The organic functionality in the mesoporous silica framework was confirmed by the cross-polarization (CP) magic-angle spinning (MAS) NMR for the ^{13}C , ^{29}Si , and ^{15}N nuclei for NPMO material. The existence of the keto-form in the organic hybrid silica was established from ^{13}C CP-MAS solid-state NMR spectroscopy (Figure 1a) and matched well with the reference ^{13}C NMR peaks for the NPMO precursor-2 (Figure S1). The corresponding ^1H NMR spectra for synthesized NPMO precursor-2 is also presented (Figure

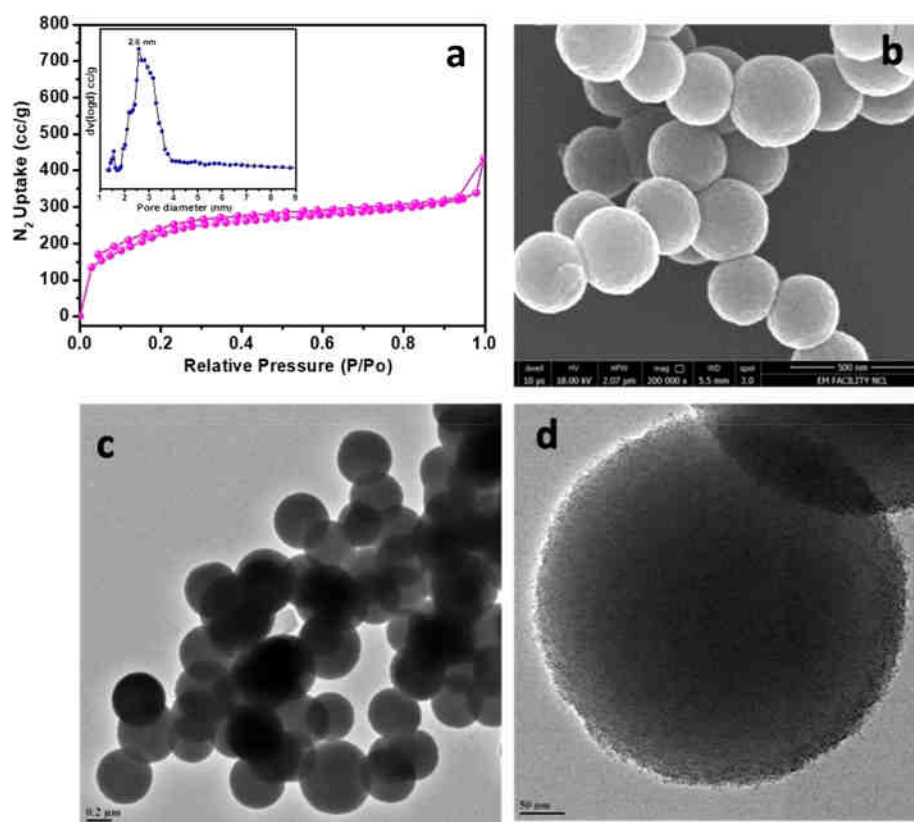


Figure 3. (a) N_2 adsorption isotherms of NPMO at 77 K. Inset shows the pore size distribution. (b) SEM (scale 500 nm) and (c, d) TEM images of NPMO showing spherical morphology (scale: 200 and 50 nm, respectively).

S3). The resonance peak for the carbonyl carbon of the aldehyde in the starting material was observed at 192 ppm (Figure S2) and was absent in the organic silica precursor (Figure S1) and the final NPMO silica material (Figure 1a) which indicated the complete consumption of the starting material during the Schiff-base reaction. Both the silane precursor and N-incorporated PMO clearly showed the signal corresponding to the carbonyl group at 184 ppm which unambiguously confirmed the existence of keto-form (Figure 1a and Figure S1).

In ^{29}Si NMR spectra (Figure 1b), the presence of two different types of Si atoms in the framework was observed in the ranges from -90 to -113 ppm and -50 to -65 ppm corresponding to the Q^n sites and T^n sites, respectively.²⁶ The peaks at -55 and -66 ppm in the T^n region represent the T^2 [$\text{SiC}(\text{OSi})_2\text{OH}$] and T^3 [$\text{SiC}(\text{OSi})_3$] linkages from the organic spacer bridge in the siliceous framework. The signals from the Q^n sites at -91 , -100 , and -110 ppm from [$\text{Si}(\text{OSi})_2(\text{OH})_2$], [$\text{Si}(\text{OSi})_3(\text{OH})$], and [$\text{Si}(\text{OSi})_4$], respectively, were observed from the inorganic bridge in the framework. Both ^{13}C and ^{29}Si NMR showed the successful integration of the keto-form of the organic silane into the hybrid silica through our optimized synthesis methodology. ^{15}N CP-MAS NMR spectra for NPMO hybrid silica displayed a peak at 137 ppm chemical shift assigned to the N–H species in the bridging organic functionality.⁴⁰ The N–H peak was visible due to the efficient ^1H cross-polarization effects. The absence of other peaks in Figure 1c further confirmed the absence of the NH_2 group from the starting APTMS.

The formation of a keto-enamine framework in the hybrid NPMO was further confirmed by FT-IR spectroscopy. The

FT-IR spectra for the starting material trialdehyde showed the carbonyl stretching ($\text{C}=\text{O}$) band at 1642 cm^{-1} (Figure 2a).⁴¹ Most of the peaks in the FT-IR spectrum of the NPMO silica (Figure 2c) matched well with the organic silane precursor-2 which exists in the keto-form (Figure 2b). The $\text{C}=\text{O}$ peak was observed at 1616 cm^{-1} along with a strong peak at 1548 cm^{-1} from the $\text{C}=\text{C}$ bond. The absence of a peak at 1642 cm^{-1} in the synthesized silane precursor and NPMO confirms the complete utilization of aldehyde during the Schiff-base reaction which corroborated with the NMR results. The IR band for C–N at 1298 cm^{-1} in the silica framework showed the retention of the keto-form after the hydrolysis and polycondensation reaction at basic conditions while forming hybrid silica. The band at 1075 cm^{-1} shows the Si–O–Si vibration from the framework confirming the formation of a siliceous network in the material.

The porosity and surface area of the hybrid silica was estimated by N_2 gas sorption and carried out on the activated NPMO. The results showed a type-IV isotherm which is typical for mesoporous materials with a H1 hysteresis loop (Figure 3a). By using the BET model, the surface area for hybrid NPMO was calculated to be $823\text{ m}^2/\text{g}$, and the pore size distribution was calculated using the BJH desorption method, showing a peak maxima at a pore diameter of 2.6 nm (Figure 3a, inset). The N-content in the NPMO obtained was calculated to be 4.6% from the CHN elemental analysis. The surface morphology and size of N-incorporated hybrid silica were confirmed from the electron microscopy images. The SEM (Figure 3b) and TEM (Figure 3c) images showed a spherical morphology having an average particle size of 250 nm. The porous nature of the hybrid silica was clearly visible

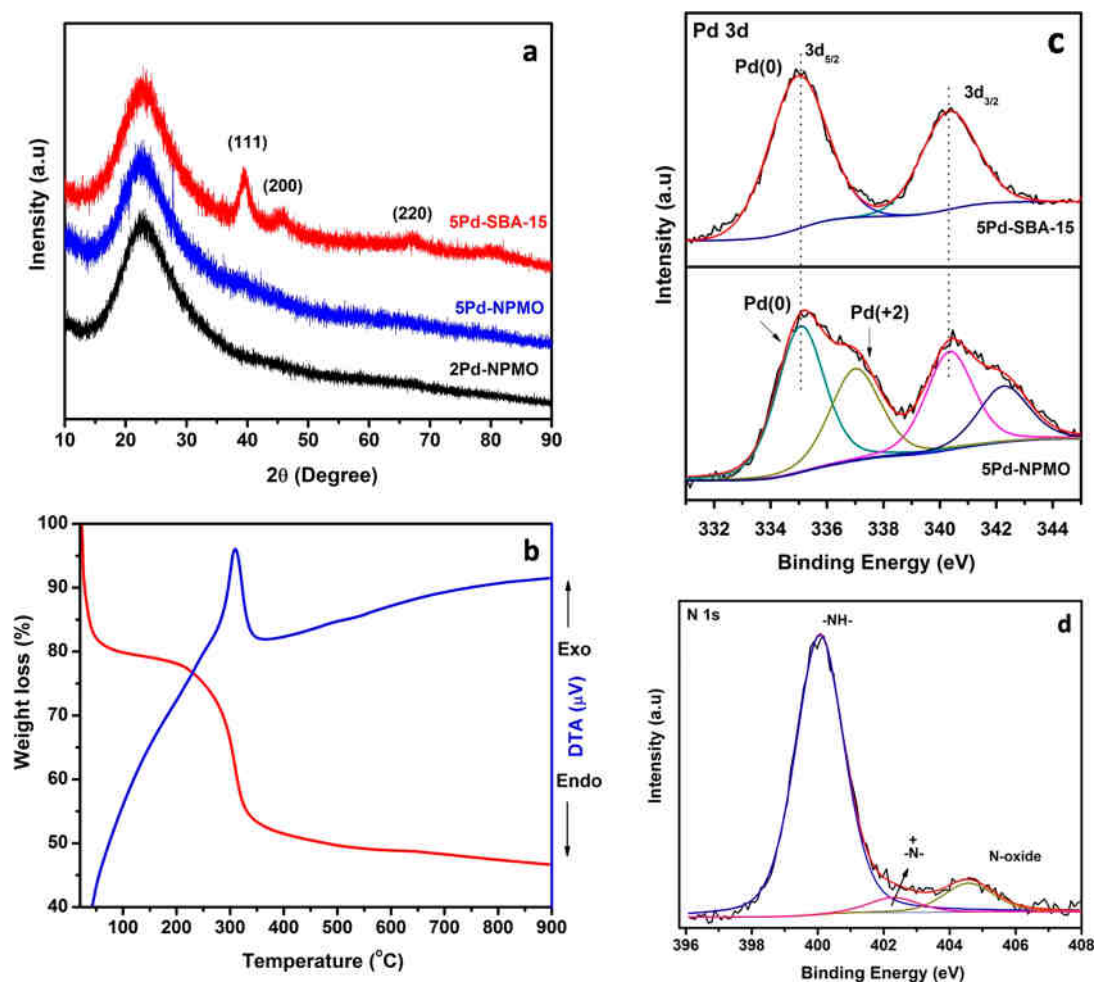


Figure 4. (a) Comparison of PXRD patterns of 2Pd-NPMO, 5Pd-NPMO, and 5Pd-SBA-15 catalysts. (b) TG-DTA study on 5Pd-NPMO catalyst. XPS plots for 5Pd-NPMO catalyst: (c) Pd 3d and (d) N 1s.

from the TEM images at higher magnification (Figure 3d) which was in support of the surface area results.

In order to explore the hybrid NPMO material in catalysis, we choose it as a platform for the stabilization of small well-dispersed Pd nanoparticles. However, silica-based supports often suffer from weak interactions with the nanoparticles leading to low metal loading along with formation of agglomerated particles due to sintering. Stabilization of monodispersed fine Pd nanoparticles on NPMO was achieved successfully in the absence of any surfactant or ligand by chemical reduction with NaBH_4 .

The PXRD patterns for Pd supported on NPMO and SBA-15 catalysts showed a broad peak at 2θ , value 23° , due to the amorphous nature of the silica material (Figure 4a). The absence of any diffraction peaks in the 2Pd-NPMO and 5Pd-NPMO catalysts suggested the formation of small, well-dispersed Pd nanoparticles on N-incorporated hybrid silica, whereas the 5Pd-SBA-15 catalyst synthesized following a similar method showed the diffraction lines attributed to the metallic Pd (fcc), hinting at the formation of appreciably large Pd nanoparticles on SBA-15. The significance of the nitrogen sites in the hybrid PMO as a pseudoligand to stabilize nanoparticles is established from this result. The surface area of NPMO reduced from 823 to 547 m^2/g after 5 wt % Pd loading, a trend followed with the SBA-15 catalyst also (Table S1 and Figure S4). The synthesized Pd nanoparticles

supported on hybrid NPMO occupies the surface as well as inside the pores (average pore size of 2.6 nm) which can partially or fully block some of the mesopores resulting in a decrease in textural properties like surface area.²³ Thermogravimetric analysis (TGA) of 5Pd-NPMO silica without any prior activation treatment displayed thermal stability up to 220 °C, and by further increasing the temperature, a gradual weight loss by about ~30% was observed between 230 and 400 °C, which is due to the decomposition of organic fragments from the framework accompanied by a sharp exothermic peak centered at 310 °C in the DTA profile due to the combustion of organic moieties (Figure 4b). Below 100 °C, the hybrid PMO catalyst showed a weight loss of ~18% due to the removal of adsorbed water. To study the electronic surface properties of Pd-NPMO and Pd-SBA-15 catalysts, XPS measurements on Pd and N were carried out. From Figure 4c, it can be concluded that Pd on the SBA-15 support exists in the metallic state (335 eV), whereas in the Pd-NPMO catalyst, both metallic (335 eV) and oxidized (337 eV) Pd were present, suggesting the existence of support-induced modification while forming well-dispersed fine Pd nanoparticles on the NPMO support. The relative percentage of Pd(0) and Pd(+2) species in the 5Pd-NPMO catalyst was found to be 55:45 from the fitted peak area (Figure 4c). The predominance of oxidized Pd species hints at the N-induced charge transfer from Pd nanoparticles to the NPMO silica support.⁴² But the

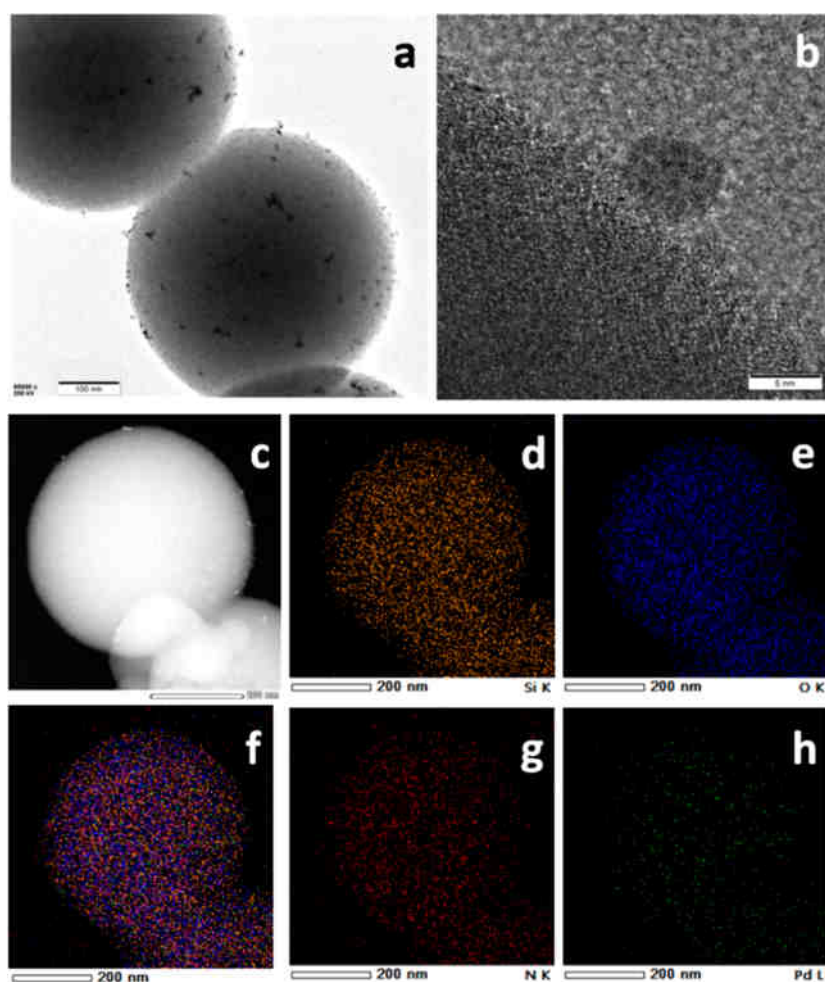


Figure 5. Structural characterization of SPd-NPMO catalyst: (a) high resolution TEM image (scale 100 nm), (b) magnified HR-TEM image (scale 5 nm), (c) HAADF-STEM image (scale 200 nm), and (d–h) STEM-EDX elemental mapping of the (d) Si K, (e) O K, (g) N K, and (h) Pd L edges and (f) overlay image.

complete reduction of the Pd precursor to Pd(0) was achieved on SBA-15 using same amount of reducing agent. The N 1s spectrum for SPd-NPMO (Figure 4d) by further deconvolution showed the presence of different N chemical species. The major contribution from the peak at 400 eV corresponding to —NH— species⁴³ from the support confirms the existence of a keto-form, which is in accordance with results from other analytical techniques, along with the relatively small content of quaternary-N and oxidized-N species on the catalyst surface at 402.3 and 404.5 eV, respectively.^{44,45}

The structural characterization of the SPd-NPMO catalyst carried out by TEM analysis (Figure 5) showed the porous spherical morphology of the hybrid PMO material with metallic Pd nanoparticles (Figure 5a). The images clearly revealed that the spherical N-incorporated organic–inorganic hybrid silica facilitates well-dispersed small accessible Pd nanoparticles having an average particle size in the range from 3 to 5 nm for both 2Pd-NPMO and 5Pd-NPMO catalysts (Figure S5). The magnified high resolution TEM image (Figure 5b) shows the Pd (~ 5 nm) NPs stabilized on the NPMO material with a well-defined metal–support interface. The hybrid NPMO skeleton facilitates the stability of active Pd centers through a strong interaction with N atoms from the organic silane framework. A homogeneous distribution of N and Pd on the hybrid PMO matrix for Pd-NPMO

nanostructures was evident from the HAADF-STEM and STEM-EDX elemental mapping (Figure 5c–h). From the TEM images for the SPd-SBA-15 catalyst (Figure S6), poor dispersion of Pd on the SBA-15 support due to agglomeration was visible, which clearly demonstrates the role of nitrogen in acting as a pseudoligand on the PMO matrix for stabilizing metal nanoparticles. From the ICP-OES measurements, the loading of Pd on NPMO and SBA-15 catalysts was calculated to be 4.8% and 4.4%, respectively, with respect to the support. As a control experiment, well-dispersed small Pd nanoparticles were stabilized on SBA-15 using a modified deposition–precipitation protocol developed by Soni et al.,⁴⁶ and the catalyst was termed as Pd-SBA-15(DP). The TEM results (Figure S7) showed the uniform-sized Pd nanoparticles (~ 2 nm) homogeneously dispersed on the hexagonal long channels of SBA-15.

The catalytic properties of synthesized Pd-NPMO material and other control samples were evaluated for the aqueous phase CO_2 hydrogenation reaction. When the reaction was carried out with 5Pd-NPMO under 4 MPa, ($\text{CO}_2/\text{H}_2 = 1:3$) at 100 °C, 6.3 mmol of formate was generated after 20 h in 0.5 M KOH aqueous solution. The ^1H and ^{13}C NMR analyses of the reaction mixture after 20 h evidenced the formation of formate as the only liquid product under our optimized reaction conditions (Figures S8 and S9). Interestingly, no gaseous CO_2

hydrogenation products like CO and methane were detected during the catalytic run, which implies the complete selectivity for the direct synthesis of formate on 5Pd-NPMO making separation of products effortless. To the best of our knowledge, this is the first time for a demonstration of the catalytic utilization of Pd nanoparticles on chemically modified PMO in the selective CO₂ reduction to formate with a good yield under mild conditions. In order to highlight the role of N-incorporation in a periodic mesoporous hybrid silica matrix in CO₂ catalysis, reactions were also performed under similar conditions using Pd on SBA-15 (5Pd-SBA-15) which produced only 0.9 mmol of formate.

TOF was calculated for 5Pd-NPMO and 5Pd-SBA-15 catalysts and gave 108 and 9.4 h⁻¹ respectively. The active metal exposed for the reaction obtained using the ICP-OES and percentage metal dispersion from CO chemisorption was used for calculation. To confirm the positive effect of the N moiety from the PMO framework on enhancing the CO₂ hydrogenation to formate, we carried out the reaction using the 3Pd-SBA-15(DP) catalyst which had a narrow particle size distribution (~2 nm) along with a very good dispersion on the SBA-15 support. This catalyst showed a TOF of only 25.6 h⁻¹ emphasizing the importance of N incorporation. Even under a reaction temperature of 60 °C, using a 5Pd-NPMO catalyst yielded 2.2 mmol of formate with a TOF of 38 h⁻¹ showing the ability of the material to activate the reactants at much lower temperature. Further, increasing the CO₂ reduction temperature from 100 to 150 °C resulted in the decline of activity to TOF 83 h⁻¹. This can be attributed to the structural deformation of hybrid framework during the reaction under a 0.5 M KOH aqueous solution which led to the Pd particle agglomeration (Figure S10). Our control experiments confirmed no formate being produced in the absence of a catalyst (Table 1, entry 7), and also no carbon moiety from the

formate formation, which is much higher compared to the Pd-SBA-15 catalysts.

During the course of the reaction (Figure 6b), the 5Pd-NPMO catalyst showed a linear increase in formate (6.9 mmol) production, where the TOF increased up to 108 h⁻¹ in 20 h and decreased to 99 h⁻¹ by further increasing the reaction time to 24 h. Hence, the reaction time was optimized to 20 h for further studies. The effect of the base concentration on CO₂ hydrogenation was studied, and the results showed that by increasing 0.5 M KOH aqueous solution to 1 M, the TOF for formate on the 5Pd-NPMO catalyst increased from 108 to 140 h⁻¹ (Table 1, entry 5 and Figure S11) confirming the role of base in the reaction. The reaction in the absence of base did not yield appreciable formic acid from CO₂ under our reaction conditions, which implies the vital role of a basic medium to improve the reaction by stabilizing HCOOH in the form of formate salts as well as the solubility of gaseous reactants in water.^{47,48} In comparison with previously reported heterogeneous Pd catalysts on both active and inactive supports (Table S2), the 5Pd-NPMO silica catalyst exhibited remarkable TOF (140 h⁻¹) under similar reaction conditions.

The heterogeneous nature of the Pd-NPMO catalyst was studied by the hot-filtration method under the optimized reaction conditions. After a 12 h reaction (3.5 mmol formate produced), the catalyst was filtered off, and the filtrate was allowed to proceed further for the CO₂ hydrogenation reaction for the remaining 12 h under identical condition. No increase in the formate yield was observed maintaining the 3.5 mmol in the reaction medium, suggesting that the catalysis is purely heterogeneous (Figure 7a). Also, in order to confirm the reusability and stability of the Pd-NPMO catalyst, the reaction was performed for two consecutive runs by using the recovered catalyst after the fresh run. As shown in Figure 7b, the first run of the recovered 5Pd-NPMO catalyst produced 5.8 mmol of formate showing a negligible decrease in the yield compared to the fresh reaction, but the consecutive second cycle showed a dip in the formate production to 3.8 mmol.

Further, to investigate the cause for a decrease in activity after the second run, spent catalyst analysis was carried out. The high resolution TEM images of the spent 5Pd-NPMO catalyst after the second cycle (Figure S12) revealed that during the reaction under 0.5 M KOH solution at a boiling temperature for a prolonged time resulted in the partial destruction of the silica support morphology generating islands of agglomerated Pd nanoparticles along with well-dispersed small particles. It is true that complete dissolution of silica was not observed even under our reaction conditions, and the well-dispersed small Pd nanoparticles observed were likely those protected inside the N sites of mesopores which prevented agglomeration. HAADF-STEM elemental mapping of the spent 5Pd-NPMO catalyst (Figure S13) showed the presence of nitrogen on the PMO which in combination with small Pd nanoparticles yielded 3.8 mmol of formate after the second cycle. The formation of large voids in hybrid NPMO spheres after the reaction may be due to the etching of silica under the basic reaction conditions.⁴⁹ A similar result was observed with the 3Pd-SBA-15(DP) catalyst after the reaction, where the ordered SBA-15 channels were collapsed with concomitant agglomeration of Pd nanoparticles producing 0.46 mmol formate in the second run (Figure S14). The XPS measurements of the spent 5Pd-NPMO catalyst showed the existence of both Pd(0) and Pd(+2) species (Figure S15), and the relative percentage was found to be 78:22. The XPS peak

Table 1. CO₂ Hydrogenation Catalyzed by Pd-NPMO^a

$$\text{CO}_2 + \text{H}_2 \xrightarrow[\text{H}_2\text{O, base}]{\text{Pd-NPMO}} \text{HCOO}^-$$

Entry	Temp (°C)	[HCO ₂ ⁻] ^c (mmol)	TOF ^f (h ⁻¹)
1	60	2.2	38
2	80	4.1	71
3	100	6.3	108
4	150	4.8	83
5 ^b	100	8.2	140
6 ^c	100	n.d	—
7 ^d	100	n.d	—

^aReaction conditions: 5Pd-NPMO catalyst (20 mg), aqueous KOH solution (20 mL, 0.5 M), CO₂:H₂ (1:3, 4 MPa), time (20 h).

^bAqueous KOH (20 mL, 1 M). ^cOnly using H₂ (4 MPa). ^dWithout catalyst.

^eDetermined by HPLC. ^fDetermined from [moles of formate formed]/[mole of active Pd sites in catalyst per hour]. Number of moles of active Pd sites determined from ICP-OES and CO chemisorption.

hybrid catalyst framework was utilized in the formate formation as ensured by carrying the reaction only in H₂ pressure (4 MPa) (Table 1, entry 6). Screening of different Pd catalysts on both NPMO and SBA-15 for CO₂ hydrogenation was carried out, and results showed the promising effect of our NPMO support for the reaction (Figure 6a). Even the 2% Pd-loaded NPMO (2Pd-NPMO) catalyst showed 3.1 mmol of

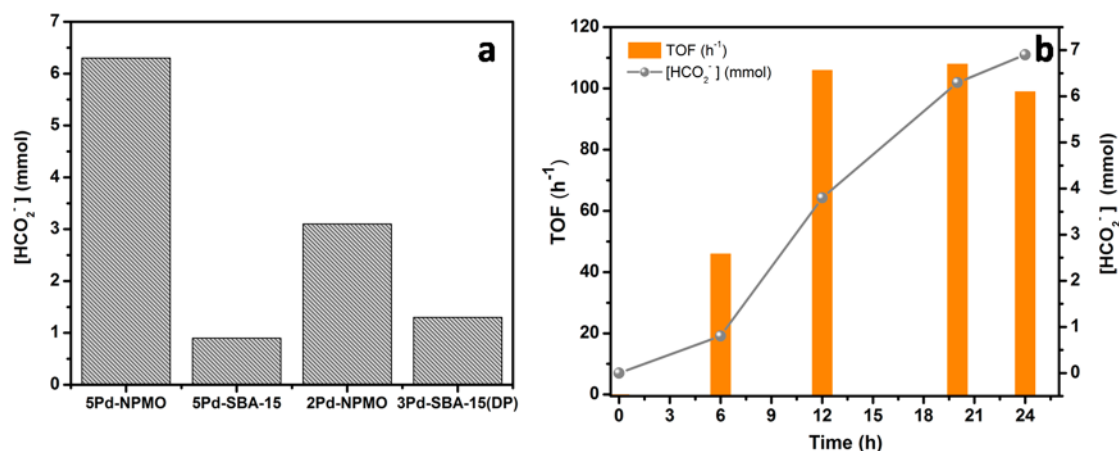


Figure 6. (a) Screening of CO_2 reduction to formate on various Pd catalysts. (b) Time course of CO_2 hydrogenation to formate catalyzed by 5Pd-NPMO. Reaction conditions: catalyst (20 mg), aqueous KOH solution (20 mL, 0.5 M), $\text{CO}_2\text{:H}_2$ (1:3, 4 MPa), temperature (100 °C), and time (20 h).

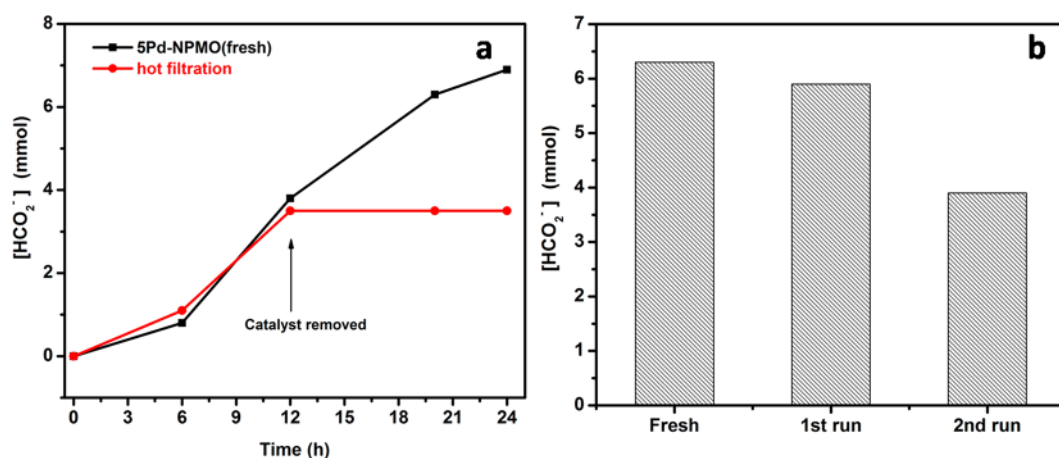


Figure 7. (a) Heterogeneity study of Pd-NPMO catalyst by hot-filtration test (catalyst removed after 12 h reaction, and further reaction carried in the absence of catalyst). (b) Recycling experiment to study reusability. Reaction conditions: 5Pd-NPMO (20 mg), aqueous KOH solution (20 mL, 0.5 M), $\text{CO}_2\text{:H}_2$ (1:3, 4 MPa), temperature (100 °C), and time (20 h).

intensities for Pd 3d in the spent 5Pd-NPMO had decreased considerably along with the reduction of oxidized Pd(+2) species indicating the growth of Pd nanoparticles with concomitant loss in dispersion, a result in good agreement with the TEM results. The N 1s spectrum for the spent 5Pd-NPMO showed similar species compared to the fresh catalyst and the major peak at 400 eV corresponding to N–H species and confirmed no structural change in the keto-form of the organic moiety in the framework under the CO_2 hydrogenation reaction environment (Figure S16). The Pd content in the spent 5Pd-NPMO was calculated from ICP-OES and was found to be $\sim 4.8\%$ with respect to the support which showed no metal leaching from the catalyst under our reaction conditions confirming that the catalyst behaves purely heterogeneously in nature, and the N content in the spent catalyst was determined as 2.8% from the CHN elemental analysis. The plausible reason for the drop in activity after the second run may be due to the combination of agglomerated Pd nanoparticles along with a decrease in N content under the basic reaction conditions. It is indeed envisaged that the flexibility of PMO materials allows one to design specific sites (like solid base sites) where nitrogen-containing PMO-based

material for catalyzing CO_2 hydrogenation under base free or milder conditions is a possibility in the near future.

CONCLUSIONS

In summary, an efficient heterogeneous Pd-based aqueous phase CO_2 hydrogenation catalyst was developed using a new N-incorporated periodic mesoporous organosilica in the framework (Pd-NPMO). High loading (~ 5 wt %) of Pd was achieved while maintaining the particle size in the range of 2–5 nm. The catalytic activity of the NPMO catalyst (TOF 108 h^{-1}) was superior compared to Pd-SBA-15 (9.4 h^{-1}), demonstrating the role of nitrogen sites on NPMO supports for boosting the CO_2 reduction with complete selectivity to formate under mild reaction conditions. A combination of characterization and catalytic results confirmed the CO_2 hydrogenation catalysis on Pd-NPMO to be purely heterogeneous in nature. This chemically modified new NPMO silica support proved to facilitate the stabilization of small Pd nanoparticles without any expensive dendrimers or stabilizing agents and can be extended for other catalytic applications. Finally, future developments on metal nanoparticle-based materials on a N-containing PMO for sustainable catalysis can find several insights from the present study.

■ ASSOCIATED CONTENT

SI Supporting Information

The Supporting Information is available free of charge at <https://pubs.acs.org/doi/10.1021/acssuschemeng.0c03860>.

General information, synthesis procedures, characterization details, NMR plots, TEM images, XPS plots, N₂ sorption isotherms, and CO₂ hydrogenation activity plots (PDF)

■ AUTHOR INFORMATION

Corresponding Author

C. P. Vinod – Catalysis and Inorganic Chemistry Division, CSIR-National Chemical Laboratory, Pune 411 008, India; Academy of Scientific and Innovative Research (AcSIR), Ghaziabad, Uttar Pradesh 201002, India; orcid.org/0000-0001-9857-4907; Email: cp.vinod@ncl.res.in

Authors

K. J. Betsy – Catalysis and Inorganic Chemistry Division, CSIR-National Chemical Laboratory, Pune 411 008, India; Academy of Scientific and Innovative Research (AcSIR), Ghaziabad, Uttar Pradesh 201002, India

Anish Lazar – Catalysis and Inorganic Chemistry Division, CSIR-National Chemical Laboratory, Pune 411 008, India

Anjuna Pavithran – Catalysis and Inorganic Chemistry Division, CSIR-National Chemical Laboratory, Pune 411 008, India

Complete contact information is available at: <https://pubs.acs.org/doi/10.1021/acssuschemeng.0c03860>

Notes

The authors declare no competing financial interest.

■ ACKNOWLEDGMENTS

B.K.J. thanks the CSIR for a senior research fellowship. C.P.V. thanks the Council of Scientific and Industrial Research (CSIR), INDIA for generous funding.

■ REFERENCES

- (1) Behrens, M.; Studt, F.; Kasatkin, I.; Köhl, S.; Hävecker, M.; Abild-Pedersen, F.; Zander, S.; Girsgeles, F.; Kurr, P.; Knief, B.-L.; Tovar, M.; Fischer, R. W.; Nørskov, J. K.; Schlögl, R. The active site of methanol synthesis over Cu/ZnO/Al₂O₃; industrial catalysts. *Science* **2012**, *336*, 893–897.
- (2) Kuld, S.; Thorhauge, M.; Falsig, H.; Elkjær, C. F.; Helveg, S.; Chorkendorff, I.; Sehested, J. Quantifying the promotion of Cu catalysts by ZnO for methanol synthesis. *Science* **2016**, *352*, 969–974.
- (3) Chinchin, G. C.; Denny, P. J.; Parker, D. G.; Spencer, M. S.; Whan, D. A. Mechanism of methanol synthesis from CO₂/CO/H₂ mixtures over copper/zinc oxide/alumina catalysts: use of ¹⁴C-labelled reactants. *Appl. Catal.* **1987**, *30*, 333–338.
- (4) Jiang, X.; Koizumi, N.; Guo, X.; Song, C. Bimetallic Pd–Cu catalysts for selective CO₂ hydrogenation to methanol. *Appl. Catal., B* **2015**, *170–171*, 173–185.
- (5) Moret, S.; Dyson, P. J.; Laurency, G. Direct synthesis of formic acid from carbon dioxide by hydrogenation in acidic media. *Nat. Commun.* **2014**, *5*, 4017.
- (6) Wang, S.; Mao, D.; Guo, X.; Wu, G.; Lu, G. Dimethyl ether synthesis via CO₂ hydrogenation over CuO–TiO₂–ZrO₂/HZSM-5 bifunctional catalysts. *Catal. Commun.* **2009**, *10*, 1367–1370.
- (7) Grasemann, M.; Laurency, G. Formic acid as a hydrogen source – recent developments and future trends. *Energy Environ. Sci.* **2012**, *5*, 8171–8181.
- (8) Reutemann, W.; Kieczka, H. H. *Ullmann's Encyclopedia of Industrial Chemistry*; Wiley, 2005.
- (9) Ji, X.; Lee, K. T.; Holden, R.; Zhang, L.; Zhang, J.; Botton, G. A.; Couillard, M.; Nazar, L. F. Nanocrystalline intermetallics on mesoporous carbon for direct formic acid fuel cell anodes. *Nat. Chem.* **2010**, *2*, 286–293.
- (10) Kattel, S.; Liu, P.; Chen, J. G. Tuning Selectivity of CO₂ Hydrogenation Reactions at the Metal/Oxide Interface. *J. Am. Chem. Soc.* **2017**, *139*, 9739–9754.
- (11) Lao, D. B.; Galan, B. R.; Linehan, J. C.; Heldebrandt, D. J. The steps of activating a prospective CO₂ hydrogenation catalyst with combined CO₂ capture and reduction. *Green Chem.* **2016**, *18*, 4871–4874.
- (12) Guan, C.; Pan, Y.; Ang, E. P. L.; Hu, J.; Yao, C.; Huang, M.-H.; Li, H.; Lai, Z.; Huang, K.-W. Conversion of CO₂ from air into formate using amines and phosphorus-nitrogen PN³P–Ru(II) pincer complexes. *Green Chem.* **2018**, *20*, 4201–4205.
- (13) Maru, M. S.; Ram, S.; Shukla, R. S.; Khan, N.-ul. H. Ruthenium-hydroxalate (Ru-HT) as an effective heterogeneous catalyst for the selective hydrogenation of CO₂ to formic acid. *Mol. Catal.* **2018**, *446*, 23–30.
- (14) Wang, L.; Zhang, W.; Zheng, X.; Chen, Y.; Wu, W.; Qiu, J.; Zhao, X.; Zhao, X.; Dai, Y.; Zeng, J. Incorporating nitrogen atoms into cobalt nanosheets as a strategy to boost catalytic activity toward CO₂ hydrogenation. *Nat. Energy* **2017**, *2*, 869–876.
- (15) Azua, A.; Sanz, S.; Peris, E. Water-soluble Ir^{III} N-heterocyclic carbene based catalysts for the reduction of CO₂ to formate by transfer hydrogenation and the deuteration of aryl amines in water. *Chem. - Eur. J.* **2011**, *17*, 3963–3967.
- (16) Weillhard, A.; Qadir, M. I.; Sans, V.; Dupont, J. Selective CO₂ hydrogenation to formic acid with multifunctional ionic liquids. *ACS Catal.* **2018**, *8*, 1628–1634.
- (17) Mondelli, C.; Puértolas, B.; Ackermann, M.; Chen, Z.; Pérez-Ramírez, J. Enhanced base-free formic acid production from CO₂ on Pd/g-C₃N₄ by tuning of the carrier defects. *ChemSusChem* **2018**, *11*, 2859–2869.
- (18) Mori, K.; Masuda, S.; Tanaka, H.; Yoshizawa, K.; Che, M.; Yamashita, H. Phenylamine-functionalized mesoporous silica supported PdAg nanoparticles: a dual heterogeneous catalyst for formic acid/CO₂-mediated chemical hydrogen delivery/storage. *Chem. Commun.* **2017**, *53*, 4677–4680.
- (19) Bhunia, M. K.; Das, S. K.; Pachfule, P.; Banerjee, R.; Bhaumik, A. Nitrogen-rich porous covalent imine network (CIN) material as an efficient catalytic support for C–C coupling reactions. *Dalton Trans.* **2012**, *41*, 1304–1311.
- (20) Tang, Y.; Landskron, K. CO₂-sorption properties of organo-silicas with bridging amine functionalities inside the framework. *J. Phys. Chem. C* **2010**, *114*, 2494–2498.
- (21) Zhang, X.; Liu, D.; Xu, D.; Asahina, S.; Cychosz, K. A.; Agrawal, K. V.; Al Wahedi, Y.; Bhan, A.; Al Hashimi, S.; Terasaki, O.; Thommes, M.; Tsapatsis, M. Synthesis of self-pillared zeolite nanosheets by repetitive branching. *Science* **2012**, *336*, 1684–1687.
- (22) Pachfule, Q.; Kandambeth, S.; Díaz Díaz, D.; Banerjee, R. 3D Highly stable covalent organic framework–Au nanoparticles hybrids for enhanced activity for nitrophenol reduction. *Chem. Commun.* **2014**, *50*, 3169–3172.
- (23) Pascanu, V.; González Miera, G.; Inge, A. K.; Martín-Matute, B. Metal–Organic Frameworks as catalysts for organic synthesis: A critical perspective. *J. Am. Chem. Soc.* **2019**, *141*, 7223–7234.
- (24) Betsy, K. J.; Nayak, C.; Lazar, A.; Krishnan, A.; Bhattacharyya, D.; Jha, S. N.; Vinod, C. P. Selective oxidation of cyclohexane to cyclohexanone using chromium oxide supported mesoporous MCM-41 nanospheres: probing the nature of catalytically active chromium sites. *ChemCatChem* **2018**, *10*, 3291–3298.
- (25) Betsy, K. J.; Lazar, A.; Vinod, C. P. Highly selective aqueous phase hydrogenation of phenols over nanostructured RuO₂ on MCM-41 catalysts. *Nano-Structures & Nano-Objects* **2018**, *13*, 36–43.
- (26) Lazar, A.; Betsy, K. J.; Vinod, C. P.; Singh, A. P. Ru(II)-functionalized SBA-15 as highly chemoselective, acid free and

sustainable heterogeneous catalyst for acetalization of aldehydes and ketones. *Catal. Commun.* **2018**, *104*, 62–66.

(27) Hoffmann, F.; Cornelius, M.; Morell, J.; Fröba, M. Silica-based mesoporous organic–inorganic hybrid materials. *Angew. Chem., Int. Ed.* **2006**, *45*, 3216–3251.

(28) Inagaki, S.; Guan, S.; Fukushima, Y.; Ohsuna, T.; Terasaki, O. Novel mesoporous materials with a uniform distribution of organic groups and inorganic oxide in their frameworks. *J. Am. Chem. Soc.* **1999**, *121*, 9611–9614.

(29) Asefa, T.; MacLachlan, M. J.; Coombs, N.; Ozin, G. A. Periodic mesoporous organosilicas with organic groups inside the channel walls. *Nature* **1999**, *402*, 867–871.

(30) Burleigh, M. C.; Markowitz, M. A.; Spector, M. S.; Gaber, B. P. Direct synthesis of periodic mesoporous organosilicas: functional incorporation by co-condensation with organosilanes. *J. Phys. Chem. B* **2001**, *105*, 9935–9942.

(31) Zhu, F.-X.; Wang, W.; Li, H.-X. Water-medium and solvent-free organic reactions over a bifunctional catalyst with Au nanoparticles covalently bonded to HS/SO₃H functionalized periodic mesoporous organosilica. *J. Am. Chem. Soc.* **2011**, *133*, 11632–11640.

(32) Qi, G.; Fu, L.; Duan, X.; Choi, B. H.; Abraham, M.; Giannelis, E. P. Mesoporous amine-bridged polysilsesquioxane for CO₂ capture. *Greenhouse Gases: Sci. Technol.* **2011**, *1*, 278–284.

(33) De Canck, E.; Ascoop, I.; Sayari, A.; Van Der Voort, P. Periodic mesoporous organosilicas functionalized with a wide variety of amines for CO₂ adsorption. *Phys. Chem. Chem. Phys.* **2013**, *15*, 9792–9799.

(34) Liu, M.; Lu, X.; Shi, L.; Wang, F.; Sun, J. Periodic mesoporous organosilica with a basic urea-derived framework for enhanced carbon dioxide capture and conversion under mild conditions. *ChemSusChem* **2017**, *10*, 1110–1119.

(35) Kuramochi, Y.; Sekine, M.; Kitamura, K.; Maegawa, Y.; Goto, Y.; Shirai, S.; Inagaki, S.; Ishida, H. Photocatalytic CO₂ reduction by periodic mesoporous organosilica (PMO) containing two different ruthenium complexes as photosensitizing and catalytic sites. *Chem.–Eur. J.* **2017**, *23*, 10301–10309.

(36) Soni, Y.; Kavaya, I.; Ajithkumar, T. G.; Vinod, C. P. One pot ligand exchange method for a highly stable Au–SBA-15 catalyst and its room temperature CO oxidation. *Chem. Commun.* **2018**, *54*, 12412–12415.

(37) Sekhar, A. C. S.; Meera, C. J.; Ziyad, K. V.; Gopinath, C. S.; Vinod, C. P. Synthesis and catalytic activity of monodisperse gold–mesoporous silica core–shell nanocatalysts. *Catal. Sci. Technol.* **2013**, *3*, 1190–1193.

(38) Karakhanov, E.; Maximov, A.; Kardasheva, Y.; Semernina, V.; Zolotukhina, A.; Ivanov, A.; Abbott, G.; Rosenberg, E.; Vinokurov, V. Pd nanoparticles in dendrimers immobilized on silica–polyamine composites as catalysts for selective hydrogenation. *ACS Appl. Mater. Interfaces* **2014**, *6*, 8807–8816.

(39) Chong, J. H.; Sauer, M.; Patrick, B. O.; MacLachlan, M. J. Highly stable keto-enamine salicylideneanilines. *Org. Lett.* **2003**, *5*, 3823–3826.

(40) Hu, Y.; Shim, Y.; Oh, J.; Park, S.; Park, S.; Ishii, Y. Synthesis of ¹³C-, ¹⁵N-labeled graphitic carbon nitrides and NMR-based evidence of hydrogen-bonding assisted two-dimensional assembly. *Chem. Mater.* **2017**, *29*, 5080–5089.

(41) Kandambeth, S.; Mallick, A.; Lukose, B.; Mane, M. V.; Heine, T.; Banerjee, R. Construction of crystalline 2D covalent organic frameworks with remarkable chemical (acid/base) stability via a combined reversible and irreversible route. *J. Am. Chem. Soc.* **2012**, *134*, 19524–19527.

(42) Zhou, Y.; Holme, T.; Berry, J.; Ohno, T. R.; Ginley, D.; O'Hayre, R. Dopant-induced electronic structure modification of HOPG surfaces: implications for high activity fuel cell catalysts. *J. Phys. Chem. C* **2010**, *114*, 506–515.

(43) Ravi, S.; Zhang, S.; Lee, Y.-R.; Kang, K.-K.; Kim, J.-M.; Ahn, J.-W.; Ahn, W.-S. EDTA-functionalized KCC-1 and KIT-6 mesoporous silicas for Nd³⁺ ion recovery from aqueous solutions. *J. Ind. Eng. Chem.* **2018**, *67*, 210–218.

(44) Kelemen, S. R.; Gorbaty, M. L.; Kwiatek, P. J. Quantification of nitrogen forms in Argonne premium coals. *Energy Fuels* **1994**, *8*, 896–906.

(45) Huang, Y.-K.; Jena, A.; Chen, Y.-T.; Fang, M.-H.; Yang, N.-H.; Chang, H.; Liu, R.-S. Nanosized-Fe₃PtN supported on nitrogen-doped carbon as electro-catalyst for oxygen reduction reaction. *Int. J. Hydrogen Energy* **2017**, *42*, 15761–15769.

(46) Soni, Y.; Pradhan, S.; Bamnia, M. K.; Yadav, A. K.; Jha, S. N.; Bhattacharyya, D.; Khan, T. S.; Haider, M. A.; Vinod, C. P. Spectroscopic evidences for the size dependent generation of Pd species responsible for the low temperature CO oxidation activity on Pd-SBA-15 nanocatalyst. *Appl. Catal., B* **2020**, *272*, 118934.

(47) Mitchell, C. E.; Terranova, U.; Alshibane, I.; Morgan, D. J.; Davies, T. E.; He, Q.; Hargreaves, J. S. J.; Sankar, M.; de Leeuw, N. H. Liquid phase hydrogenation of CO₂ to formate using palladium and ruthenium nanoparticles supported on molybdenum carbide. *New J. Chem.* **2019**, *43*, 13985–13997.

(48) Duan, Z.; Sun, R. An improved model calculating CO₂ solubility in pure water and aqueous NaCl solutions from 273 to 533 K and from 0 to 2000 bar. *Chem. Geol.* **2003**, *193*, 257–271.

(49) Zhu, Z.; Zhang, S.; Li, C.; Zhang, J.; Yu, J.; Du, X.; He, L.; Zhang, X. A mechanistic study of silica-etching by hot water. *Phys. Chem. Chem. Phys.* **2018**, *20*, 1440–1446.

Selective Oxidation of Cyclohexane to Cyclohexanone Using Chromium Oxide Supported Mesoporous MCM-41 Nanospheres: Probing the Nature of Catalytically Active Chromium Sites

Kurisingal J. Betsy,^[a] Chandrani Nayak,^[b] Anish Lazar,^[a, c] Athira Krishnan,^[a] Dibyendu Bhattacharyya,^[b] Shambhu N. Jha,^[b] and Chathakudath P. Vinod^{*[a, c, d]}

Highly dispersed chromium oxide supported mesoporous MCM-41 nanosphere catalysts have been synthesized using a simple wet impregnation method. This work is devoted to a systematic study to reveal the active Cr sites in chromium oxide supported MCM-41 nanosphere catalysts for the selective oxidation of cyclohexane to cyclohexanone. To probe the nature of the active species, we synthesized 0.5–10 wt% Cr loaded catalysts and characterized them by using XRD, UV/Vis spectroscopy, Raman spectroscopy, X-ray photoelectron spec-

troscopy, extended X-ray absorption fine structure analysis, X-ray absorption near edge structure analysis, N₂ sorption analysis, FTIR spectroscopy, ²⁹Si NMR spectroscopy, SEM, and TEM. The liquid-phase oxidation of cyclohexane to cyclohexanone (99% selectivity) was performed under mild reaction conditions, and the results reveal clearly that the 5 wt% Cr loaded catalyst was optimum for the reaction. The initial composition of isolated Cr³⁺ species in the catalyst is the major factor that influences the enhanced activity for cyclohexane oxidation.

Introduction

Cyclohexanone and cyclohexanol (KA oil) are important chemical feedstock in a variety of industrially important commodities.^[1] KA oil is a precursor to Nylon-6 and Nylon-6,6 and has a global consumption of approximately 10⁶ tons per year. Conventionally, KA oil is manufactured either by the oxidation of cyclohexane or by the hydrogenation of phenol. Cyclohexane oxidation requires a high activation energy for C–H bond cleavage, which dictates harsh reaction conditions such as a high temperature (413–433 K) and pressure (1–2 MPa).^[2] Moreover, these processes suffer from significant shortcomings such as a low yield, low selectivity, and high waste production.^[3] The great demand for these oxidation products and the high energy consumption of the existing process necessitate a

more effective, stable, feasible, and sustainable catalytic process.

Over recent decades, various transition-metal-based heterogeneous catalyst systems, such as V-MCM-41,^[4] Co/ZSM-5,^[5] (Cr)MCM-41,^[6] Au,^[7] and Fe^[8] heterogeneous catalysts, Cr-Ti-Si ternary mixed oxides,^[9] and Cr-PMO^[10] have been reported to be active for cyclohexane oxidation. Among them, Cr-incorporated silica is promising because of its good activity and stability.^[11] The enhanced activity exhibited by chromium oxide catalysts was attributed to the presence of the various oxidation states of Cr, coordination environments, as well as its extent of polymerization.^[12] Although most of these catalysts yield KA oil as the major product, a high selectivity for cyclohexanol has been reported for Au supported on Fe₂O₃.^[7d] The determination of the active sites is an important area in heterogeneous catalysis, and active site determination for chromium oxide for oxidation reactions has been attempted.^[13] The nature of the Cr active species depends on its location such as framework or extraframework positions in which Cr^{VI} species are the active site in a Cr-incorporated silica framework.^[6] In contrast, the presence of coordinatively unsaturated Cr^{III} or Cr^{VI} species in chromium oxide as active sites in cyclohexane oxidation reactions has also been reported.^[14] The dispersion of Cr species on the support and the Cr loading are important factors that influence the catalytic activity.^[15] The nature of the active species in the chromium oxide catalyst for different organo-transformation reactions has been a subject of interest over recent years.^[10, 14b, 16]

The major cause of deactivation in Cr-based catalysis is the leaching of active Cr ions, and a need for stable catalysts has

[a] K. J. Betsy, A. Lazar, A. Krishnan, Dr. C. P. Vinod
Catalysis and Inorganic Chemistry Division
CSIR-National Chemical Laboratory
Dr. Homi Bhabha Road, Pashan, Pune-411008 (India)
E-mail: cp.vinod@ncl.res.in

[b] C. Nayak, Dr. D. Bhattacharyya, Dr. S. N. Jha
Atomic and Molecular Physics Division
Bhabha Atomic Research Centre
Mumbai-400085 (India)

[c] A. Lazar, Dr. C. P. Vinod
Academy of Scientific and Innovative Research (AcSIR)
Anusandhan Bhawan, 2, Rafi Marg, New Delhi-110001 (India)

[d] Dr. C. P. Vinod
Center of Excellence on Surface Science
CSIR-National Chemical Laboratory
Dr Homi Bhabha Road, Pune-411 008 (India)

Supporting information and the ORCID identification number(s) for the author(s) of this article can be found under:
<https://doi.org/10.1002/cctc.201800309>.

led to the design of new heterogenized Cr catalysts.^[14a,17] There is an intimate relationship between the compositional, structural, and physicochemical properties of the oxide support and the surface nature of Cr. The oxide support acts as a ligand that controls the redox properties of the supported Cr ions. Hence the selection of a support that can stabilize the chromium active sites is tedious. Among oxide supports, mesoporous M41S molecular sieves (MCM-41 and MCM-48) are promising candidates that exhibit good textural properties and act as an ideal scaffold for the incorporation of metal oxides on mesoporous channels. These properties prevent the agglomeration of chromium oxide particles and also favor the diffusion of reacting molecules.^[18]

In this study, we aim to examine the nature of active Cr species on the silica-supported catalyst for cyclohexane oxidation. A series of samples with uniformly dispersed chromium oxide supported on mesoporous MCM-41 silica nanospheres was prepared by varying the amount of Cr by a facile wet impregnation method. The nature of the Cr active species for cyclohexane oxidation was determined by correlating the catalytic activity with the characterization results. Under mild reaction conditions, the optimum catalyst gave 72% conversion and 99% selectivity towards cyclohexanone.

Results and Discussion

Characterization

The powder XRD patterns of the CrO_x-MCM-41 catalysts were collected in two different 2θ regions. In the small-angle X-ray diffraction (SAXRD) pattern (Figure 1 A) a peak at 2θ = 2.5° corresponds to the d₁₀₀ reflection in agreement with the XRD pattern of the MCM-41-type materials.^[19] As the Cr loading in the catalyst increases from 0.5 to 10 wt%, the intensity of the (100) peak becomes weak. Nevertheless, the peak is still detectable, which indicates that the mesoporous structure of the materials was preserved even after impregnation followed by calcination. A decrease in the peak intensity with an increase of the Cr loading also infers the anchoring of Cr in the MCM-41 pores. If we compare the unit cell parameter (a₀) for pristine MCM-41 (a₀ = 39.4 Å) and 5CrO_x-MCM-41 (a₀ = 40.1 Å), no clear incorporation of Cr into the silica framework can be inferred. From the wide-angle XRD patterns (Figure 1 B), the diffraction lines are attributable to the rhombohedral phase of Cr₂O₃ (JCPDS No: 84-1616) with a clear increase in intensity as the metal loading increases.

The textural properties of catalysts were explored by using N₂ adsorption–desorption analysis, and the results are summarized in Table 1. The chromium oxide supported MCM-41 catalysts 0.5CrO_x-MCM-41, 5CrO_x-MCM-41, and 10CrO_x-MCM-41 show typical type-IV isotherms with H1 hysteresis (Figure 2), which indicate that the overall mesoporous structure of the catalysts was retained. The pure MCM-41 material exhibits a high surface area (957 m²g⁻¹), large pore volume (0.529 ccg⁻¹), and a bimodal distribution (Figure 2, inset) with pore radii of 2.9 and 5.4 nm. After MCM-41 was loaded with Cr species, the surface area, pore diameter, and pore volume of the material

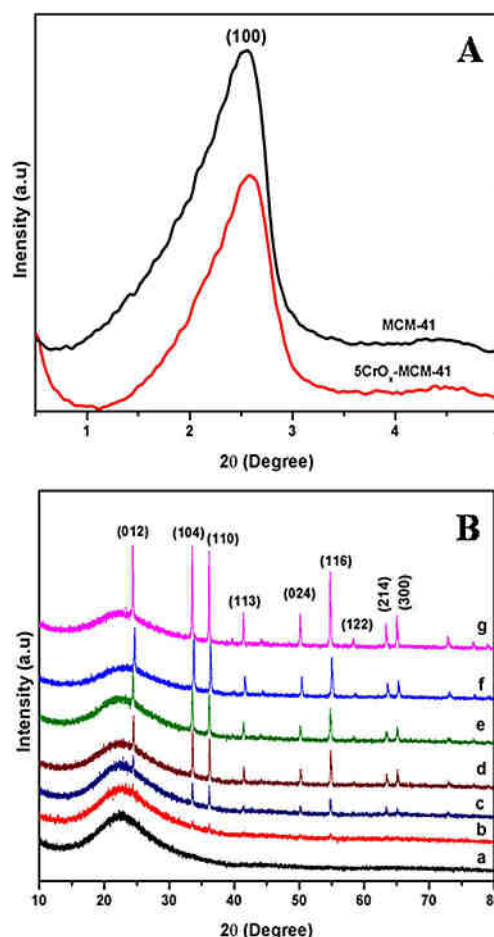


Figure 1. Powder XRD patterns of the CrO_x-MCM-41 catalysts in two different 2θ regions. A) Small-angle XRD and B) Wide-angle XRD patterns of a) 0.5CrO_x-MCM-41, b) 1CrO_x-MCM-41, c) 2.5CrO_x-MCM-41, d) 4CrO_x-MCM-41, e) 5CrO_x-MCM-41, f) 7CrO_x-MCM-41, and g) 10CrO_x-MCM-41.

Table 1. Textural properties of MCM-41 and nCrO_x-MCM-41^[a] catalysts.

Catalyst	BET surface area [m ² g ⁻¹]	Pore diameter [nm]	Pore volume [ccg ⁻¹]
MCM-41	957	2.9 and 5.4	0.53
0.5CrO _x -MCM-41	926	2.9 and 5.4	0.52
5CrO _x -MCM-41	859	2.7 and 5.2	0.50
10CrO _x -MCM-41	535	2.8 and 5.3	0.27

[a] nCrO_x-MCM-41 in which n indicates the Cr loading [wt%] with respect to the support.

decreased, which indicates that chromium oxide was anchored on the MCM-41 mesoporous channels.

²⁹Si cross-polarization magic-angle spinning (CPMAS) NMR spectra of pure MCM-41 and 5CrO_x-MCM-41 are shown in Figure S1. Three distinct peaks exist at δ = -92, -102, and -112 ppm that correspond to the Q², Q³, and Q⁴ sites on the silica framework, respectively. There is no noticeable difference in the intensity and width of these distinct peaks observed in both pure MCM-41 and the 5CrO_x-MCM-41 catalysts. Zhang and Pinnavaia proposed that a broadening of the peak width and increase in the intensity of the Q⁴ sites along with a de-

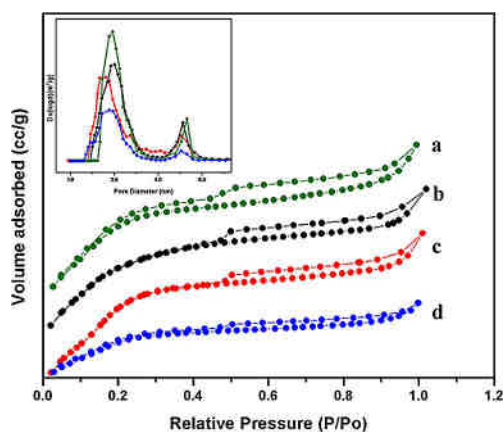


Figure 2. N_2 adsorption–desorption isotherms and pore size distributions (inset) of a) pure MCM-41, b) $0.5CrO_x$ -MCM-41, c) $5CrO_x$ -MCM-41, and d) $10CrO_x$ -MCM-41.

crease in the intensity of the Q^2 and Q^3 sites is mainly caused by isomorphous transition metal substitution into the Si framework.^[20] Thus, the retention of three sites in silica indicates that isomorphous Cr metal substitution into the silica framework was improbable in this case.

We used TEM and SEM to monitor the surface morphology and pore structures of the synthesized materials. A spherical morphology of the synthesized MCM-41 material with an average particle size of approximately 70 nm was confirmed (Figure 3a), and the hexagonal mesoporous nature of the catalyst is in good agreement with the SAXRD results. The TEM image of $5CrO_x$ -MCM-41 (Figure 3b) shows the spherical morphology and the mesoporous nature of the material even after calcination to obtain the chromium oxide species. Energy-dispersive X-ray analysis (EDAX) from the TEM image of $5CrO_x$ -MCM-41 showed the presence of Cr (≈ 4.6 wt%) in the spherical MCM-41 sample (Figure S2). SEM analysis of $5CrO_x$ -MCM-41 also supports the retention of the spherical morphology (Figure S3).

FTIR spectroscopy is a convenient technique to study the nature of Cr species present in porous CrO_x -MCM-41 catalysts (Figure 4). The IR bands at $\tilde{\nu} = 800$, 950, and 1105 cm^{-1} correspond to Si–O–Si symmetric stretching, Si–OH stretching, and Si–O–Si asymmetric stretching vibrations in the silica framework, respectively.^[21] The IR band for O– Cr^{VI} species in CrO_x -MCM-41 occurs at $\tilde{\nu} = 950\text{ cm}^{-1}$ ^[22] and its peak is not measurable quantitatively because of the overlap of the Si–OH stretching band in the same region. Meanwhile, a distinct band is observed at $\tilde{\nu} = 623\text{ cm}^{-1}$ that corresponds to chromium oxide species,^[23] which can be taken as an indicator for the presence of CrO_x species in MCM-41 channels.

To investigate the oxidation state and coordination environment of Cr in CrO_x -MCM-41 catalysts, UV/Vis diffuse reflectance spectroscopy (DRS) was performed. Two absorption bands centered at $\lambda = 275$ and 365 nm are observed in the spectra of all synthesized catalysts and are assigned to tetrahedrally coordinated isolated chromium oxide species O– Cr^{VI} (Figure 5). These bands are typical for the transitions of ${}^1T_2 \leftarrow {}^1A_1$ (${}^1t_1 \rightarrow {}^7t_2$ and ${}^6t_2 \rightarrow 2e$) and ${}^1T_2 \leftarrow {}^1A_1$ (${}^1t_1 \rightarrow 2e$), respectively.^[24] A peak at $\lambda = 467\text{ nm}$ is assigned to a Cr^{3+} transition that has a distorted

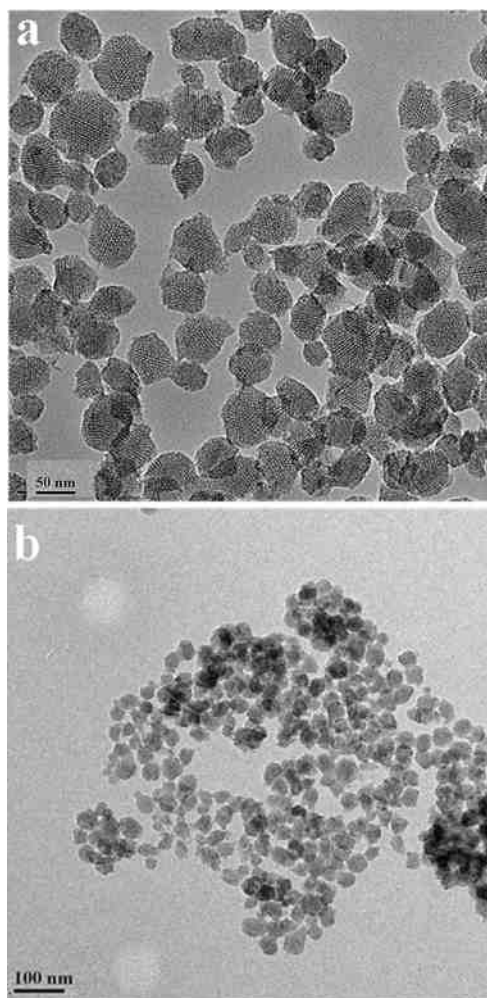


Figure 3. TEM images of a) pure MCM-41 and b) $5CrO_x$ -MCM-41.

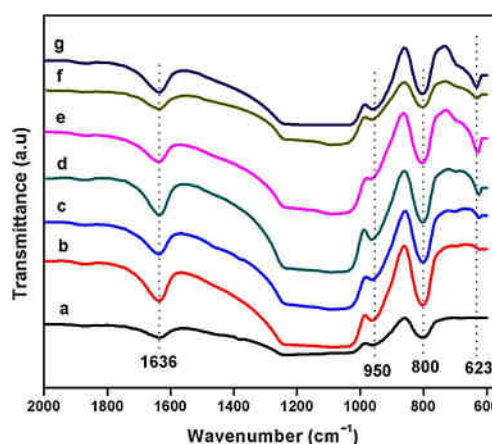


Figure 4. FTIR spectra of a) $0.5CrO_x$ -MCM-41, b) $1CrO_x$ -MCM-41, c) $2.5CrO_x$ -MCM-41, d) $4CrO_x$ -MCM-41, e) $5CrO_x$ -MCM-41, f) $7CrO_x$ -MCM-41, and g) $10CrO_x$ -MCM-41.

octahedral symmetry, (${}^4T_{1g} \leftarrow {}^4A_{2g}$),^[24,25] which increased in intensity with an increase in the Cr content.

The intensity of this peak is weaker than that of the charge transition bands in the catalysts that contained less Cr. An ad-

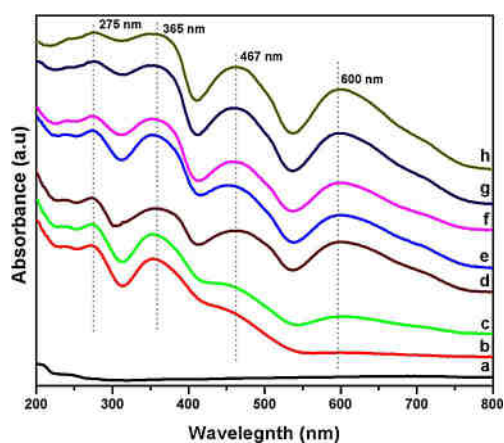


Figure 5. UV/Vis spectra of a) pure MCM-41, b) 0.5CrO_x-MCM-41, c) 1CrO_x-MCM-41, d) 2.5CrO_x-MCM-41, e) 4CrO_x-MCM-41, f) 5CrO_x-MCM-41, g) 7CrO_x-MCM-41, and h) 10CrO_x-MCM-41.

ditional broad band located at $\lambda = 600$ nm caused by the d–d transitions related to Cr³⁺ species in octahedral coordination indicates the presence of Cr₂O₃ clusters. As we move to catalysts with a higher Cr loading, the synthesized materials exhibit a gradual increase in peak intensity at $\lambda = 275$ nm, which is because of the overlap of the charge transfer band of Cr³⁺ with the Cr⁶⁺ signal,^[24] whereas an increase in the peak intensity at $\lambda = 600$ nm corresponds to the agglomeration of Cr³⁺ species to crystalline α -Cr₂O₃ at a high Cr content.

To probe the molecular nature of the supported Cr species in all solid catalysts, Raman spectroscopy was used. We measured the Raman spectra of the series of synthesized catalysts in which an increase in the Cr loading led to bands that correspond to different Cr surface species (Figure 6). A peak at $\tilde{\nu} = 350$ cm⁻¹ is assigned to monochromatic Cr⁶⁺ surface species which increases in intensity above 5 wt% Cr loading.^[26] The intensity of the two bands centered at $\tilde{\nu} = 553$ and 609 cm⁻¹, characteristic of crystalline Cr₂O₃ and distorted octahedral Cr³⁺ species, respectively, increases with the increase in the Cr content.^[12,27] Moreover, two broad bands located at $\tilde{\nu} = 868$ and

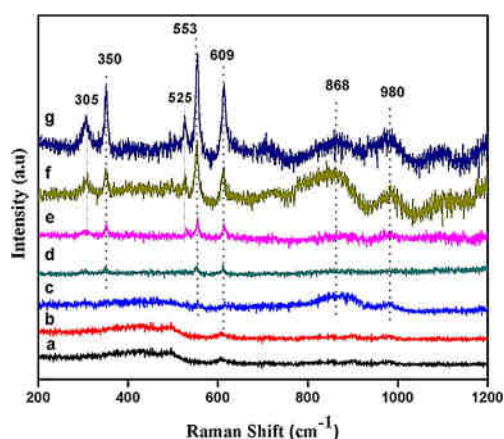


Figure 6. Raman spectra of a) 0.5CrO_x-MCM-41, b) 1CrO_x-MCM-41, c) 2.5CrO_x-MCM-41, d) 4CrO_x-MCM-41, e) 5CrO_x-MCM-41, f) 7CrO_x-MCM-41, and g) 10CrO_x-MCM-41.

980 cm⁻¹ observed in the spectra of only the catalysts with a high Cr loading are evident and confirm the existence of polymeric Cr⁶⁺ species.^[26] The peaks at $\tilde{\nu} = 305$ and 525 cm⁻¹, which are absent in the spectra of the catalysts with a low loading, confirm the absence of crystalline α -Cr₂O₃ species, which is clearly visible in the spectra of catalysts with a high Cr loading, that is, above the monolayer coverage. As the metal loading increases, the mono- and dichromate species tend to agglomerate to form trichromate species and lead to the formation of crystalline Cr₂O₃ clusters, which is in good agreement with the results obtained by using UV/Vis spectroscopy and XRD.

The Cr2p XPS plots of the *n*CrO_x-MCM-41 samples are shown in Figure 7 and provide evidence of the oxidation state of surface Cr species. The calibration of all the peak positions was performed by considering the C1s standard binding energy (BE) of 284.6 eV. The broad nature of the Cr2p_{3/2} and Cr2p_{1/2} regions of the chromium oxide catalysts indicates the existence of more than one Cr species on the surface. We used an XPS peak-fitting program to deconvolute the Cr2p_{3/2} region into two peaks centered at BE = 576 and 579 eV, which are attributed to the Cr³⁺ and Cr⁶⁺ species, respectively.^[28]

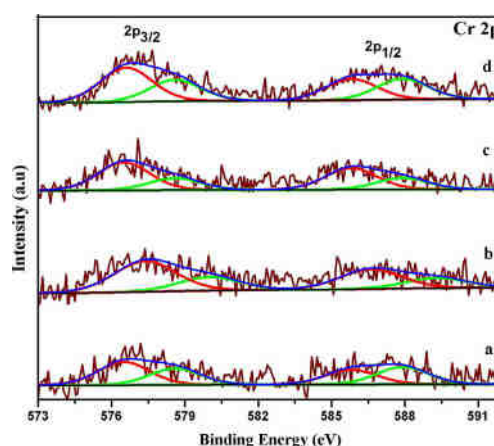


Figure 7. Cr 2p XPS spectra of a) 2.5CrO_x-MCM-41, b) 4CrO_x-MCM-41, c) 5CrO_x-MCM-41, and d) 10CrO_x-MCM-41.

To garner further insight into the structure and coordination environment of the Cr species, synchrotron X-ray absorption spectroscopy (XAS) was performed. X-ray absorption near edge structure (XANES) spectra at the Cr K edge of the MCM-41-supported catalyst samples along with Cr metal, Cr₂O₃, and CrO₃ standards are presented in Figure 8a. CrO₃ shows a strong pre-edge peak near 5991 eV, which is caused by the dipole-forbidden 1s–3d transition. This forbidden transition is allowed if Cr cations exist in a non-centrosymmetric environment. In CrO₃, Cr^{VI} cations exist in a tetrahedral coordination environment that facilitates the hybridization of the 3d and 4p orbitals, and therefore, the 1s–3d transition becomes allowed and results in a strong pre-edge. In Cr₂O₃, the Cr^{III} cations exist in an octahedral coordination that forbids the 1s–3d transition and results in no pre-edge.^[29] Linear combination fitting (LCF) of the XANES spectra of the samples was performed using

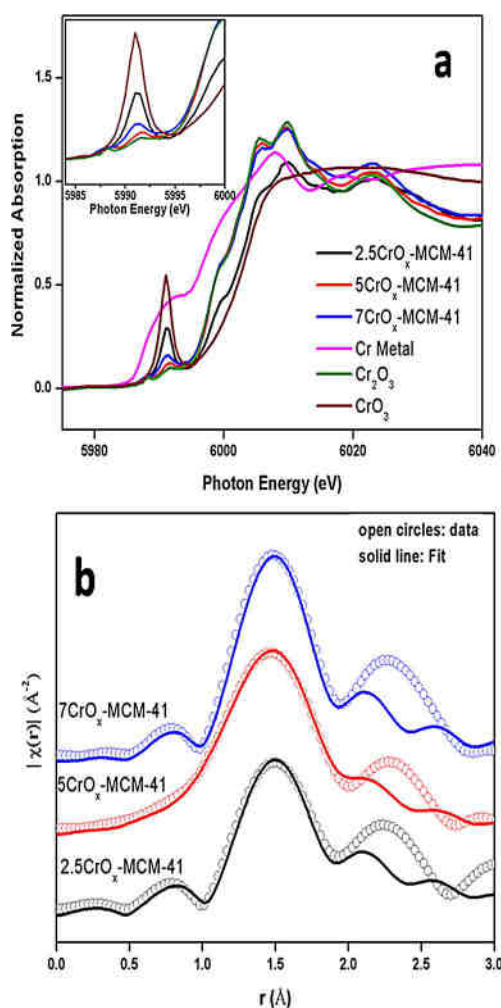


Figure 8. a) XANES and b) EXAFS spectra of the $n\text{CrO}_x\text{-MCM-41}$ catalysts.

standard XANES spectra of Cr_2O_3 and CrO_3 to determine the molar percentage of Cr^{III} and Cr^{VI} species. The results of the LCF are tabulated in Table S1. From the LCF results, it can be concluded that in $5\text{CrO}_x\text{-MCM-41}$ and $7\text{CrO}_x\text{-MCM-41}$, Cr cations exist mostly as octahedral Cr^{III} species, whereas above 5 wt% Cr loading, most of the Cr^{3+} species occur as $\alpha\text{-Cr}_2\text{O}_3$. However, in $2.5\text{CrO}_x\text{-MCM-41}$, Cr cations exist as both octahedral Cr^{III} species and tetrahedral Cr^{VI} species with a $\text{Cr}^{\text{III}}/\text{Cr}^{\text{VI}}$ molar percentage ratio of 55:45. The LCF results corroborate the intensity variation of the pre-edge peaks as shown in the inset of Figure 8a on an enlarged scale.

Experimental extended X-ray absorption fine structure (EXAFS; $\mu(E)$ vs. E) spectra of the chromium oxide supported on MCM-41 catalyst samples measured at the Cr K edge and the experimental $\chi(r)$ versus r plots of the Cr oxide supported on MCM-41 catalyst samples at Cr K edge fitted from 1–2 Å and assuming a Cr–O ($\times 6$) shell are presented in Figure S4. Experimental $\chi(r)$ versus r plots of the chromium oxide supported on MCM-41 catalyst samples

at the Cr K edge along with best fit theoretical plots obtained as above are shown in Figure 8b, and the fitting results are tabulated in Table S2. From the EXAFS results, it can be observed that for $5\text{CrO}_x\text{-MCM-41}$ and $7\text{CrO}_x\text{-MCM-41}$, six O atoms exist around Cr cations at a distance of approximately 1.95 Å. This local environment resembles the Cr_2O_3 structure, which suggests the presence of octahedral Cr^{III} species. However, for $2.5\text{CrO}_x\text{-MCM-41}$, the Cr–O bond length decreases to 1.89 Å with a coordination number of 5. This decrease in the bond length and coordination number may be attributed to the presence of tetrahedral Cr^{VI} cations in this sample. From XANES analysis, the $\text{Cr}^{\text{III}}/\text{Cr}^{\text{VI}}$ molar percentage ratio is 55:45 in this sample, which gives an average coordination number of $0.55 \times 6 + 0.45 \times 4 = 5.1$. Therefore, the EXAFS analysis results corroborate with the XANES LCF results.

Thus from XANES LCF and EXAFS analysis, it can be concluded that Cr cations mostly exist as octahedral Cr^{III} in $5\text{CrO}_x\text{-MCM-41}$ and $7\text{CrO}_x\text{-MCM-41}$, and a major portion of Cr^{III} exists in the crystalline $\alpha\text{-Cr}_2\text{O}_3$ phase in the latter. In $2.5\text{CrO}_x\text{-MCM-41}$, Cr cations exist as both octahedral Cr^{III} species and tetrahedral Cr^{VI} species with a $\text{Cr}^{\text{III}}/\text{Cr}^{\text{VI}}$ molar ratio of 55:45.

Catalytic activity

The catalytic performance of the 0.5, 1, 2.5, 4, 5, 7, and 10 wt% Cr loaded catalysts ($\text{CrO}_x\text{-MCM-41}$) was investigated in the liquid-phase cyclohexane oxidation reaction. The reaction was performed under mild conditions (70 °C). Acetonitrile was used as the solvent, and *tert*-butyl hydroperoxide (TBHP) was used as both the oxidizer and radical initiator to overcome the induction period.

The catalytic activity trend of the different catalysts in the oxidation reaction to achieve the direct production of cyclohexanone from cyclohexane is shown in Table 2, entries 5–11.

Table 2. Catalytic oxidation of cyclohexane to cyclohexanone. ^[a]					
Entry	Catalyst	Conversion ^[b] [%]	Selectivity [%] ^[c,d]		Ref.
			Cyclohexanone	Cyclohexanol	
1	–	0	0	0	this work
2	Pure MCM-41	0	0	0	this work
3	Bulk Cr_2O_3	9	91	9	this work
4	CrO_3	6	83	17	this work
5	$0.5\text{CrO}_x\text{-MCM-41}$	14	99	–	this work
6	$1\text{CrO}_x\text{-MCM-41}$	18	99	–	this work
7	$2.5\text{CrO}_x\text{-MCM-41}$	36	99	–	this work
8	$4\text{CrO}_x\text{-MCM-41}$	54	99	–	this work
9	$5\text{CrO}_x\text{-MCM-41}$	72	99	–	this work
10	$7\text{CrO}_x\text{-MCM-41}$	12	99	–	this work
11	$10\text{CrO}_x\text{-MCM-41}$	8	99	–	this work
12	(Cr)MCM-41 [TBHP]	61	81	–	[6]
13	(Cr)MCM-41 [H_2O_2]	99	1	89	[11]
14	(Cr)PMO [TBHP]	12	70	22	[10]
15	Cr-MCM-41 [air]	7	66	26	[30]
16	Cr-Co-TUD-1 [TBHP]	43	84	5	[31]

[a] Reaction conditions: catalyst (50 mg), cyclohexane (1 mmol), 70% TBHP (1.2 mmol), CH_3CN (5 mL), 70 °C, 24 h; [b] (initial concentration of C_6H_{12} – concentration of C_6H_{12} at time t /initial concentration of C_6H_{12}) $\times 100$; [c] (moles of individual product/ moles of total products) $\times 100$; [d] includes trace amounts of adipic acid.

Remarkably, the 5 wt% Cr loaded catalyst showed a conversion of 72% and a selectivity of 99% towards cyclohexanone. To validate the performance of our CrO_x -MCM-41 catalysts for their high selectivity towards cyclohexanone from cyclohexane with a comparable conversion, activity results were compared with previous reports on Cr-based silica catalysts in which TBHP, H_2O_2 , and air were used as oxidants (Table 2, entries 12–16). Generally, cyclohexanone was the major product obtained if TBHP was used as the oxidant, which is in agreement with previous reports.^[6, 16b, 32] From previous studies, the active site for cyclohexane oxidation on Cr-MCM-41 catalysts was the tetrahedral Cr species in the silica framework.^[6]

A volcano-type trend in activity was observed from the conversion plot as the Cr loading increases in the catalyst (Figure 9, green line) in good agreement with the XPS and XAS

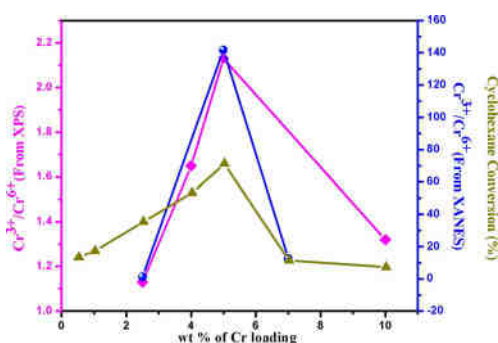


Figure 9. Plot that shows the relative effectiveness of $\text{Cr}^{3+}/\text{Cr}^{6+}$ to catalyze the oxidation of cyclohexane over the $n\text{CrO}_x$ -MCM-41 catalysts.

data. The conversion of cyclohexane over the Cr catalysts increases sharply with the increase in the total Cr content up to 5 wt%, and a further increase of the metal content (7 and 10 wt%) leads to a decrease in cyclohexane conversion. Interestingly, all of the synthesized catalysts exhibit 99% selectivity towards cyclohexanone. This unfavorable decrease in conversion could be explained either by the decrease in dispersed Cr^{3+} species or by the formation of inactive crystalline $\alpha\text{-Cr}_2\text{O}_3$ on the surface, which results in pore blocking and limits the diffusion of reactant molecules. A plot of the ratio of Cr^{3+} to Cr^{6+} throws more light onto the nature of the active Cr species for this reaction. The $\text{Cr}^{3+}/\text{Cr}^{6+}$ ratios of catalysts with different Cr loadings were determined from the fitted peaks of the XPS and XANES spectra, and the results revealed that as we increase the Cr content, the ratio of $\text{Cr}^{3+}/\text{Cr}^{6+}$ species increases up to 5 wt% and decreases with further loading (Figure 9).

The formation of crystalline $\alpha\text{-Cr}_2\text{O}_3$ and polymeric chromium oxide species were significant in 7CrO_x -MCM-41 and 10CrO_x -MCM-41. At lower loadings, Cr exists in both isolated Cr^{3+} and Cr^{6+} species, whereas the catalyst with a 5% loading consists exclusively of dispersed chromium(III) oxide sites. A further increase in the metal loading showed the presence of polymeric Cr^{6+} along with Cr^{3+} species, of which the major Cr^{3+} contribution is from crystalline $\alpha\text{-Cr}_2\text{O}_3$ and was detected by using XRD, Raman spectroscopy, and UV/Vis spectroscopy. This confirms that crystalline $\alpha\text{-Cr}_2\text{O}_3$ and polymeric Cr^{6+} spe-

cies passivate the activity of amorphous Cr^{3+} species on the silica surface at higher loadings. Although a small number of Cr_2O_3 cluster peaks were observed for all of the solid catalysts except 0.5CrO_x -MCM-41, the increase in the conversion of cyclohexane by using a catalyst with a low metal loading reveals clearly that these clusters do not block the accessible Cr active sites. These characterization and activity results indicate the existence of two different types of Cr^{3+} species such as crystalline $\alpha\text{-Cr}_2\text{O}_3$ and an amorphous or microcrystalline phase of nonframework chromium(III) oxide sites. Cyclohexane oxidation was also performed without catalyst and with bare MCM-41, bulk Cr_2O_3 , and CrO_3 (Table 2, entries 1–4), which all exhibit a lower conversion. In control experiments, the absence of oxidized products or a lower conversion from cyclohexane evidence that isolated amorphous Cr^{3+} species in the supported MCM-41 catalyst play a key role in the transfer of oxygen from the oxidant to cyclohexane during the reaction.

To check the leaching of Cr ions from the MCM-41 channels in the catalyst, a recycling study of the active 5CrO_x -MCM-41 catalyst was performed by using the spent catalyst continuously in the next two cycles of catalytic oxidation. The regenerated catalyst was pretreated at 120°C for 12 h to remove the physisorbed water molecules before the spent catalyst was used for each cycle. In this step, the catalyst was recovered by centrifugation, washed repeatedly with acetonitrile, and dried at 120°C for 12 h. The catalyst showed a gradual loss of activity in each successive run (Table S3). To investigate the cause for the decrease in the activity after each cycle, the spent catalyst was investigated by using XPS. A comparison of the ratio of $\text{Cr}^{6+}/\text{Cr}^{3+}$ in fresh (0.47) and spent (0.40) 5CrO_x -MCM-41 catalysts indicates that nonframework Cr^{6+} species were leached significantly during the reaction along with a small amount of Cr^{3+} species. UV/Vis spectra were measured for the spent catalysts (Figure S5). A decrease in the peak intensity at $\lambda = 275$, 365, and 467 nm was observed in the spectra of the spent catalyst compared to that of the fresh, which indicates the leaching of Cr ions from the catalysts during the reaction. The peak at $\lambda = 600$ nm was present, which shows that Cr^{3+} species from crystalline Cr_2O_3 are not affected during the recycling experiment and are not the likely reason for the catalyst deactivation. Thus, the UV/Vis spectra correlate well with the XPS analysis, which showed Cr^{3+} species to be unaffected during the reaction. The Cr content in the spent 5CrO_x -MCM-41 catalyst was confirmed by using inductively coupled plasma optical emission spectroscopy (ICP-OES) and was approximately 4% with respect to the catalyst. As the amount of Cr^{3+} species is nearly unchanged in the catalyst, the loss of catalytic activity during the second and third cycle was intriguing. To probe this, the used catalyst was pretreated by calcination at 600°C for 8 h and used for cyclohexane oxidation. The pretreated used catalyst showed a similar activity ($\approx 70\%$ conversion) as the fresh 5CrO_x -MCM-41 catalyst, which indicates that nonframework Cr^{3+} species in the catalyst are active under the reaction conditions and that the deactivation might be caused by the blocking of active sites by carbonaceous species. Further efforts are ongoing to obtain a thorough understanding of the plausible species that account for the deactivation.

Conclusions

To probe the nature of catalytically active Cr sites in cyclohexane oxidation, we synthesized chromium oxide supported MCM-41 nanosphere catalysts by a facile wet impregnation method. Among the catalysts with different Cr loadings, the 5 wt% metal loaded catalyst showed an unprecedentedly high activity with 72% cyclohexane conversion and 99% selectivity for cyclohexanone. A better understanding of the active Cr species was obtained by correlating the catalytic and characterization results for cyclohexane oxidation. The volcano-type catalytic performance could be attributed to the interplay between the surface Cr^{6+} and Cr^{3+} species in the material, which varies with the Cr content. From our results, the excellent activity towards the cyclohexanone product under mild reaction conditions can be attributed to the initial concentration of the extraframework amorphous Cr^{3+} species in the MCM-41-supported catalyst. Efforts are ongoing to identify the cause of deactivation by using spectroscopic techniques.

Experimental Section

Chromium(III) nitrate nonahydrate ($\text{Cr}(\text{NO}_3)_3 \cdot 9\text{H}_2\text{O}$; Alfa Aesar, 98.5%) cetyltrimethyl ammonium bromide (CTAB; 98%), tetraethylorthosilicate (TEOS, Sigma Aldrich), TBHP (Acros Chemicals), NaOH (Loba Chemie), cyclohexane (Ran Kem), acetonitrile (Thomas Baker), cyclohexanone (Thomas Baker), and cyclohexanol (Thomas Baker) were used as received. Ultrapure Millipore water was used in all experiments.

Spherical MCM-41 nanospheres were synthesized using the modified sol-gel procedure reported previously.^[19b] Typically, NaOH solution (3.5 mL, 2 M) was mixed with Millipore water (480 mL). CTAB (1 g) was added to the solution, and the mixture was heated at 70 °C with stirring. After the solution became homogeneous, TEOS (5 mL) was dropwise to form a white slurry. The stirring was continued at 70 °C for 2 h. The resulting white residue was collected by filtration and washed thoroughly with water and ethanol to remove excess of NaOH and CTAB. The obtained powder was dried at 100 °C for 12 h and calcined in air at 500 °C for 4 h (at a ramp rate of 2 °C min⁻¹).

Heterogeneous CrO_x -MCM-41 catalysts with different Cr loadings were synthesized by a wet impregnation method by utilizing a procedure reported elsewhere^[33] with slight modifications. Briefly, the desired amount of active $\text{Cr}(\text{NO}_3)_3 \cdot 9\text{H}_2\text{O}$ metal precursor was dissolved in the minimum amount of water, and MCM-41 (1 g) was added slowly with continuous stirring. The slurry was allowed to stir for 8 h after which the resulting material was dried at 100 °C for 12 h and calcined at 600 °C for 8 h (at a ramp rate of 2 °C min⁻¹). The Cr loading on MCM-41 was controlled at 0.5, 1, 2.5, 4, 5, 7, and 10 wt% by varying the amount of metal precursor.

Liquid-phase cyclohexane oxidation was performed in a two-necked round-bottomed flask equipped with a condenser and charged with cyclohexane (1 mmol), acetonitrile (5 mL) as the solvent, catalyst (50 mg), and TBHP (1.2 mmol) as the oxidant. The reaction was performed at 70 °C for 24 h with continuous stirring. After the reaction, the catalyst was separated by simple centrifugation, and the products were analyzed by using GC (Agilent 7890 connected with HP5 column and flame ionization detector; FID) and confirmed by using GC-MS (Varian connected with an HP5

column). The products were determined by comparison with authentic samples by using GC and GC-MS. HPLC with a Rezex ROA H+ column was used to analyze acid products. To test reusability, after each cycle, the catalyst was washed repeatedly with acetonitrile and pretreated at 120 °C for 12 h.

Powder XRD analysis of all catalysts was measured by using a PANalytical X'pert Pro dual-goniometer diffractometer with Ni-filtered $\text{CuK}\alpha$ radiation (1.5418 Å) at 40 kV and 30 mA. A Shimadzu UV/Vis spectrophotometer with a dual beam was used to measure UV/Vis spectra. N_2 adsorption-desorption isotherms and pore size distributions of the samples were collected by using an Autosorb 1C Quantachrome, USA. The program consisted of both adsorption and desorption branches and was performed typically at 77 K after the samples were degassed at 150 °C for 4 h. Calculation of the specific surface area was done by the Brunauer-Emmett-Teller (BET) method at $P/P_0=0.06-0.3$. The Barrett-Joyner-Halenda (BJH) model was applied to the desorption branch of the isotherm to determine the total pore volume and average pore diameter. Pore size distribution curves were obtained by the BJH approach. FTIR spectroscopy of the solid samples was performed by using a Bruker Tensor 27 FTIR spectrophotometer with a DTGS detector at RT by using KBr as an internal standard. TEM images were recorded by using an FEI Tecnai TF-20 electron microscope operated at 200 kV. SEM images were obtained by using a dual-beam scanning electron microscope (FEI company, model Quanta 200 3D) operated at 30 kV. ²⁹Si MAS NMR spectra were recorded by using a BRUKER DSX300 spectrometer at 7.05 T (resonance frequencies 59.595 MHz, rotor speed 10000 Hz; and 75.43 MHz, rotor speed 10000 Hz). XPS was performed under ultra-high vacuum conditions by using a near-ambient-pressure X-ray photoelectron spectrometer (NAP-XPS) from Prevac, Poland. All the spectra were charge corrected with respect to C 1s at BE=284.6 eV. The peak-fitting of the Cr 2p spectra was performed using CasaXPS software with a Shirley-type background. A Horiba Jobin Yvon LabRaman HR 800 micro Raman spectrometer (HJY, Kyoto, Japan) with a laser wavelength of 514 nm was used to collect Raman spectra.

XAS measurements of the catalysts were performed at the Cr K edge in fluorescence mode at the Scanning EXAFS Beamline (BL-9) at the INDUS-2 Synchrotron Source (2.5 GeV, 100 mA) at the Raja Ramanna Centre for Advanced Technology (RRCAT), Indore, India.^[34] A double crystal monochromator (DCM) was used as the beamline, which works in the photon energy range of 4–25 KeV with a resolution of 10⁻⁴ at 10 KeV. A horizontal premirror of 1.5 m with a meridional cylindrical curvature is used to collimate the beam, and a higher harmonic rejection was used before the DCM. A sagittal cylinder with a radius of curvature of 1.28–12.91 m was used as the second crystal. This provides the horizontal focusing of the beam, whereas a Rh/Pt-coated bendable post mirror that faced down was used for the vertical focusing of the beam. For fluorescence-mode measurements, the sample was placed at 45° to the incident X-ray beam and the fluorescence signal (I_f) was detected using a Si drift detector placed 90° to the incident X-ray beam. An ionization chamber detector was used to measure the incident X-ray flux (I_0) and the sample absorbance ($\mu = I_f/I_0$) as a function of energy obtained by scanning the monochromator over a specified energy range.

EXAFS oscillations were extracted from the XAS spectra following the standard procedure.^[35] The EXAFS oscillations, $\chi(k)$ were weighted by k to amplify the oscillation at high k . The $\chi(k)$ k functions were Fourier transformed using a k range of 2–9 Å⁻¹ to generate the $\chi(r)$ versus r (or FT-EXAFS) spectra in terms of the real distances from the center of the absorbing atom. The Demeter soft-

ware package was used for EXAFS data analysis by the reduction and fitting of the experimental EXAFS data.^[36] The EXAFS data fitting parameters were bond distance (r), coordination number (N), and Debye–Waller factor (σ^2), which give the static and thermal disorder of the system. The k range for Fourier transform and the R range for data fitting were chosen in such a way that in each case during fitting, the number of free variables was always kept below the upper limit set by the Nyquist theory ($N_{\text{free}} = 2\Delta k \Delta r / \pi + 1$).^[37] The goodness of the fit in the above process is generally expressed by the R_{factor} [Eq. (1)]:

$$R_{\text{factor}} = \sum \frac{[\text{Im}(\chi_{\text{dat}}(r_i) - \chi_{\text{th}}(r_i))^2 + [\text{Re}(\chi_{\text{dat}}(r_i) - \chi_{\text{th}}(r_i))^2]}{[\text{Im}(\chi_{\text{dat}}(r_i))^2 + [\text{Re}(\chi_{\text{dat}}(r_i))^2]}$$

in which χ_{dat} and χ_{th} refer to the experimental and theoretical $\chi(r)$ values, respectively, and Re and Im refer to the real and imaginary parts of the respective quantities. The R_{factor} of all the fitting is less than 0.01, which indicates the good fitting of the data.

Acknowledgements

C.P.V. thanks Director, CSIR-NCL for continuous support. This work was funded by CSIR-NCL through a grant MLP030626, DST INDO DUTCH bilateral project on functional materials (DST/INT/NL/FM/P-002/2013/1) and partially supported by a GAP-309826 BRNS grant.

Conflict of interest

The authors declare no conflict of interest.

Keywords: chromium • heterogeneous catalysis • nanostructures • oxidation • supported catalysts

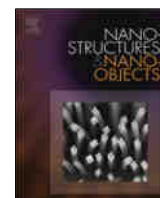
- [1] M. T. Musser in *Ullmann's Encyclopedia of Industrial Chemistry*, Wiley-VCH, 2000, Weinheim.
- [2] R. A. Sheldon, J. K. Kochi, *Advances in Catalysis*, Vol. 25 (Eds.: H. P. D. D. Eley, B. W. Paul), Academic Press, 1976, 272–413.
- [3] a) H. Hattori, Y. Ide, S. Ogo, K. Inumaru, M. Sadakane, T. Sano, *ACS Catal.* 2012, 2, 1910–1915; b) C. Wang, L. Chen, Z. Qi, *Catal. Sci. Technol.* 2013, 3, 1123–1128.
- [4] K. Wu, B. Li, C. Han, J. Liu, *Appl. Catal. A* 2014, 479, 70–75.
- [5] H. X. Yuan, Q. H. Xia, H. J. Zhan, X. H. Lu, K. X. Su, *Appl. Catal. A* 2006, 304, 178–184.
- [6] A. Sakthivel, P. Selvam, *J. Catal.* 2002, 211, 134–143.
- [7] a) S. A. C. Carabineiro, L. M. D. R. S. Martins, A. J. L. Pombeiro, J. L. Figueiredo, *ChemCatChem* 2018, 10, 1804–1813; b) S. A. C. Carabineiro, L. M. D. R. S. Martins, M. Avalos-Borja, J. G. Buijnsters, A. J. L. Pombeiro, J. L. Figueiredo, *Appl. Catal. A* 2013, 467, 279–290; c) M. P. de Almeida, L. M. D. R. S. Martins, S. A. C. Carabineiro, T. Lauterbach, F. Rominger, A. S. K. Hashmi, A. J. L. Pombeiro, J. L. Figueiredo, *Catal. Sci. Technol.* 2013, 3, 3056–3069; d) L. M. Dias Ribeiro de Sousa Martins, S. A. Correia Carabineiro, J. Wang, B. Gonalo Martins Rocha, F. J. Maldonado-Hodar, A. J. Latourrette de Oliveira Pombeiro, *ChemCatChem* 2017, 9, 1211–1221.
- [8] a) L. M. D. R. S. Martins, M. P. de Almeida, S. A. C. Carabineiro, J. L. Figueiredo, A. J. L. Pombeiro, *ChemCatChem* 2013, 5, 3847–3856; b) A. P. C. Ribeiro, L. M. D. R. S. Martins, S. A. C. Carabineiro, J. G. Buijnsters, J. L. Figueiredo, A. J. L. Pombeiro, *ChemCatChem* 2018, 10, 1821–1828.
- [9] D. Tsukamoto, A. Shiro, Y. Shiraishi, T. Hirai, *J. Phys. Chem. C* 2011, 115, 19782–19788.
- [10] S. Shylesh, C. Srilakshmi, A. P. Singh, B. G. Anderson, *Microporous Mesoporous Mater.* 2007, 99, 334–344.
- [11] S. E. Dapurkar, A. Sakthivel, P. Selvam, *New J. Chem.* 2003, 27, 1184–1190.
- [12] B. M. Weckhuysen, I. E. Wachs, R. A. Schoonheydt, *Chem. Rev.* 1996, 96, 3327–3350.
- [13] a) J.-M. Jehng, I. E. Wachs, B. M. Weckhuysen, R. A. Schoonheydt, *J. Chem. Soc. Faraday Trans.* 1995, 91, 953–961; b) L. M. Baker, W. L. Carrick, *J. Org. Chem.* 1968, 33, 616–618.
- [14] a) H. E. B. Lempers, R. A. Sheldon, *J. Catal.* 1998, 175, 62–69; b) E. V. Spinace, U. Schuchardt, D. Cardoso, *Appl. Catal. A* 1999, 185, L193–L197.
- [15] P. Michorczyk, J. Ogonowski, P. Kustrowski, L. Chmielarz, *Appl. Catal. A* 2008, 349, 62–69.
- [16] a) A. P. Singh, T. Selvam, *J. Mol. Catal. A* 1996, 113, 489–497; b) K. Li, D. Zhou, J. Deng, X. Lu, Q. Xia, *J. Mol. Catal. A* 2014, 387, 31–37.
- [17] a) N. Ulagappan, C. N. R. Rao, *Chem. Commun.* 1996, 1047–1048; b) T. J. Pinnavaia, M. S. Tzou, S. D. Landau, *J. Am. Chem. Soc.* 1985, 107, 4783–4785; c) D. L. Myers, J. H. Lunsford, *J. Catal.* 1986, 99, 140–148.
- [18] J. S. Beck, J. C. Vartuli, W. J. Roth, M. E. Leonowicz, C. T. Kresge, K. D. Schmitt, C. T. W. Chu, D. H. Olson, E. W. Sheppard, S. B. McCullen, J. B. Higgins, J. L. Schlenker, *J. Am. Chem. Soc.* 1992, 114, 10834–10843.
- [19] a) H. I. Melendez-Ortiz, L. A. Garcıa-Cerda, Y. Olivares-Maldonado, G. Cas-truita, J. A. Mercado-Silva, Y. A. Perera-Mercado, *Ceram. Int.* 2012, 38, 6353–6358; b) Q. Cai, Z.-S. Luo, W.-Q. Pang, Y.-W. Fan, X.-H. Chen, F.-Z. Cui, *Chem. Mater.* 2001, 13, 258–263.
- [20] W. Zhang, T. J. Pinnavaia, *Catal. Lett.* 1996, 38, 261–265.
- [21] S. Music, N. Filipovi-Vincekovic, L. Sekovanic, *Braz. J. Chem. Eng.* 2011, 28, 89–94.
- [22] X. Zhao, X. Wang, *J. Mol. Catal. A* 2007, 261, 225–231.
- [23] T. Ivanova, K. Gesheva, A. Cziraki, A. Szekeres, E. Vlaikova, *J. Phys. Conf. Ser.* 2008, 113, 012030.
- [24] F. Cavani, M. Koutyrev, F. Trifiro, A. Bartolini, D. Ghisletti, R. Iezzi, A. Santucci, G. Del Piero, *J. Catal.* 1996, 158, 236–250.
- [25] M. Roy, S. Ghosh, M. K. Naskar, *Mater. Chem. Phys.* 2015, 159, 101–106.
- [26] P. Michorczyk, P. Pietrzyk, J. Ogonowski, *Microporous Mesoporous Mater.* 2012, 161, 56–66.
- [27] M. Cheriau, M. S. Rao, A. M. Hirt, I. E. Wachs, G. Deo, *J. Catal.* 2002, 211, 482–495.
- [28] L. F. Liotta, A. M. Venezia, G. Pantaleo, G. Deganello, M. Gruttadauria, R. Noto, *Catal. Today* 2004, 91–92, 231–236.
- [29] a) Y. Wang, Y. Ohishi, T. Shishido, Q. Zhang, W. Yang, Q. Guo, H. Wan, K. Takehira, *J. Catal.* 2003, 220, 347–357; b) M. L. Peterson, G. E. Brown, G. A. Parks, C. L. Stein, *Geochim. Cosmochim. Acta* 1997, 61, 3399–3412; c) K. Takehira, Y. Ohishi, T. Shishido, T. Kawabata, K. Takaki, Q. Zhang, Y. Wang, *J. Catal.* 2004, 224, 404–416.
- [30] A. P. Singh, N. Torita, S. Shylesh, N. Iwasa, M. Arai, *Catal. Lett.* 2009, 132, 492–499.
- [31] A. A. Alshehri, A. M. Alhanash, M. Eissa, M. S. Hamdy, *Appl. Catal. A* 2018, 554, 71–79.
- [32] S. Samanta, N. K. Mal, A. Bhaumik, *J. Mol. Catal. A* 2005, 236, 7–11.
- [33] X. Zhang, Y. Yue, Z. Gao, *Catal. Lett.* 2002, 83, 19–25.
- [34] a) A. K. Poswal, A. Agrawal, A. K. Yadav, C. Nayak, S. Basu, S. R. Kane, C. K. Garg, D. Bhattacharyya, S. N. Jha, N. K. Sahoo, *AIP Conf. Proc.* 2014, 1591, 649–651; b) S. Basu, C. Nayak, A. K. Yadav, A. Agrawal, A. K. Poswal, D. Bhattacharyya, S. N. Jha, N. K. Sahoo, *J. Phys. Conf. Ser.* 2014, 493, 012032.
- [35] D. C. Koningsberger, R. Prins, *X-ray absorption: principles, applications, techniques of EXAFS, SEXAFS, and XANES*, Wiley, New York, 1988.
- [36] B. Ravel, M. Newville, *J. Synchrotron Radiat.* 2005, 12, 537–541.
- [37] S. Kelly, D. Hesterberg, B. Ravel, *Methods of soil analysis* 2008, 5, 387–464.

Manuscript received: February 25, 2018

Revised manuscript received: April 17, 2018

Accepted manuscript online: April 23, 2018

Version of record online: June 1, 2018



Highly selective aqueous phase hydrogenation of phenols over nanostructured RuO₂ on MCM-41 catalysts

K.J. Betsy^a, Anish Lazar^{a,b}, C.P. Vinod^{a,b,c,*}

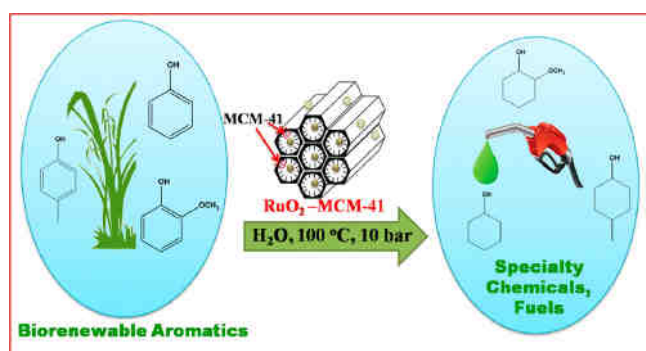
^a Catalysis Division, CSIR-National Chemical Laboratory, Dr Homi Bhabha Road, Pune, 411 008, India

^b Academy of Scientific and Innovative Research (AcSIR), Anusandhan Bhawan, 2, Rafi Marg, New Delhi-110 001, India

^c Center of Excellence on Surface Science, CSIR-National Chemical Laboratory, Dr Homi Bhabha Road, Pune, 411 008, India



GRAPHICAL ABSTRACT



ARTICLE INFO

Article history:

Received 10 July 2017

Received in revised form 28 September 2017

Accepted 4 November 2017

Keywords:

RuO₂ catalysts

Phenol

Cyclohexanol

Cyclohexanone

Aqueous phase hydrogenation reactions

ABSTRACT

Selective aqueous phase hydrogenation of phenol as well as its derivatives is important for the synthesis of chemical intermediates which are crucial for the manufacture of high-tonnage commodities and a multitude of value added platform chemicals. Herein, we report a facile catalyst made of highly dispersed small RuO₂ nanoparticles supported on mesoporous MCM-41 using one-pot approach. The optimal 5RuO₂-MCM-41 catalyst with particle size 6–8 nm showed excellent activity and selectivity in aqueous phase hydrogenation of phenol and other functionalized substrates, which are building blocks of lignin, to corresponding cyclohexanol products without any additives. These catalysts showed better stability and can be reused several times without any significant drop in activity which proves the heterogeneity of the immobilized oxide catalyst.

© 2017 Elsevier B.V. All rights reserved.

1. Introduction

Catalytic transformations of biorenewable aromatics to value added chemicals and fuels through economic and energy efficient process have currently attracted considerable attention. Global demand for polymers like nylon-6, nylon-6,6, and also the depletion

* Corresponding author at: Catalysis Division, CSIR-National Chemical Laboratory, Dr Homi Bhabha Road, Pune, 411 008, India.

E-mail address: cp.vinod@ncl.res.in (C.P. Vinod).

in the products derived from non-renewable energy sources has forced to identify a renewable feedstock that replace the existing materials [1–3]. Lignocellulosic biomass is considered as the most accessible renewable feedstock for a variety of fine chemicals and biofuels [4]. Among which, lignin accounts for the second most abundant biomass in nature [5], which after depolymerization yields highly oxygenated aromatic monomers mainly, phenolic compounds [6]. By utilizing both heterogeneous and homogeneous catalysts of transition metals, including Pd [7], Ru [8], Pt [9], biomass derived phenolic bio-oil components (phenols, guaiacols

and syringols) are transformed to their corresponding cycloalkanes with high selectivity. Selective hydrogenation of phenols are desirable strategy to yield a variety of products involving cycloketones, cycloalcohols, arenes, cycloalkanes and methane which are key intermediates to higher value commodities.

Generally, the phenol hydrogenation reactions are carried out in the vapor phase at elevated temperatures and pressures over supported Pd catalysts, but they suffers deactivation due to coke formation [10]. Later on, many researchers have contributed to the liquid phase hydrogenation reaction of phenol using Pd [11], Pt [12], Rh [13] catalysts on different supports for improving the activity. Previous investigations suggest that the metal sites facilitate the activation of H_2 and basic sites in support adsorb phenol during hydrogenation reactions. Depending on the geometry of phenol adsorption on different sites on the support, the product selectivity can be tuned [14]. Designing a heterogeneous catalyst using ruthenium nanoparticles is of great interest due to its excellent intrinsic ability for hydrogenation reactions [15–17] and cost effective compared to other noble metals like Pd. A detailed insight in to the literature reveals that, to date, there are very few efforts to utilize ruthenium as a catalyst to selectively hydrogenate phenolic entities. In the recent past, studies on ruthenium catalysts has been a subject of great interest to hydrogenate arenes [6], hydrodeoxygenation of lignin derived phenols [8], and selective hydrogenolysis of phenols [18], since they contributes to the concept of chemicals from nature. Main shortcoming with Ru based catalysts is the metal detachment from the support and resulting in leaching which reduces the efficiency of the catalyst in liquid phase phenol hydrogenation. Hence it is challenging to develop a stable, highly efficient and selective catalyst for phenol hydrogenation in liquid phase. By tuning the size and shape of the nanoparticles and the properties of the support, the catalytic performance can be improved by achieving better physical and chemical reactivity [19]. Somorjai et al. has proved the remarkable size dependence of Ru NP on the CO oxidation reactivity where 6 nm catalyst showed 8-fold higher activity compared to 2 nm particles [20]. The catalytic activity trend by nanoparticles with different size has been subject of interest due to its practical and fundamental perspective. It can predict the structure sensitivity of catalytic reaction since particle size varies the surface atomic structure, oxidation state, metal-support interaction and the electronic state which influences the nature of active sites that tunes the product selectivity and conversion [21].

Identification of suitable solvent is significant in catalytic activity as it drastically influences the rate and selectivity in hydrogenation of phenolic compounds. The solvent for phenol hydrogenation should be stable to the catalyst and reaction conditions, dissolve and transport of H_2 , retain reactants and products in solution [22]. Generally, halogenated organic compounds [23], $ScCO_2$ [24], cyclohexane [25], ionic liquids [26], water [27] are used as solvents for phenol hydrogenation, among which green solvent water have attracted great attention due to non-polluting nature of environment. Recently, Yong Wang et al. have found that hydrogenation of phenol on Pd@mpg- C_3N_4 catalyst proceeds more effectively in water than in organic solvents. Further, DFT calculations showed that water molecule can lower the activation energy for the reaction and will accelerate the proton transfer involved in the hydrogenation of phenol and cyclohexanone to cyclohexanol [28]. The complete aqueous solubility of phenol could be achieved by increase in temperature and the low aqueous solubility of products favors easy separation.

In this present work, we demonstrate a one-pot approach to synthesize finely dispersed nanostructured RuO_2 immobilized on MCM-41 with different amounts of ruthenium with a goal of engineering Ru active sites. All the Ru-oxide catalysts were well characterized and the reaction conditions were optimized systematically.

The optimized $5RuO_2$ -MCM-41 catalyst facilitates the hydrogenation of phenol and its substrates including biomass derived phenolic compounds to give corresponding cycloalcohols selectively with high activity under mild conditions in aqueous medium. The RuO_2 -MCM-41 catalyst was found to be purely heterogeneous in nature and highly stable under reducing reaction environment. Thus, we have designed cost effective, greener, reusable, one-pot RuO_2 -MCM-41 heterogeneous catalyst for highly selective aqueous phase hydrogenation reactions of phenols to cycloalcohols.

2. Experimental

2.1. Materials

Ruthenium(III) chloride hydrate (99.9%), cetyltrimethyl ammonium bromide CTAB (98%), Tetraethylorthosilicate TEOS (Sigma Aldrich), Ethylenediamine (Fluka), Ethanol (Merck) and Phenol (Spectrochem), unless otherwise mentioned, reagents and solvents were purchased from Thomas Baker, Aldrich, Acros, all chemicals were used as received. All the experiments were done using ultra Millipore water.

2.2. One-pot synthesis of RuO_2 nanoparticles supported on MCM-41

Typically, 8 mmol of CTAB was dissolved in 60 mL of water under stirring at 95 °C for 15 min and calculated amount of $RuCl_3$ was added. Simultaneously, in another beaker, 2.5 ml of TEOS was added to 20 mL of ethanol mixed thoroughly and 1.5 mL of ethylenediamine was added in drops and stirred at RT for 30 min to get clear solution. The resulting clear solution was added in drop wise manner into the above metal precursor solution which is maintained at 75 °C and kept for stirring for next 2 h. The resulting reaction mixture was cooled to room temperature and aged overnight. The residue was filtered, washed thoroughly with water and ethanol to remove excess of ethylenediamine and CTAB. The obtained powder was dried at 80 °C for 12 h and calcined at 400 °C for 6 h (at a ramp rate of 2 °C/min). The Ru loading on MCM-41 was controlled to 0.5, 1, 2.5, 4, 5, and 10 wt% by changing the amount of metal precursor to explore the effect of metal content and particle size. Compared to the dry synthesis method [29], one-pot approach provides better uniform dispersion as well as controllable particle size of RuO_2 nanoparticle supported on silica materials like MCM-41.

2.3. Catalytic aqueous phase hydrogenation of phenols

The hydrogenation of phenol over RuO_2 -MCM-41 catalysts was investigated in a Parr 4842 autoclave (100 mL) equipped with a mechanical stirrer and temperature controller. The reaction pot was charged with phenol (1.6 mmol), water (10 mL), and catalyst (50 mg) and the autoclave was sealed and purged twice with H_2 to exclude air. A range of experiments were carried out to optimize the reaction conditions by varying temperature, pressure, solvent, amount of catalyst and time. After reaction, the catalyst was separated by centrifugation and the product extraction was done using chloroform, the phenol conversion and selectivity were determined using GC (Agilent 7890 connected with HP5 column and FID detector) and confirmed by GC-MS (Varian connected with HP5 column) (Figure S1). The crude product in chloroform was purified using column chromatography and analyzed by 1H NMR (Figure S2). To check reusability, after each cycle, the separated catalyst was washed repeatedly with water and acetone and dried at 100 °C for 12 h.

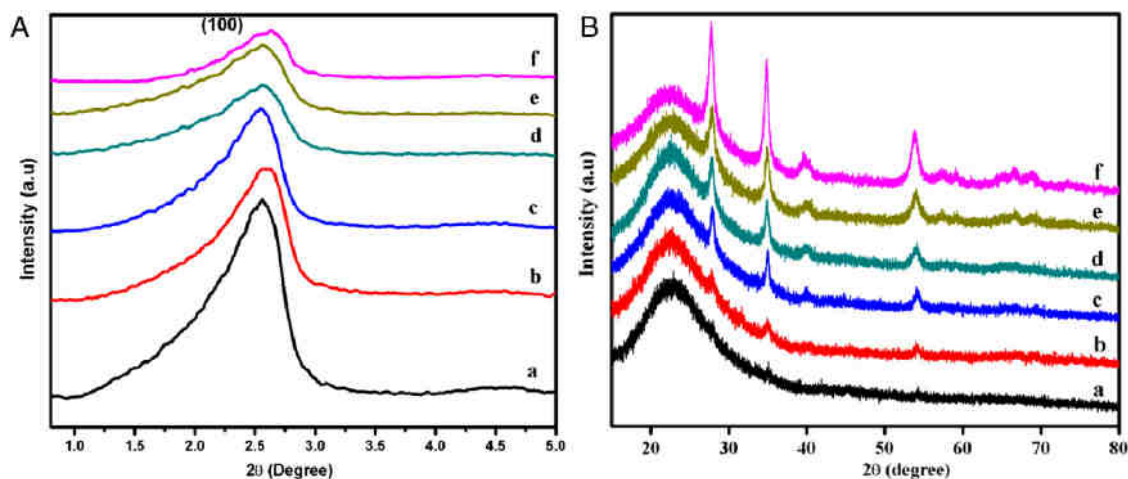


Fig. 1. Powder XRD patterns of RuO₂-MCM-41 catalysts in two different 2θ regions. (A) Small angle-XRD and (B) Wide angle-XRD: (a) 0.5RuO₂-MCM-41, (b) 1RuO₂-MCM-41, (c) 2.5RuO₂-MCM-41, (d) 4RuO₂-MCM-41, (e) 5RuO₂-MCM-41 and (f) 10RuO₂-MCM-41.

2.4. Catalyst characterization

(i) *Powder X-ray diffraction analysis:* PXRD analysis of all catalysts were measured using PANalytical X'pert Pro dual goniometer diffractometer with a Ni filtered Cu K α radiation (1.5418 Å) working under 40 kV and 30 mA.

(ii) *N₂ Sorption analysis:* Nitrogen adsorption/desorption isotherms and pore size distributions of the samples were collected by using Autosorb 1C Quantachrome, USA. The calculation of specific surface area was done by the BET model at a relative pressure of $P/P_0 = 0.06-0.3$.

(iii) *Transmission Electron Microscopy (TEM):* TEM images were recorded by FEI Tecnai TF-20 electron microscope, operating at 200 kV.

(iv) *Nuclear Magnetic Resonance Spectroscopy (NMR):* Magic angle spinning (MAS) NMR spectra for ²⁹Si nuclei was recorded on BRUKER DSX300 spectrometer at 7.05 T (resonance frequencies 59.595 MHz, rotor speed 10000 Hz and 75.43 MHz, rotor speed 10000 Hz)

(v) *X-ray Photoelectron Spectroscopy (XPS):* XPS measurements for the samples were carried out using an Ambient Pressure X-ray photoelectron spectrometer (AP-XPS) from Prevac, Poland.

3. Results and discussions

3.1. Catalyst characterization

The PXRD patterns of the synthesized RuO₂-MCM-41 catalysts were carried out in two different 2θ regions. To evaluate the regularity and formation of the mesoporous MCM-41 silica material by one-pot synthesis strategy was confirmed by the small angle XRD spectrum. A peak at 2.5° in Fig. 1A and Figure S3 (pure MCM-41) corresponds to the d_{100} reflection which is in accordance with the previously reported MCM-41 material [30,31]. Intensity of the (100) peak has decreased gradually with the loading of ruthenium which could be due to the anchoring of Ru on the MCM-41 mesoporous channels. In the wide angle XRD analysis (Fig. 1B) of different wt% of Ru loaded catalysts exhibited the typical reflections which are attributable to the tetragonal structure of RuO₂ (JCPDS No: 00-018-1139). The reflections from RuO₂ increased sharply with increase in metal content which indicates the growth of particle size. The Ru content in the fresh 5RuO₂-MCM-41 catalyst was confirmed by using ICP analysis (Spectro Acros ICP-OES) and was found to be ~4.8% with respect to the catalyst.

The textural properties of the synthesized material were analyzed by using N₂ adsorption-desorption method and the results

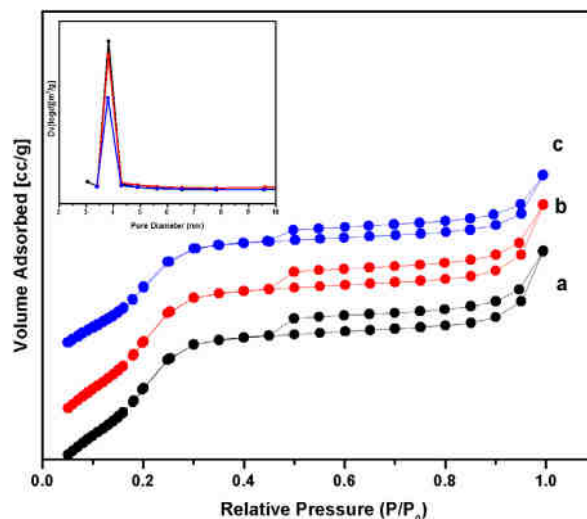


Fig. 2. N₂ adsorption-desorption isotherms and pore size distributions (inset) of (a) 0.5RuO₂-MCM-41, (b) 5RuO₂-MCM-41 and (c) 10RuO₂-MCM-41.

are outlined in Table S1. All RuO₂-MCM-41 catalysts showed typical type-IV isotherms with H1 hysteresis (Fig. 2) and the pore size distribution (inset) with unimodal pore having diameter of 3.8 nm which indicates the mesoporous nature of the support. The surface area and pore volume was found to decrease with increase in metal loading. To gain more insight into the size and morphology of the RuO₂-MCM-41 catalysts, transmission electron microscopy analysis was carried out. The TEM images of the catalysts shown in Fig. 3 reveal that RuO₂ nanoparticles were well dispersed on mesoporous MCM-41 support and the inset of Fig. 3a-c shows the average particle size distributions of the catalysts which increases from 3 nm to 15 nm for 2.5RuO₂-MCM-41, 5RuO₂-MCM-41 and 10RuO₂-MCM-41, respectively. In the higher metal loaded catalyst (10 wt%), the RuO₂ particle size was found to be <15 nm which clearly portrays the advantage of the one pot synthesis strategy using ethylenediamine as ligand which act as the metal coordination sites to stabilize and tune the particle size, and also maintains the basic pH for the formation of MCM-41 silica material. The mesoporous nature of the MCM-41 material from TEM images is in good agreement with the N₂ sorption and the PXRD results. In ²⁹Si CPMAS NMR spectra for RuO₂-MCM-41 catalysts shown in Fig. 4, a gradual decrease in the intensity was observed for the

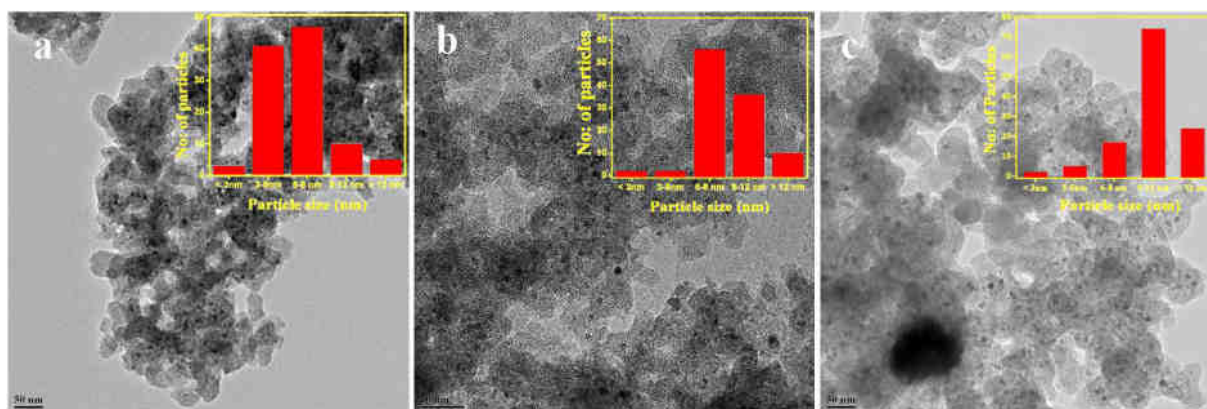


Fig. 3. TEM images and particle size distributions (inset) of (a) 2.5RuO₂-MCM-41, (b) 5RuO₂-MCM-41 and (c) 10RuO₂-MCM-41.

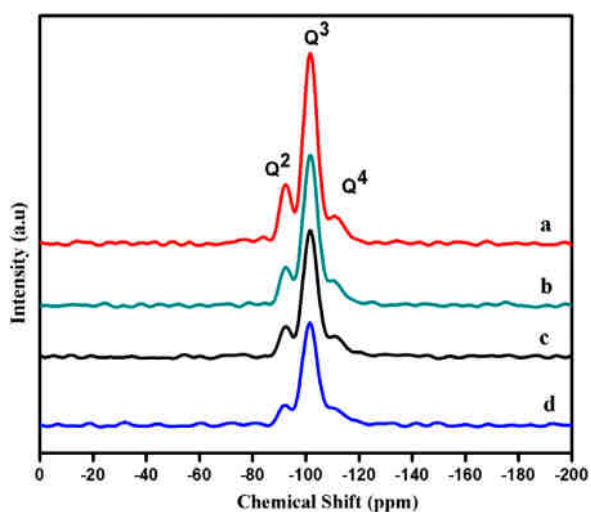


Fig. 4. ²⁹Si CPMAS NMR spectra of (a) 2.5RuO₂-MCM-41, (b) 4RuO₂-MCM-41, (c) 5RuO₂-MCM-41 and 10RuO₂-MCM-41.

three distinct peaks centered at -92 ppm, -102 ppm and -112 ppm correspond to the Q², Q³ and Q⁴ sites on silica framework, respectively, as the metal loading increased.

To better understand the oxidation state and chemical composition of RuO₂, XPS analysis was carried out. Fig. 5a shows the Ru

3d and C 1s spectra of the 5RuO₂-MCM-41 catalyst. Typically, Ru 3d_{5/2} spectrum is considered for identifying the electronic states of Ru, unfortunately, the Ru 3d_{3/2} spectrum are generally overlapped with C 1s spectrum which is observed at 284.5 eV. The Ru 3d_{5/2} peak of the Ru-oxide catalyst which is located at 280.9 eV shows that the metal is in +4 oxidation state [32]. In order to avoid the intervention from carbon, Ru 3p_{3/2} of the Ru-oxide catalyst was performed and peak at 462.5 eV confirms that the metal is in +4 oxidation state with the successful deposition of RuO₂ on MCM-41 [33].

3.2. Catalytic activity

The catalytic performances of the heterogenised RuO₂-MCM-41 catalysts were screened in liquid phase phenol hydrogenation reaction. In order to check the role of Ru metal in hydrogenation, we controlled the metal loading to 0.5, 1, 2.5, 4, 5 and 10 wt% by varying the amount of Ru precursor. The phenol conversion over RuO₂-MCM-41 catalysts increased sharply with the increase in total Ru content and showed 100% activity for 5 wt% loaded system, further increase in metal content did not show any decline in activity. It is worth mentioning that the selectivity also increased linearly towards cyclohexanol with metal loading. This activity trend in phenol hydrogenation reaction could be correlated with the Ru particle size which increased with the metal loading in the catalyst. The enhanced activity for larger RuO₂ particles compared to the smaller ones in low metal content may be due to the

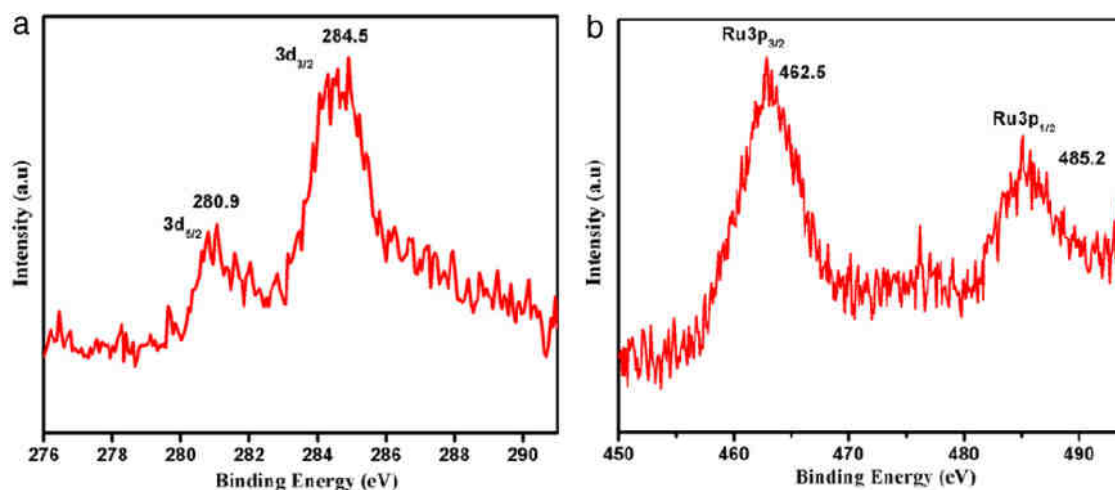


Fig. 5. Ru XPS spectra of 5RuO₂-MCM-41 catalyst. (a) Ru 3d and (b) Ru 3p.

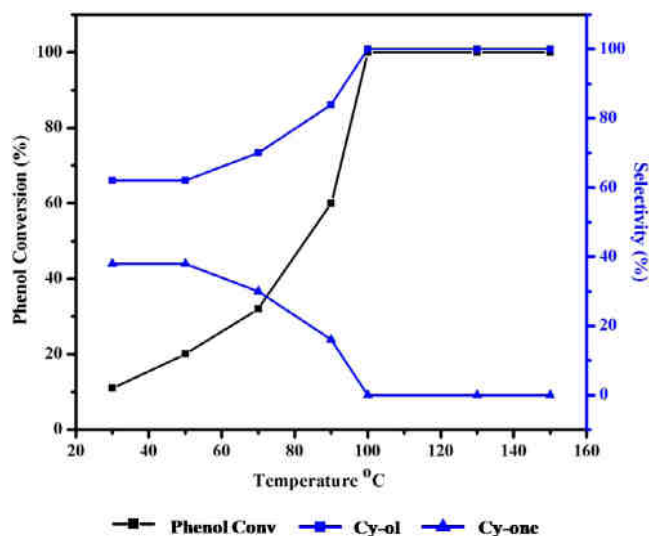


Fig. 6. Influence of reaction temperature on phenol conversion over 5RuO₂-MCM-41 catalyst. Reaction conditions as mentioned in footnote of Table 1.

formation of well defined facets which act as an active site for phenol hydrogenation reaction or due to easily reducible surface Ru oxide in larger particle size [20,34]. To confirm the importance of 5RuO₂-MCM-41 catalyst, activity (100%) of the catalyst was compared with pure MCM-41 (5%) and blank reaction (3%) and further control experiments were carried out using optimal 5RuO₂-MCM-41 catalyst.

Fig. 6 depicts the effect of reaction temperature on conversion of phenol and the product selectivity on 5RuO₂-MCM-41 catalyst. Cyclohexanol was found to be the major product with increase in temperature along with the increase in phenol conversion. As the reaction temperature was lowered to room temperature the phenol conversion rate was found to decrease along with the formation of mixture of cyclohexanol and cyclohexanone which shows that the formation of cyclohexanol occurs at the expense of cyclohexanone. Full conversion of phenol was attained at 100 °C with 100% selectivity towards cyclohexanol within 12 h. Further increase in temperature does not show any effect on conversion as well as selectivity. The reason for the increased rates at higher temperature may attribute to the augmentation of the diffusion rate of phenol in the channels of the catalyst. The time dependent study on phenol hydrogenation reaction using 5RuO₂-MCM-41 catalyst performed at 100 °C (Fig. 7) also points to the fact that cyclohexanone may be the intermediate for cyclohexanol formation. The conversion of phenol increased almost linearly with time and reached 50% within 6 h and full conversion was attained by 12 h with full selectivity for cyclohexanol. This result shows that the reaction time influenced the phenol conversion as well as the cyclohexanol selectivity to a great extent.

To extent the scope of 5RuO₂-MCM-41 catalyst, we have investigated the hydrogenation reactivity of various phenol derivatives which contains electron donating and electron withdrawing groups. According to the results shown in Table 2, all phenolic substrates exhibited >90% conversion with higher selectivity. Phenolic substrates with electron donating substituents exhibited higher activity compared to electron withdrawing system and also lower conversion for ortho-substitution (entries 3, 6, 8) compared to para- (entries 2, 4, 5, 7) due to higher steric effect. In short, cyclohexanol and substituted cyclohexanol are found to be the major products for these reactions using Ru-oxide catalysts. In halophenols (entries 2–4), hydrodehalogenation has occurred with the elimination of mineral acids such as HCl and HBr to form

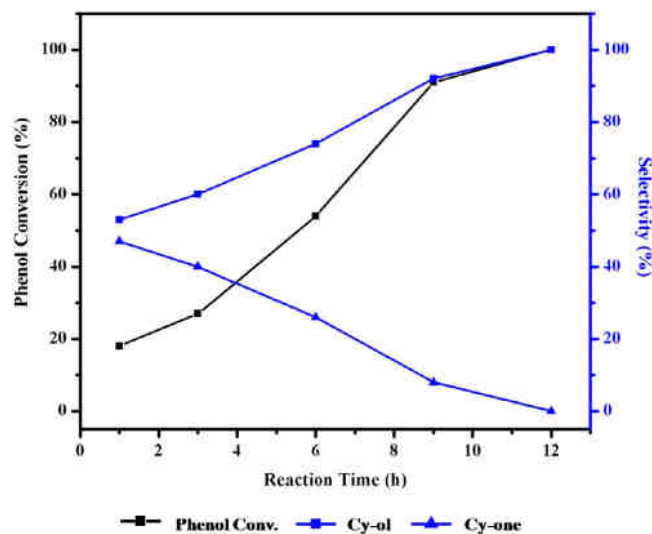


Fig. 7. Effect of reaction time on phenol conversion over 5RuO₂-MCM-41 catalyst. Reaction conditions as mentioned in footnote of Table 1.

cyclohexanol with phenol as intermediate, via. hydrogenolysis of C–X bond (X = –Cl and –Br) and further hydrogenation to form cyclohexanol [35]. Out of these halophenols, reduction rate of chlorophenols are higher than bromophenol owing to its less bulkier effect and geometrical position in phenolic ring [36]. Moreover, it is worthy to note that hydrogenation of guaiacols which is obtained from lignin depolymerization showed 95% conversion with selectivity to cycloalcohols (entry 6). In addition, hydrogenolysis pathway of guaiacols favors the formation of cyclohexanol which diminishes product selectivity (entries 5, 6). But in the case of alkyl substituted phenols (entries 7 and 8), hydrogenolysis reaction is inhibited due to the higher dissociation energy of –CH₃ group which adopts low energy hydrogenation pathway to form substituted cyclohexanols.

The reusability test of 5RuO₂-MCM-41 catalyst for selective hydrogenation of phenols in aqueous medium was performed as it represents the important part in the economic evaluation of the catalyst for various chemical transformations. The catalyst was recovered after each reaction by centrifugation, washed, dried and reused for next run. As shown in Fig. 8, 5RuO₂-MCM-41 catalyst was found to be stable, highly reusable in phenol hydrogenation where both phenol conversion and cyclohexanol selectivity remains same even after five successive runs. The ICP analysis of spent 5RuO₂-MCM-41 catalyst was found to be ~4.6% which indicates negligible metal leaching from the catalyst during reaction. This retention of activity clearly reveals that RuO₂-MCM-41 catalysts synthesized by one-pot approach are purely heterogeneous in nature as no metal loss observed under the reaction conditions for five cycles. No obvious deactivation of the catalyst was realized from XRD and TEM analysis of the spent catalyst (Figure S2) where the morphology and particle size of RuO₂ has maintained in the range of 6–10 nm even after several cycles of hydrogenation reaction, which supports the experimental results.

4. Conclusion

In this contribution, we report a facile one-pot approach to synthesize size controlled RuO₂ nanostructures supported MCM-41 catalysts. Optimum RuO₂ loaded catalyst exhibited excellent activity in selective aqueous phase hydrogenation of phenol and lignin derived phenols under mild conditions. The RuO₂ nanoparticle size of the optimum catalyst was found to be around 6–8 nm. The combination of different characterization techniques

Table 1
Aqueous-Phenol hydrogenation with nRuO₂-MCM-41^a catalysts.

Entry	Catalyst	Conversion (%)	Selectivity (%)		Ref.
			Cy-ol	Cy-one	
1	Without catalyst	3	100	0	Present work
2	Pure MCM-41	5	92	8	"
3	0.5RuO ₂ -MCM-41	24	73	27	"
4	1RuO ₂ -MCM-41	33	75	25	"
5	2.5RuO ₂ -MCM-41	47	90	10	"
6	4RuO ₂ -MCM-41	88	96	4	"
7	5RuO ₂ -MCM-41	100	100	0	"
8	10RuO ₂ -MCM-41	100	100	0	"
9 ^b	Ru/Al ₂ O ₃	95	52	48	[25]
10 ^b	Ru/ACC	89	99	1	[37]

Reaction conditions: phenol–1.6 mmol, H₂O–10 mL, Cat–50 mg, T–100 °C, P H₂ –1 MPa, t–12 h.

^a nRuO₂-MCM-41, where n indicates wt% of Ru loading with respect to support.

^b By the use of state-of-the-art catalysts.

Table 2
Substrate Study of phenol and its derivatives for hydrogenation reactions.

Entry	Substrates	Conversion (%)	Product Selectivity (%)				
			1	2	3	4	5
1		100	-	-	100	-	-
2		95	8	6	86	-	-
3		90	11	9	80	-	-
4		93	53	8	39	-	-
5		100	-	3	31	31	35
6		95	-	5	20	20	55
7		98	-	-	-	-	100
8		91	-	-	-	8	92

Reaction conditions: Reactant- 0.16 mmol, H₂O-10 mL, Cat- 50 mg (5RuO₂-MCM-41), T- 100°C, P H₂- 1 MPa, t- 24 h

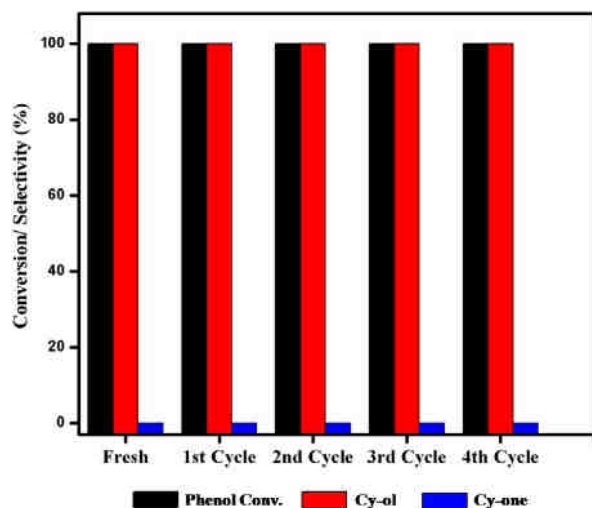


Fig. 8. Reusability of 5RuO₂-MCM-41 catalyst in aqueous phase phenol hydrogenation reaction. Reaction conditions as mentioned in footnote of Table 1.

and activity results showed that RuO₂-MCM-41 catalysts are highly active, stable and reusable and is a better candidate to hydrogenate bio-renewable aromatics to useful platform chemicals.

Acknowledgments

CPV thanks Director, CSIR-NCL for continuous support. This work was funded by CSIR-NCL through a grant MLP030626 and partially supported by GAP-309826 BRNS grant.

Appendix A. Supplementary data

Supplementary material related to this article can be found online at <https://doi.org/10.1016/j.nanos.2017.11.004>.

References

- [1] A. Corma, S. Iborra, A. Vely, Chemical routes for the transformation of biomass into chemicals, *Chem. Rev.* 107 (2007) 2411–2502.
- [2] J. Zakzeski, P.C.A. Bruijninx, A.L. Jongerius, B.M. Weckhuysen, The catalytic valorization of lignin for the production of renewable chemicals, *Chem. Rev.* 110 (2010) 3552–3599.
- [3] R.D. Perlack, L.L. Wright, A.F. Turhollow, R.L. Graham, B.J. Stokes, D.C. Erbach, Biomass as Feedstock for Bioenergy and Bioproducts Industry: The Technical Feasibility of a Billion Ton Annual Supply, Oak Ridge National Laboratory, Oak Ridge, TN, 2005.
- [4] C. Xu, R.A.D. Arancon, J. Labidi, R. Luque, Lignin depolymerisation strategies: towards valuable chemicals and fuels, *Chem. Soc. Rev.* 43 (2014) 7485–7500.
- [5] B.M. Upton, A.M. Kasko, Strategies for the conversion of lignin to high-value polymeric materials: Review and perspective, *Chem. Rev.* 116 (2016) 2275–2306.
- [6] X. Cui, A.-E. Surkus, K. Junge, C. Topf, J. Radnik, C. Kreyenschulte, M. Beller, Highly selective hydrogenation of arenes using nanostructured ruthenium catalysts modified with a carbon–nitrogen matrix, *Nature Commun.* 7 (2016) 11326.
- [7] C. Zhao, Y. Kou, A.A. Lemonidou, X. Li, J.A. Lercher, Highly selective catalytic conversion of phenolic bio-oil to alkanes, *Angew. Chem. Int. Ed.* 48 (2009) 3987–3990.
- [8] K.L. Luska, P. Migowski, S. El Sayed, W. Leitner, Synergistic interaction within bifunctional ruthenium nanoparticle/SILP catalysts for the selective hydrodeoxygenation of phenols, *Angew. Chem.* 127 (2015) 15976–15981.
- [9] D.-Y. Hong, S.J. Miller, P.K. Agrawal, C.W. Jones, Hydrodeoxygenation and coupling of aqueous phenolics over bifunctional zeolite-supported metal catalysts, *Chem. Commun.* 46 (2010) 1038–1040.
- [10] L.M. Sikhvivilu, N.J. Coville, D. Naresh, K.V.R. Chary, V. Vishwanathan, Nanotubular titanate supported palladium catalysts: The influence of structure and morphology on phenol hydrogenation activity, *Appl. Catal., A* 324 (2007) 52–61.

- [11] H. Liu, T. Jiang, B. Han, S. Liang, Y. Zhou, Selective phenol hydrogenation to cyclohexanone over a dual supported Pd–Lewis acid catalyst, *Science* 326 (2009) 1250.
- [12] A.K. Talukdar, K.G. Bhattacharyya, S. Sivasanker, Hydrogenation of phenol over supported platinum and palladium catalysts, *Appl. Catal., A* 96 (1993) 229–239.
- [13] S.-i. Fujita, T. Yamada, Y. Akiyama, H. Cheng, F. Zhao, M. Arai, Hydrogenation of phenol with supported Rh catalysts in the presence of compressed CO₂: Its effects on reaction rate, product selectivity and catalyst life, *J. Supercrit. Fluids* 54 (2010) 190–201.
- [14] Y. Wang, J. Yao, H. Li, D. Su, M. Antonietti, Highly selective hydrogenation of phenol and derivatives over a Pd@Carbon nitride catalyst in aqueous media, *J. Am. Chem. Soc.* 133 (2011) 2362–2365.
- [15] S. Galvagno, G. Capannelli, G. Neri, A. Donato, R. Pietropaolo, Hydrogenation of cinnamaldehyde over Ru/C catalysts: effect of Ru particle size, *J. Mol. Catal.* 64 (1991) 237–246.
- [16] J. Ning, J. Xu, J. Liu, F. Lu, Selective hydrogenation of benzene to cyclohexene over colloidal ruthenium catalyst stabilized by silica, *Catal. Lett.* 109 (2006) 175–180.
- [17] R. Marcos Esteban, K. Schütte, D. Marquardt, J. Barthel, F. Beckert, R. Mülhaupt, C. Janiak, Synthesis of ruthenium@graphene nanomaterials in propylene carbonate as re-usable catalysts for the solvent-free hydrogenation of benzene, *Nano-Struct. Nano-Objects* 2 (2015) 28–34.
- [18] Y.-B. Huang, L. Yan, M.-Y. Chen, Q.-X. Guo, Y. Fu, Selective hydrogenolysis of phenols and phenyl ethers to arenes through direct C–O cleavage over ruthenium–tungsten bifunctional catalysts, *Green Chem.* 17 (2015) 3010–3017.
- [19] B.F. Machado, M. Oubenali, M. Rosa Axet, T. Trang Nguyen, M. Tunckol, M. Girleanu, O. Ersen, I.C. Gerber, P. Serp, Understanding the surface chemistry of carbon nanotubes: Toward a rational design of Ru nanocatalysts, *J. Catal.* 309 (2014) 185–198.
- [20] S.H. Joo, J.Y. Park, J.R. Renzas, D.R. Butcher, W. Huang, G.A. Somorjai, Size effect of ruthenium nanoparticles in catalytic carbon monoxide oxidation, *Nano Lett.* 10 (2010) 2709–2713.
- [21] A. Aho, S. Roggan, O.A. Simakova, T. Salmi, D.Y. Murzin, Structure sensitivity in catalytic hydrogenation of glucose over ruthenium, *Catal. Today* 241 (Part B) (2015) 195–199.
- [22] J. He, C. Zhao, J.A. Lercher, Impact of solvent for individual steps of phenol hydrodeoxygenation with Pd/C and HZSM-5 as catalysts, *J. Catal.* 309 (2014) 362–375.
- [23] H. Liu, T. Jiang, B. Han, S. Liang, Y. Zhou, Selective phenol hydrogenation to cyclohexanone over a dual supported Pd–Lewis acid catalyst, *Science* 326 (2009) 1250–1252.
- [24] H. Yoshida, S. Narisawa, S.-i. Fujita, M. Arai, Multiphase reaction media including dense phase carbon dioxide and/or water: A case study for hydrogenation of phenol with a Pd/Al₂O₃ catalyst, *J. Mol. Catal. A: Chem.* 379 (2013) 80–85.
- [25] A.N. Raut, S.U. Nandanwar, Y.R. Suryawanshi, M. Chakraborty, S. Jauhari, S. Mukhopadhyay, K.T. Shenoy, H.C. Bajaj, Liquid phase selective hydrogenation of phenol to cyclohexanone over Ru/Al₂O₃ nanocatalyst under mild conditions, *Kinet. Catal.* 57 (2016) 39–46.
- [26] A. Chen, G. Zhao, J. Chen, L. Chen, Y. Yu, Selective hydrogenation of phenol and derivatives over an ionic liquid-like copolymer stabilized palladium catalyst in aqueous media, *RSC Adv.* 3 (2013) 4171–4175.
- [27] Y. Xiang, L. Ma, C. Lu, Q. Zhang, X. Li, Aqueous system for the improved hydrogenation of phenol and its derivatives, *Green Chem.* 10 (2008) 939–943.
- [28] Y. Li, X. Xu, P. Zhang, Y. Gong, H. Li, Y. Wang, Highly selective Pd@mpg-C₃N₄ catalyst for phenol hydrogenation in aqueous phase, *RSC Adv.* 3 (2013) 10973–10982.
- [29] M. Gopiraman, S. Ganesh Babu, Z. Khatri, W. Kai, Y.A. Kim, M. Endo, R. Karvemu, I.S. Kim, Dry synthesis of easily tunable nano ruthenium supported on graphene: novel nanocatalysts for aerial oxidation of alcohols and transfer hydrogenation of ketones, *J. Phys. Chem. C* 117 (2013) 23582–23596.
- [30] Q. Cai, Z.-S. Luo, W.-Q. Pang, Y.-W. Fan, X.-H. Chen, F.-Z. Cui, Dilute solution routes to various controllable morphologies of MCM-41 silica with a basic medium, *Chem. Mater.* 13 (2001) 258–263.
- [31] H.I. Meléndez-Ortiz, L.A. García-Cerda, Y. Olivares-Maldonado, G. Castruita, J.A. Mercado-Silva, Y.A. Perera-Mercado, Preparation of spherical MCM-41 molecular sieve at room temperature: Influence of the synthesis conditions in the structural properties, *Ceram. Int.* 38 (2012) 6353–6358.
- [32] K.S. Kim, N. Winograd, X-ray photoelectron spectroscopic studies of ruthenium-oxygen surfaces, *J. Catal.* 35 (1974) 66–72.
- [33] P. Wang, H. Liu, Q. Tan, J. Yang, Ruthenium oxide-based nanocomposites with high specific surface area and improved capacitance as a supercapacitor, *RSC Adv.* 4 (2014) 42839–42845.

- [34] J. Jae, W. Zheng, A.M. Karim, W. Guo, R.F. Lobo, D.G. Vlachos, The role of Ru and RuO₂ in the catalytic transfer hydrogenation of 5-hydroxymethylfurfural for the production of 2,5-dimethylfuran, *ChemCatChem* 6 (2014) 848–856.
- [35] T.T. Bovkun, Y. Sasson, J. Blum, Conversion of chlorophenols into cyclohexane by a recyclable Pd-Rh catalyst, *J. Mol. Catal. A: Chem.* 242 (2005) 68–73.
- [36] T. Tsukinoki, T. Kakinami, Y. Iida, M. Ueno, Y. Ueno, T. Mashimo, H. Tsuzuki, M. Tashiro, Hydrogenation of halophenols to cyclohexanols using Raney Nickel-Aluminium alloy in saturated Ba(OH)₂ solution under mild conditions, *J. Chem. Soc. Chem. Commun.* (1995) 209–210.
- [37] Z. Li, M. Garedew, C.H. Lam, J.E. Jackson, D.J. Miller, C.M. Saffron, Mild electrocatalytic hydrogenation and hydrodeoxygenation of bio-oil derived phenolic compounds using ruthenium supported on activated carbon cloth, *Green Chem.* 14 (2012) 2540–2549.

About the Author

Ms. Betsy K. J. was born on 08th October 1991 in Cochin, Kerala. She finished her high school education from Lady of Hope Anglo Indian High School, Vypin, and pursued Bachelor's Degree in Science from St. Teresa's College, Ernakulam (2009-2012). She completed her Master's Degree in Applied Chemistry from Cochin University of Science and Technology, Kerala, in 2014. She joined the Ph.D. program under the supervision of Dr. Vinod C. Prabhakaran, Senior Principal Scientist in Catalysis and Inorganic Chemistry Division, CSIR-National Chemical Laboratory, Pune, after qualifying CSIR-SRF. During her stay at CSIR-NCL, she published five research articles in peer-reviewed international journals. Her work was based on the synthesis of metal nanoparticles supported chemically modified silica-based heterogeneous catalysts and their applications for industrially important reactions results presented in this thesis.
